Summer 8-7-2020

Experimental Investigation into the Boundary Layer of a Robotic Anguilliform Propulsor

Jonathan R. Eastridge
jeastrid@uno.edu

Recommended Citation

Eastridge, Jonathan R., "Experimental Investigation into the Boundary Layer of a Robotic Anguilliform Propulsor" (2020). *University of New Orleans Theses and Dissertations*. 2807.
https://scholarworks.uno.edu/td/2807

Experimental Investigation into the Boundary Layer of a Robotic Anguilliform Propulsor

A Dissertation

Submitted to the Graduate Faculty of the
University of New Orleans
in partial fulfillment of the
requirements for the degree of

Doctor of Philosophy
in
Engineering and Applied Science
Naval Architecture and Marine Engineering

by

Jonathan R. Eastridge

B.S. University of New Orleans, 2016
M.S. University of New Orleans, 2017

August, 2020

Dedicated with love to my wife

Kristy Truong Eastridge

for making this experience worthwhile

Acknowledgments

First, I would like to thank Brandon Taravella, my dissertation advisor. He has done all one could expect a good advisor to do, including offering new perspectives in approaching problems, asking insightful questions, providing constructive critique, suggesting references and avenues for publishing or presenting my work, giving encouragement where necessary, and helping me cope with the basic struggles of being a graduate student. In short, he has taught me a great deal, and it has been a pleasure to work with him.

Each of my committee members, Kazim Akyuzlu, Lothar Birk, Nikolas Xiros, and Ralph Saxton, have taught and supported me with useful insight at various stages of my doctoral education. I appreciate the suggestions, recommendations, and advice provided by each of them.

The Office of Naval Research is acknowledged and thanked for providing funding and support.

Next, I would like to thank two other people who helped me complete this work, George Morrissey and Ryan Thiel. Both of them helpfully assisted with the setup of each experimental configuration and remained interested in my progress throughout. They regularly challenged my decisions and helped me think about issues with a different perspective. George, in particular, has always worked tirelessly with me on problems until they are solved. He would not rest until he exhausted his imagination for possible solutions (which always took a while). Without Ryan's patient training, experiments with NEELBOT would certainly *not* have been accomplished in a timely manner, and I would have undoubtedly destroyed the robot before actually getting to use it.

I would also like to thank my family and friends, especially my two cohorts and fellow PhD students, Shivank Srivastava and David Bonneval, for their friendship and assistance. Surviving graduate school was greatly facilitated by going through it with these two. Thanks to both of you. Shivank also provided the numerical simulations that are discussed at various places throughout. Additionally, I want to thank Anastassia Kosmopoulos for her eager assistance in the towing tank and for performing some of the time-consuming and monotonous processing of the PIV data.

Finally, I would like to thank my lovely wife, Kristy. We were married in the first year of my PhD, and she has been so industrious, humble, patient, and supportive throughout this journey. I am immensely thankful for her love and willingness to support me in this endeavor. Here's to our next adventure together!

Table of Contents

List of Figures

List of Tables

Abstract

Boundary layer information local to three longitudinal positions has been characterized for a 130 cm long biomimetic self-propulsor known as NEELBOT-1.1 that swims with undulatory anguilliform-like motions, via analysis of stereo particle image velocimetry (PIV) measurements for key moments in the undulation cycle and for numerous combinations of swimming conditions and motion parameters, ideal and non-ideal. No obvious turbulent flow structures or indications of boundary layer separation were observed at nonzero advance speeds, and skin friction coefficients were subsequently estimated for magnitude relative to the dynamic pressure associated with operation at the design swimming speed of $U_o = 0.25\,\mathrm{m/s}$. Estimates were correlated with measurements made for an oscillating and non-oscillating cylindrical test article that were benchmarked by initial mono PIV investigations of steady laminar flow over a flat plate at zero incidence which was tested while stationary and oscillating in its own plane. Behavior of boundary layer profiles pertaining to the robot, apparently significantly influenced by the traveling flexion waves characteristic of the anguilliform motions, is clearly distinguished from local oscillatory flow structures related to the other two test articles. Approximately 10–15% increases in local skin friction are observed for the robot over similar conditions for the cylinder, and downstream vortex shedding is readily observed for the oscillating cylinder.

The results of this thesis will be used in validation of numerical analyses performed in parallel with this research for the purpose of calculating the time-mean frictional drag experienced by the robot and to determine whether it can produce enough thrust to overcome its drag without simultaneously increasing it beyond realizable thrust generation capabilities. Theoretical hydrodynamic descriptions of the wake velocity field agreed well with previous PIV measurements, but the theory does not treat viscous effects. Furthermore, the preliminary semi-empirical, quasi-static attempts to estimate frictional drag were shown to under-predict the actual drag by net force measurements taken while towing the robot at its design speed which was undulating for that expected swimming speed, hence the necessity of this thesis as further investigation.

Keywords: anguilliform swimmer; undulating propulsor; hydrodynamics; boundary layer theory; wall shear stress; skin friction; drag; particle image velocimetry (PIV); experimental methods

Introduction

Though modern American Naval warfare has seen a decline in surface-level activity, it has had to combat the littoral and intelligent power projection of foreign navies which often force operations to proceed in hazardous shallow-water areas and riverine environments. Such conditions are confronted in missions such as Intelligence, Surveillance, and Reconnaissance (ISR) which frequently pose difficult and perilous affairs for Navy personnel in monitoring and data collection. To reduce risk and expand collection opportunities, new methods and sensors are constantly undergoing research and development. Autonomous underwater vehicles (AUVs) have been of great concern for a few decades, especially in pursuit of minimal acoustic, radar, and optical signatures. Such "quiet" robots are entreated to carry sensors into hazardous areas in support of littoral ISR assignments.

The present investigation concerns the development of a fundamental understanding of the fluid dynamics associated with a particular AUV that could eventually meet some special Naval maritime sensing objectives. This is in reference to the underwater biomimetic robot, known colloquially as NEELBOT-1.1 or just NEELBOT, that was developed at the University of New Orleans (UNO) under research Grant N00014-11-1-0830 from the Office of Naval Research (ONR) and Grant N00014-12-1-0782 from the Defense University Research Instrumentation Program (DURIP). It was designed specifically to imitate members of the biological order Anguilliformes in response to the theory developed by Vorus (2005) and Vorus and Taravella (2011) and thus is said to swim with an anguilliform swimming motion. These works sought to develop a hydrodynamic model for wakeless swimming, i.e. self-propulsion where no free vortices are shed downstream, at constant advancement speed. More details regarding the historical narrative for this project are given in chapter 1.

As described by Potts (2015), a further application of the anguilliform robot—aside from the more obvious and likely use as a tool within the U.S. Navy's arsenal—may include implementation by environmental scientists to monitor various bodies of water while carrying a suite of measurement devices such as salinometers, thermometers, cameras, etc. Leaving behind minimal traces in the natural environment is desirable and should be achievable thanks to the robot's unique design.

To be more imaginative, one may apply this unique form of undulatory propulsion to improve the mobility, efficiency, and affordability of low speed ships and submarines. AUV technology often requires high efficiency and quiet operation, both of which are potential outcomes for the anguilliform robot. These ideas have arisen in response to limited onboard power supply and, for military application, undesirable acoustic signature detection due to wake vortices. It is also conceivable that the results of the current research may lead to improved performance of underwater appendages including rudders, roll stabilizers and/or lifting planes. This would be made possible by obtaining a more thorough understanding of the transitional nature of the flow field local to the body surface.

Boundary layer information is crucial to the estimation of swimming performance and is, expectedly, quite difficult to predict. The behavior of near-body flow fields is highly dependent on numerous factors; some important ones include local Reynolds numbers and body surface shape (in this case, most importantly, both transverse and stream-wise curvature). Inertial-to-viscous force ratios are always challenging to estimate, especially in oscillatory flows where characteristic velocities vary and numerous length scales are at play. Thus, a statement on the Reynolds number is reneged.

However, to qualitatively describe the importance of surface curvature effects on local skin friction, White (1969) provides the following example for laminar axial flow over a long, smooth cylinder: at $x/d = 100$, the local skin friction is nearly twice that of a flat plate with equivalent Reynolds number. NEELBOT has constant circular cross-section which should exhibit similar behavior for laminar conditions, assuming stream-wise curvature produces minimal disturbance.

A number of researchers, notably Lighthill (1971) and Ehrenstein, Marquillie, and Eloy (2014), have hypothesized that the thrust-drag balance associated with undulatory swimmers is strongly influenced by a viscous drag that “must for some reason be *many times greater* than that which would be associated with gliding motion” (Lighthill, 1971, emphasis added). Ehrenstein, Marquillie, and Eloy (2014) arrive at ~ 1.7 for the factor of skin friction increase. This conclusion of drag augmentation assumes that skin friction is entirely the culprit. Pressure drag is mentioned by Ehrenstein, Marquillie, and Eloy but mostly omitted from the discussion, as it is difficult to define since reactive thrust forces are also associated with pressure forces. A hypothesis, now known as the Bone–Lighthill boundary layer thinning hypothesis, states that skin friction over a large portion of the body surface is greater than would typically be expected at a rigid body length with corresponding Reynolds numbers, because lateral movements prevent boundary layers from growing to anything like the thickness associated with such a body length.

Other studies, e.g. Anderson, McGillis, and Grosenbaugh (2001), Vorus (2005), Lauder and Tytell (2006), Vorus and Taravella (2011), and Potts (2015), to name a few, suggest that the near-body flow conditions will be transitional in the sense that the boundary layer will transition from laminar to turbulent and possibly back to laminar. This type of intermittent flow is of interest to mostly all scientists and engineers dealing with fluid flow. Transitional boundary layer flow exists in various aerospace applications such as flow over wings (stationary and flapping) and flow within rocket nozzles. It also arises in many hydrodynamic applications such as flow around submarine hulls and flow through pipes. This suggestion is in opposition to the Bone–Lighthill hypothesis in that turbulent boundary layers almost always manifest as *thicker* than laminar boundary layers. A redemptive similarity may exist, however, assuming that the wall shear stresses associated with turbulent boundary layers are typically greater.

Vorus and Taravella (2011) conclude, based on their ideal flow theory model, that the anguilliform swimmer experiences normal surface stresses due entirely to Bernoulli pressures. This allowed them to separate these effects from tangential surface stresses. The arrival at this conclusion relied on the important assumption that boundary layers remain thin and, critically, no separation occurs. Justification was provided stating that mean flow Reynolds numbers for the swimming lamprey are around $\mathrm{Re} = 23{,}000$, providing laminar, though unsteady, boundary layers. Carling, Williams, and Bowtell (1998) mention even smaller Reynolds numbers for typical fish of 50–5,000. Tytell (2004) and Tytell and Lauder (2004) report their live American eels to swim at Reynolds numbers in the range 20,000–80,000, and Potts (2015) calculated the Reynolds number for NEELBOT swimming with motions designed for $0.25\,\mathrm{m/s}$ advancement to be 292,898.

Potts (2015) claims that the separation argument made by Vorus and Taravella (2011) is invalid and cites Sarpkaya (2006) who observed readily-occurring flow separation on oscillating cylinders. Vorus and Taravella (2011) continue their conclusions stating that boundary layer thinness and attachment are promoted by unsteady flow attributes and by the premise that anguilliform swimmers “slide” tangentially with minimum lateral disturbance in avoiding the creation of a vortical wake.

Ideal flow theory with a separately estimated drag coefficient has been applied extensively in the fish swimming research of the past, e.g. (Lighthill, 1960). Transient swimming modes, i.e. those for acceleration and maneuvering, necessarily involve hydrodynamic lift, which implies vortex shedding, and accompanies the transient displacement distributions required to execute the maneuver.

Lauder and Tytell (2006) note importantly that in their natural environment fishes rarely swim in controlled flows like those produced in laboratory flow tanks. On the contrary, fish locomotion likely proceeds in turbulent flows far more often than the unusually laminar, “calm-water” condition used in analysis. Flowing bodies of water are typically unsteady and rapid relative to fish locomotion, and often the benthic zone is characterized by uneven topographies; additionally, effects of windage manifest beneath the surface, all of which contribute to the turbulent nature of submarine habitats.

Still, one finds that ideal-condition analysis leads to improvement. Investigations within NEELBOT’s near-body flow regions are required for advancing one’s understanding of this inventive swimming technique and the hydrodynamics of undulating self-propulsion in general. Lighthill (1971) actually initiates a call to stimulate further experimental research into the thrust-drag balance to obtain the needed data for understanding drag augmentation. Specifically, the boundary layer behavior associated with NEELBOT’s swimming is of interest here. But since analytical mathematical theory presently remains elusive for general, unsteady boundary layers and intermittent flow regimes, one finds recourse in coupling experimental and numerical investigations. This paper is a report primarily on the former approach. A parallel effort under the same research grant persists in which numerical solutions to the flow problem at hand are pursued. These efforts are supported by the Office of Naval Research Grant N00014-17-1-2099 titled, “Investigation into the Boundary Layer of an Anguilliform-like Propulsor.”

This thesis is arranged as follows, representing approximately the current project’s chronological progression:

Chapter 1: Historical backdrop for the current project is provided which describes the position this study of undulatory self-propulsors takes in the field of experimental and numerical fluid dynamics.

Chapter 2: A brief mathematical description of the fluid mechanics associated with the flow problems at hand and a review of ideal anguilliform swimming theory are summarized.

Chapter 3: Some descriptive background and illustrative explanations regarding the experimental method used presently are given here.

Chapter 4: This chapter discusses experimental testing of a flat plate situated in a hydraulic flume which provides steady flow over the plate at zero incidence. Mono PIV is used here, and the results are compared with those from accompanying numerical studies.

Chapter 5: Implementing stereoscopic extensions to PIV is discussed and tested for a cylindrical test article in the UNO towing tank. Image and vector processing techniques are developed that carry over directly to experiments with the robotic eel, and CFD simulations are again compared.

Chapter 6: Near-body flow properties for the robotic eel are measured and analyzed for local estimates of wall shear stress and skin friction coefficients. Multiple swimming conditions are considered.

Chapter 7: Finally, conclusive remarks are provided to summarize this investigation and to flesh out lessons learned from these experimental studies.

1 Project History and Background

The nineteenth century saw great accomplishments in the mathematical development of solutions to the inviscid Euler equations, but it was not until the early twentieth century that great progress was made toward the connection of viscous effects to the motion and behavior of fluids interacting with immersed bodies. This was famously done by the German engineer Ludwig Prandtl (1904). He postulated that a thin region of fluid existing directly in contact with a moving body's surface and extending some small perpendicular distance away is where the entirety of the flow's viscous characteristics are bound and guaranteed to appear. This thin bounding region has, of course, become known as the *boundary layer* and has been the focus of a tremendous amount of effort throughout the last hundred plus years. A diverse range of test subjects, conditions, and arrangements have beckoned the application of Prandtl's theory to investigations frequently involving experimentation coupled with numerical analysis.

Today's modern computational infrastructure allows researchers to employ, for greatly simplified flow conditions, direct numerical simulation (DNS) of the full Navier–Stokes equations. However, most flow problems in application present computational tasks that remain too expensive for DNS. For these cases, and absolutely those where turbulence arises, a modified version of the Navier–Stokes equations are typically solved which are called the Reynolds averaged Navier–Stokes equations (RANS). An additional, initially unknown term called the Reynolds stress tensor is introduced to represent turbulence which requires further numerical modeling. These equations are given in chapter 2.

As previously mentioned, it has been hypothesized by numerous researchers that intermittently laminar-turbulent flow transitions may well be present in the boundary layer of undulatory self-propulsors even amid steady-state swimming modes. Such problems pose tremendous numerical demands for simulation, therefore experimental verification of its presence or absence may be of great value. Various modeling avenues may be chosen depending on the characteristic flow structures of one's particular problem.

The following section briefly describes the progression of adapting theoretical anguilliform swimming motion concepts to the mechanical movements of a biomimetic robot.

1.1 Adapting Anguilliform Motions to a Mechanical Robot

1.1.1 Theoretical Description of Anguilliform Swimming

Vorus first realized a possible AUV when observing a water snake swimming through a surfactant field of pollen in a pond on his farm in North Carolina (Vorus, 2005). It is mentioned that the snake left a very clean and distinct serpentine track of its progression through the pollen, barely wider than the width of its body. This led to surveying historical descriptions of swimming flexible strips as idealized mathematical models of various fish swimming characteristics. Work had been done by Wu (1961, 1971a,b) regarding the disturbance-free movements of a two-dimensional plate producing zero thrust, but none had yet developed the advancing swimmer capable of producing thrust while maintaining a circulation-free wake.

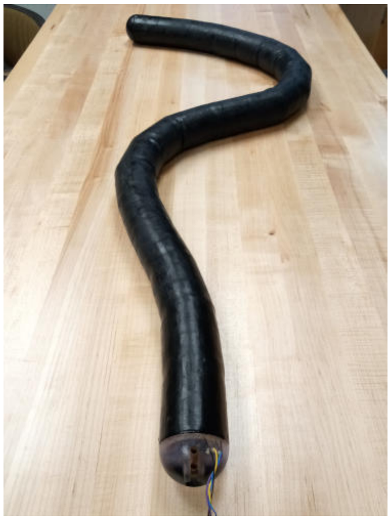

Figure 1.1: Photograph of NEELBOT with its black latex waterproofing skin

Vorus (2005) developed a mathematical model via two-dimensional slender-body theory to describe such a phenomenon. Three-dimensional extensions were subsequently made with Taravella (Vorus and Taravella, 2011) to permit axial variation of body contour. A brief synopsis of this theory is provided in section 2.3. A semi-empirical estimation of frictional drag is suggested by Vorus and Taravella (2011), an approach which utilizes a skin friction formula, e.g. the ITTC-1957 skin friction formula or Blasius' laminar results, to estimate the frictional drag as flat plate friction with wetted surface area and Reynolds number equal to that of the immersed body. Potts (2015) further extended the three-dimensional theory to account for non-ideal (off-design) scenarios, i.e. where the displacement wavelength to body length ratio is not equal to body velocity to wave velocity ratio. Requisite experimental validation of the ideal motion theory was in accompaniment, emphasizing the purpose of proving that a robot could achieve high efficiency swimming by means of wake vortex cancellation.

1.1.2 Robotic Adaptation and Initial Testing

To achieve experimental validation, Potts (2015) designed and constructed a robot (NEELBOT, see Figure 1.1) and investigated its wake field via particle image velocimetry (PIV). He concluded that with adequate motion replication and constant advancement at the appropriate design speed the robot's wake *could be* circulation-free. However, the product was not perfect, since trouble was experienced in the transient modes of acceleration and maneuvering and in exactly achieving the required motions. Much detail regarding motion replication is provided in the sections on motion programming and kinematic verification (Potts, 2015). Additionally, constant advancement at the design speed required towing. Net thrust/drag measurements collected while towing indicated that the robot's thrust production capabilities were insufficient to overcome its attendant frictional drag at that design speed.

Attempts were made to estimate the viscous drag via empirical quasi-static prediction methods, but under-predictions plagued the calculations. Justification seems to be found in the near-body viscous effects residing inside the undulating body's boundary layer. More specifically, turbulence inception may be the cause for experiencing greater frictional drag than expected, as larger friction coefficients are generally associated with turbulent boundary layers. As mentioned previously, the Bone–Lighthill thinning hypothesis for the unsteady boundary layer could also explain the under-predictions.

The ideal theory requires a particular swimming motion accompanied by a specific advance speed. Difficulties, however, were experienced apparently in getting the robot to accelerate from rest to the desired advance speed for a given motion. Since vortex-free wake is only theoretically achievable at design speed, expectant resistance arising from losses due to lift production is expected to play a role in preventing the robot from achieving the design speed. More thrust is required to overcome this drag than is produced when waving with the desired motion. Since, this appears to remain true even when towed at the design speed, further investigations are required to determine whether this robotic anguilliform propulsor is reasonably suited for application.

This led to the current phase of this anguilliform robot project. It is necessary to determine the drag for arbitrary swimming modes in order to program a motion that produces enough thrust to achieve a specified speed. Investigations into the boundary layer and characterization of the transient drag, transience in a *velocity-changing* sense, are necessary to sufficiently understand this problem and to adjust the motion programming to account for such transience.

According to Prandtl's theory and Vorus' intuitive note on the swimming water snake, investigations should reveal that the frictional drag experienced by the robot is due to fluid activity near the body. Specifically, the surrounding fluid's internal shear forces are significant only within the unsteady boundary layer which may intermittently transition between turbulent and laminar, and possibly separate and reattach. Moreover, the phrasing *near the body* may be too vague. One typically means *within the boundary layer* which resides sufficiently close to the wetted surface to justify the description *near.* If transverse motions exceed axial progression causing adverse pressure gradients, however, boundary layer separation may be induced and local vortices will appear not far from the body. Additionally, because of the asymptotic approach to external mean flow, no well-defined edge exists for even an attached boundary layer. Consequentially, flow properties must be observed at distances from the body selected based on approximate characteristic Reynolds numbers, observances of diffusive and convective behavior, and oscillatory interactions with the external mean flow.

In light of the aforementioned challenges of computer simulations, experimental techniques involving non-intrusive measurements of fluid velocity are employed to investigate within the robot's thin boundary layer at various flow conditions, locations, and stages of the undulation cycle. This establishes the circumstances for the current project. The same stereo PIV system used by Potts (2015) is reconfigured and reemployed to accomplish these investigations.

1.2 Survey of Relevant Literature

1.2.1 Flat Plates

Historically, the experimental treatment of boundary layer flows over flat plates has a rich history. Select examples of studies are provided here for brevity of motivation, but the reader is advised to see (Schlichting and Gersten, 2017) for more information and sources on this subject.

Since the work of Prandtl (1904), many advancements have been made in understanding the forces imposed by fluids on bodies. The early twentieth century saw great achievements in similarity solutions to the boundary layer equations. Possibly the most significant analytical work done on flat plate boundary layers since Prandtl is that of his own doctoral student, Blasius (1908). His model describes the steady two-dimensional boundary layer in zero pressure gradient flow on a flat plate at zero incidence. Falkner and Skan (1931) later generalized Blasius' solution to flows in which the plate is not necessarily parallel to the flow, i.e. wedge flows.

Even earlier than Prandtl, though boundary layer theory had not yet been formalized and most analysis was done via the inviscid Euler equations, Stokes (1856) worked on a number of problems related to the interactions between bodies and viscous fluids. The problem treated in (Stokes, 1856, pp. 20–21) is now known as *Stokes second problem* and involves an infinite plane boundary beneath a quiescent, viscous fluid making oscillations in the direction of a fixed line in the plane. Its solution is remarkably simple and elegant and is often used as a benchmark test for experimental and numerical investigations into all sorts of boundary layer flows, e.g. (Akhavan, Kamm, and Shapiro, 1991a,b) who investigated oscillatory flow internal to a pipe. Laser Doppler anemometry (LDA) was utilized in the experimental part (Akhavan, Kamm, and Shapiro, 1991a) for velocity and turbulence statistics measurements at various cycle steps. The numerical counterpart (Akhavan, Kamm, and Shapiro, 1991b) consisted of direct numerical simulation of the Navier–Stokes equations using spectral techniques.

An analytical extension for the startup of Stokes' second problem was developed by Erdogan (2000). The mathematical approach incorporated the Laplace transform. Since transient characteristics are included in the treatment, solution information for flow at small and large times after the start of the boundary is provided. It is concluded that the time required to achieve periodic steady state for cosine oscillations of the boundary is one-half cycle, and it is a full cycle for the sine oscillation.

Glauert (1956) derived exact solutions via series expansion methods to the two-dimensional laminar boundary layer on an infinite flat plate situated perpendicular to an oncoming stream, the plate making transverse oscillations in its own plane. This problem is also known as the *oscillating wall in stagnation-point flow.* The known steady solution was superimposed with a periodic part, and expansions were carried out to sufficient accuracy to cover the entire frequency range (including zero which corresponds to a steadily moving plate). A similar situation with a small plate has recently been studied experimentally using PIV (Shrestha, Ahsan, and Aureli, 2018). The goal was to study the interactions between hydrodynamic forces, vortex shedding, and convection mechanisms and to apply the findings to energy harvesting devices as well as biomimetic robots.

Some of the earliest authoritative, experimental investigations into boundary layers involved the study of flows over flat plates at zero incidence in wind tunnels and were performed by (Burgers, 1924; Van der Hegge Zijnen, 1924; Hansen, 1928; Dryden, 1934, 1937, 1939), to name a few. Their contributions were integral in setting the groundwork for experimental methods in boundary layer theory and developing most of the current understanding of boundary layer behavior. Most of these authors participated in the exploration of laminar-turbulent transition, stability theory, and various effects that influence indifference Reynolds numbers. Subtopics of these include Heisenberg–Tollmien–Schlichting waves, vortex formation and decay, turbulent spot formation, and primary and secondary instabilities. An indifference Reynolds number is the upper limit on conditional stability, i.e. exceeding the indifference Reynolds number guarantees instability for a particular flow.

Subsequent testing focused on the study of separation, unsteady boundary layers, and the ever-elusive phenomenon of turbulence including three-dimensional perturbations. Example sources include (Schubauer and Skramstad, 1947, 1948; Schubauer and Klebanoff, 1950; Emmons, 1951; Emmons and Bryson, 1952; Schubauer and Klebanoff, 1955; Klebanoff, Tidstrom, and Sargent, 1962; Freymuth, 1966; Kreplin and Eckelmann, 1979). Most boundary layer investigations performed today are purely computational and are coupled with turbulence modeling. The experimental studies mentioned here, along with those previously given, are the benchmark data collections used for verification and validation.

Further experimental investigations were performed by Schubauer and Skramstad (1948) which represent important early studies of oscillatory boundary layers, transition, stability, and fully-developed turbulence. Experimental confirmation and observation of the mathematical theory of stability was sought which, at the time, had been in development around 40 years. Fully turbulent flow over a smooth surface with separation due to adverse pressure gradients was performed by

Schubauer and Klebanoff (1950). Notably, they present longitudinal and transverse correlation coefficients and indicate that even some irregularities outside the edge of the boundary layer may tend to cause separation. Schubauer and Klebanoff (1955) more closely studied laminar-turbulent transition via artificially produced turbulent spots. The results of this study are found readily in (Schlichting and Gersten, 2017).

Early numerical simulations of oscillating turbulent boundary layers over plane surfaces were performed by Spalart and Baldwin (1987). A theory was formulated for the velocity and stress profiles of a boundary layer at high Reynolds number oscillatory flow over a flat surface. One further experimental work includes that of Freymuth (1966) who investigated the growth of small disturbances in a separated laminar boundary layer for high Reynolds numbers. It is shown that spatially growing disturbances are not dependent on Reynolds number, but only on Strouhal number.

Significant effort has also been invested in understanding the effects of suddenly setting a semi-infinite flat plate into motion parallel to itself. An early study includes that of Rozin (1958) who investigated a plate which abruptly achieves constant velocity from zero in a motionless fluid. Later, Rozin (1960) developed integral methods for approximately solving the equations of a non-stationary laminar boundary layer in an incompressible fluid using a one-parameter family of velocity profiles based on similarity. Van Gorder and Vajravelu (2009) is a more recent example of numerical analysis of impulsively moved plates. Certain simplifications are introduced for which analytical solutions are known, and validity of the numerical method is established via comparison with these known exact solutions.

1.2.2 Cylinders

A great deal of research related to cylinder flow has been accomplished in response to the many engineering applications. Both interior and exterior flows have been of interest to researchers, the former primarily concerning axial inflow and the latter transverse. Some literature regarding each of these approaches is discussed briefly here.

Analysis of axisymmetric, zero pressure gradient external flow near a straight, thin cylinder with a distinct leading edge is apparently difficult to perform. It is well-known, however, that the boundary layer near the leading edge behaves much like the Blasius boundary layer due to its relative thinness compared to the cylinder's radius. Transverse curvature quickly becomes important, though. Researchers readily observe that boundary layers associated with cylinders are thinner and have larger skin friction coefficients than flat plates with equivalent Reynolds numbers. The transition from Blasius applicability to curvature importance is not necessarily well-defined, but it is usually analyzed in terms of the non-dimensional flow parameter, $\nu x/(U_o r_o^2)$. This ratio provides some measurement of the relative importance of each variable included, which include the kinematic viscosity ν, axial coordinate x, steady external flow velocity U_o, and cylinder radius r_o.

Historically, in seeking formulae for a skin friction coefficient for axial flow over a finite cylinder, theoretical developments have sought some factor to be added to Blasius' flat plate solution. The earliest known attempt at this was (Young, 1939), but Glauert and Lighthill (1955) claim the estimates over-predict. Glauert and Lighthill (1955) also derive solutions for the skin friction coefficient using two methods, a Pohlhausen method and an symptotic series method, but only the first is of interest here as it deals with small values of the flow parameter $\nu x/(U_o r_o^2) < 0.04$. Actually, since Glauert and Lighthill assume the boundary layer to have zero thickness at $x = 0$, their Pohlhausen estimate only provides better results closer to the 0.04 threshold. Perhaps the best approximations have been achieved by Seban and Bond (1951) coupled with the subsequent numerical improvements provided by Kelly (1954). Thus, these results, along with Blasius', will be used later in chapter 5 for comparing values of skin friction with experimental results.

White (1969) employed a modified version of the turbulent law-of-the-wall to predict the properties of an arbitrarily thick turbulent boundary layer in axial flow past a long cylinder. Transverse curvature effects were properly accounted for using this approach. Numerical results were also given to further demonstrate curvature effects such as skin friction and drag coefficients. White concluded that skin friction and drag coefficients can be greatly increased and boundary layer thickness decreased due to the presence of strong curvature. Displacement and momentum thicknesses are also found to decrease. Significant experimental efforts were also made by Lueptow in studying turbulent boundary layers on cylinders in axial flow. For example, see (Lueptow and Haritonidis, 1987; Lueptow, 1988).

Switching gears to external, transverse inflow to an infinite circular cylinder, an early notable example of theoretical development is given by Glauert (1956) who studied transverse and rotational oscillations of a cylinder's cross-section. In this case, axial rotation is considered for torque calculations in aerodynamic flutter problems. As with the accompanying flat plate analysis, series expansions were utilized. Lighthill (1954) considered a stationary cylinder subjected to an oncoming transverse flow whose velocity oscillates in magnitude but not direction.

Sarpkaya extensively researched transverse fluid interactions with cylinders, especially cases where the cylinders were excited at resonant von Kármán frequencies and where fixed cylinders were exposed to both uniform and sinusoidal flows of water. For examples, see (Sarpkaya, 1977, 1978, 1995, 2002, 2006). A majority of these were experimental investigations. Force measurements on a rigid cylinder vibrating sinusoidally transverse to a uniform flow were made by Sarpkaya (1977, 1978). Later, Sarpkaya (1995) characterized the hydrodynamic damping of transversely oscillating cylinders as well as the biharmonic, vibratory response of a fixed cylinder subjected to uniform flow. Sarpkaya (2002) examined properties of stability associated with sinusoidal flows, and, as a follow-up, Sarpkaya (2006) was written which focused on separation associated with the periodic flows. Concerned solely with diameter-based length scales, none of these investigations considered axial flow components.

Early contributions in calculating inertia and drag coefficients associated with cylinders and plates subjected to oscillatory flow were made by Keulegan and Carpenter (1958). This work quickly became important due to the results being widely incorporated in the semi-empirical Morison equation which is used to estimate wave loads on cylindrical components of platforms and offshore structures. Keulegan and Carpenter defined a ratio, which they called a period parameter, that relates drag and inertial forces in sinusoidal currents as U_mT/D where U_m is the water particle velocity amplitude, T is the wave period, and D is the cylinder diameter or plate breadth. Experiments were performed in a wave basin wherein the drag and inertia forces were measured. The average values of the inertia and drag coefficients over a wave cycle were shown to vary with changing U or D, and strong correlation with the period parameter is observed. Generally, lower ratios indicate inertial dominance while larger ratios indicate drag significance. A critical value of $U_mT/D = 15$ was identified for the cylinder experiments as it yielded the lowest value of the inertia coefficient and the largest value of the drag coefficient. This period parameter proposed by Keulegan and Carpenter is now referred to as the Keulegan–Carpenter number, $\mathrm{K_C}$, and will be used later in this paper, beginning in chapter 5.

Recent experimental investigations of flow near cylinders includes (S.-J. Lee and J.-Y. Lee, 2008; S. Kumar et al., 2013; Gao et al., 2017). In the lattermost case, PIV was used to examine the near wake of a cylinder's transverse cross-section at a Reynolds number of 300 undergoing oscillatory rotations about the longitudinal axis at various angle amplitudes and rotational frequencies. Significant wake modifications were observed primarily for the rotation amplitude of 180°. S. Kumar et al. (2013) experimented with a rotationally oscillating cylinder at $\mathrm{Re_D} = 185$ and oscillation amplitudes between 22.5°–180°. A hydrogen bubble technique, hot-wire anemometry, and PIV were all utilized for flow visualization. Characteristics of wake structures, such as far-field disturbances and von Kármán vortex streets, were closely examined. Gao et al. (2017) considered non-dimensional forcing frequencies (ratio of cylinder oscillation frequency to vortex-shedding frequency from a stationary cylinder) between 0–2, while S. Kumar et al. (2013) considered frequency ratios between 0–5. (S.-J. Lee and J.-Y. Lee, 2008) is another example of PIV measurements of the wake behind a rotationally oscillating cylinder, and Mittal and B. Kumar (2003) is an example of a numerical study of similar problems via two-dimensional finite element techniques for $\mathrm{Re}_\mathrm{D} = 200$.

Although no research on the unsteady yawing of a finite cylinder is known to the author, various works are known which deal with cylinders at fixed yaw inclinations. Sears (1948) derived the equations for the boundary layer and the outer potential flow for an infinite yawed cylinder and commented on separation and stability. Chiu and Lienhard (1967) resolved these equations from (Sears, 1948) into cross-wise and span-wise velocity components and concluded that the laminar separation location of the chord-wise flow is independent of yaw inclination. Following the solutions of Glauert (1956) which included results for infinite cylinders, Sarma and El-Hadi (1986) developed and matched asymptotic solutions for oscillatory flow past a fixed, yawed cylinder and provided skin friction coefficients for small and large frequencies. Kestin, Maeder, and H. E. Wang (1961) described the effects which are produced in laminar boundary layers by the presence of oscillations in the free stream. This work also contains a series solution for the skin friction coefficient on which a harmonic oscillation is superimposed that progresses with a velocity equal to the mean velocity of the flow.

(King, 1977) considered a cylinder fixed at yaw angles $\pm 45°$, including every 15° increment in between, from the vertical for the Reynolds number range 2,000–20,000 to study the oscillations induced by shed vortices. Stability criteria and drag coefficients were evaluated, and flow visualizations were examined. It was concluded that even cylinders yawed at $\pm 45°$ are susceptible to vortex-induced oscillation due to cross-flow, even though relative flow velocities are decreased along with natural frequencies. R. Wang, Cheng, and Ting (2019) studied the same problem numerically using OpenFOAM with $\mathrm{Re}_\mathrm{D} = 1.4 \times 10^4$ and substantiated the conclusions of King (1977). Large yaw angles were seen to induce an axial flow component which causes a reduction of the cross-flow force, stabilizes the separated shear flow, and suppresses the formation of von Kármán vortices.

1.2.3 Undulatory Self-Propulsors

For a mostly historical, yet moderately technical, evolutionary overview of marine propulsion, see (Taggart, 1969). In particular, chapter 4 summarizes mechanical implementations which were inspired by and intended to imitate members of the animal kingdom. Gray's paradox (Gray, 1936a) is discussed which famously miscalculates swimming power requirements for drag balance in dolphins. Gray also extensively studied eels and developed some of the earliest theories on how they produce thrust (c.f. Gray, 1933a,b, 1936b,c).

The earliest waving-strip idealizations of fish swimming were contributed by G. Taylor (1952), Lighthill (1960), Wu (1961), Lighthill (1970, 1971), and Wu (1971a,b). The pioneers of ideal flow theories for body thrust generation (self-propulsion) with no shed vortical wake include Benjamin and Ellis (1966) and Saffman (1967), and later establishments were developed by Miloh and Galper (1993), Vorus (2005), and Vorus and Taravella (2011). The two lattermost sources propose swimming motions which produce thrust with no attendant vortical wake; these contributions provide the theoretical groundwork for the current project (Figure 1.2 was created to illustrate how the present investigation is related to other works). Again, see section 2.3 for a truncated summary of this theory. Viscous drag was addressed yet handled empirically with a quasi-static estimation. Attention was concentrated on developing the mathematical description and establishing plausibil-

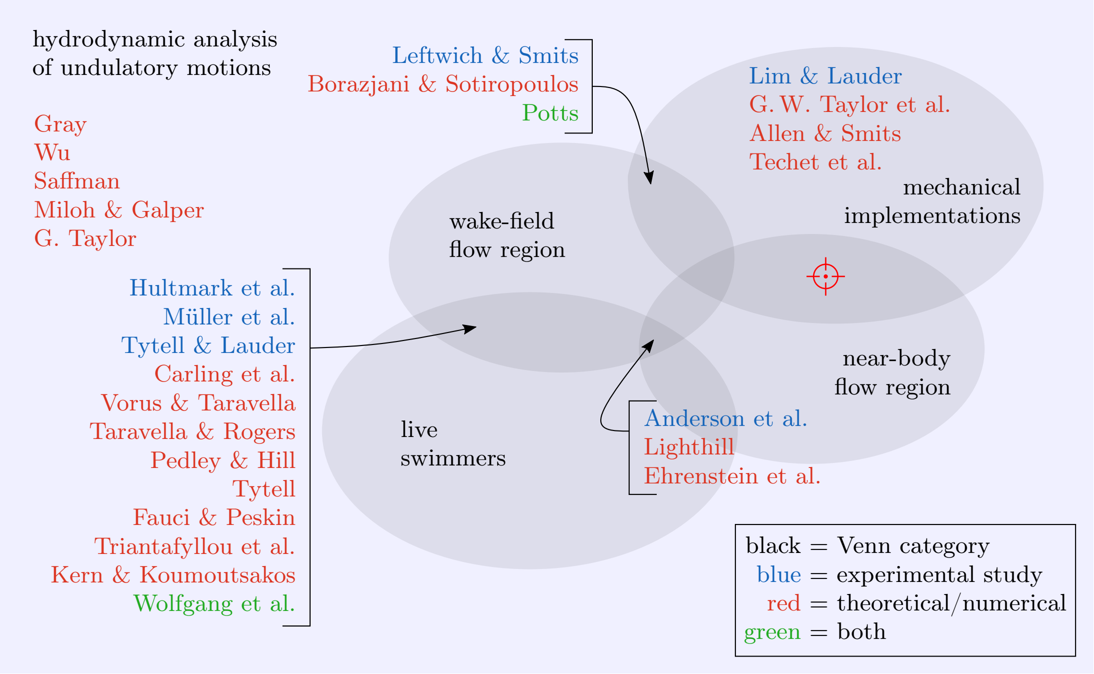

Figure 1.2: Illustration of the connections between relevant pieces of literature and the target contribution of the present investigation as indicated by the red reticle

ity, given the assumptions of a relatively large Reynolds number and thin boundary layer, for the possibility of wakeless swimming for practical application.

Two additional published developments in fish swimming theory include the works of Pedley and Hill (1999) and M. S. Triantafyllou, G. S. Triantafyllou, and Yue (2000). Pedley and Hill (1999) provide theoretical analysis of fish swimming with emphasis on coupling fluid forces to body loads. M. S. Triantafyllou, G. S. Triantafyllou, and Yue (2000) review experimental and theoretical works and makes connections with studies on live fish.

Implementations of anguilliform motions which deviate from self-propelled swimming have also been sought, e.g. (Allen and Smits, 2001; G. W. Taylor et al., 2001; Techet, Allen, and Smits, 2002). These researchers explored the innovative idea of using robots or membranes as a means of sustainable harvesting energy from oceanic and fluvial currents by converting mechanical energy into electrical energy. Lim and Lauder (2016), studied anguilliform fish locomotion via the hydrodynamic forces produced by vibrating slender, flexible polyurethane rods at the leading edge to generate passively propagating waves. Observations and measurements in the excited test articles' wake fields were made using PIV.

Hultmark, Leftwich, and Smits (2007) investigated the wake of a robotic lamprey swimmer—this robot is notably similar to NEELBOT-1.1—using PIV. The motion was programmed to achieve similar swimming patterns as produced by the American eels used by Tytell (2004) and Tytell and Lauder (2004). Leftwich and Smits (2011) analyze PIV results from Hultmark, Leftwich, and Smits (2007) and hydrodynamic pressure measurements from a transducer to investigate the wake formation, shed vortices, and the relationship between thrust and body surface pressure. According to Potts (2015), Leftwich and Smits (2011) also contradict the results of Müller et al. (2001) in saying that Hultmark, Leftwich, and Smits (2007) observed that body undulations are not contributing to thrust production. This shows that the understanding of propulsive forces from anguilliform swimming wake morphology is still very much in progress.

Potts (2015) completed experimental work at the University of New Orleans using an anguilliform robot and was primarily interested in determining whether a circulation-free wake field is achievable. Measurements from a six degree of freedom load cell fixed to the robot's tether were also collected which included longitudinal (thrust/drag) and transverse (lift) load measurements. This permitted both time-series and steady-state analyses. The viscous drag on the robot was estimated by analytically computing the thrust component thereby decoupling the robot's drag from its predicted, produced thrust. These results were compared with the quasi-static empirical approach that was initially used to predict the viscous drag, and it is shown that the quasi-static empirical approach significantly under-predicts the viscous drag by nearly half. Potts' results show that the viscous drag of the anguilliform swimmer is significant and more work is required to understand the hydrodynamics inside the boundary layer.

Taravella and Rogers (2017) completed a computational fluid dynamics (CFD) evaluation of the theory proposed by Vorus and Taravella (2011) using a body model similar to the robot designed by Potts (2015). Good agreement with the theory is achieved for near-body velocity, and effectively zero circulation is present in the wake indicating the absence of wake-induced drag. They conclude that it is plausible for an undulating body to produce purely inertial thrust via body accelerations acting through hydrodynamic added mass. A few more examples of numerical analysis of fish swimming include (Fauci and Peskin, 1988; Carling, Williams, and Bowtell, 1998; Wolfgang et al., 1999).

Wolfgang et al. (1999) performed experimental studies using PIV with live carangiform fish. They coupled their analysis with inviscid numerical studies for comparison. Müller et al. (2001) used PIV to visualize the wake flow field of live eels and conclude that they generally undulate either for maximum swimming efficiency or maximum maneuverability as suggested by their wake characteristics.

Kern and Koumoutsakos (2006) performed three-dimensional CFD simulations in search for optimal anguilliform swimming motions by not specifying the waving shape *a priori* but by obtaining it through an evolutionary algorithm used to optimize swimming efficiency and the burst swimming speed. They found for efficient swimming that the whole body undulates laterally with a slightly increasing amplitude towards the tail. Most of the thrust production was found to occur at the tail, consistent with the conclusions of Müller et al. (2001). A double row of wake vortex rings aligned with the swimming direction were found to be present as noted similarly by Tytell (2004) and Tytell and Lauder (2004).

Only one known attempt has been made—experimental or numerical—to characterize the boundary layer of undulating swimmers: an experimental study by Anderson, McGillis, and Grosenbaugh (2001). Particle tracking velocimetry (PTV, similar to PIV, but individual particles are tracked *manually* rather than the automated tracking of groups of particles) was utilized and supplemented by PIV to study live carangiform and anguilliform swimmers in both calm and flowing water. The Reynolds numbers based on length ranged from 3,000 to 300,000. Laminar flow was always observed while swimming in calm water, and in the free stream, depending on the Reynolds number, laminar, intermittently turbulent, and fully turbulent boundary layers were observed. Local skin friction coefficients, boundary layer thickness, and fluid velocities at the edge of the boundary layer were suggestive of local oscillatory and mean stream-wise acceleration of the boundary layer. These properties differed significantly when observed for rigid fish. Total skin friction was determined, and swimming fish were found to experience greater drag than the same fish held rigid. Notably, no boundary layer separation was observed for swimming fish.

Clearly the hydrodynamics of undulatory swimmers have been studied extensively, but none has generated boundary layer characteristics for biomimetic self-swimmers, hence the principal objective of the present investigation.

2 Mathematical Problem Description

Obtaining thorough intuition of a particular flow's characteristic behavior requires the development of a mathematical description and the statement of all known applicable constraints. The nature of these constraints can vary widely and may include any, all, or more than the following: temporal conditions, physical boundary conditions, constitutive relations, and fluid characteristics. This description and a subsequent statement of assumptions typically leads to a mathematical model that is simpler and, ideally, well-defined in contrast to the general equations governing fluid flow.

Proper interpretation of the system of equations at hand should reveal useful information such as dimensionless ratios, order of magnitude evaluation, solution categorization and behavior, computational domain requirements, scaling and similitude studies, experimental applicability, etc. These items are important to experimental and computational hydrodynamics and are given to indicate the wide-ranging possibilities of mathematically describing a flow. These usually will be helpful even if analytical solutions are not easily achievable as is the case herein. Nonetheless, a proper definition of the boundary conditions is helpful for post-processing experimental data.

2.1 Fundamental Fluid Mechanics and Boundary Conditions

Depending on the flow problem at hand, one may choose from a number of different formulations to describe their problem. For example, certain situations may be described more simply using less-conventional coordinate systems. Since the current situation involves water at constant temperature, the presence of physical, rigid boundaries, and time-varying flow properties where viscosity plays a significant role, the Navier–Stokes equations along with the continuity equation are employed with simplifications applied reflecting assumptions for incompressible, isoviscous Newtonian fluids. Conservation of mass and momentum for a fluid continuum are modeled by these equations. Here, thermodynamic effects are ignored, eliminating the need to consider energy conservation. When accompanied by appropriate conditions, these equations theoretically describe any general flow problem. They are written in vector form as follows for momentum and mass, respectively:

$$\begin{cases} \dfrac{\partial \mathbf{v}}{\partial t} + \left(\mathbf{v}^{\mathrm{T}} \cdot \nabla\right)\mathbf{v} = \mathbf{f} - \dfrac{1}{\rho}\nabla p + \nu \,\triangle \mathbf{v} \\ \nabla^{\mathrm{T}} \cdot \mathbf{v} = 0 \end{cases} \tag{2.1}$$

Here $\nabla = (\partial_x,\, \partial_y,\, \partial_z)^{\mathrm{T}}$ is the vector Nabla operator for computing gradients and $\triangle = \nabla^{\mathrm{T}} \cdot \nabla = \partial_x^2 + \partial_y^2 + \partial_z^2$ is the scalar Laplace operator. Cartesian coordinates are used here, since they provide the most intuitive and simplest description possible. Note, however, that cylindrical coordinates will be later adopted for the boundary conditions constraining flow around the cylinder and robot. Position and velocity vectors are written in Cartesian coordinates as $\mathbf{x} = (x,\, y,\, z)^{\mathrm{T}}$ and $\mathbf{v} = (u,\, v,\, w)^{\mathrm{T}}$, respectively. $p(\mathbf{x}, t)$ represents the scalar pressure, and t is time.

Often it is helpful to expand vector operations into their respective scalar quantities to identify unique behavior in each dimension. While conservation of mass is written as a scalar equation that remains one equation after expanding vector operations, conservation of momentum is expressed by a vector equation that expands into three equations, one for each principal direction. The system (2.1) may be thus expanded and written as

$$\begin{cases} \dfrac{\partial u}{\partial t} + u\dfrac{\partial u}{\partial x} + v\dfrac{\partial u}{\partial y} + w\dfrac{\partial u}{\partial z} = f_x - \dfrac{1}{\rho}\dfrac{\partial p}{\partial x} + \nu\left(\dfrac{\partial^2 u}{\partial x^2} + \dfrac{\partial^2 u}{\partial y^2} + \dfrac{\partial^2 u}{\partial z^2}\right) \\ \dfrac{\partial v}{\partial t} + u\dfrac{\partial v}{\partial x} + v\dfrac{\partial v}{\partial y} + w\dfrac{\partial v}{\partial z} = f_y - \dfrac{1}{\rho}\dfrac{\partial p}{\partial y} + \nu\left(\dfrac{\partial^2 v}{\partial x^2} + \dfrac{\partial^2 v}{\partial y^2} + \dfrac{\partial^2 v}{\partial z^2}\right) \\ \dfrac{\partial w}{\partial t} + u\dfrac{\partial w}{\partial x} + v\dfrac{\partial w}{\partial y} + w\dfrac{\partial w}{\partial z} = f_z - \dfrac{1}{\rho}\dfrac{\partial p}{\partial z} + \nu\left(\dfrac{\partial^2 w}{\partial x^2} + \dfrac{\partial^2 w}{\partial y^2} + \dfrac{\partial^2 w}{\partial z^2}\right) \\ \dfrac{\partial u}{\partial x} + \dfrac{\partial v}{\partial y} + \dfrac{\partial w}{\partial z} = 0 \end{cases} \tag{2.2}$$

The body force vector will include only gravitational effects, so here it will be written as $\mathbf{f} = (0,\, 0,\, f_z)^{\mathrm{T}}$ with $f_z = g = -9.81\,\mathrm{m/s^2}$.

One arrives at the Navier–Stokes equations after applying force balance to a fluid element. Each term is a force per unit volume normalized on fluid density ρ, thus the units are written as acceleration units $\left[\mathrm{m/s^2}\right]$. The left side of the momentum equation contains a temporal/local derivative in addition to three convective derivatives which capture spatial momentum changes. The right side contains, in order, the following: a body force, a surface pressure force, and surface shear/viscous forces.

The continuity equation governs local mass transport at an instant in time—note that no term appears which depends on time. It may also be interpreted as the divergence of velocity, which measures the outward mass flux emanating from a point in the velocity field. Thus the units are $[(\mathrm{m/s})/\mathrm{m}]$ or simply $\left[\mathrm{s^{-1}}\right]$.

The experiments treated herein are categorized as external flows, so appropriate boundary conditions are stated. The object of interest, i.e. the *test article* or *body*, is situated in a tank of large dimensions (large compared to the immersed body dimensions). A body-fixed coordinate system is assumed where the body may oscillate, change shape, both, or neither and where the body does not advance. Rather, a parallel, steady, and external flow is considered to move past the body. A no-slip body boundary condition is also assumed which states that the velocity of fluid particles directly in contact with the body surface move at the same velocity as the body surface. Immersion is assumed sufficient to consider vanishing disturbances in the far-field such that the tank boundary conditions become $\mathbf{v} = (U_o,\, 0,\, 0)^{\mathrm{T}}$.

A result of the no-slip body boundary condition is the applicability of Prandtl's boundary layer theory (Prandtl, 1904). Using the coordinate system shown in Figure 2.1, wall shear stress can be calculated as

$$\tau_{\mathrm{w}x} = \mu\left(\frac{\partial u}{\partial y}\right)_{\mathrm{w}}, \qquad \tau_{\mathrm{w}z} = \mu\left(\frac{\partial w}{\partial y}\right)_{\mathrm{w}} \tag{2.3}$$

for y perpendicular to the wall. As pointed out by Schlichting and Gersten (2017) and earlier by

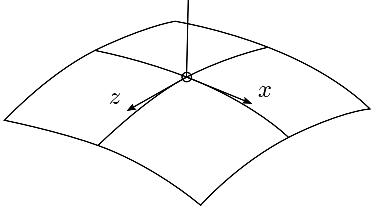

Figure 2.1: Coordinate system for an arbitrary body surface element (redrawn from (Schlichting and Gersten, 2017))

Prandtl (1904), the position of boundary layer separation is given by the condition that the velocity gradient perpendicular to the wall vanishes at the wall, i.e. the wall shear stress τ_w vanishes:

$$\left(\frac{\partial u}{\partial y}\right)_\mathrm{w} = \left(\frac{\partial w}{\partial y}\right)_\mathrm{w} = 0 \qquad \Longrightarrow \qquad \tau_{\mathrm{w}x} = \tau_{\mathrm{w}z} = 0 \tag{2.4}$$

Note that Equation (2.4) is not a boundary condition. Rather, it is a flow condition *at* the boundary describing the situation where flow reversal begins in a stream-wise direction due to the presence of increasing pressure in that direction. This spatially increasing pressure is known as a negative or adverse pressure gradient, and downstream of the position (x, z) where the gradient vanishes is where flow reversal may be observed.

2.2 Turbulence

Schlichting and Gersten (2017) remarks that most flows occurring in practical applications demonstrate turbulent behavior. This means that their motion may be described as having irregular fluctuations interspersed in the main stream. Potts (2015) and Lauder and Tytell (2006)—also Akhavan, Kamm, and Shapiro (1991a), indirectly—suggest that typical swimming conditions for Anguilla likely will introduce turbulence, at least periodically in the undulation cycle. This may or may not be the case for robotic implementations of undulating swimmers, depending on environmental factors and circumstantial conditions. For the present study, experimental flow visualization is developed to determine whether turbulence and separation arise for NEELBOT at steady swimming. In any case, a basic physical understanding of turbulence as it arises in practice is still desired as the behavior of (2.2) is non-obvious.

According to Bailly and Comte-Bellot (2015), several advantages and disadvantages are associated with turbulent flow for the submerged body. Advantages include increases in transport efficiency, e.g. diffusion and thermal exchanges, the reduction and delay of flow separation, and typical decreases in form/pressure drag. Drawbacks include increases in wall shear stress and therefore skin friction drag and the introduction of broadband acoustic radiation (mixing noise for subsonic flows). These consequences must be recalled and analyzed for applicability when investigating NEELBOT's near-body flow.

With the governing equations for general, incompressible fluid flow already established, a mathematical description of fully developed turbulent flow can be relatively easily given using a decomposition of the governing primitive variables into the superposition of time-averaged and turbulent fluctuations:

$$q(t) = \overline{q}(t) + q'(t) \tag{2.5}$$

Here, q can represent any of the four unknowns found in (2.2): u, v, w, and p. In a more general sense, it can also represent ρ, $\mathbf{f}$, and temperature, but these are considered constant here. $\overline{q}$ is the time-averaged *mean* primitive quantity, and q' is the turbulent fluctuation. Time-averaging is defined here as

$$\overline{q} = \frac{1}{t_1} \int\limits_{t_0}^{t_0+t_1} q(t)\,\mathrm{d}t \tag{2.6}$$

where t_1 is an interval of time small enough to follow the trend of the mean value over time but sufficiently large such that the time-averaged fluctuating quantity $\overline{q'}$ vanishes when integrated:

$$\overline{q'} = \frac{1}{t_1} \int\limits_{t_0}^{t_0+t_1} q'(t)\,\mathrm{d}t\ = 0 \tag{2.7}$$

When expanded using (2.6), the continuity equation can be written in vector form as $\nabla^{\mathrm{T}}\cdot\overline{\mathbf{v}}+\nabla^{\mathrm{T}}\cdot\mathbf{v}' = 0$. But, by definition, each component of $\overline{\mathbf{v}'}$ is zero, therefore their derivatives are also zero. Thus, continuity is enforced using

$$\frac{\partial \overline{u}}{\partial x} + \frac{\partial \overline{v}}{\partial y} + \frac{\partial \overline{w}}{\partial z} = 0 \tag{2.8}$$

One could write the obvious trivial statement of continuity using the turbulent velocity fluctuations as a reminder for use in deriving the time-averaged momentum equations:

$$\frac{\partial \overline{u'}}{\partial x} + \frac{\partial \overline{v'}}{\partial y} + \frac{\partial \overline{w'}}{\partial z} = 0 \tag{2.9}$$

Conservation of momentum is represented for turbulent flow problems by the Reynolds averaged Navier–Stokes equations—typically abbreviated as RANS equations—at which one may arrive after applying (2.6) to the momentum equations. These represent the primary system discretized and solved in computational fluid dynamics simulations of turbulent flows. They are written in expanded form as

$$\begin{aligned}
\frac{\partial \overline{u}}{\partial t} + \overline{u}\frac{\partial \overline{u}}{\partial x} + \overline{v}\frac{\partial \overline{u}}{\partial y} + \overline{w}\frac{\partial \overline{u}}{\partial z} &= \overline{f}_x - \frac{1}{\rho}\frac{\partial \overline{p}}{\partial x} + \nu \triangle \overline{u} + \left(\frac{\partial \overline{u'u'}}{\partial x} + \frac{\partial \overline{u'v'}}{\partial y} + \frac{\partial \overline{u'w'}}{\partial z}\right) \\
\frac{\partial \overline{v}}{\partial t} + \overline{u}\frac{\partial \overline{v}}{\partial x} + \overline{v}\frac{\partial \overline{v}}{\partial y} + \overline{w}\frac{\partial \overline{v}}{\partial z} &= \overline{f}_y - \frac{1}{\rho}\frac{\partial \overline{p}}{\partial y} + \nu \triangle \overline{v} + \left(\frac{\partial \overline{u'v'}}{\partial x} + \frac{\partial \overline{v'v'}}{\partial y} + \frac{\partial \overline{v'w'}}{\partial z}\right) \\
\frac{\partial \overline{w}}{\partial t} + \overline{u}\frac{\partial \overline{w}}{\partial x} + \overline{v}\frac{\partial \overline{w}}{\partial y} + \overline{w}\frac{\partial \overline{w}}{\partial z} &= \overline{f}_z - \frac{1}{\rho}\frac{\partial \overline{p}}{\partial z} + \nu \triangle \overline{w} + \left(\frac{\partial \overline{u'w'}}{\partial x} + \frac{\partial \overline{v'w'}}{\partial y} + \frac{\partial \overline{w'w'}}{\partial z}\right)
\end{aligned} \tag{2.10}$$

Again, presently, $\overline{f}_x = \overline{f}_y = 0$. The terms in parentheses on the right hand side are known as *Reynolds stresses* which are time-averaged spatial derivatives of turbulent momentum fluctuations. They represent new unknowns and thus require the incorporation of a closure model when numerically solving (2.10). Arranging these terms in tensor form produces the Reynolds stress tensor:

$$\boldsymbol{\tau} = \begin{pmatrix} \sigma'_{xx} & \tau'_{xy} & \tau'_{xz} \\ \tau'_{xy} & \sigma'_{yy} & \tau'_{yz} \\ \tau'_{xz} & \tau'_{yz} & \sigma'_{zz} \end{pmatrix} = -\rho \begin{pmatrix} \overline{u'u'} & \overline{u'v'} & \overline{u'w'} \\ \overline{u'v'} & \overline{v'v'} & \overline{v'w'} \\ \overline{u'w'} & \overline{v'w'} & \overline{w'w'} \end{pmatrix} \tag{2.11}$$

For more details regarding the mathematical treatment of turbulent flows, transition, and stability theory, see, e.g. (Cebeci and Smith, 1974; Libby, 1996; White, 2006; Bailly and Comte-Bellot, 2015; Schlichting and Gersten, 2017). (Tropea, Yarin, and Foss, 2007, ch. 10) provides some methods for experimentally measuring turbulent quantities.

A physical state may be described as *stable* if, when disturbed, it returns to its original state (White, 2006). In boundary layer theory, one may predict only some critical Reynolds numbers at which a laminar flow becomes unstable (indifference Reynolds numbers). Mathematical evidence that turbulence is the proper stable state at high Reynolds numbers does not formally exist; to date, turbulence remains purely an experimentally observed phenomenon.

This indicates that stability analysis is indeed important to the present study. Boundary layer separation and vortex shedding in the swimmer's wake will occur when the local flow has succumbed to instability. Strong transient accelerations in oscillatory modes can lead to separation which seem to direct one to the use of perturbation theory for analysis, wherein a disturbance is added to the basic solution of a physical problem followed by subtracting basic terms already satisfied by the basic solution. Investigation of the remainder should lead to a notion of stability that depends on the relative magnitude of the disturbance.

The main difficulty in boundary layer theory remains that inviscid flows do not have unique solutions. Inviscid flows are important because they represent the limiting case where $\mathrm{Re} = \infty$ and inertial effects are dominant. Real flows may be considered to have finite but large Reynolds numbers which should deviate from the limiting case only slightly, i.e. they can be considered small perturbations from the limiting case. Usually, the no-slip boundary condition is employed as the starting point. But since it normally cannot be satisfied by inviscid flows, one often cannot normally identify a starting point in perturbation theory a priori (Schlichting and Gersten, 2017).

The primary pragmatic problem in dealing with turbulent flow structures numerically is the restriction made to mesh spacing in the computational domain. As explained by Cebeci and Smith (1974, p. 41), the size of the smallest eddies associated with the flow, i.e. the Kolmogorov eddies, govern the required mesh spacing. When associated Reynold numbers grow, the ratio of the characteristic length to the smallest eddy diameter increases even more rapidly. This leads to exorbitant computing times. Cebeci and Smith shows that the mesh spacing must vary on the order of the inverse of the Reynolds number $1/\mathrm{Re}$. Thus, for a planar domain, doubling the Reynolds number leads to a quadrupled cell count and tripling leads to an eightfold increase. Small eddies appearing in the flow also present experimental difficulties which will be discussed in chapter 3.

Researchers have for a long time known that the following effects contribute to the onset of turbulence: flow entrance disturbances, wall roughness, adverse pressure gradients, wall heat transfer, compressibility, and irregularities in the outer flow. For the purposes of the present study, transverse curvature and periodic transience (outer flow irregularities) are of primary concern. Schlichting and Gersten (2017, p. 323) discuss the validity of Prandtl's 1904 theory and where it breaks down due to transversal curvature in axisymmetric flows. The region $\delta/r_\mathrm{w} = \mathcal{O}(1)$, where the ratio of boundary layer thickness to curvature radius approaches 1, is where effects of transverse curvature act as a non-negligible higher order boundary layer effect.

2.3 Review of Ideal Anguilliform Swimming Theory

It is well-known that anguilliform swimmers in nature, e.g. eels and lamprey, undulate, or rather they propagate a flexion wave backwards along their bodies. However, specifics regarding the complex nature of these motions are lesser-known. A few quick notes on the swimming characteristics of the marine animals in consideration may therefore be of interest.

First, Anguilla are capable of producing positive thrust during 100% of the undulation period unlike most other swimmers which oscillate their bodies and caudal fins, and often other fins, transversely to produce thrust during only several portions of the cycle. Anguilliform swimmers, when advancing straight at constant speed, can continuously operate in lateral force equilibrium due to the nature of the flexion wave length being less than the flexed body length. In contrast, most other swimmers repeatedly oscillate their fins side-to-side, and in some cases vertically as with Cetaceans, e.g. whales, porpoises, and Bottlenose dolphins, with equal and opposing strength, assuming maintaining a straight course in calm water is the animal's objective. These oscillatory strokes exploit lift mechanisms with shed vorticity induction to produce first order thrust forces, enabling these animals to achieve higher speeds than Anguilla.

It will subsequently be shown that to obtain the high Froude efficiencies theorized to be possible by mimicking anguilliform-like motions, the swimmers must necessarily rely on second order thrust forces from large amplitude displacements and therefore are slower, naturally. Note however that no presumption is made that the animals themselves always, or even at any time, swim in such a way as to leave no wake vorticity. Rather they inspired investigations into such motions.

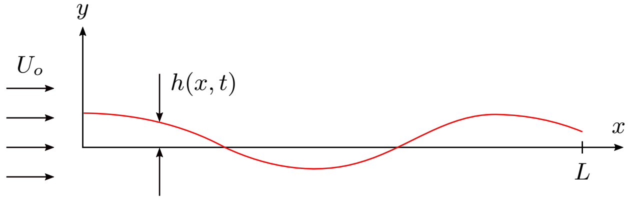

Figure 2.2: Coordinate system for the swimming strip (redrawn from (Vorus, 2005))

A quick word of disclosure for the reader: what follows is simply a summary of the derivation of the waveform used to program the motions of NEELBOT. Sufficient background information is provided to motivate the progression, however a number of verbose discussion points are omitted to accelerate the procedure. The full story is found in the original published papers (c.f. Vorus, 2005; Vorus and Taravella, 2011; Potts, 2015), but the following should suffice for self-containment of the present paper. Any resemblance is entirely intentional to preserve nomenclature and convention.

2.3.1 Two-dimensional Theory

The following is a condensed overview of the two-dimensional theory developed by Vorus (2005) in which a displacement waveform is derived for a semi-infinite strip that produces nonzero thrust absent of vortex wake and induced drag with continuously zero circulation over the strip length in time. Thus the thrust is reactive, generated by local acceleration processes, rather than inductive via relative velocity and lift. It is of second order magnitude in the displacement amplitude, implying that relatively large displacement coils are required to produce relatively small thrust at low advancement speeds. This indicates why anguilliform swimmers are typically observed moving at lower speeds when compared to carangiform, thunniform, and ostraciiform swimmers.

The derivation is based on the coordinate system shown in Figure 2.2 in which the strip advances in the $-x$-direction with speed U_o. The oscillatory displacement is specified as

$$h(x,t) = \Re\left\{H(x)\,\mathrm{e}^{-i\omega t}\right\} \tag{2.12}$$

where $h(x,t)$ is the transverse displacement of the shape function and $H(x)$ is the complex amplitude. The undulation is sinusoidal with frequency $\omega = 2\pi f$ in time. $\Re$ denotes the "real part of" the complex product.

For the element contour function $F = y - h(x,t)$, the kinematic boundary condition requires that the fluid normal velocity on the contour be equal to the normal contour velocity:

$$\frac{\mathrm{D}F}{\mathrm{D}t} = 0 \qquad \text{on } \; F(x,t) = 0 \tag{2.13}$$

Expansion of the substantial derivative gives

$$h_t(x,t) + (U_o + u)\,h_x(x,t) = v(x,t) \qquad \text{on } \; F(x,t) = 0 \tag{2.14}$$

The subscripts denote derivatives. The functions $u(x,t)$ and $v(x,t)$ are the longitudinal and transverse components of fluid perturbation velocity on the contour, respectively.

Assuming $h(x,t)/L$ is acceptably small such that $u/U_o \ll 1$, (2.14) can be linearized as

$$h_t(x,t) + U_o h_x(x,t) = v(x,t) \qquad \text{on } \; y = 0;\; 0 \le x \le L \tag{2.15}$$

At this point, Vorus (2005) derives a trivial undulatory mode, simply a pure sinusoid, which causes $v(x,t) \equiv 0$ and produces zero thrust. With the knowledge that $v(x,t)$ must be nonzero, the next step

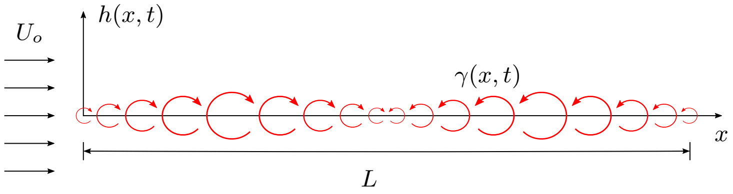

Figure 2.3: Simplified model of vortex line distribution for the two-dimensional strip (redrawn from (Potts, 2015))

assumes the Biot-Savart law can acceptably approximate $v(x,t)$ in terms of a vortex distribution $\gamma(x,t)$ along the x-axis with the assumed linearity and allowing for a probably (hopefully) laminar, yet still thin boundary layer. Equation (2.15) becomes in this case

$$h_t(x,t) + U_o h_x(x,t) = \frac{1}{2\pi}\int_0^L \frac{\gamma(\xi,t}{x-\xi}\,\mathrm{d}\xi \tag{2.16}$$

where ξ is the coordinate in the x-direction on the $y = 0$ axis and is used to distinguish from the general x-coordinate. Traditional foil theory extends L to infinity in x to allow for the induction due to vortex shedding. This is the general case where the displacement is an arbitrarily specified function. In such cases, Equation (2.16) is viewed as an integral equation to be inverted for the vortex strength $\gamma(\xi,t)$. However, for this application, (2.16) assumes explicitly that no net vorticity is left in the downstream wake of the element. It is consistent with minimum work, since the wake-induced drag is zero. The value $h(x,t)$ is the unknown function to be determined in achieving the condition of no wake, and not $\gamma(x,t)$ (Vorus, 2005).

From here, additional conditions are imposed on the solution to achieve the desired behavior. First, the time rate of change of net vortex element circulation must be zero for all time to enforce wakeless motion. Figure 2.3 qualitatively illustrates the vortex distribution along the x-axis modeling an element of the unknown anguilliform shape $h(x,t)$ in a uniform flow. The vortex distribution is thus a traveling wave with length L and frequency ω. The length of the wave in $h(x,t)$ is defined as λ which is equal to L only for the trivial, purely sinusoidal case.

Some convenience is found in non-dimensionalizing the formulation (2.16). These are made using a nominal length L and displacement wave speed V with r_o defined as the radius of body circular cross-sections (to come into play in the three-dimensional formulation of subsection 2.3.2).

$$\begin{aligned} \overline{r}_o &= \frac{r_o}{L} & \overline{h}(\overline{x},\overline{t}) &= \frac{h(x,t)}{L} \\ \overline{x} &= \frac{x}{L} & \overline{t} &= \frac{Vt}{L} = \frac{t}{T} \\ C_T &= 2\pi U^2 \overline{r}_o C_f \end{aligned} \tag{2.17}$$

U represents an advance ratio defined as $U \equiv U_o/V$. Then, slip can be written as slip $= S = 1 - U$. In addition to satisfying the condition that the integral of $\gamma(x,t)$ over the length L be identically zero for all $t \in [0, T$, the vortex distribution must satisfy the shockless entry condition $\gamma(0,t) = 0$ at the leading edge as well as the Kutta condition $\gamma(L,t) = 0$ at the trailing edge. After applying these conditions and substituting of the resulting function for γ into (2.16), a first order linear differential equation for $H(x)$ is achieved which is solved (Vorus, 2005) to give

$$H(x) = \exp\left(\frac{2\pi i\xi}{U}\right)\left(H(0) + \frac{\mathit{\Gamma}}{U}\int_0^1 \exp\left(-\frac{2\pi i\xi}{U}\right)\mathit{\Lambda}(x)\,\mathrm{d}\xi\right) \tag{2.18}$$

where

$$\varLambda(x) \equiv \frac{1}{2\pi} \int_0^1 \frac{\mathrm{e}^{2\pi i\xi}}{x-\xi}\,\mathrm{d}\xi \tag{2.19}$$

In (2.18), $H(0)$ is the head (leading edge) displacement amplitude, which has appeared as the constant of integration in the solution. The product of the leading factor and $H(0)$ represents a sinusoidal wave in x, the amplitude of which is modified over the element length, $0 \leq x \leq 1$, by the second term. The dimensional wave length λ of the function is established by the leading factor in (2.18). This dimensional wave length is

$$\lambda = L\,\frac{U_o}{V} \tag{2.20}$$

and the time period $T = L/V$ leads to

$$T = \frac{L}{V} = \frac{\lambda}{U_o} = \frac{2\pi}{\omega} \tag{2.21}$$

Thus, the time required for the strip to advance one wavelength λ at strip speed U_o is the same as the time required for the wave to advance one strip length at wave speed V. Reorganizing, one can write the following non-dimensional ratios:

$$\frac{\lambda}{L} = \frac{U_o}{V} = U \tag{2.22}$$

which states that the wavelength ratio must be equal to the advance ratio for wakeless swimming to occur. When the equality is unity, i.e. $\lambda/L = U = 1$, the aforementioned trivial case reappears. For other cases when this equality is true, this is the kinematic condition where nonzero axial load is developed but with necessarily unity ideal Froude efficiency due to the absence of vortex shedding.

Returning to the displacement amplitude of Equation (2.18), $H(0)$ and $\varGamma$ are the unknown parameters to be found, assuming the advance ratio U is specified. The head amplitude can be eliminated in terms of the total mean thrust coefficient C_T. Prior to this, a force consideration of the articulating anguilliform shape can be performed via a momentum integral analysis to obtain the thrust coefficient:

$$C_T(t) = 2(1-U)\int_0^1 \gamma(x,t)\,h_x(x,t)\,\mathrm{d}x \tag{2.23}$$

A time-mean thrust coefficient is subsequently obtained which can be written as

$$C_T = \frac{C_P}{U} = 2\pi\frac{\varGamma}{U}(1-U)\Re\left\{ i\int_0^1 H(x)\,\mathrm{e}^{-2\pi i x}\,\mathrm{d}x \right\} \tag{2.24}$$

One may substitute (2.18) into (2.24) and reorganize to obtain

$$H(0) = \frac{1}{\exp\!\left(2\pi i\frac{1-U}{U}\right)-1}\left[\frac{C_T}{\varGamma} - 2\pi i\frac{1-U}{U}\int_0^1 \exp\!\left(2\pi i x\frac{1-U}{U}\right)\Delta H(x)\,\mathrm{d}x\right] \tag{2.25}$$

with $\Delta H(x)$ defined as

$$\Delta H(x) \equiv \frac{\varGamma}{U}\int_0^x \exp\!\left(-\frac{2\pi i\xi}{U}\right)\varLambda(\xi)\,\mathrm{d}\xi \tag{2.26}$$

The formulation of (2.18), (2.25), and (2.26) provide the strip displacement amplitude in terms of the single unknown parameter $\varGamma$, when U and C_T are assumed to be specified. At this point, $\varGamma$ is not a physically controllable value but must be evaluated to proceed. An additional closure relationship is needed for uniqueness of the solution. A *minimum displacement* criterion is used which determines $\varGamma$ to minimize the maximum modulus of $H(x)$ for specified C_T and U, i.e.

$$\varGamma = \varGamma[\min(\mathrm{mod}(H(x)_{\max}));\ C_T,\, U] \tag{2.27}$$

This condition states that of the family of displacements that give no wake and maximum (ideally, 100%) efficiency, the animal selects the one that requires the minimum maximum displacement. This condition, even if not necessarily a unique condition, is consistent with the achievement of least-work swimming which the animal would be expected to seek.

In the scenario studied by Vorus (2005), two conditions are analyzed for different values of U, one with $U < 1$, a sub-critical case, and the other super-critical with $U > 1$. The latter is noted as mathematically intuitive yet not physically feasible in terms of propulsion as it requires *negative slip* in the midst of positive thrust. Clearly, $U < 1$ provides the solution sought.

The definition of Froude propulsive efficiency is output power, or thrust power, over input power. The ideal propulsive efficiency of the elements is, by this definition

$$\eta_i = \frac{UC_T}{C_P} \tag{2.28}$$

Equation (2.24) therefore implies $\eta_i \equiv 1.0$, for all time. This confirms the perfect Froude efficiency possibility with this class of motions, assuming absence of viscous effects, separation drag, and large amplitude nonlinearities. Vorus (2005) predicts that viscous skin friction will manifest in a drag of the same magnitude as C_T as needed for speed equilibrium.

2.3.2 Three-dimensional Theory

The following gives an abbreviated overview of the derivation of three-dimensional anguilliform swimming motions detailed in (Vorus and Taravella, 2011). This formulation is based on slender-body theory as derived by Lighthill (1960), which applies to low aspect ratio bodies where the cross-sectional dimensions are small relative to length. Slender-body theory still employs two-dimensional hydrodynamics but in cross-sectional planes normal to the longitudinal axis, rather than chord-wise in x–y. The solution development follows the same general steps as the preceding two-dimensional analysis of subsection 2.3.1.

A circular cylindrical cross-section is used for convenience of the development as shown in Figure 2.4, but the solution will apply generally to all ellipses with semi-major axis directed in z and equal to the circle radius. Here, the surface function, a three-dimensional version of (2.13), is

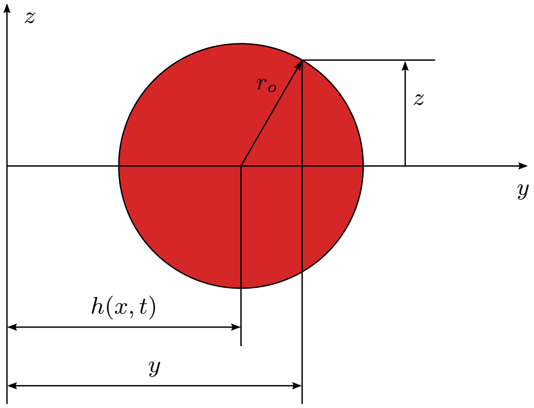

Figure 2.4: Coordinates of the body cross-section (redrawn from (Vorus and Taravella, 2011))

defined as

$$F(x, y, z) = -y + h(x, t) + \sqrt{\overline{r}_o^2 - z^2} \tag{2.29}$$

The first order inward normal vector on the surface is

$$\mathbf{n} = -\mathbf{e}_r + h_x \cos(\theta)\, \mathbf{i} \tag{2.30}$$

with velocity vector $\mathbf{V} = (U_o + u)\, \mathbf{i} + v\, \mathbf{j} + w\, \mathbf{k}$. The substantial derivative of F gives the same linearized boundary condition as in the previous development but now on a cylindrical surface. As before, in the correct context subscripts denote the variable with which partial differentiation is taken.

$$h_t(x, t) + U_o h_x(x, t) = v(x, t) \qquad \text{on } r = r_o;\ 0 \le x \le L \tag{2.31}$$

From typical ideal flow theory, the two-dimensional perturbation potential for the circular section with velocity v in y is

$$\phi(x, r, \theta, t) = -\frac{v(x, t)\, r_o^2 \cos(\theta)}{r} \tag{2.32}$$

Equation (2.32) is based on the assumption that no stream-wise vortex shedding occurs in the sectional planes, which is required for the reactive wakeless swimming solution sought. On the cylinder surface r_o substitution of (2.31) into (2.32) gives

$$\phi(x, \theta, t) = -(h_t + U_o h_x)\, r_o \cos(\theta) \tag{2.33}$$

Using the Bernoulli equation, the linearized pressure on the surface is

$$p(x, \theta, t) = -\rho\, (\phi_t + U_o \phi_x) \tag{2.34}$$

By substituting (2.33) into (2.34), one arrives at

$$p(x, \theta, t) = \rho k(x, t)\, r_o \cos(\theta) \tag{2.35}$$

where $k(x, t) \equiv h_{tt} + 2U_o h_{xt} + U_o^2 h_{xx}$. Following the standard analytical procedure of slender-body theory, Vorus and Taravella (2011) proceed to integrate this pressure distribution (2.35) component-wise over the body surface using the normal stress vector which is written as

$$p\, \mathbf{n} = \rho k(x, t)\, r_o \cos(\theta)(-\mathbf{e}_r + h_x \cos(\theta)\, \mathbf{i}) \tag{2.36}$$

to calculate sectional forces. Since the normal vector's components are written in cylindrical coordinates for clarity, they are projected into the principal axes directions $\mathbf{i}, \mathbf{j}$ during integration to provide the following sectional thrust and lift force components:

$$f_y(x, t) = -\rho \pi r_o^2 k(x, t) \tag{2.37}$$

$$f_x(x, t) = \rho \pi r_o^2 k(x, t)\, h_x(x, t) \equiv -f_y(x, t)\, h_x(x, t) \tag{2.38}$$

These forces may be normalized on the transverse dynamic stagnation pressure $\rho V^2/2$, and the axial component is plotted in Figure 2.5 for equally-spaced time steps of the undulation period. Motion parameters from round 1 of Table 6.1, i.e. $U = 0.7$, $U_{o,d} = 0.25\,\mathrm{m/s}$, $\mathit{\Gamma} = 0.11767$, and $C_T = 0.7985 \times 10^{-3}$, were used in the calculations.

Vorus and Taravella (2011) then derive a trivial solution that has no slip and 100% ideal efficiency. Non-trivial displacement shapes which do slip and produce thrust may also have 100% ideal efficiency. Following the two-dimensional development, the explicit requirements on $h(x, t)$ for ideal wakeless propulsion are

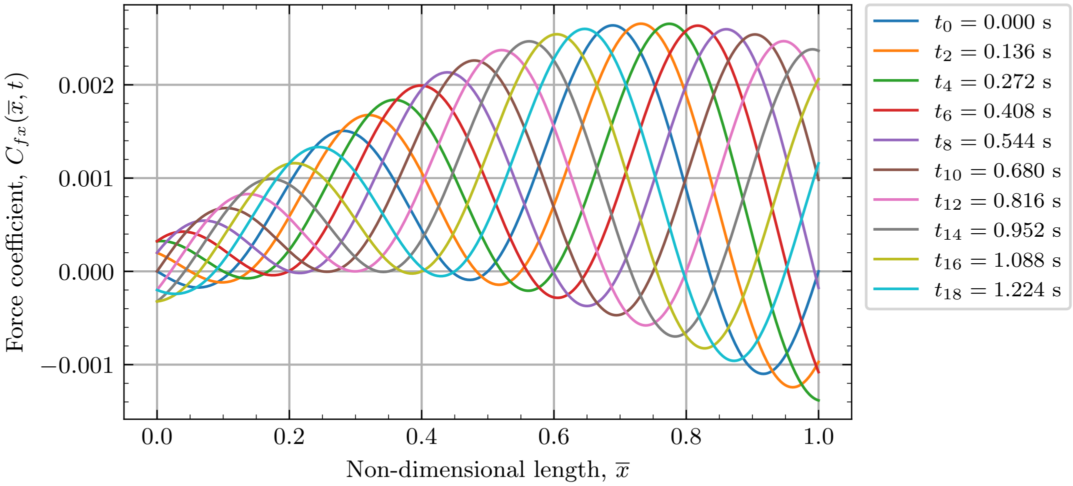

Figure 2.5: Sectional force coefficient distributions shown for every other time step for the first half of the ideal motion cycle using the parameters from round 1 of Table 6.1 (replotted with different parameters from (Potts, 2015))

1. The total body side lift, $C_{Fy}(t)$, is continuously zero for all t.
2. The Froude efficiency of the mean hydrodynamic processes is unity for all x and t.
3. The maximum of the real displacement amplitude in x is minimum.

The first of the above conditions is equivalent to the restrictions imposed on the vortex distribution in the two-dimensional analysis in avoiding shedding vortex wake. The condition of continuously zero circulation resulted in no net lift in time. In the three-dimensional case, any lateral vorticity shed in the body section planes has already been excluded in the formulation, enforced by (2.32). The vortex wake shed from the tail does not directly enter the slender-body formulation; its upstream induction, while not zero, is inherently treated as higher order in the sectional flow components by slender-body theory and is thus neglected due to the linearization. Net unsteady lift, however, must still be the manifestation of circulation change and associated shed wake from the tail (Lighthill, 1960, 1970). Nonzero shedding off the animal tail is indirectly eliminated here by requiring that the net lift be continuously zero in both space and time.

Eventually, a three-dimensional complex amplitude is initiated as a form, selected on the basis of the character of the two-dimensional solution, which incorporates the relationship of the displacement wave length to the body length. Superposition is exploited to combine a head amplitude (at $x = 0$) and an unknown function which satisfies the above three conditions. The amplitude $H(x)$ can take on any number of solutions, and Vorus and Taravella (2011) provide a detailed formulation of the solution that minimizes the modulus of the maximum displacement $H(x)_{\max}$ for a specified U and C_T. This is enforced by the Froude efficiency being set to the ideal case of 1.0. It is determined that the minimum occurs on the boundary $H(0) = 0$; it makes no physical sense to have a negative head amplitude which, mathematically, could lead to further minimization. Vorus and Taravella (2011) eventually develop the following solution for the three-dimensional complex displacement waveform:

$$H(x) = i\mathit{\Gamma}\left(\mathrm{e}^{2\pi i x} - \mathrm{e}^{2\pi i x/U}\right) \tag{2.39}$$

where $\mathit{\Gamma}$ represents the non-dimensional motion amplitude

$$\mathit{\Gamma} = \sqrt{\frac{C_T}{4\pi^3 \overline{r}_o^2 (1-U)\left(1-\cos\left(\frac{2\pi}{U}\right)\right)}} \tag{2.40}$$

Using Euler's formula and taking the real part and also returning the over bars from (2.17) to indicate normalized quantities, the three-dimensional displacement waveform (2.12) becomes

$$\overline{h}(\overline{x},\overline{t}) = \mathit{\Gamma}\left[\sin\left(2\pi\left(\frac{\overline{x}}{U}-\overline{t}\right)\right) - \sin\bigl(2\pi(\overline{x}-\overline{t})\bigr)\right] \tag{2.41}$$

where $\overline{x}$ and $\overline{t}$ are the normalized position along the body's length and normalized time, respectively (described below), and U is the advance ratio, i.e. the ratio of advance speed to displacement wave speed. Plots of this function are shown later in Figure 6.3. Thanks to the product-to-sum trigonometric identity

$$\sin(A) \pm \sin(B) = 2\sin\left(\frac{A \pm B}{2}\right)\cos\left(\frac{A \mp B}{2}\right) \tag{2.42}$$

Equation (2.41) can be written as a product of sinusoids as

$$\overline{h}(\overline{x},\overline{t}) = 2\mathit{\Gamma}\sin\left(\pi\left(\frac{\overline{x}}{U}-\overline{x}\right)\right)\cos\left(\pi\left(\frac{\overline{x}}{U}+\overline{x}-2\overline{t}\right)\right) \tag{2.43}$$

This combines the difference into a product of two functions, one of which depends only on the non-dimensional spatial variable $\overline{x}$ while the other depends on both space $\overline{x}$ and time $\overline{t}$.

The principal objectives of this thesis are related to analyzing viscous effects on the robot's performance, specifically its thrust generation capabilities and frictional drag, and determining whether the notion of a thin boundary layer is physically observed in experimental testing for various conditions. Viscous effects, however, are not considered in the idealizing assumptions of the foregoing theoretical description. As previously mentioned, they were treated empirically by Potts (2015) and found to be underestimated. The numerous hypotheses that have been proposed to explain this behavior are to be subsequently explored.

3 PIV Methods

Non-intrusive, instantaneous measurements of fluid velocity at particular regions of flow are desired making particle image velocimetry (PIV) a sensible choice for investigations of near-body fluid flow and self-propelling hydrodynamics. In particular, intermittent turbulence, boundary layer separation, and wall shear stress are of primary concern. Optical flow visualization provides at least one advantage not offered by other methods such as laser Doppler anemometry and hot-wire anemometry being that two- or three-dimensional vector fields are provided as output data rather than velocity magnitude at a single point.

Since near-body flow characteristics are required, special attention is placed on PIV arrangements suited for boundary layer investigations. The test articles of interest will undergo both translational and rotational oscillatory motions, thus the respective PIV configurations will need to be adjusted accordingly. A brief description of PIV is provided here. For further details, see (Raffel et al., 2018) or (Tropea, Yarin, and Foss, 2007).

3.1 PIV Description, Equipment, and Limitations

PIV is a method for measuring fluid velocity in a fixed region by optically tracking tracer particles added to the fluid. The tracer particles used here, also called seeding or seed particles, are neutrally buoyant, hollow, and silver-coated microspheres that are illuminated in the region of interest, usually by a dual cavity laser, twice within a short and known time interval. The light scattered by the particles is collected by a high speed camera which has been spatially calibrated for the illuminated region of interest and synchronized with the laser flashes. The calibration provides a relationship of displacement in the image plane (pixels) to displacement in real world coordinates (physical dimensions), and temporal equipment synchronization is typically handled externally by a computer or other device. The fixed region of interest could be a plane if one or two cameras are used or a volume if three or more cameras are used.

Spatial calibration is straightforward for mono PIV (single camera). A precisely machined planar target consisting of a grid of dot markers on at least one side is placed coincident with the light sheet. A single image of these marks, the physical spacing of which is known, is then sufficient to calculate adequate mappings from image space to object space (Raffel et al., 2018). This provides two-component, planar velocity measurements within the light sheet. Reconstruction of the third velocity component (normal to the light sheet) calculated from out-of-plane displacements requires information regarding the viewing angles of at least two cameras. The use of two cameras for stereo reconstruction (stereo PIV or SPIV) provides three-component velocity measurements within the two-dimensional overlap region of the two image planes. Methods for calculating camera orientation parameters and reconstruction geometry are described in (Raffel et al., 2018).

Usually PIV images are subdivided into interrogation windows for evaluation of fluid velocity at an array of points providing a vector field of displacement information. The local displacement vector for a single interrogation window is determined by cross-correlation between the two images collected at the first and second illuminations. The velocity field is obtained by dividing the displacement vector field by the scalar time interval Δt elapsed between frame collections. Various levels of post-processing are performed to detect and remove invalid measurements and to compute flow

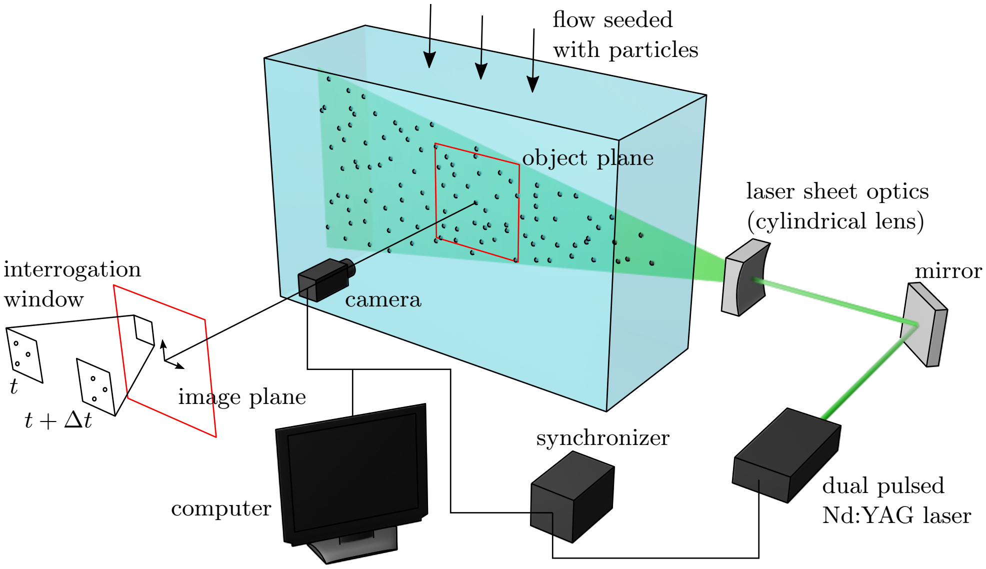

Figure 3.1: Typical PIV arrangement illustrating the data collection general workflow

quantities of interest. An illustration of the fundamental principle of PIV and a typical equipment arrangement is given in Figure 3.1.

Stereo PIV processing begins with mono PIV processing of each camera's output images. Three-dimensional triangulation is subsequently performed on the two-dimensional vector fields produced by mono processing using information stored in a calibration file obtained before commencing experiments (or after, for the irrationally audacious). This is all accomplished using the algorithms in TSI's Insight 4G (ver. 11.1.0.5).

The experimental method used presently is limited to the measurement of average velocity over the short time interval Δt. The word *short* is used loosely here as it is the time interval necessarily adjusted a priori to fit the region of interest relative to the local uniform flow velocity U_o expected. It likely is not short enough to capture the smallest-scale Kolmogorov eddies found within a fully turbulent boundary layer. Also, since the velocities of interest exist within the test article's boundary layer, a necessary consequence is measuring velocity magnitudes ranging from zero at the wall (for boundaries not moving relative to the PIV camera(s)) to U_o and beyond at the boundary layer's edge. For high external flow speeds, no single Δt will suffice to accurately measure all flow speeds without further refinement of the grid near the boundary. Therefore, it must be selected carefully to capture the desired velocities and to accommodate the magnification at imaging. Else, numerous trials must be performed for the same region of interest using a range of Δt, and this is only valid for steady flows or for corresponding time steps of periodic flows.

An additional limitation of PIV involves the fact that only first order displacement approximations are feasible due to using image pairs rather than triples or more groups of images spaced temporally by Δt (Raffel et al., 2018). This results in losses of accelerative and stream-wise curvature effects such as where rotating or circulatory flows are present. Reducing Δt gradually minimizes these displacement under-estimations but only at the cost of the aforementioned issues and increased noise in differential estimates.

For the case where a non-optimal, yet decent, value for Δt was chosen, one may account for such minor errors by adjusting the interrogation window starting and final sizes. This changes the expected displacement as a percentage of interrogation spot dimensions. Rules of thumb for "optimal" displacements indicate that in-plane displacements should not exceed 25% of the final

Table 3.1: PIV Equipment

seeding	silver-coated hollow glass sphere particles with mean diameter of 5 µm and density of 1,000 kg/m^3
CCD cameras	TSI Model 630059 PowerView 4MP and TSI Model 630091 PowerView 4MP-HS
camera lens	Tokina Macro 100 mm f/2.8 D manual focus lens
magnification	Kenko Teleplus Pro 300 DGX: 1.4× and 2.0× together for 2.8× total magnification
PIV laser	Quantel Evergreen 200, dual pulsed Nd:YAG, 532 nm wavelength, 200 mJ @ 15 Hz
synchronizer	TSI Model 610036 LaserPulse Synchronizer

interrogation window size, and out-of-plane displacements should not exceed 25% of the light sheet thickness. Cases where these are only slightly exceeded may be remedied in processing. Otherwise, the PIV images would need recapture.

Further assumptions are made regarding the seeding particles. First, the particles are considered perfectly spherical and must be large enough to scatter adequate light such that the cameras can detect their reflections; however, inertial contributions are presumed negligible. The particles are also assumed to move naturally with local flows without noticeable gravitational effects, i.e. they are neutrally buoyant. In the case where particle density differs from that of the fluid's, the undesirable gravitational effects may be described by Stokes' drag law (Raffel et al., 2018). Additionally, the fluid's physical properties are assumed to remain constant with the particulate additions, i.e. the density, viscosity, and thermal properties are unaffected.

Table 3.1 summarizes the equipment used for PIV data collection to accomplish the present work. A photograph of the system used for stereo PIV—TSI Model 6800 SPIV system—in the present investigation is shown in Figure 3.2. A photograph of this system situated on the towing carriage is given in Figure 3.3. The experimental data discussed herein was collected using two similar camera models—TSI Model 630059 PowerView 4MP and TSI Model 630091 PowerView 4MP-HS. These models have identical resolutions, but the latter model is capable of higher frame rates. The School of Naval Architecture & Marine Engineering at UNO owns three of the 630059s and two of the 630091s. One of the latter model was used for the flat plate experiments (chapter 4) in the hydraulic flume for mono PIV, but one of these cameras failed later while preparing for the towing tank experiments. Thus the 630059 cameras were used for stereo PIV with the cylinder (chapter 5) and robotic eel (chapter 6).

Images from both of these cameras are stored in 16-bit lossless TIFF image containers at 2,048 px × 2,048 px resolution. The highest (left-most) 4 bits are unused, i.e. they all have values of 0, making the greatest achievable pixel intensity values $2^{12} - 1 = 4{,}095$. However, when an image stored in a 16-bit container is displayed on a monitor, completely saturated pixels are expected to have values of $2^{16} - 1 = 65{,}535$. To correct the display of these images, one could encode the container with a custom color profile that may only be recognized by certain programs. A more robust correction, the one used herein, involves the following: pixel values are first left bit-shifted 4 places, then a LUT (lookup table) is applied for logarithmic gamma correction. The 12-bits of data stored in the raw camera images are linearly related to the number of impacting photons at each pixel site, so the gamma correction is applied for better correspondence to the human eye's perception of light. The gamma correction used is $I_c = I_r^{1/\gamma}$, where I_c is the gamma-corrected

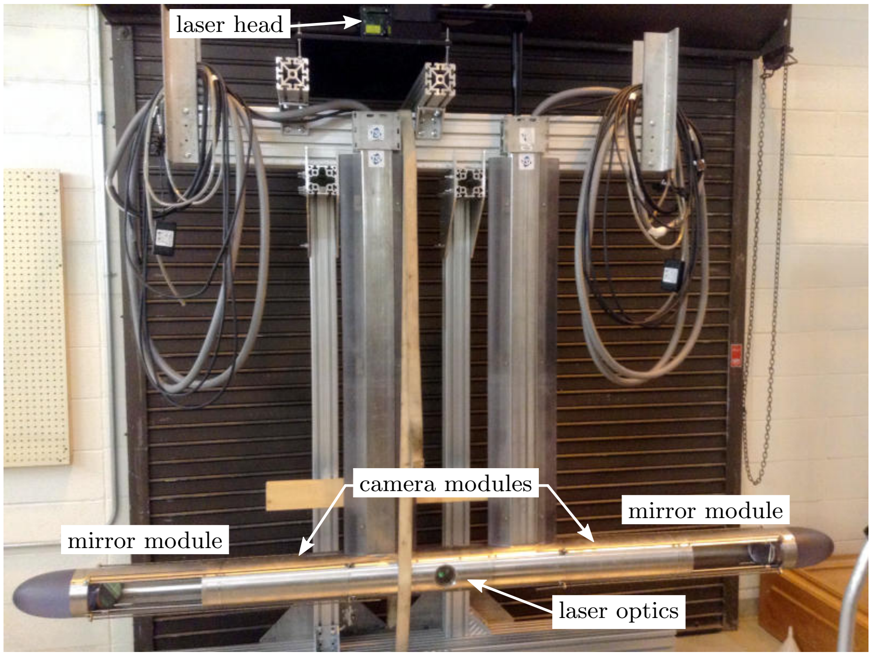

Figure 3.2: SPIV system with key components labeled

image, I_r is the raw image, and $1/\gamma = 1/1.66 \approx 0.6024$. Sample PIV images displayed later, Figures 4.7, 5.8, and 6.10, have these modifications applied as well as downscaling and conversion to a lossy 8-bit container for minimal file size.

The Scheimpflug principle is exploited to correct for the non-parallel relationship between the cameras' focal plane and the desired image plane. See (Tropea, Yarin, and Foss, 2007) or (Raffel et al., 2018) for more details regarding this principle. Each camera is subtly rotated and focused until both sides of the displayed image are in focus.

One of the difficulties with experimental methods such as PIV is the experimenter practically needs to know the results before performing the experiment; otherwise, the settings used in collecting data can be drastically miscalculated. As an obvious example, the flow rate may be too high for the given exposure time resulting in blurred images. A less obvious but equally detrimental issue is when a relatively large Δt is used for high flow rates. Then the microspheres' images will appear to move too far—greater than 50% of one interrogation spot—in the field to obtain meaningful velocity data. Instead, if the high velocity is local, i.e. small compared to the image plane, the displacement vector conditioning engine will have to interpolate between neighboring vectors or simply throw out the vector all together.

Theoretical formulations and numerical simulations bear the advantage that one may learn enough about the flow problem of interest to anticipate expected behavior and to apply correct (or close) experimental parameters before even starting. This suggests that some up-front efforts may reduce time and frustration in data collection during the experiments. This principle illustrates one purpose of the first two phases of this project, the analyses involving a flat plate and a straight cylinder (alas, performing SPIV experiments with simpler test articles and conditions before working with the robot indeed mitigated difficulties which would have arisen during the final phase without prior PIV experience). Oftentimes, however, the necessary resources are not available to perform any precursory analysis, so iterations over combinations of the experimental parameters are required.

Typically one gets stuck in the analytical approach to solving external fluid flow problems

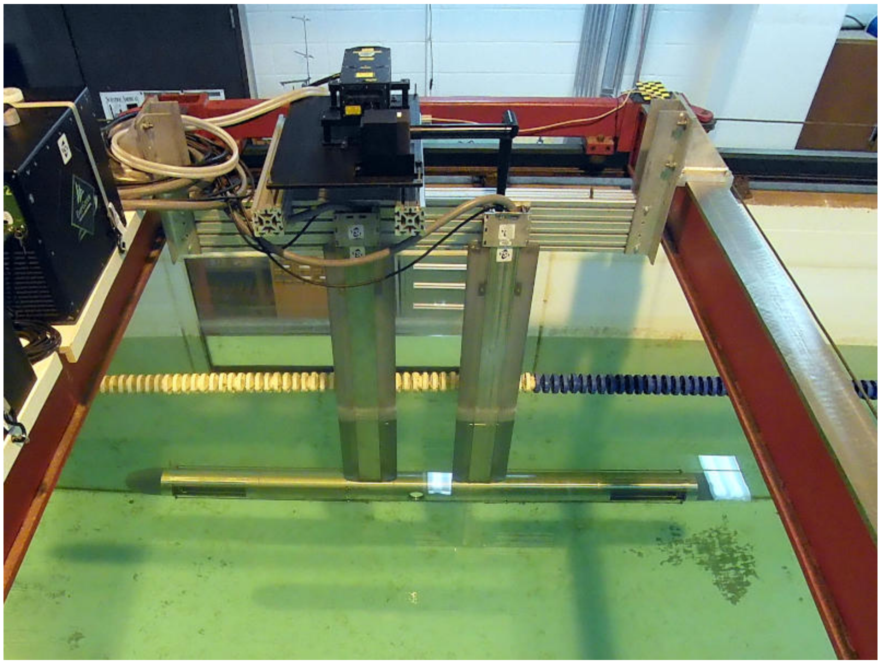

Figure 3.3: SPIV system situated on the towing carriage

because of the nonlinearities present in the governing equations, except for unrealistically simplified geometry and flow conditions. For this reason, and due to advancements made in modern computing, numerical analysis coupled with experimental validation is most often the fallback.

3.2 Error and Uncertainty

Measurement error in PIV can arise anywhere from model construction and experiment setup to data acquisition and post-processing. Many steps are involved even between data collection and analyzing velocity measurements, each of which allows opportunity for error introduction. When dealing with turbulent fluctuations, setting PIV parameters gets tricky since the time interval Δt needs to be adjusted for various velocities, and the grid of interrogation subdivisions needs to be refined well enough to capture even the smallest eddies. Fortunately, these issues are not present in the flat plate experiments since the flow is characteristically entirely laminar. Additional difficulties arise when velocity components perpendicular to the laser light sheet are significant. This may be caused by misalignment of the light sheet with the expected flow direction or, again, strong vorticity causing out-of-plane displacements. Further still, when the camera is not situated perpendicular to the measurement plane, perspective and distortion errors can arise. Due to the simplistic nature of the flat plate experiments and the convenient arrangement of the experimental apparatus and equipment, not one of the issues mentioned thus far introduce considerable error into the data. However, stereo PIV does introduce perspective challenges that are solved via the Scheimpflug principle, as previously mentioned.

Likely the greatest source of uncertainty inherent with the present experimental measurements lies in user error regarding imperfect alignment of the calibration targets within the laser light sheet. This step involves one's best approximation for where the target should be, but even relatively small misalignment can lead to considerable differences in mapping out-of-plane displacements. Fortunately, its consequences are abated significantly for mono PIV, especially when associated with perpendicular camera perspectives of the light sheet. Though some quantifiable error is certainly present in the measurements, it may be equally important to determine what velocity information inside the boundary layer was *missed* due to physical measurement limitations rather than highlighting deviations of the collected data from exact values.

3.2.1 Hydraulic Flume Arrangement

The inherently unstable nature of the flow over the flat plate at zero incidence is assumed herein to be steady and uniform. This assumption is indisputably erroneous despite efforts invested in producing entirely steady and parallel flow incident to the plate. Regardless, some undesirable fluctuations, which manifested as misdirection and magnitude deviation, were unavoidable. To quantify the deviations from free stream velocity expected to arise at any given location or time, PIV images were collected of the free stream itself at the location of the plate's leading edge but without the presence of the plate in the flow. This led to a time-averaged free stream velocity with standard deviations situated between 2.1 and 2.4% of the average free stream velocity. Therefore, errors of 2.1 to 2.4% are expected to arise in the velocity measurements. One might argue that these errors are mitigated at smaller flow velocities since small displacements are easier to track. Unfortunately, no trends of periodic fluctuations were evident which would allow better estimation of velocity magnitude deviation and control.

Due to the easily repeated nature of experiments performed in the hydraulic flume, a great deal of trial and error was incorporated into finding optimal seeding density and PIV imaging time intervals to well suit the relatively high spatial resolution achieved in the arrangement. This allowed velocity gradients within the boundary layer to be characterized more readily. Time was of the essence in performing SPIV investigations in the towing tank, however. Additionally, sufficient seeding density was difficult to achieve requiring sub-optimal spatial resolution thereby negatively affecting velocity gradient characterization. Nevertheless, some measures were taken to quantify the relative error within the stereo investigations as well.

3.2.2 Towing Tank Arrangement

The best and most specific error estimation may be obtained in a manner similar to the procedure used in the hydraulic flume: velocity measurements made without the test article in place are compared with the known/actual carriage speed. Preemptive experiments made without the cylinder revealed disparities of 0.0040 to 0.0095 m/s for a carriage speed of 0.25 m/s. This yields 1.6 to 3.8% difference. Similar measurements for a carriage speed of 0.5 m/s resulted in disparities of 0.0091 to 0.0198 m/s, which yields 1.8 to 4% difference. In both cases, PIV measurements over-predicted the carriage speed. This is likely due to imperfections in calibration, especially in light of the almost exactly linear increase in measurement error. These estimates account for uncertainty in the out-of-plane displacement measurements which are known to produce confidence concerns in the desired velocity data.

Two types of global error are estimated during processing in Insight 4G and may be reported when exporting velocity vectors (a fact not known by the author until well after all processing of the flat plate data was complete): pixel-displacement errors and residual stereo disparity errors. The two-dimensional pixel-displacement errors are evaluated for each camera from cross-correlation using the peak ratio (PR) uncertainty method (Charonko and Vlachos, 2013). The algorithm assumes that uncertainty must be expressed with a corresponding confidence level which implies that 95% of displacement vectors will have their true value lie within the bound of uncertainty. Average lower bounds for each component of the vector results relating to the cylinder data were found to be

0.0001 m/s, while average upper bounds were 0.0649 m/s. These bounds were estimated as averages for all the runs assessed, with the highest Δt applied to the lower bound and the lowest Δt applied to the upper bound. No correlation with mean inflow speed or test article oscillations is made presently. However, these errors represent worst-case scenarios and should be analyzed individually for specific vectors as desired. This component of error reporting was unintentionally switched off when processing data from the robotic eel experiments, so pixel-displacement uncertainty must be assumed to correspond similarly with estimations made for the cylindrical test article.

Residual stereo disparity error basically evaluates discrepancies between cameras via calibration information and are exported along with three-dimensional velocity vector data only. Average lower and upper bounds corresponding to data from experiments with the cylinder were found to be 0.0031 m/s and 0.0805 m/s, respectively, while bounds from the robotic eel data were found to be 0.0028 m/s and 0.0458 m/s. Again, these errors represent worst-case scenarios and do not reflect correspondence with specific flow conditions. Relevant error estimation for the data reported by Insight 4G should be performed on a per-run basis, as desired.

Other nonquantifiable sources of measurement error may also be described. To the detriment of greater forward speeds, the largest component (and only component for these preemptive tests in a quiescent tank) of fluid velocity travels perpendicularly through the laser light sheet, necessitating a rather small time interval Δt. This forces enlarged grid spacing during PIV processing. The benefit of reducing Δt on the other hand is abatement of the adverse time-averaging effects as described in section 3.1. In order to capture the larger velocities, reducing the PIV imaging time interval becomes necessary. This provides a better estimation of fluid speed at an *instant* of time, rather than the average velocity over the time Δt.

Interrogation window sizes were necessarily increased to accommodate diminished seeding density, however, reduced spatial resolution additionally smooths high velocity gradients. Peak magnitudes are generally retained except for issues with temporal averaging over Δt. However, it is the velocity gradients that are crucial in determining wall shear stress for friction coefficient estimations, and thus these nonquantifiable errors may propagate under-predictions into the resulting calculations.

A final erroneous artifact present only in experiments with the robotic eel is related to the local body's cross-sectional inclination horizontally through the measurement plane within the light sheet. Velocity gradients perpendicular to the wall are required for estimations of local wall shear stress, but this is technically infeasible due to the inclination angles. Body slopes (shown later in Table 6.2) achieved by the robot corresponding to measurement locations and moments appear in the range $23.98°$–$56.67°$ which could lead to under-predictions scaled by approximately $\cos(23.98°) \approx 0.914$ to $\cos(56.67°) \approx 0.549$.

4 Flat Plate Experiments

A first step in understanding and visualizing oscillatory boundary layers involves experimental analysis of flow over a flat plate, both while at rest and oscillating in its own plane. Capturing *changes* in flow velocity near the boundary surface is of chief importance for estimating shear forces experienced by the immersed body. Planar surfaces present a benchmark case study for both steady and oscillatory boundary layers where a flow-directional length scale is present due to leading edge effects. This allows dialing in the parameters and gaining experience with using the system before testing in the towing tank. A schematic diagram of the problem studied herein is shown in Figure 4.1.

4.1 Experimental Setup

Experimental investigations regarding uniform flow near a flat plate were accomplished via mono PIV in a hydraulic flume powered by two 3 hp pumps. These pumps operate in parallel to generate flow in the open channel by creating a pressure difference across the upstream and downstream end tanks and allowing transfer through 76.2 mm (3″) schedule 80 PVC pipe. Two 480 V three-phase motors provide the pumps with power that is controlled by an ABB ACS355 motor controller. One pump operates only at a fixed speed of 3,450 rpm, while the other is variable thanks to the motor controller. Three valves are situated in the pipes which can be used to throttle or free the flow for pressure equalization. A few of the channel's particulars are summarized in Table 4.1.

A 76.2 mm (3″) long flow straightening grid, with cross section dimensions equal to the channel's, made up of 3.18 mm (1/8″) thick acrylic slats positioned on 12.7 mm (1/2″) centers was placed directly in the flow at the exit of the upstream end tank for the purpose of removing swirl in the flow. The slats are fitted together by means of slot joints and acrylic cement. Two perforated stainless steel sheets were included upstream of the flow conditioner to provide resistance for breaking up larger eddies and free surface disturbances. Each sheet is 1.59 mm (1/16″) thick, and one sheet has 2.38 mm (3/32″) holes on 3.97 mm (5/32″) centers. The second sheet has 6.35 mm (1/4″) holes on 7.94 mm (5/16″) centers.

A schematic showing the flume arrangement is given in Figure 4.2, and a photograph of an early version of the setup is shown in Figure 4.3. The channel walls and bottom are 25.4 mm (1″) transparent acrylic allowing the camera to see plainly through to the light sheet. The tripod that

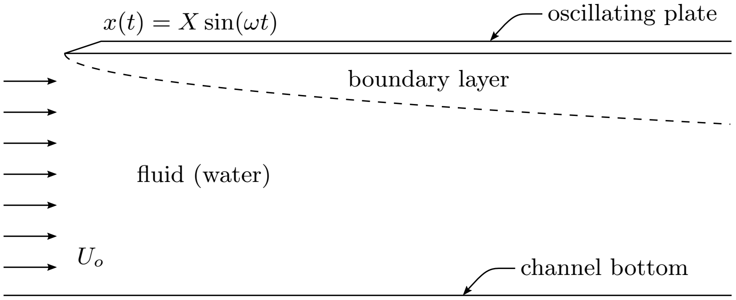

Figure 4.1: Schematic of flow problem for flat plate

Table 4.1: Flume characteristics

channel length	3.35	m
channel breadth	60.96	cm
channel depth	36.83	cm
maximum water depth	25.00	cm
maximum flow rate	1000	gpm
maximum pump speed	3450	rpm
pump power at 3450 rpm	3	hp

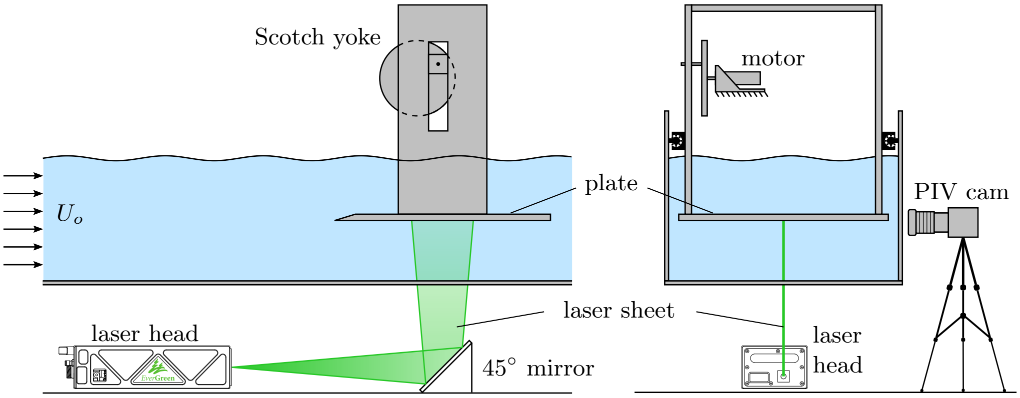

Figure 4.2: Side (left) and cross-sectional (right) views of the PIV configuration for flume experiments

is present in both Figure 4.2 and Figure 4.3 was replaced by a track that was carefully aligned to be parallel with the flume walls. The track has a block and slider that traverse a single direction by means of a crank at one end allowing for precise placement of the camera. Twenty turns of the crank yield exactly 25.4 mm (1″) translation along the channel. The PIV camera was mounted to this block and carefully leveled and aligned such that movement along the track produced parallel motion relative to the ground and the light sheet which was aligned with the channel's centerline. This track and a better perspective of the camera's viewpoint can be seen in Figure 4.4.

Power for the plate's oscillatory motions was provided by an 80 W Maxon brushed DC motor equipped with an HEDS-6310 encoder in accompaniment with a Maxon ADS 50/5 servo-amplifier motor controller. This combination provides motor performance feedback and load response via the encoder and controller card. The response is important for maintaining a constant rate of rotation in the midst of a varying external load. These components, along with a power supply, were mounted above the channel to move the plate. These are shown schematically in Figure 4.2 and in Figures 4.3 and 4.4.

The plate is set into motion via a slotted linking mechanism known as a Scotch Yoke. A flywheel was mounted directly to the motor's output shaft, and a bolt was fastened at a known distance, X, away from the center of rotation, parallel to the motor shaft. This bolt acts as a piston which drives the Scotch Yoke. The bolt's radial offset determines the plate's periodic translational amplitude of motion ($|x(t)| = X$ in Figure 4.1). Clamped to one of the yoke's uprights was a trigger switch which sends a 5 V signal to the PIV synchronizer when the flywheel passes through its 12 o'clock position. The plate is suspended from two horizontal rails mounted to the channel's sidewalls along which it rides enforcing the translational motions.

The two-dimensional laser sheet is aligned parallel with the flow direction on centerline and illuminates the bottom edge of the plate. The laser head is positioned horizontally beneath the

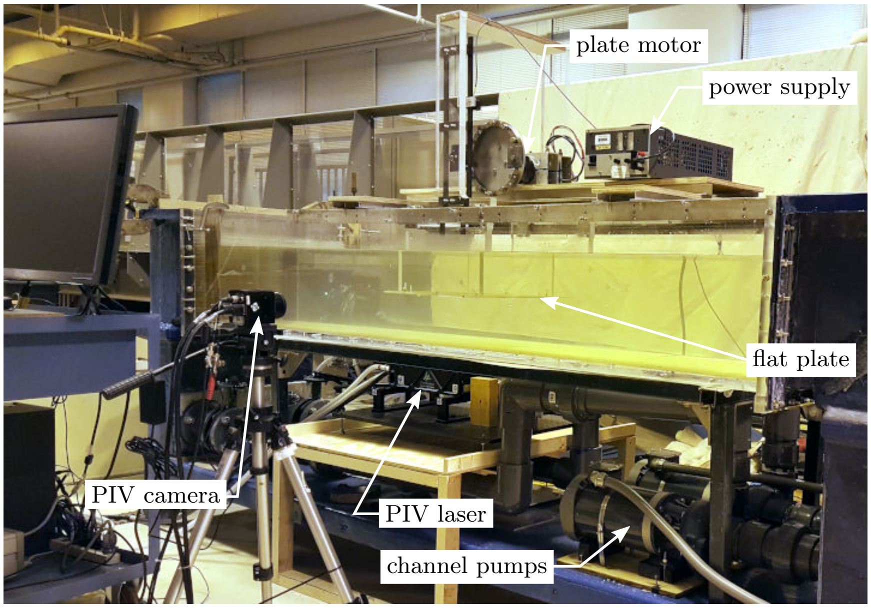

Figure 4.3: Experimental setup for flat plate experiments

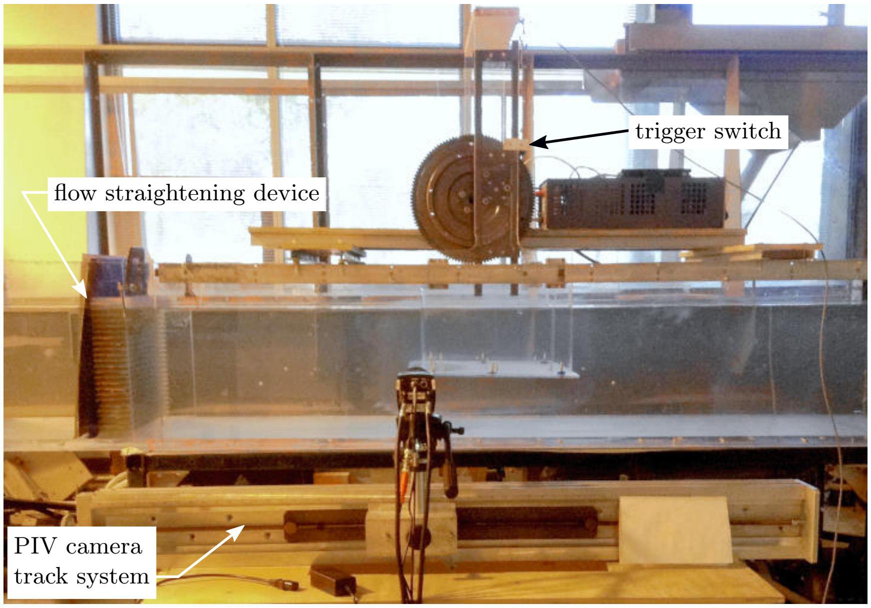

Figure 4.4: PIV camera perspective

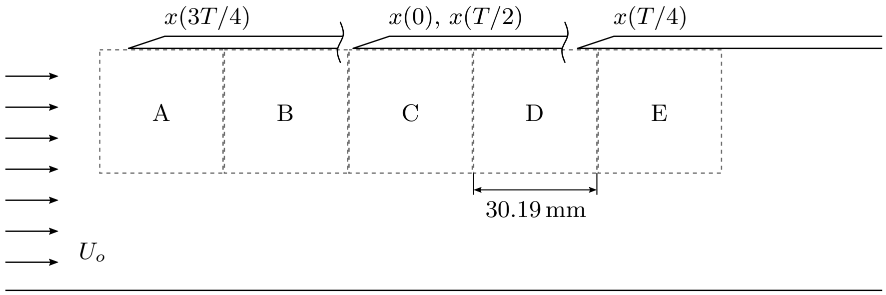

Figure 4.5: PIV regions of interest for the flat plate experiments

Table 4.2: PIV processing settings for experimental flat plate data

spatial calibration	14.74 µm/px	
time interval, Δt	1,200 µs	
interrogation resolution	32 px/16 px (starting/final)	
grid engine	recursive Nyquist	
correlation engine	FFT correlator	
peak engine	Gaussian peak	
vector conditioning	recursive with	
	neighborhood size	2
	kernel radius	2
	Gaussian sigma	0.8

channel on centerline, with the sheet being redirected upward by means of a 45° mirror as shown in Figure 4.2. The laser head is fitted with a 1 m lens immediately upstream from the cylindrical sheet maker. The plate's leading edge is cut to a clean knife edge to reduce its effect on the near-body flow. Velocity measurements are made within the laser sheet beneath the plate.

Exploiting the track system, five camera views were used to collect velocity information beneath the plate. This was the minimum number required to observe at least 30 mm of the plate downstream of the leading edge throughout the plate's oscillatory journey. Figure 4.5 illustrates the movement of the plate and the five adjacent regions of interest used in collecting data. For cases where the plate remained stationary, it was set at the forward-most position, i.e. the position where the leading edge resides at $3T/4$ in oscillation, or the flywheel's 9 o'clock position. Here, T is the time-period of oscillation. Inscribed into the track itself is a ruler which indicates the slider's (and thus the camera's) exact global position. This was necessary for precisely placing the camera to collect data only within a particular region of interest with no overlap.

4.2 PIV and Processing Settings

Processing PIV images was performed in TSI's Insight 4G version 11.1.0.5. A summary of relevant PIV processing settings can be seen in Table 4.2. The 630059 PowerView cameras are incompatible with Insight 4G version 11.X, so Insight 4G version 10.1.0.5 was used instead when collecting images with those cameras. Data processing was still handled in version 11 to exploit its updated ability to evaluate user-defined masks which indicate pixel-level image regions to be interrogated or ignored (more discussion on this in section 5.3).

The calibration image used to estimate the spatial calibration factor provided in Table 4.2 is shown in Figure 4.6. The calibration board's physical vertical and horizontal marker spacings are equivalent at 1 cm. Since the camera was carefully placed to view the light sheet from an exactly

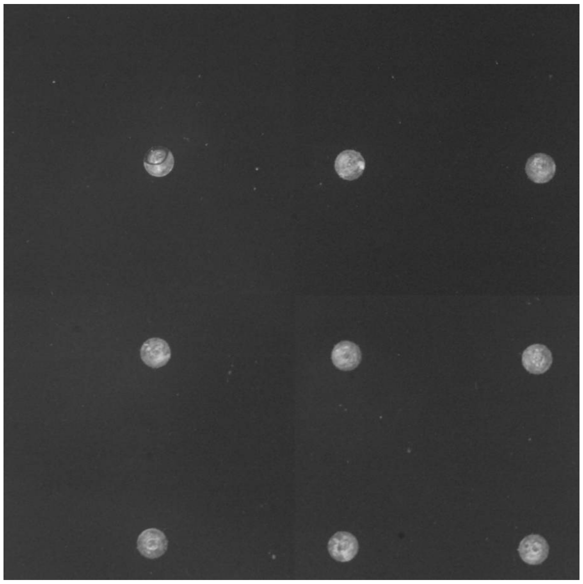

Figure 4.6: Calibration image used in flat plate experiments

perpendicular perspective, this single calibration factor is considered valid at any part of the image. Oblique viewing angles and warping lens effects would require more sophisticated interpolation which is assumed unnecessary here. An additional calibration image was captured after experiments were completed to verify consistency.

Characterizing boundary layer information was done in post-processing of the PIV velocity vector data and began with careful filtering of unneeded data and determination of corresponding images, keeping in mind:

- their respective spatial locations according to Figure 4.5 and
- temporal correspondence of equivalent periodic progression.

Combining these vector fields is done easily when working with meshgrids—rectangular grids (matrices) where elemental positions are representative of Cartesian indexing and separated by $\mathrm{d}x$ and $\mathrm{d}y$. Basically, columns of the meshgrid's x-component increase from left to right by increments of $\mathrm{d}x$ where each value is an x-coordinate of the vector field. Similarly, rows of the y-component decrease from top to bottom by increments of $\mathrm{d}y$ where values are y-coordinates. This makes "stitching" neighboring vector fields simply a matter of appending meshgrids in the appropriate directions and adding the required offsets. Overlapping vector fields with identical $\mathrm{d}x$ and $\mathrm{d}y$ are also handled with relative ease by summing data in the overlap and dividing by the number of vector fields included, effectively averaging the data at corresponding (x, y) points. If a partial overlap is desired, each matrix of velocity data is first padded with zeros such that the x and y-components of the meshgrid extend to the extreme dimensions of *both* vector fields. This greatly facilitates a common averaging technique utilized in PIV post-processing known as *ensemble-averaging*.

PIV results for steady and periodic flows may best be visualized and analyzed after performing ensemble-averaging (Libby, 1996; Tropea, Yarin, and Foss, 2007; Bernard, 2019). To do this, overlapping vector fields must be collected for corresponding moments during the flow cycle and averaged at corresponding locations in space. For transitional and fully turbulent flows, ensemble-averaging may tend to smooth moving and intermittent eddies that arise in different spatial regions rather than a fixed location or those that do not appear in all temporal components of the ensemble. The goal is to achieve a maximum signal-to-noise ratio; consequently, eddies of low-magnitude

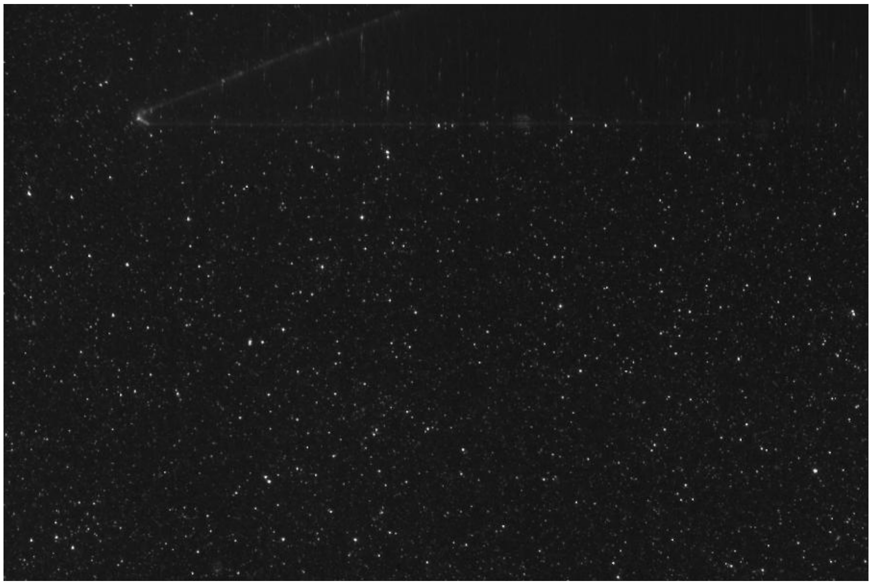

Figure 4.7: Cropped sample PIV image from flat plate experiments

vorticity may diffuse in the ensemble as representative of noise. Issues arise mainly where vortex shedding is strongly evident which is not presently the case (likely, not even for later experiments with the cylinder and robotic eel).

Ensemble averaging of M velocity vector fields $\mathbf{v}_m$ where $m \in [1, \ldots, M]$ is accomplished as follows. Each component is first ensemble-averaged as

$$\widehat{u} = \frac{1}{M} \sum_{m=1}^{M} u_m \tag{4.1}$$

at corresponding spatial locations. Averaged $\widehat{v}$ and $\widehat{w}$ are calculated similarly. Thus, $\widehat{\mathbf{v}} = (\widehat{u}, \widehat{v}, \widehat{w})^{\mathrm{T}}$. Velocity vectors are plotted in this manner, but contours are plotted using the scalar magnitude as

$$|\widehat{\mathbf{v}}| = \sqrt{\widehat{u}^2 + \widehat{v}^2 + \widehat{w}^2} \tag{4.2}$$

Prior to inclusion in the ensemble for averaging, velocities are normalized according to $\mathbf{v}/|\mathbf{v}|$ where

$$|\mathbf{v}| = \sqrt{U_o^2 + |\dot{x}|^2} \tag{4.3}$$

for consistency and better comparison of relative magnitude between inflow speeds and plate velocity amplitudes. Here, $\dot{x}$ represents the oscillating plate's translational velocity, defined later in Equation (4.13). Note that for the non-oscillating plate, $\dot{x} = 0$ which simplifies the normalization to $|\mathbf{v}| = U_o$.

4.3 Stationary Plate Results

A cropped sample PIV image is shown in Figure 4.7. The plate's lower edge and leading edge are faintly visible in the upper half of the image, as well as some minor particle reflections inside the plate itself. The distance from the plate's leading edge to the right side of the image is approximately 17.39 mm. A reasonably dense particulate distribution is shown in the image. This is effortless to achieve in such a small flow channel. Sufficiently seeding the towing tank with comparable density and evenness is quite challenging due to the tank's volume and lack of flow control. Also, since the

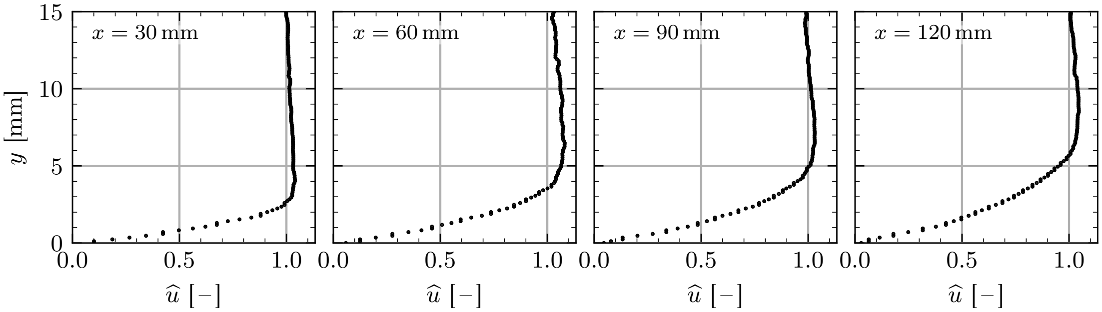

Figure 4.8: Horizontal velocity profiles for $U_o = 0.0941\,\mathrm{m/s}$

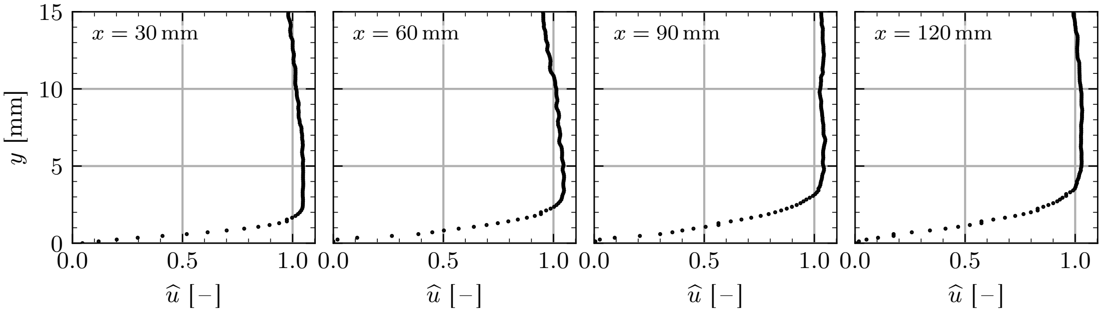

Figure 4.9: Horizontal velocity profiles for $U_o = 0.1865\,\mathrm{m/s}$

towing tank's water is mostly stationary, one must stir up the particles before every test for decent distribution. This is unnecessary in the flume, since the seed particles are satisfactorily scattered by the pumps—another benefit of performing PIV measurements in a flume.

4.3.1 Velocity Profiles and Wall Shear Stress

Velocity profiles at various distances from the plate's leading edge are plotted for each flow speed in Figures 4.8 and 4.9. Generally Blasius-shaped profiles are evident with slight overshoots in estimated skin friction, presumably due to the presence of a nonzero pressure gradient. Local skin friction coefficients are estimated by fitting a linear curve via least-squares to the approximately linear, laminar sublayer of the boundary layer profile. This is the recommended procedure according to Anderson, McGillis, and Grosenbaugh (2001) for PIV/PTV measurements of near-body flow. The slope of this curve provides the value of $\partial u/\partial y$ in the left equation of (2.3) allowing for the calculation of the local skin friction coefficient as

$$C_f = \frac{\tau_\mathrm{w}}{\frac{1}{2}\rho U_o^2} = \frac{\text{wall shear stress}}{\text{dynamic pressure}} \tag{4.4}$$

Skin friction estimates are summarized along with local Reynolds numbers in Table 4.3. Here, the local Reynolds number is defined according to the usual flat plate boundary layer with length scale in x originating at the leading edge:

$$\mathrm{Re_x} = \frac{U_o x}{\nu} \tag{4.5}$$

Table 4.3: Tabulated summary of experimental estimation of friction coefficients, C_f [10^{-3}], with local Reynolds numbers

	0.0941 m/s			0.1865 m/s		
x	$\mathrm{Re_x}$	$C_{f,\mathrm{Blasius}}$	$C_{f,\mathrm{exp}}$	$\mathrm{Re_x}$	$C_{f,\mathrm{Blasius}}$	$C_{f,\mathrm{exp}}$
30 mm	2,479	13.091	16.924	4,914	9.501	10.602
60 mm	4,959	9.136	12.625	9,828	6.698	7.426
90 mm	7,438	7.699	10.433	14,742	5.469	5.845
120 mm	9,917	6.614	8.448	19,656	4.736	4.785

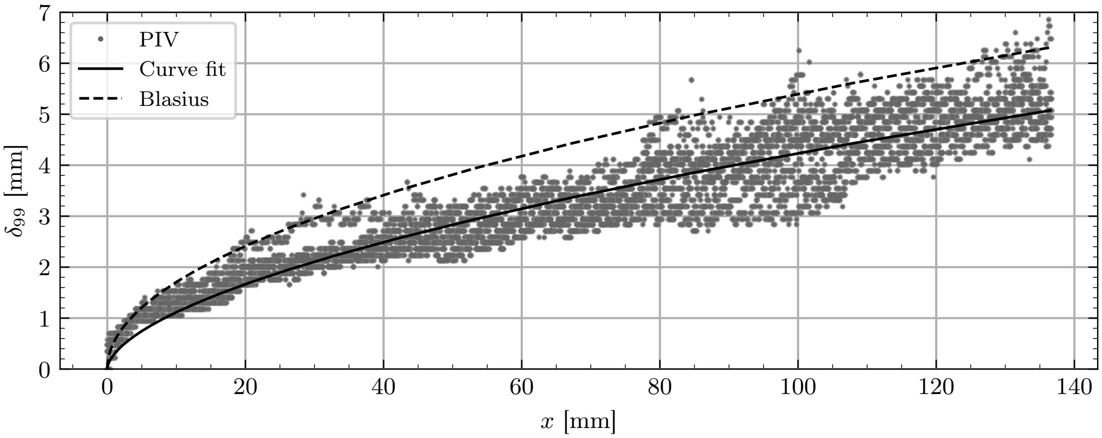

Figure 4.10: Boundary layer thickness measurements for $U_o = 0.0941$ m/s

4.3.2 Boundary Layer Thickness

The concept of boundary layer thickness is arbitrary in a sense, since the effect of viscosity decreases asymptotically in the direction moving outward from the wall (Schlichting and Gersten, 2017). However, it is commonly measured in a rudimentary way by checking the standard criterion: determine the first point, measured normal to the boundary, at which a certain percentage of the outer velocity, usually 99%, is reached, $u \geq 0.99U_o$. In theory, this distance should match the results of Blasius (1908) for completely laminar, planar boundary layers with zero pressure gradient:

$$\delta_{99}(x) \approx 4.91\sqrt{\frac{\nu x}{U_o}} \tag{4.6}$$

An additional criterion may be imposed along with the velocity threshold to improve upon this estimation for noisy data in the presence of a nonzero stream-wise pressure gradient: since the boundary layer is defined as the near-body region of fluid where viscous effects are considered significant, and since the flat plate at zero incidence in laminar regimes theoretically has a single length scale, determine the point at which the fluid's internal shear stress falls below some arbitrary value, perhaps 1% of the shear stress value at $y = 0$, $\tau(y) \leq 0.01\tau_\mathrm{w}$. For profiles with a pronounced "elbow" near the boundary layer edge, i.e. where the profile juts beyond the mean flow value and asymptotically returns from the right side, this extra criterion should produce estimations more similar to Blasius'.

Evaluating these criteria for every discrete x-coordinate in the domain of the stationary flat plate for each of the two external mean stream flow speeds produces the results plotted as scatters in Figures 4.10 and 4.11. Blasius' boundary layer thickness equation is also plotted for comparison,

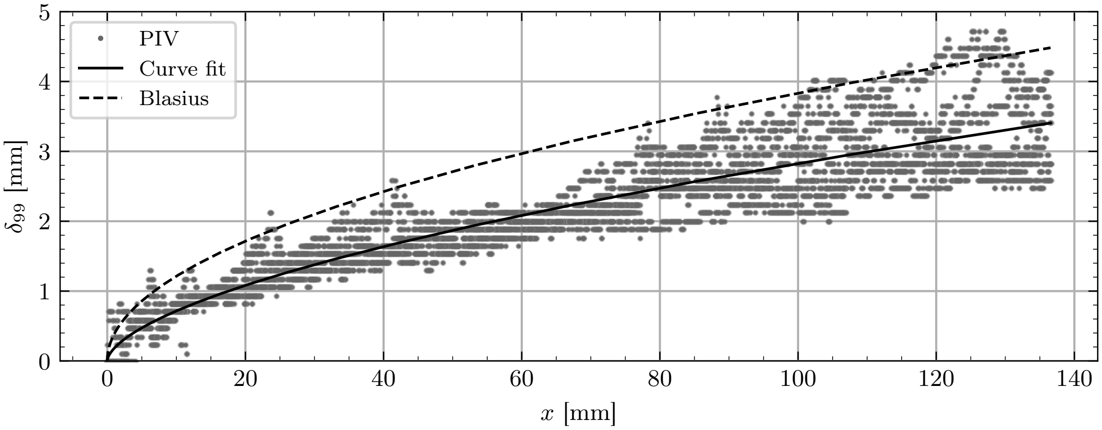

Figure 4.11: Boundary layer thickness measurements for $U_o = 0.1865\,\text{m/s}$

showing its over-prediction.

A curve fit of the data was accomplished by means of a nonlinear least-squares minimization routine known as the Levenberg–Marquardt algorithm as implemented in MINPACK and accessed by SciPy's `leastsq` routine in the `optimize` module. For more information on this algorithm see (Moré, 1978). The routine allows a user-defined nonlinear function with unknown coefficients to be fit to data while minimizing the sum of squared residuals. A residual represents the difference between actual data and the fitted values provided by the function. The coefficients are estimated to provide a "best fit" of the function to the data in the least-squares sense. The function chosen to fit to the data is of the form

$$\delta_{\mathrm{cf}}(x) = \frac{ax}{x^b} \tag{4.7}$$

where a and b are the unknown coefficients to be estimated. This form was selected for its correspondence to the form of Blasius' boundary layer thickness equation (4.6) which, for constant external flow speed, can be written in the same form as

$$\delta_{99}(x) \approx 4.91\sqrt{\frac{\nu x}{U_o}} = \frac{4.91x}{\sqrt{\mathrm{Re_x}}} = \frac{4.91x}{(U_o x/\nu)^{0.5}} = \frac{4.91(\nu/U_o)^{0.5}\cdot x}{x^{0.5}} \tag{4.8}$$

Here, $4.91(\nu/U_o)^{0.5}$ is the Blasius version of the unknown a, and the exponent 0.5 in the denominator represents b. The coefficients obtained for the $0.0941\,\text{m/s}$ flow speed in Figure 4.10 are $a = 0.293$ and $b = 0.420$. The maximum boundary layer thickness is measured to be $\delta_{\max} = 5.08\,\text{mm}$ at $x = 136.50\,\text{mm}$. The estimated Reynolds number at this location is $\mathrm{Re_x} = 11{,}285$. This estimate is based on a kinematic viscosity of $\nu = 1.1386 \times 10^{-6}\,\text{m}^2/\text{s}$ for fresh water at 15 °C.

For $U_o = 0.1865\,\text{m/s}$, the following coefficients are obtained for the curve in Figure 4.11: $a = 0.181$ and $b = 0.403$. The maximum boundary layer thickness is measured to be $\delta_{\max} = 3.41\,\text{mm}$ at $x = 136.50\,\text{mm}$. The estimated Reynolds number is $\mathrm{Re_x} = 22{,}367$. For reference, if the leading term a is calculated according to the Blasius (1908) profile, one obtains:

$$\begin{aligned} &\text{for } U_o = 0.0941\,\text{m/s:}\;\; 4.91(\nu/U_o)^{0.5} = 0.540 \\ &\text{for } U_o = 0.1865\,\text{m/s:}\;\; 4.91(\nu/U_o)^{0.5} = 0.384 \end{aligned} \tag{4.9}$$

4.3.3 Velocity and Vorticity Contours

The velocity contours plotted in Figures 4.13 and 4.14 for the flat plate whose leading edge is situated at $x = 0$ are colored according to magnitude as given in Equation (4.2) but with no out-of-plane

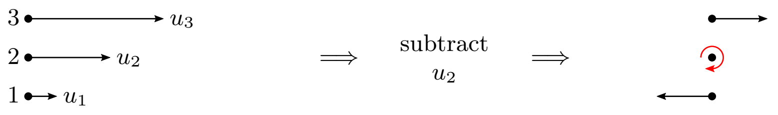

Figure 4.12: Simple illustration of circulation production in a one-dimensional shear flow

(stereo) component:

$$|\widehat{\mathbf{v}}| = \sqrt{\widehat{u}^2 + \widehat{v}^2} \tag{4.10}$$

This means that data points with negative $\widehat{u}$ or $\widehat{v}$ components are colored with positive values by definition. Overlaying actual vectors, scaled down for neatness, facilitates visualizing flow direction and relative magnitude. This is done for vorticity contours as well. Vorticity is a vector field defined as the curl of the velocity field:

$$\boldsymbol{\omega} = \operatorname{curl} \widehat{\mathbf{v}} = \nabla \times \widehat{\mathbf{v}} \tag{4.11}$$

For a two-dimensional velocity field with two-dimensional velocity components, this is expanded as

$$\boldsymbol{\omega} = \left(\frac{\partial \widehat{v}}{\partial x} - \frac{\partial \widehat{u}}{\partial y} \right) \mathbf{k} \tag{4.12}$$

where $\mathbf{k} = (0,\ 0,\ 1)^{\mathrm{T}}$. The units become $\left[\mathrm{mm}^{-1}\right]$ because velocities have previously been made non-dimensional according to (4.3), and the differential distances, ∂x and ∂y, are in [mm]. As a basic interpretation, the contours of vorticity indicate nonzero velocity derivatives. For a two-dimensional flow they simply illustrate the difference between one derivative and another, giving a relative sense of gradient magnitude and direction in the form of circulation strength.

For the results given in Figures 4.13 and 4.14, one notices mostly negligible circulation (irrotational flow) outside the boundary layer where shear stresses and velocity gradients are minimal and where viscous effects are negligible. Mostly negative vorticity is noticed within. This is due to the presence of a shear flow progression inside the boundary layer in the outward normal direction starting at the body surface.

A simple illustration of this is provided in Figure 4.12. A clockwise rotational tendency is produced on particle 2 due to the difference in velocities of neighboring particles. This type of vorticity dominates the contours far from the leading edge, but other effects appear there, such as the motion of the fluid around the leading edge. As with any submerged body, the fluid must "move aside" to allow for the structure to pass through. This results in small but nonzero transverse velocities near the plate's leading edge.

As indicated in Figures 4.13 and 4.14, higher velocity gradients and, thus, higher shear stresses within the fluid, produce stronger vorticity as indicated by darker shades of yellow, oranges, and red. Gradual reduction of circulation is observed with increasing x.

4.4 Oscillating Plate Results

To avoid transient effects, the channel's pumps were run to circulate water for close to a minute to achieve steady state before triggering data collection. Additionally, the PIV system was not triggered until the plate completed one full oscillation. Data was collected for three full periods of the plate's oscillation. Periods were chosen to be integer multiples of achievable image collection intervals such that the flow could be analyzed at exactly quarter cycles. Table 4.4 provides a summary of the primary experimental parameters of interest for the oscillating plate tests.

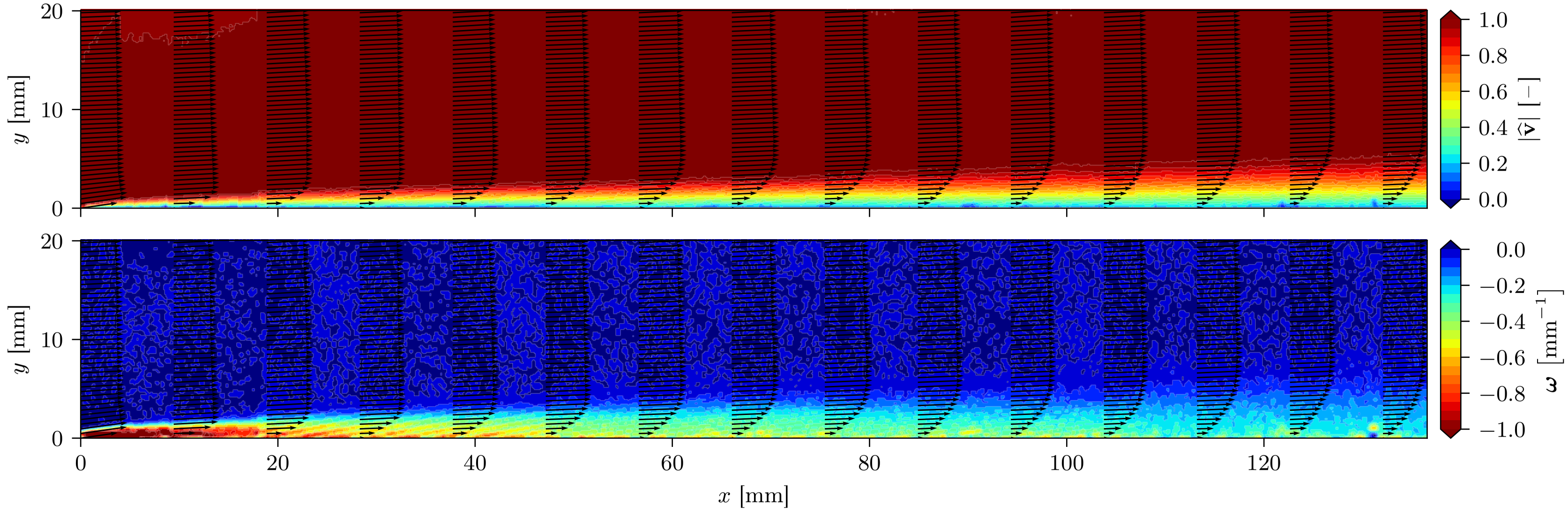

Figure 4.13: Contours of velocity magnitude (top) and vorticity (bottom) for $U_o = 0.0941\,\text{m/s}$

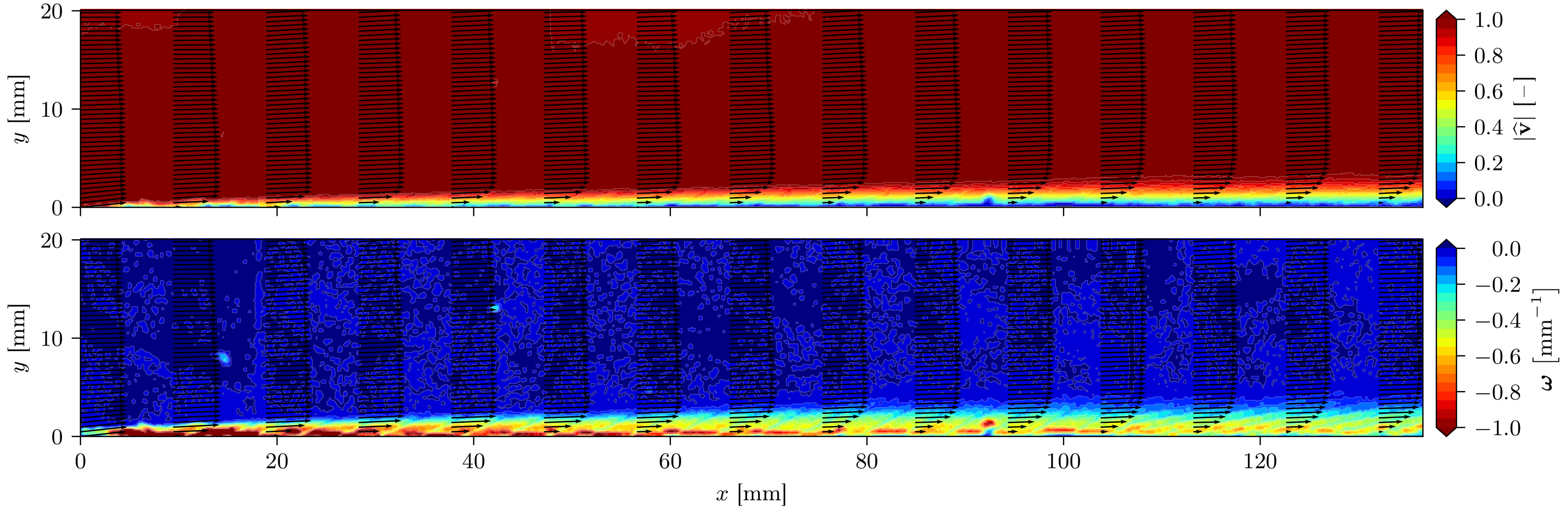

Figure 4.14: Contours of velocity magnitude (top) and vorticity (bottom) for $U_o = 0.1865\,\mathrm{m/s}$

Table 4.4: Experimental test parameters for oscillating flat plate experiments

external flow speeds	U_o	0.0941 m/s, 0.1865 m/s
measurement locations	x	5, 10, ..., 30 mm (from leading edge)
oscillation periods	T	2 s, 3 s
oscillation amplitude	X	57.15 mm

For observations to be made within the thin boundary layer near the plate's leading edge, the camera had to be focused on a relatively very small region of flow seeded densely with tracer particles. In order to capture sufficient spatial data in the oscillating plate experiments, the camera had to translate up- and downstream to increase its overall field of view. The plate's oscillation amplitude was $X = 57.15\,\mathrm{mm}$ (2.25 in). It was desired to obtain experimental flow data over at least 30 mm of the plate from the leading edge, so the number of camera views was selected to accommodate. With the arrangement shown in Figure 4.4, the single-frame PIV field of view turned out to be $(30.19 \times 30.19)\,\mathrm{mm}^2$, so five adjacent camera views were required to obtain the desired data. Actually, slightly over 30 mm of the plate length behind the leading edge was observed. This is illustrated in Figure 4.5.

The camera's movement along x imposed the requirement of stitching together the adjacent velocity vector fields in post-processing. The track system incorporated for camera translation allowed precise positioning for accurate vector placement. Figure 4.5 shows the movement of the plate through its period T in increments of $T/4$. Note that the plate thickness and channel depth are not drawn to scale, but the leading edge is positioned to closely match its actual location as found in frames A–E. Stitching the vector fields was not difficult for these experiments. The first frame, A in Figure 4.5, was established, and the leading edge location was determined and subtracted from all the x-coordinates such that the leading edge resides at $x = 0$. Then, subsequent vector fields, B–E, could just be appended to the right side of these fields and offset by $\mathrm{d}x$ to maintain constant vector spacing.

The plate's position in time may be described as follows. Since the trigger switch (shown in Figure 4.4) was located at 12 o'clock on the flywheel, this was designated as the origin $x = 0$. Assuming perfectly harmonic motion leads to the position and velocity of the plate to be

$$\begin{aligned} x(t) &= X \sin(\omega t) \\ \dot{x}(t) &= \omega X \cos(\omega t) \end{aligned} \tag{4.13}$$

Two oscillation periods, $T_1 = 2\,\mathrm{s}$ and $T_2 = 3\,\mathrm{s}$, were used yielding velocity amplitudes of

$$\begin{aligned} |\dot{x}_1| &= \omega_1 X = 2\pi X/T_1 = 0.1795\,\mathrm{m/s} \\ |\dot{x}_2| &= \omega_2 X = 2\pi X/T_2 = 0.1197\,\mathrm{m/s} \end{aligned} \tag{4.14}$$

occurring at $t = 0, T/2$. At the half period the plate travels upstream (in the minus x-direction), so it is designated as negative.

4.4.1 Velocity Profiles

Figures 4.15–4.18 display typical profiles of horizontal velocity reported at six longitudinal locations and at four increments of the oscillation period: $x \in [5, 10, 15, 20, 25, 30\,\mathrm{mm}]$ and $t \in [0, T/4, T/2, 3T/4]$. Note the generally uniform external flow field in all the plots. Qualitatively, one can readily identify boundary layer thicknesses in each case. For the time $t = T/2$, the lowermost data points should ideally be situated on the left side of zero at a distance equal to $|\dot{x}|$.

However, spatial resolution and automatic PIV grid generation caused particles very near to the boundary to be lost. Additionally, since characteristic Reynolds numbers are relatively high, shear layers are expected to be quite thin, resulting in very small distances of very high shear. Therefore it may be reasonable to assume that each profile is shifted down by nearly a millimeter. This offset seems small, but it is in fact a large displacement relative to the length scale and especially the boundary layer thickness.

In each plot, the y-coordinate is truncated to 15 mm for better clarity of the boundary layer profile shape despite there being data obtained at larger values. Data points above 15 mm should continue to behave as uniform flow, so no interesting effects are expected there anyway.

4.4.2 Velocity and Vorticity Contours

Velocity and vorticity vectors are plotted in Figures 4.19–4.26. Unlike for the stationary plate experiments, both positive and negative values for vorticity are expected to appear due to the oscillatory nature of the planar boundary. For this reason, the colorbar values in Figures 4.19–4.26 have been adjusted to accommodate zero at the middle—technically zero appears at the interface of two flood colors, so the external flow may appear noisy though the values actually are just jumping minutely around zero.

For the same reasons as provided above, few to no vectors will be found pointing to the left in $T/2$ or $3T/4$. The contours may indicate more clearly the lack of data found within the one or two millimeters nearest the plate. However, notice the deep depressions found in the vector profiles at $t = 0$. Velocity reductions from the leftward moving plate have succumbed to upstream inertial effects, diffused into positive, yet small, values, and propagated some distance away from the plate. Also notice, e.g. the vorticity in this region in the upper middle plot of Figure 4.21 where $U_o = 0.1865\,\mathrm{m/s}$, $T = 2\,\mathrm{s}$, and $t = 0$, that some wave-like irregularities appear at around 35 mm and 44 mm. These could indicate incipient transition, but some observations at larger distances x would be required for verification.

4.5 Comparison with CFD Results and Discussion

Numerical investigations were made in conjunction with this research on the stationary flat plate at zero incidence which employ fully implicit second order finite difference techniques coupled with the k–ε turbulence model to solve the RANS equations (2.10) and to simulate the flow conditions of interest. Srivastava et al. (2019), describes in detail the computative investigations related to the flat plate problem and wrote the code in reference. The results presented here were achieved using a grid of 81×81 cells with boundary conditions similar to those described in section 2.1. Body boundary conditions remain unchanged, however exceptions are made for far-field conditions to accommodate computational domain simplifications, i.e. with the plate situated at the bottom of the domain, $\partial u/\partial y = 0$ and $v = 0$ are imposed at the top boundary and constant pressure is enforced at the right (outlet) boundary.

Convergence was ensured using the following criterion:

$$\sum_{i,j}^{M,N} \frac{\left(\left(\varphi_n^{k+1} - \varphi_n^{k}\right)/\left(\varphi_{n,\mathrm{rms}}^{k+1}\right)\right)^2}{4MN} \leq \epsilon^2 \tag{4.15}$$

φ_n in (4.15) represents any one of the primitive variables (convergence of all primitive variables was ensured), M and N represent the number of nodes in the x and y-directions, respectively, k represents the iteration step, and ϵ is a residual taken as 10^{-6}.

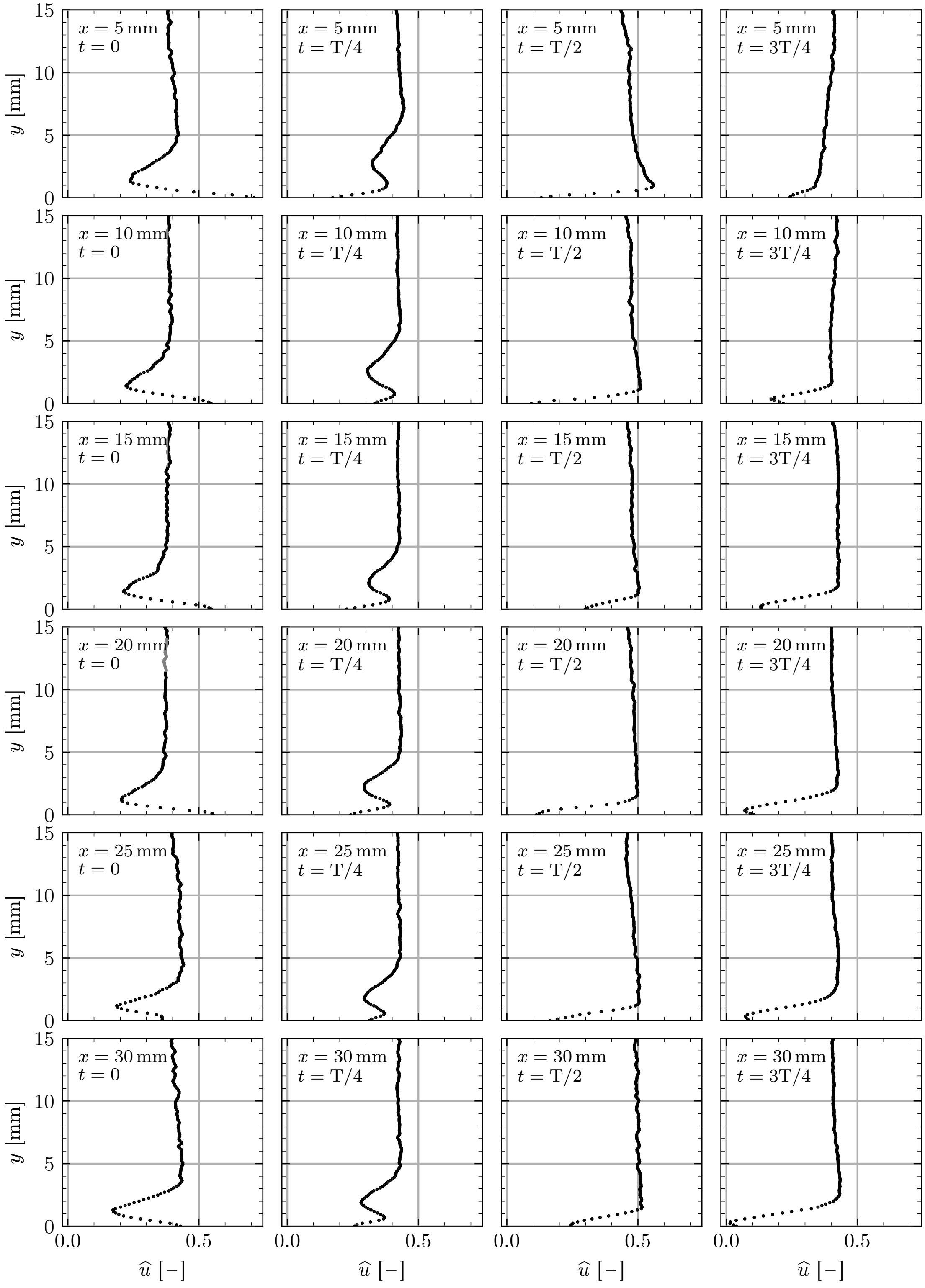

Figure 4.15: Horizontal velocity profiles for $U_o = 0.0941\,\mathrm{m/s}$ and $T = 2\,\mathrm{s}$

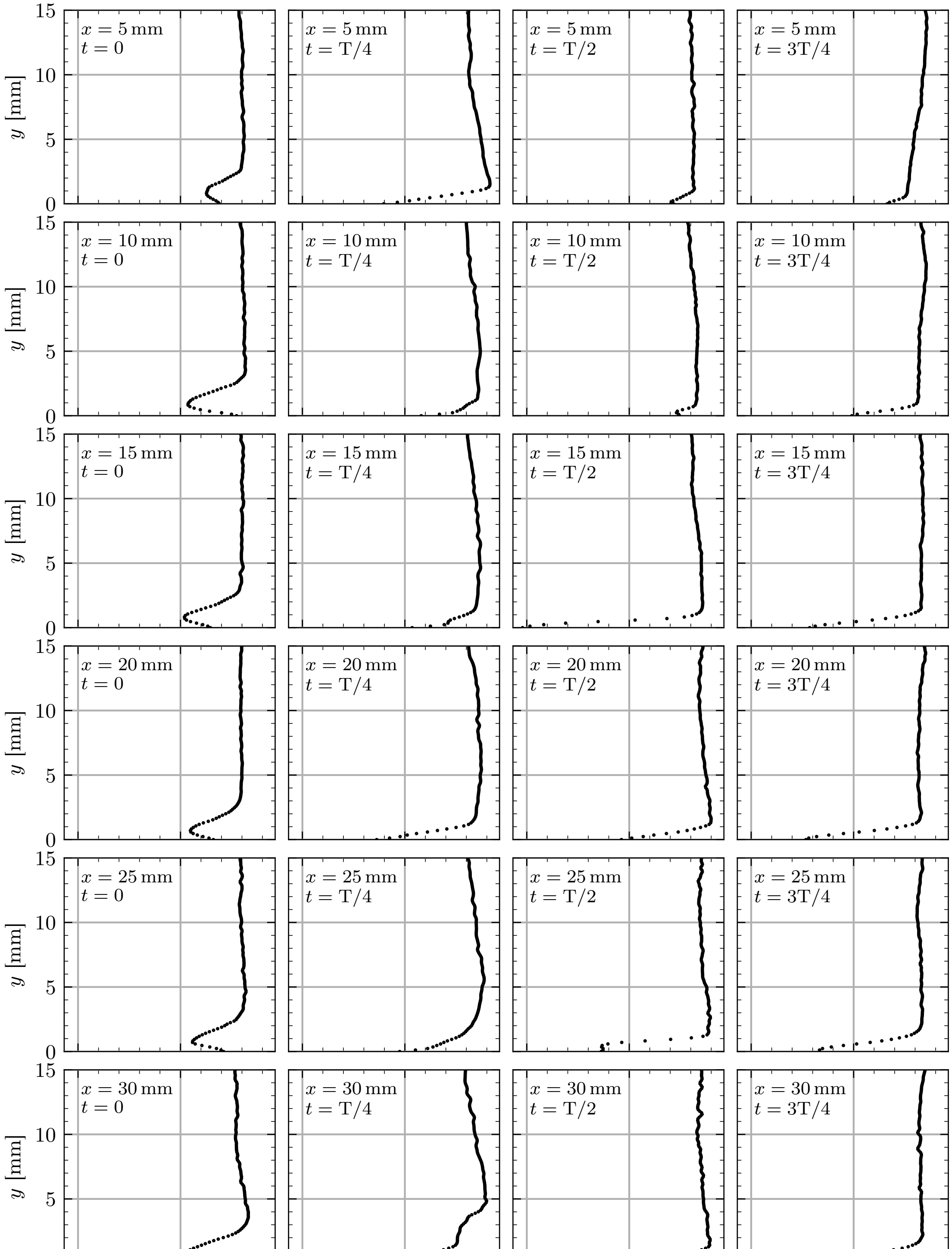

Figure 4.16: Horizontal velocity profiles for $U_o = 0.0941\,\mathrm{m/s}$ and $T = 3\,\mathrm{s}$

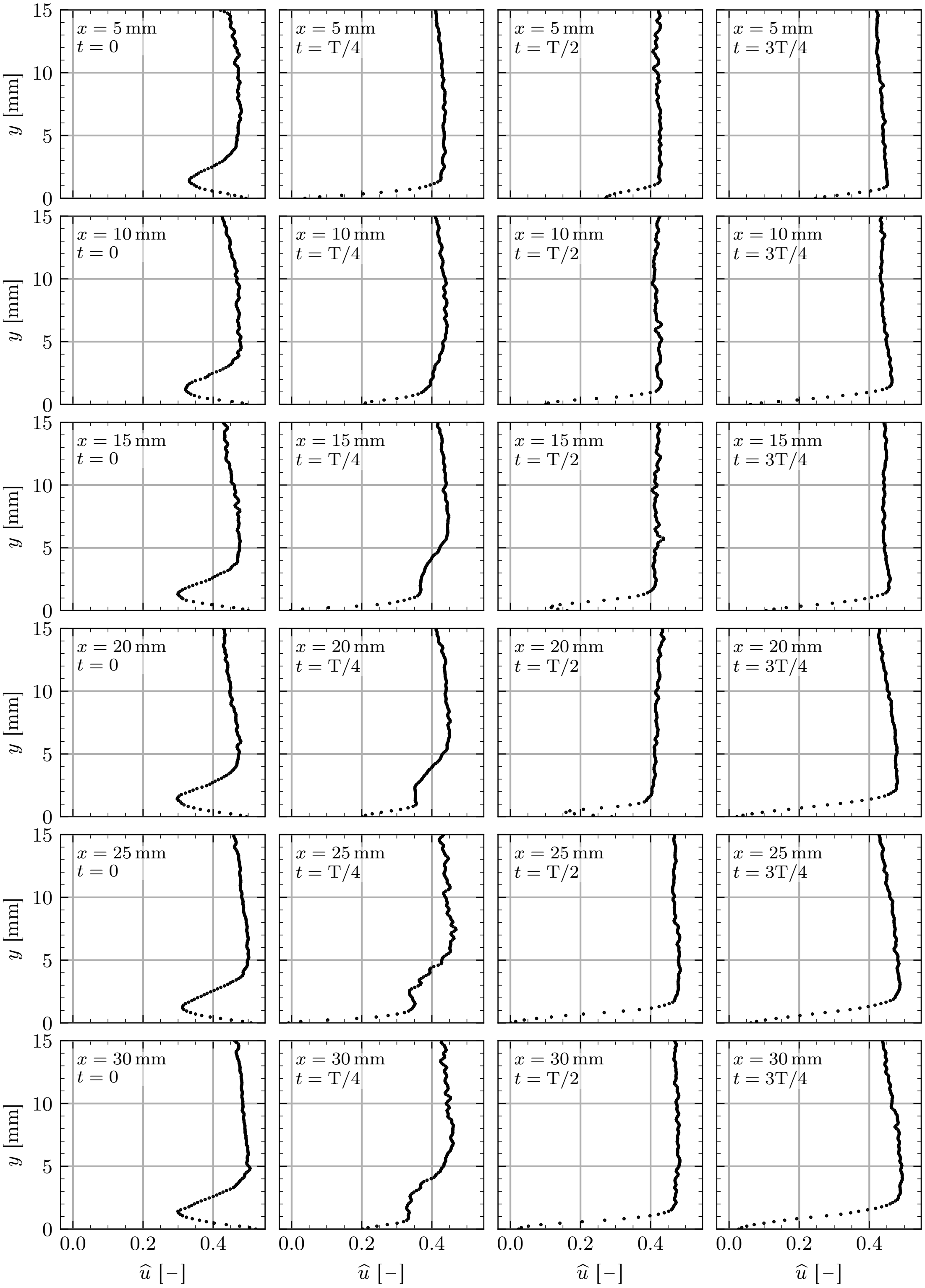

Figure 4.17: Horizontal velocity profiles for $U_o = 0.1865\,\mathrm{m/s}$ and $T = 2\,\mathrm{s}$

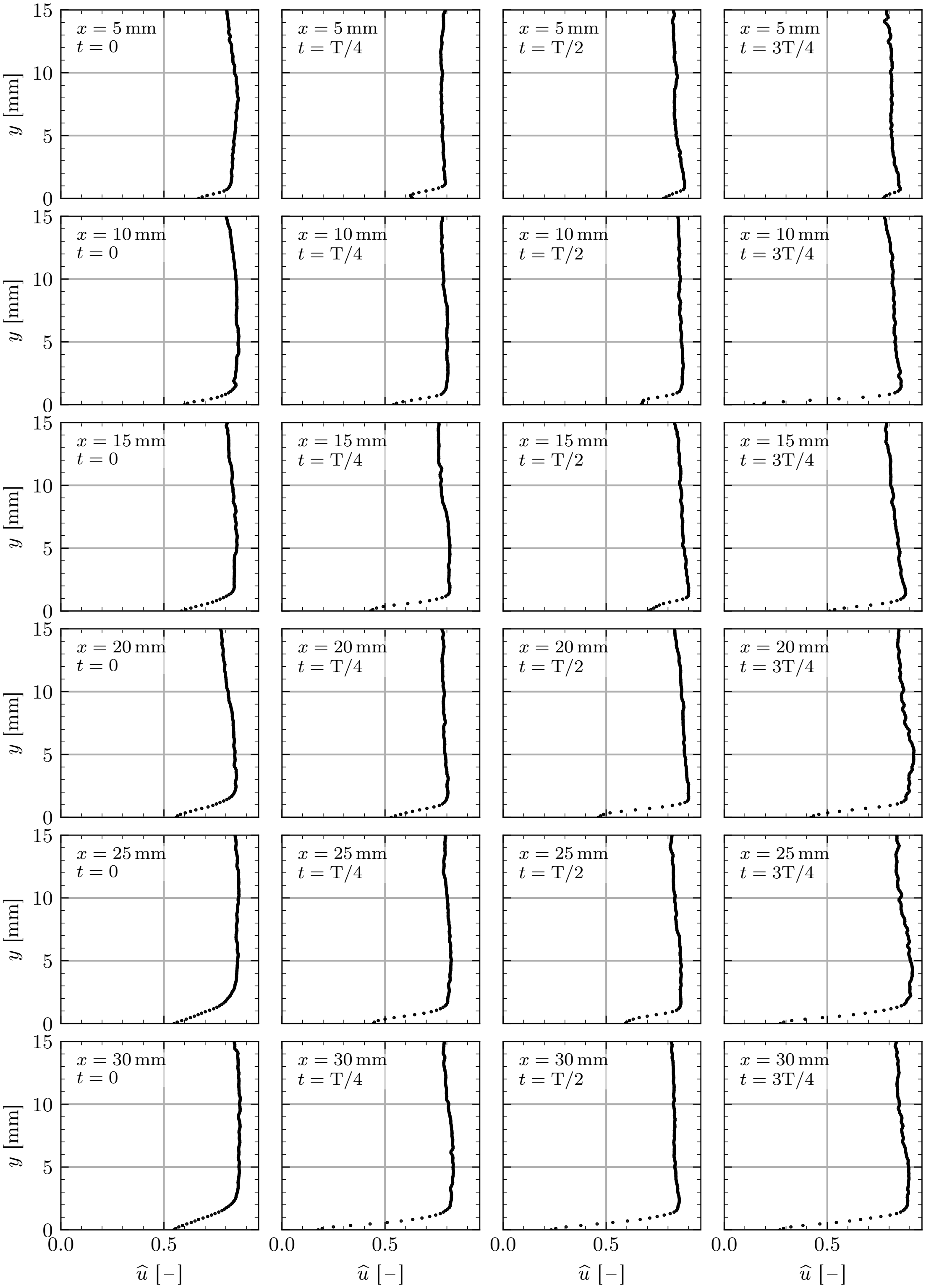

Figure 4.18: Horizontal velocity profiles for $U_o = 0.1865\,\mathrm{m/s}$ and $T = 3\,\mathrm{s}$

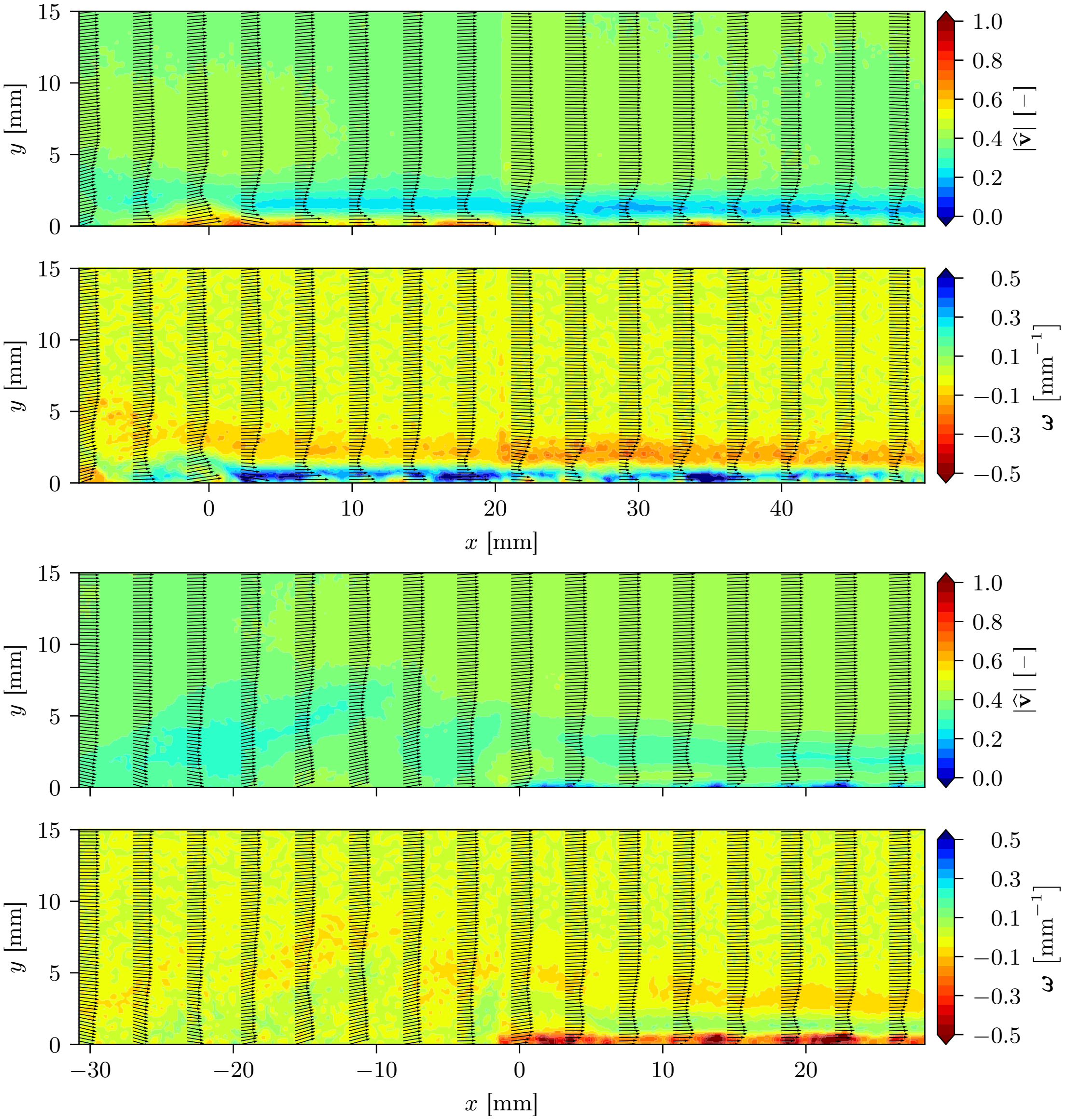

Figure 4.19: For $U_o = 0.0941\,\mathrm{m/s}$ and $T = 2\,\mathrm{s}$: Contours of velocity magnitude (top) and vorticity (upper middle) at $t = 0$; Contours of velocity magnitude (lower middle) and vorticity (bottom) at $t = T/4$

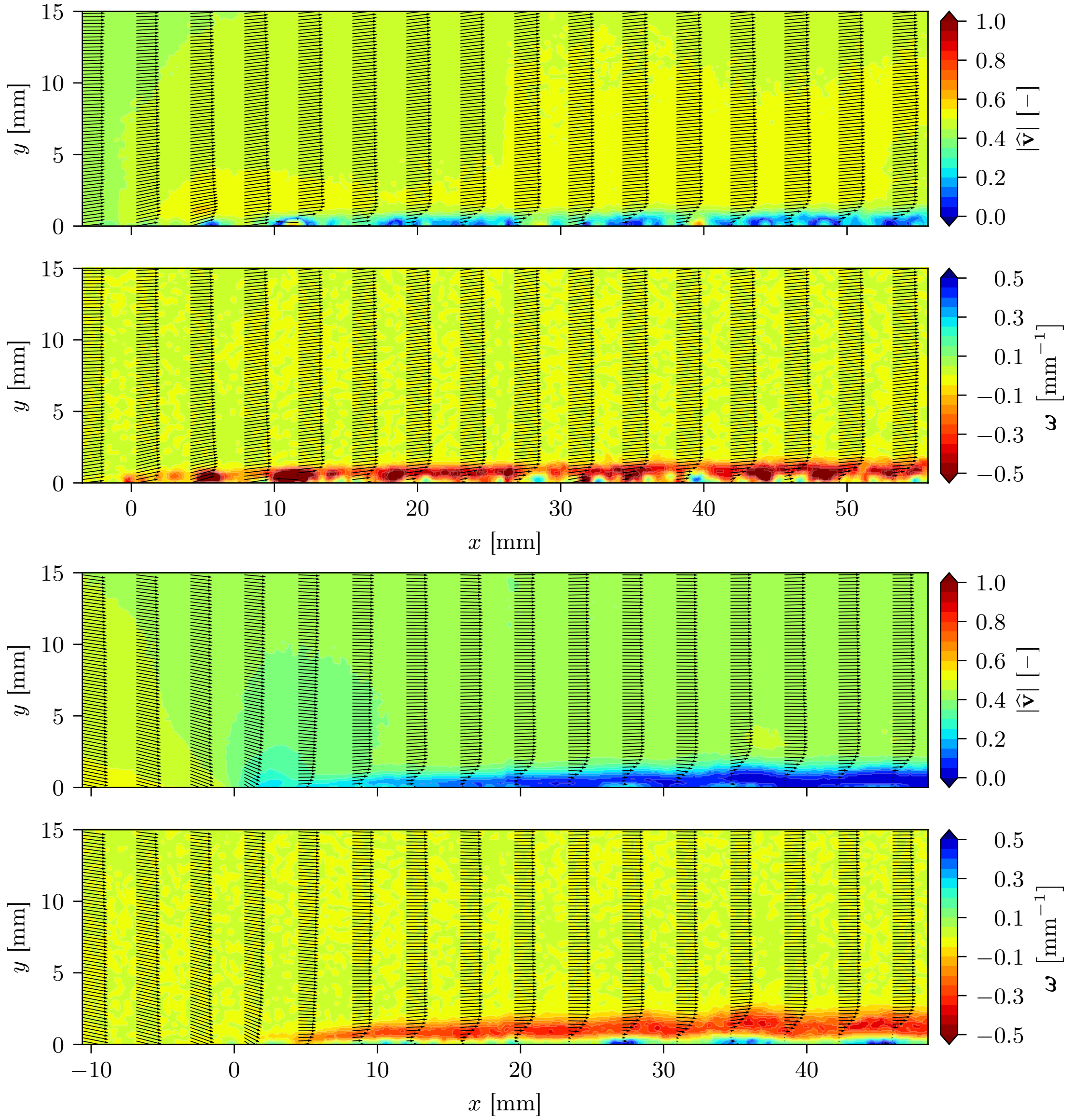

Figure 4.20: For $U_o = 0.0941\,\text{m/s}$ and $T = 2\,\text{s}$: Contours of velocity magnitude (top) and vorticity (upper middle) at $t = T/2$; Contours of velocity magnitude (lower middle) and vorticity (bottom) at $t = 3T/4$

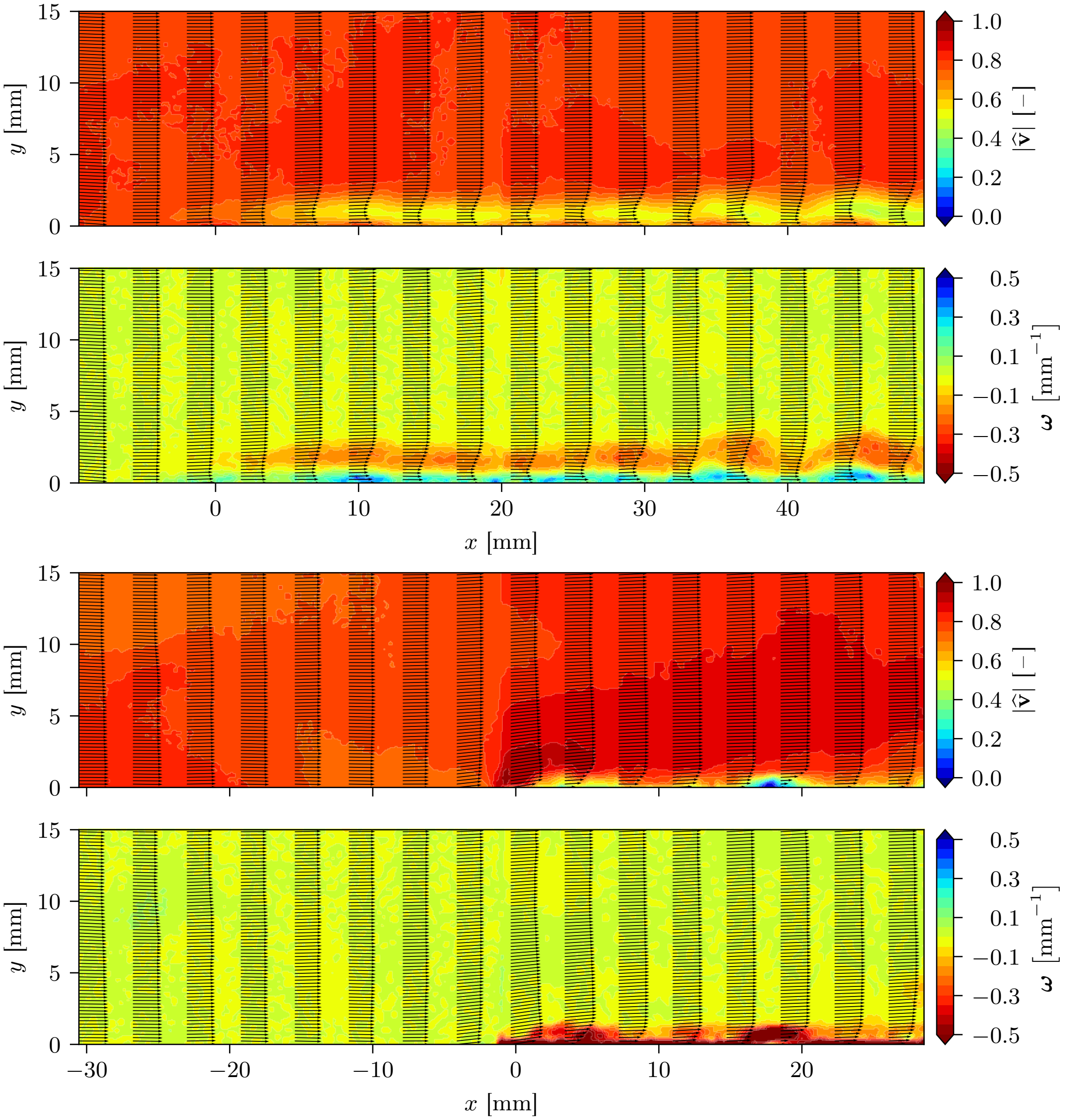

Figure 4.21: For $U_o = 0.1865\,\mathrm{m/s}$ and $T = 2\,\mathrm{s}$: Contours of velocity magnitude (top) and vorticity (upper middle) at $t = 0$; Contours of velocity magnitude (lower middle) and vorticity (bottom) at $t = T/4$

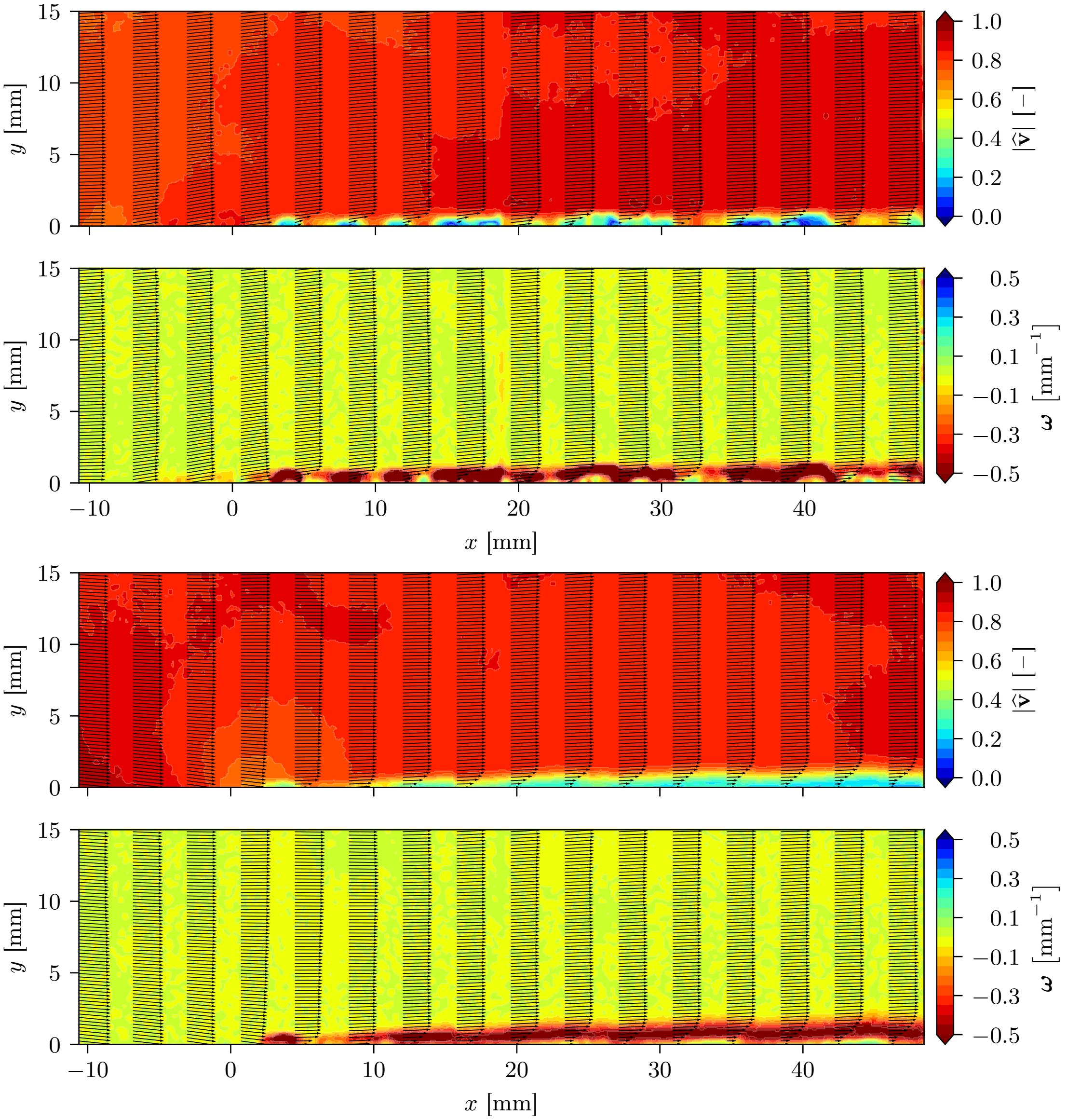

Figure 4.22: For $U_o = 0.1865\,\mathrm{m/s}$ and $T = 2\,\mathrm{s}$: Contours of velocity magnitude (top) and vorticity (upper middle) at $t = T/2$; Contours of velocity magnitude (lower middle) and vorticity (bottom) at $t = 3T/4$

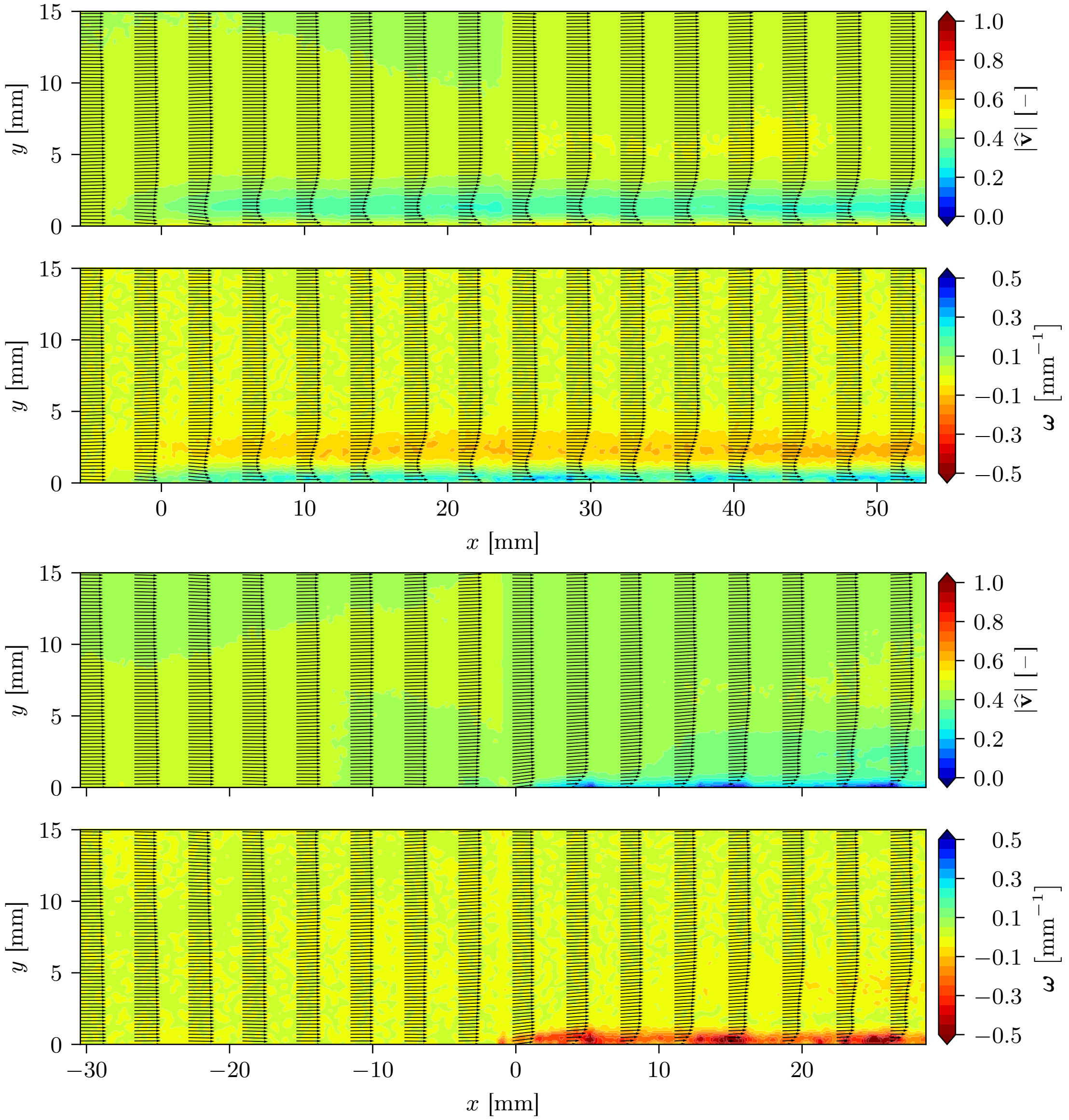

Figure 4.23: For $U_o = 0.0941\,\mathrm{m/s}$ and $T = 3\,\mathrm{s}$: Contours of velocity magnitude (top) and vorticity (upper middle) at $t = 0$; Contours of velocity magnitude (lower middle) and vorticity (bottom) at $t = T/4$

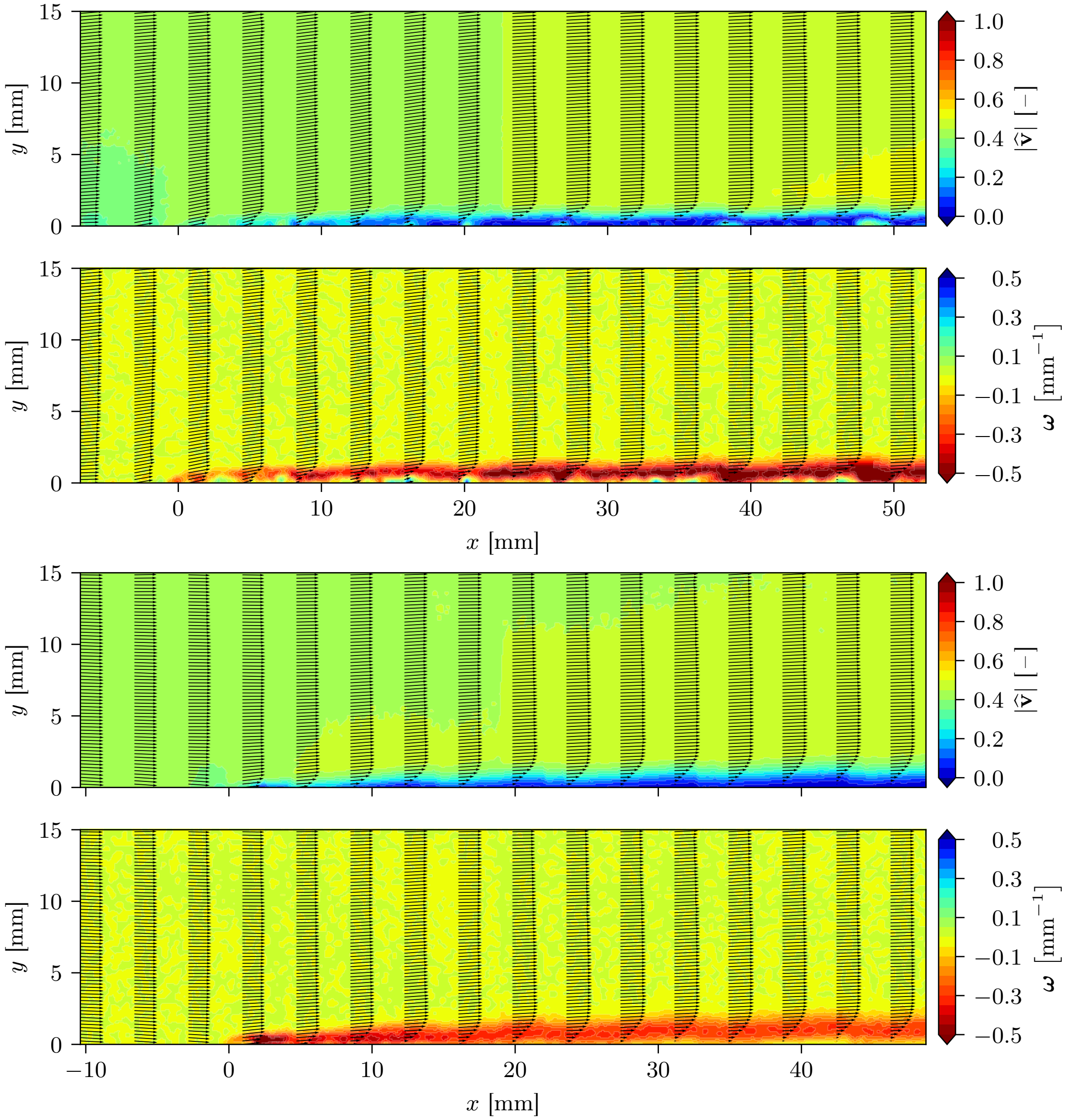

Figure 4.24: For $U_o = 0.0941\,\mathrm{m/s}$ and $T = 3\,\mathrm{s}$: Contours of velocity magnitude (top) and vorticity (upper middle) at $t = T/2$; Contours of velocity magnitude (lower middle) and vorticity (bottom) at $t = 3T/4$

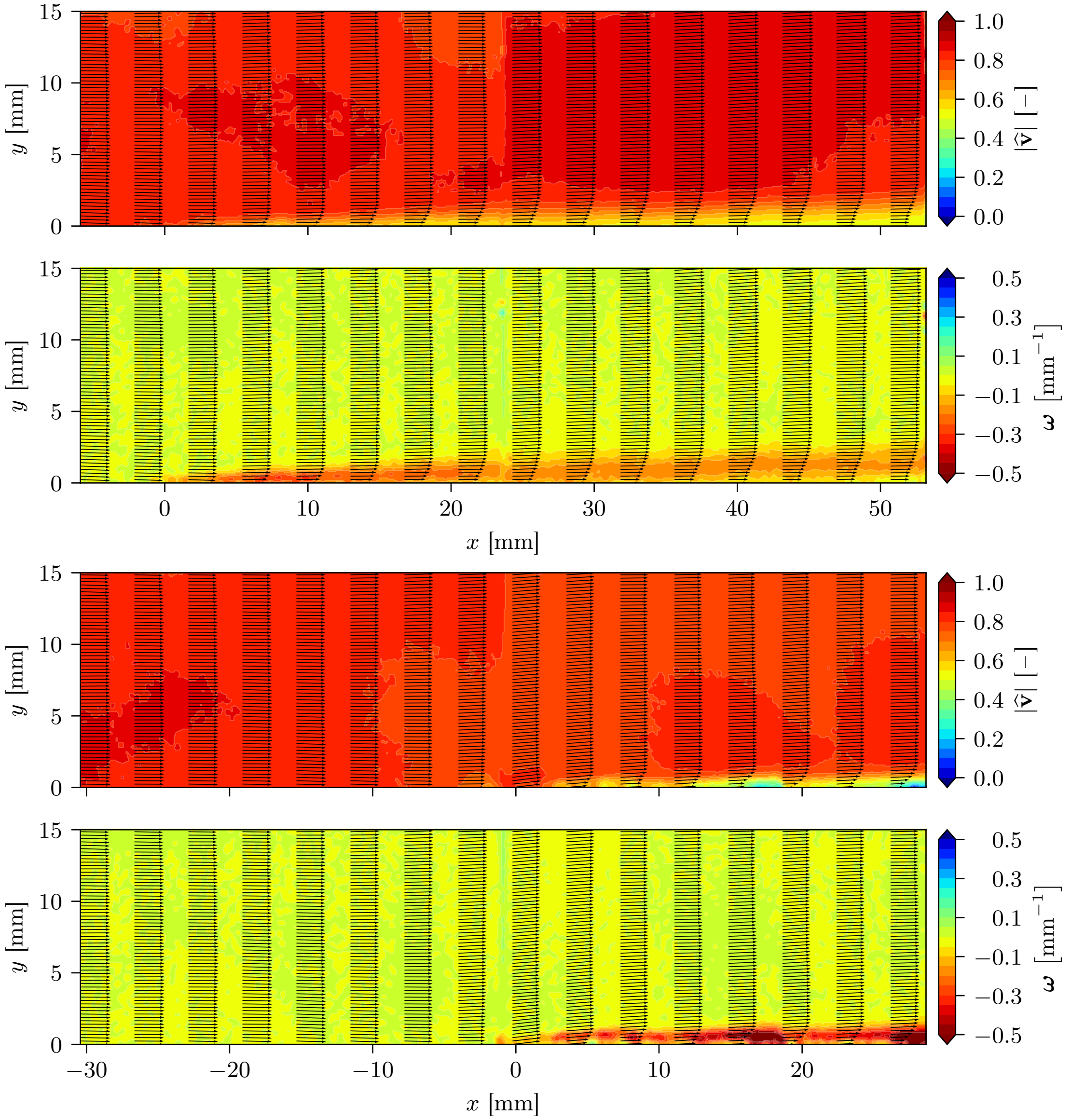

Figure 4.25: For $U_o = 0.1865\,\mathrm{m/s}$ and $T = 3\,\mathrm{s}$: Contours of velocity magnitude (top) and vorticity (upper middle) at $t = 0$; Contours of velocity magnitude (lower middle) and vorticity (bottom) at $t = T/4$

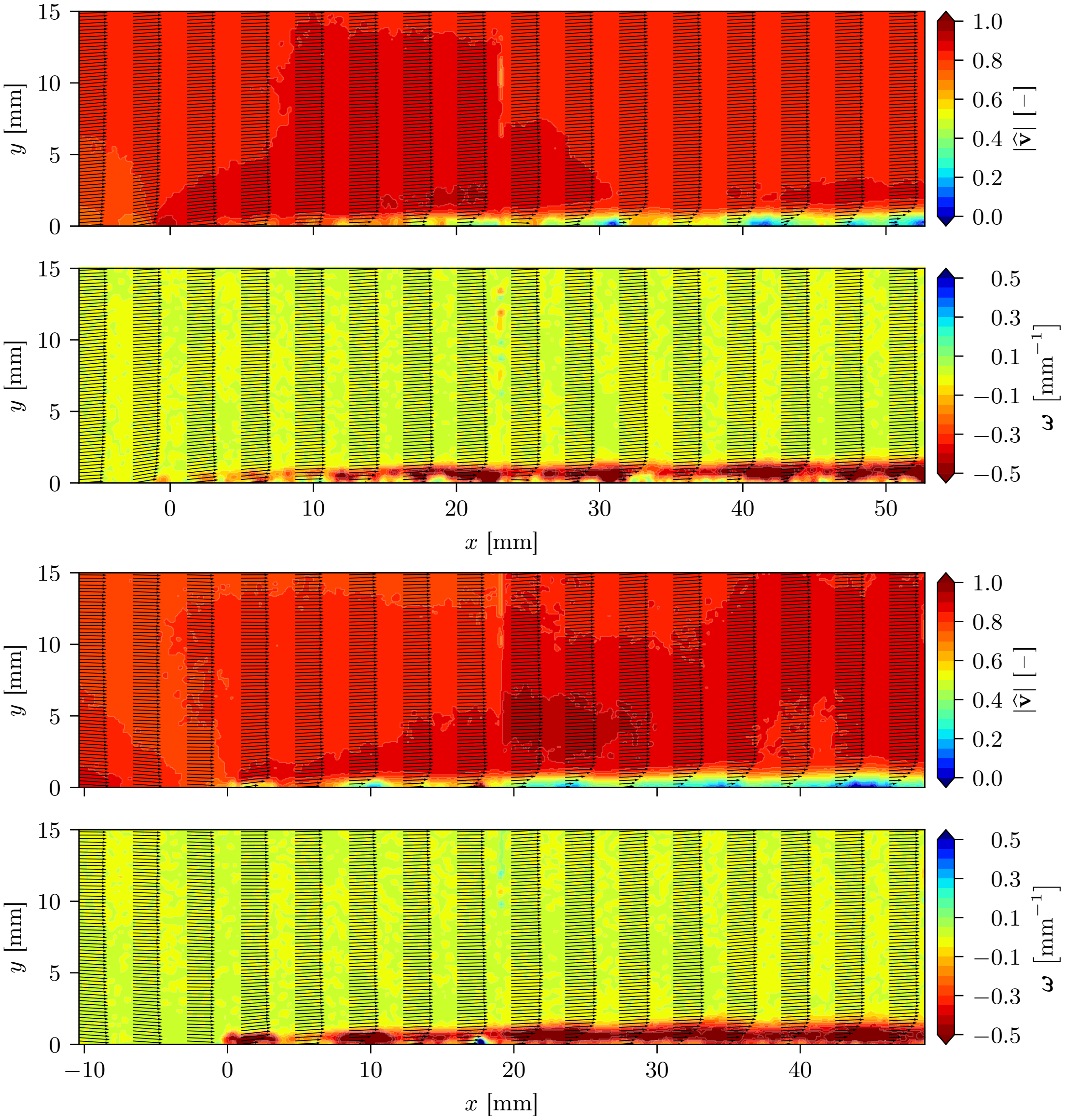

Figure 4.26: For $U_o = 0.1865\,\mathrm{m/s}$ and $T = 3\,\mathrm{s}$: Contours of velocity magnitude (top) and vorticity (upper middle) at $t = T/2$; Contours of velocity magnitude (lower middle) and vorticity (bottom) at $t = 3T/4$

This numerical method is capable of handling intermittently turbulent conditions thanks to the pseudo-compressibility model employed in the solver. See (Srivastava et al., 2019) for further details regarding this implementation and literature references for additional resources. Some further analysis of the oscillating plate problem is expected in future publications.

The numerical simulations were performed using two Reynolds numbers, $\mathrm{Re_x} = 2{,}099$ and 4,160, representing outlet measurements taken at $x = 25.4\,\mathrm{mm}$ for the two experimental mean flow speeds studied herein: $U_o = 0.0941\,\mathrm{m/s}$ and $0.1865\,\mathrm{m/s}$, respectively. Velocity field results are plotted as flooded contours in Figures 4.28 and 4.29. Wall shear stress and boundary layer thickness were estimated for both flow conditions at the outlet using the same methods used in examining the experimental profiles. For comparison with numerical predictions, experimental velocity profiles were also analyzed at the same stream-wise location beyond the plate's leading edge for measurements of wall shear stress and boundary layer thickness. The corresponding horizontal velocity profiles are plotted in Figure 4.27, and the measurement comparisons are summarized in Table 4.5.

The overshoots present near the boundary layer edge in the numerically-predicted horizontal velocity profiles arise due to the nature of the outlet boundary condition and the flow field's natural response in satisfying continuity imposition. Prescribing the outlet boundary condition effectively established a favorable pressure gradient along the plate in the computational domain. Velocity profiles associated with steady, laminar flows over plane boundaries with no pressure gradient typically increase asymptotically on their approach to mean flow when moving in the outward normal direction. However, the profiles in Figure 4.27 demonstrate asymptotically decreasing behavior toward mean flow velocity after extending beyond it near the boundary layer edge. Some profiles exhibiting both of these types of behavior are evident in the experimental findings (see Figures 4.8 and 4.9).

Perhaps additional future experimental work will be performed to test lower Reynolds numbers for which greater boundary layer thicknesses and expanded velocity profiles will be observed. This would hopefully include improvements in spatial resolution, increased image resolution (if new cameras are available), and measurements taken at locations further downstream (physically) where leading edge effects are more negligible. Supplementary velocimetry measurements made via e.g. PTV and LDA should be used for verification and refinement of the present results as well as any new data that is collected.

An initially unnoticed phenomenon occurred as a result of the decision to use the parameters listed in Table 4.4. For the lower external flow velocity $U_o = 0.0941\,\mathrm{m/s}$, the plate's own velocity amplitude $|\dot{x}|$ actually exceeds U_o for both oscillation frequencies, effectively rendering the plate's leading edge a trailing edge during its right-going journey, $3T/4 \geq t \leq T/4$. Entirely different flow phenomena are expected to arise in such a situation. Indeed some transverse mixing appears upstream in the plate's right-going wake according to the contours for $t = T/4$, e.g. see the lower two plots of Figure 4.19.

The boundary layer thickness and skin friction estimations fall justifiably within the reasonable bounds of experimental error and uncertainty, considering the absence of extra velocity measurement devices to verify mean flow speeds and pressure measurement devices to determine pressure gradients. It has been suggested that, following PIV investigations, holes could be drilled into the plate at various longitudinal locations and tapped for the placement of pressure transducers. Hydrodynamic pressure could be measured for steady flow to determine stream-wise pressure gradients, and pressure fluctuations could be characterized for unsteady, oscillatory flow. Given the lack of time and the need to move forward with stereoscopic PIV experiments, these tasks were not performed for the present study. However, the test results presented in this chapter at least qualitatively demonstrate the applicability of PIV to investigating near body flow problems and

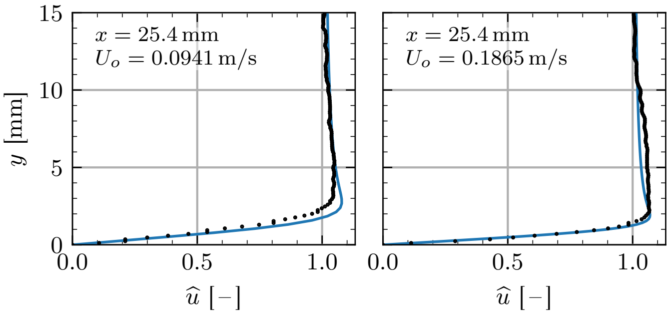

Figure 4.27: Horizontal velocity profiles for the stationary plate according to experiments (black markers) and CFD (blue curves) at $\mathrm{Re_x} = 2{,}099$ and 4,160 (left and right)

Table 4.5: Estimations of C_f $[10^{-3}]$ and δ_{99} [mm] at $x = 25.4\,\mathrm{mm}$ according to experiments, Blasius, and numerical simulations

U_o [m/s]	$\mathrm{Re_x}$	$C_{f,\mathrm{Blasius}}$	$C_{f,\mathrm{exp}}$	$C_{f,\mathrm{num}}$	$\delta_{\mathrm{Blasius}}$	δ_{exp}	δ_{num}
0.0941 m/s	2,099	14.492	16.185	17.847	2.775	1.913	2.670
0.1865 m/s	4,160	10.294	14.675	12.715	1.971	1.248	1.797

boundary layer properties, and they prepared the author for graduation to studying more complex flow with additional hardware sophistication.

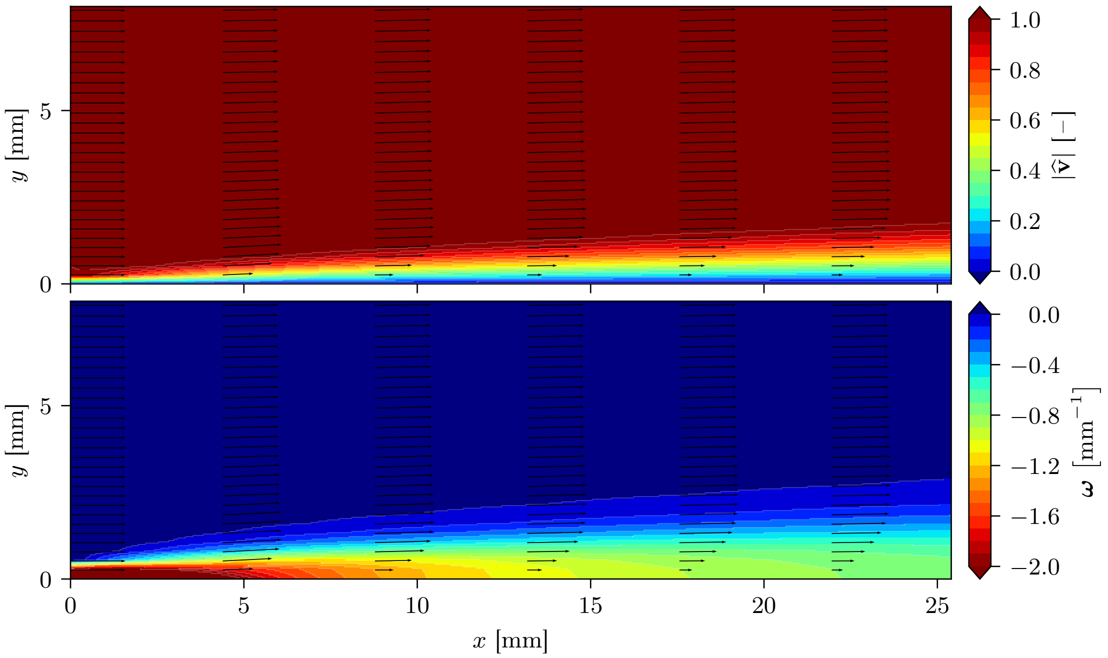

Figure 4.28: Contours of velocity magnitude (top) and vorticity (bottom) for $U_o = 0.0941\,\mathrm{m/s}$ according to numerical simulations

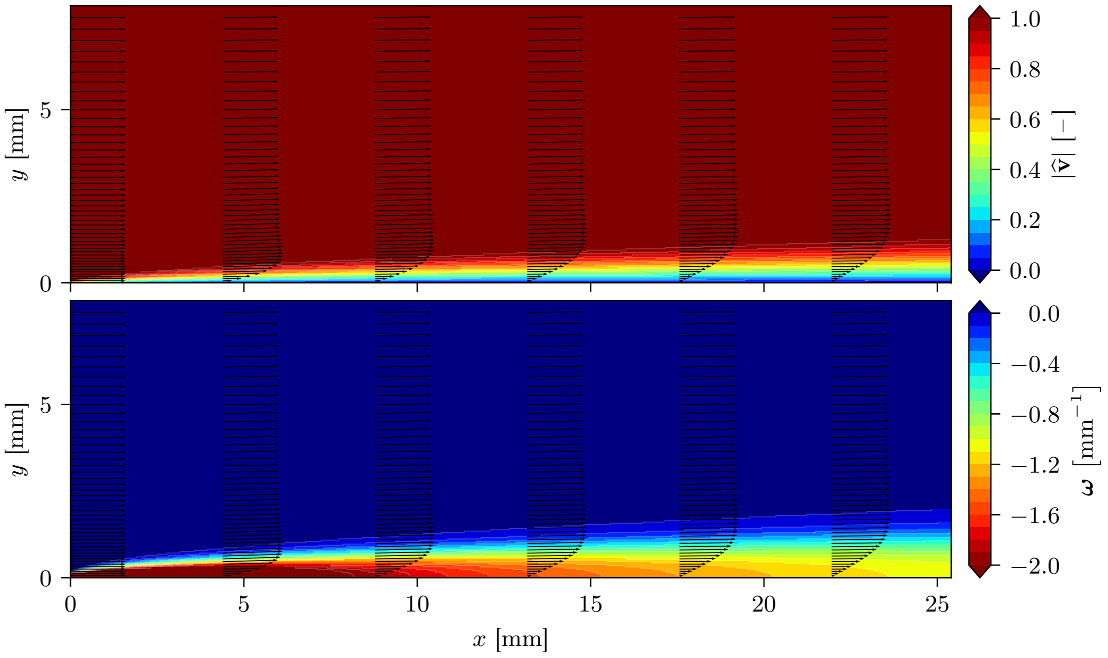

Figure 4.29: Contours of velocity magnitude (top) and vorticity (bottom) for $U_o = 0.1865\,\mathrm{m/s}$ according to numerical simulations

5 Cylinder Experiments

Characterizing boundary layer information for conditions where more than one length scale is involved requires mapping three-dimensional velocity components in the near-field which, in turn, demands additional PIV hardware. For the cylindrical and robotic test articles, the physical scale increases such that experiments are performed in the UNO towing tank rather than the hydraulic flume. In light of these added complexities, the primary purpose of the tests described in this chapter is to verify that boundary layer profiles can be successfully characterized and that vortex shedding can be successfully captured via stereo PIV for flows associated with an acrylic cylinder undergoing oscillatory motions similar to the robotic eel's segments' movements at a larger scale.

The cylinder of interest has constant 50.8 mm (2″) diameter D_c and 1.2192 m (48″) length excluding a hemispherical endcap at each end. This is the length used for numerical modeling, motion programming, as well as Reynolds number calculations. The symbol L is used in this chapter for the cylinder's length and all elsewhere for the robot's nominal length as described in Equation (6.1). The two endcaps together increase L by one diameter to form the overall wetted length. Tests were performed at 0.695 m immersion for both the cylindrical test article and the robot. This represents 13.68 diameters and 0.57 lengths of immersion for the cylinder and 12.52 diameters and 0.53 lengths for the robot.

Two modes of oscillation in an x–y plane parallel with the ground are studied: pure periodic sway, and pure periodic yaw with rotation centered at the leading edge, $x = 0$. A summary of the desired data may be listed as follows:

1. zero advancement with oscillatory motion
2. steady advancement with no oscillatory motion (axisymmetric flow)
3. steady advancement with oscillatory motion

The origin is centered at the leading edge with x positive aft, y positive athwart to starboard, and z positive upward. Yaw motions are rotational about z, positive counter-clockwise when viewed from above. A test matrix may be populated with the actual experimental parameters of interest as shown in Table 5.1, and a schematic of the flow problem is shown in Figure 5.1. The Reynolds number for these tests is defined in terms of the forward (mean inflow) speed and axial location of interest along the test article, again assuming $\nu = 1.1386 \times 10^{-6}\,\mathrm{m^2/s}$:

$$\mathrm{Re_x} = \frac{U_o x}{\nu} \tag{5.1}$$

Table 5.1: Experimental test parameters for cylinder experiments

forward (carriage) speeds	U_o	0.25 m/s, 0.5 m/s
measurement locations	x	$L/4$, $L/2$, $3L/4$
oscillation periods	T	2.7 s, 4 s
periodic sway amplitude	Y	0.1524 m
periodic yaw amplitude	Θ	10°

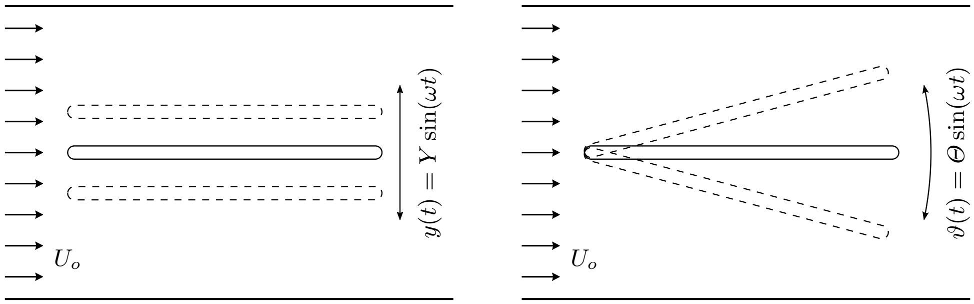

Figure 5.1: Flow problems concerning the oscillating cylinder

At $x = L$, these values would be $\mathrm{Re_L} = 267{,}697$ for $U_o = 0.25\,\mathrm{m/s}$ and $\mathrm{Re_L} = 535{,}394$ for $U_o = 0.50\,\mathrm{m/s}$. The Reynolds numbers at each of the measurement locations, illustrated in Figure 5.2, for each of the forward speeds are given in Table 5.2.

The Reynolds number, based strictly on an axial reference length and an axial velocity component, does not, however, thoroughly describe the flow problem in terms of the complex and time-dependent relationship between inertial forces and viscous forces. King (1977) used the cylindrical test article's diameter as the reference length in defining a characteristic Reynolds number, even though yaw angles of up to 45° were tested. It was determined that axial velocity components manifest significant axial flow in the cylinder's wake, but no mention is made about their effects on boundary layer separation points—only that separation appears delayed for larger yaw angles.

For the present study, since the test article's aspect ratio is high ($L/D_c \gg 1$) and the flow components of interest are primarily axial, a Reynolds number defined on length will be of greatest interest. The difference would obviously be a factor of L/D_c from one defined on diameter. However, in the case of high oscillation frequency, $T = 2.7\,\mathrm{s}$, and low forward speed, $U_o = 0.25\,\mathrm{m/s}$, sectional transverse velocities, especially near the trailing edge in oscillatory yaw, actually exceed axial velocities leading to situations similar to those studied by King (1977). Large yaw angles further increase the magnitude of transverse flow components. As mentioned in item 1 of the enumerated list above, cases with zero advancement are performed which clearly would naturally require a Reynolds number defined on cylinder diameter. Instead, to more generally handle all cases of interest, the Keulegan–Carpenter number $\mathrm{K_C}$ will be used to characterize the local ratios of transverse drag to inertial forces:

$$\mathrm{K_C} = \frac{VT}{D_c} \tag{5.2}$$

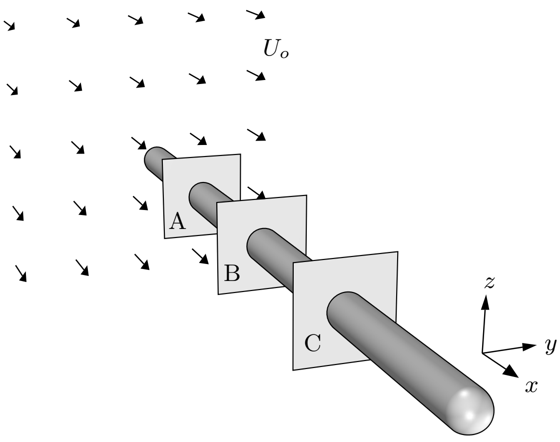

Figure 5.2: Perspective view of the three object planes used in the cylinder investigations where (A, B, C) represent ($L/4$, $L/2$, $3L/4$), respectively, as illustrated

Table 5.2: Reynolds and Keulegan–Carpenter numbers for cylinder experiment runs

	$\mathrm{Re_x}$		$\mathrm{K_C}$			
	0.25 m/s	0.50 m/s	4 s, sway	4 s, yaw	2.7 s, sway	2.7 s, yaw
$L/4$	66,924	133,849	18.850	6.580	18.850	6.580
$L/2$	133,849	267,697	18.850	13.159	18.850	13.159
$3L/4$	200,773	401,546	18.850	19.739	18.850	19.739

Typically, the velocity is represented in the ratio (5.2) as a sinusoidal wave speed with amplitude U_m. Here, since the fluid is quiescent but the test article has lateral motion, V is used which represents the amplitude of the cylindrical test article's transverse velocity at the trailing edge, calculated according to the following relations:

$$V = \begin{cases} \dfrac{Y}{T} & \text{for pure sway} \\ \dfrac{L\Theta}{T} & \text{for pure yaw} \end{cases} \tag{5.3}$$

The physical meaning of the $\mathrm{K_C}$ number, as provided by Keulegan and Carpenter (1958), is given as follows for a stationary cylinder of diameter D subjected to sinusoidal currents with velocity amplitude U_m. If one defines a length l as the distance a fluid particle would travel in one direction during a half cycle of the oscillatory current in the absence of the cylinder of interest, $l = U_m T/\pi$ then

$$\frac{U_m T}{D} = \frac{\pi l}{D} \tag{5.4}$$

Accordingly, the period parameter is proportional to the ratio of the distance traversed by a particle during the half cycle to the cylinder's diameter (Keulegan and Carpenter, 1958). Stated more simply, the Keulegan–Carpenter number provides a relationship to determine a ratio of characteristic drag forces to inertia forces for a particular flow problem with purely transverse flow. In this sense, it is closely related to the Strouhal number

$$\mathrm{St} = \frac{D}{U_m T} = \frac{1}{\mathrm{K_C}} \tag{5.5}$$

which is typically employed to qualitatively represent the ratio of oscillatory flow inertial forces to mean flow forces. The Keulegan–Carpenter number will be used here to correlate observed boundary layer behavior with relative sectional speeds. The number is evaluated for each flow condition of interest and tabulated along with the Reynolds numbers in Table 5.2.

5.1 Experimental Configuration

The test article's forward motion in the towing tank is provided by the towing carriage, and its oscillatory motions are induced by the planar motion mechanism (PMM). The PMM is secured to the towing carriage rails, and the cylindrical test article was affixed to the excited armature of the PMM, thereby subjecting the cylinder to both the carriage forward speed and the armature's sway and yaw motions. Photographs of the PMM situated on the towing carriage and the cylinder–armature attachment can be seen in Figure 5.4. Two 25.4 mm (1″) cylindrical, vertical, aluminum struts were responsible for transmitting the PMM armature's movements to the cylinder. It was observed that some undesirable vibration ensued from the transient nature of the motion startup.

Figure 5.3: Experimental test cylinder

Other factors likely contributed, including hydrodynamic effects and inertial effects caused by forcing and rotation about points located away from the cylinder's center of gravity. For this reason, at least two cycles of oscillatory motion were lapsed before triggering data collection to allow dissipation of these startup tremors.

Rotation provided by the PMM is around a vertical axis which was configured to be aligned exactly with the cylinder's centerline. However, to achieve rotation around a certain longitudinal point along the centerline, one must add a component of sway with identical period. Presently, rotation around the leading edge, $x = 0$, is desired requiring the following calculation:

$$|\dot{y}(t)| = \omega Y = \frac{2\pi Y}{T} := \Theta d \tag{5.6}$$

where $y(t) = Y \sin(\omega t)$ is the oscillatory sway motion, $\vartheta(t) = \Theta \sin(\omega t)$ is the yaw motion, T is the oscillation period, and d measures the distance in x between the PMM's rotation point and the cylinder's leading edge at $t = 0$.

Velocity data is desired in select y–z planes, i.e. transverse planes, along x (see Table 5.1 and Figures 5.2, 5.5, and 5.6). To capture this for oscillatory motion, images must be collected for both port and starboard motion, because the cylinder itself prevents the PIV cameras from viewing seed particles on the side of the cylinder opposite the PIV module. It is of particular interest to analyze flow fields for vortices shed in the local wake, corresponding to images collected for cylinder travel in the $+y$-direction to starboard, i.e. away from the PIV torpedo. Assuming flow symmetry about the longitudinal axis for steady forward advancement permits data collection on only one side of the test article, a photograph of which is shown in Figure 5.3.

A schematic showing a perspective view of the PIV arrangement used to measure the flow velocities near the cylinder is given in Figure 5.5. The laser light sheet flashes in transverse y–z planes and intersects the cylinder perpendicularly from port side when the test article is at rest. The image plane coincides with the light sheet, and the region of interest is the lower left quadrant within the image plane (when viewed from behind) and outside the cylinder's boundary as illustrated explicitly as the grayed area in Figure 5.6. Both the PIV torpedo and the cylindrical test article were mounted rigidly to the carriage eliminating the possibility of different forward speeds between the two. This is not evident in the drawing of Figure 5.5, but the connection should be more clear in Figure 5.4.

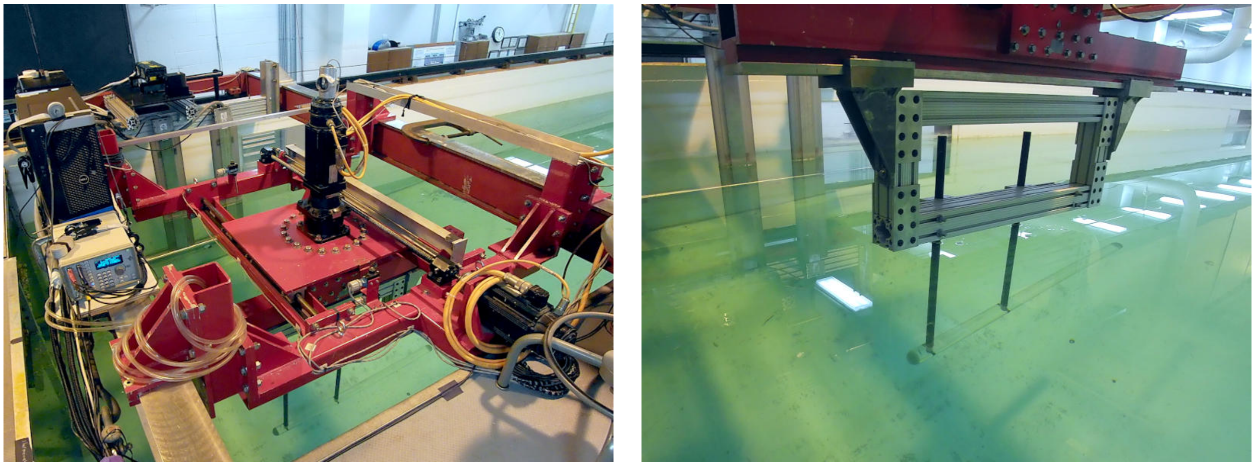

Figure 5.4: UNO planar motion mechanism on the towing carriage (left) and the cylinder attachment to the PMM's armature (right)

Stereo camera calibration was performed with a precisely-manufactured aluminum board of 10.7 mm and 11.7 mm thickness (recessed and non-recessed thickness, respectively) with 20 mm dot spacing. Calibrations were performed before and after testing was complete to verify consistency.

SPIV processing parameters are set similarly to those given in Table 4.2 for mono PIV images of flow over the flat plate. Differences arise in the spatial calibration, time interval selection, and interrogation resolution. The calibration is no longer simply a conversion from pixels to meters. Instead, as discussed briefly in section 3.1, camera orientation parameters must be estimated (or measured) and coupled with pixel location-dependent planar calibration interpolants to provide the required information for three-dimensional reconstruction. These factors are stored in a file that is accessed by Insight 4G when performing stereo vector triangulation. The camera locations relative to the test article are shown in Figure 5.7. The interrogation resolution used in SPIV image data for the recursive Nyquist grid engine is 64 px/32 px starting/final grid sizes. The time interval, Δt, is chosen with much greater care than previously as explained below.

5.2 Choosing Δt

The steady advancement cases lacking lateral motion were performed and coupled with runs made without the test article in the field of view to verify the calibration and to assist in uncertainty analysis and error estimation for the mean inflow speed measurements. Due to the configuration requirement for observation of flow around the cylinder's cross-section, the longitudinal/axial component of fluid velocity passes perpendicularly through the light sheet, the x-direction. This implies that in order to keep track of particles in the light sheet at two temporal instants, the elapsed time Δt from frame A to B must be set small enough to capture *most* of those particles in both frames. In other words, Δt is constrained to prevent particles in the free stream from traveling distances greater than the light sheet thickness at the given carriage forward speed. Of course, inflow velocity remains constant throughout a run, and light sheet thickness also does not change. Residual measurement error and noise amplify with $1/\Delta t$ as $\Delta t \to 0$ (Raffel et al., 2018), so one is behooved to maximize its value. However, bias errors inflate with increasing Δt, and prominently so for flows with high spatial velocity gradients. Differential estimates are additionally worsened and curvature/accelerative effects lost.

In the present tests, the light sheet thickness was estimated, based on the optics used and the

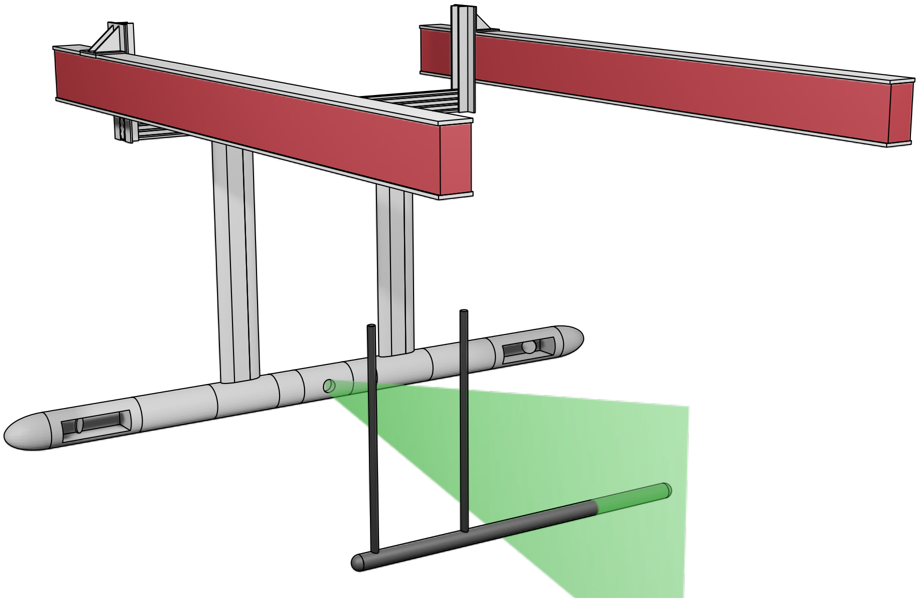

Figure 5.5: PIV configuration for cylinder investigations

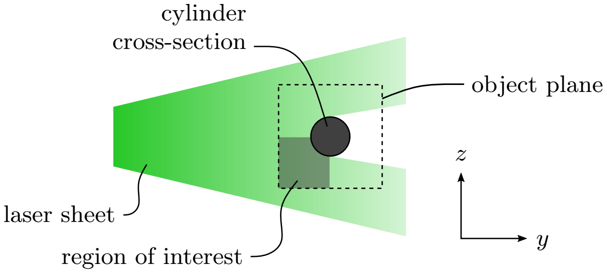

Figure 5.6: PIV region of interest for cylinder investigations, looking forward

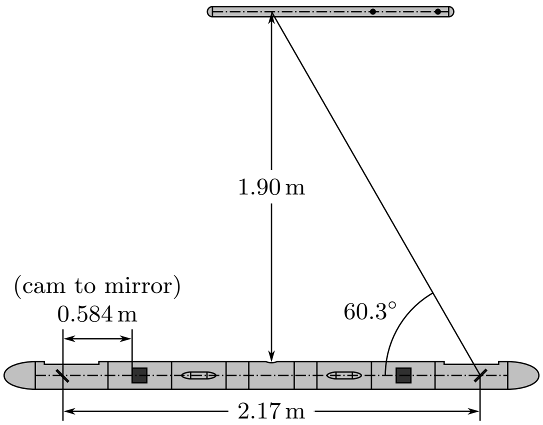

Figure 5.7: Top view of carriage schematic with key dimensions annotated

Table 5.3: Δt (in µs) for cylinder experiment runs. Values given for port/stbd runs.

		0 m/s	0.25 m/s	0.5 m/s
$L/4$	no motion	—	2400	1200
	4 s, sway	3600/3400	2400/2400	1200/1200
	4 s, yaw	9600/9400	2400/2400	1200/1200
	2.7 s, sway	2600/2400	2400/2400	1200/1200
	2.7 s, yaw	6600/6400	2400/2400	1200/1200
$L/2$	no motion	—	2400	1200
	4 s, sway	3000/2600	2400/2400	1200/1200
	4 s, yaw	4200/3800	2400/2400	1200/1200
	2.7 s, sway	2000/1600	2400/2400	1200/1200
	2.7 s, yaw	2700/2300	2400/2400	1200/1200
$3L/4$	no motion	—	2400	1200
	4 s, sway	3000/2600	2400/2400	1200/1200
	4 s, yaw	2600/2600	2400/2200	1200/1200
	2.7 s, sway	2000/1600	2000/1600	1200/1200
	2.7 s, yaw	1600/1200	1600/1200	1200/1200

distance between the light source and test article, to be approximately 3 mm at the measurement location. The distance traveled by particles in the free stream may then easily be estimated as the quotient of the light sheet thickness divided by the forward speed. As a rule of thumb, out-of-plane displacements—particle motions perpendicular to the light sheet—should not exceed 25% of the light sheet thickness. This gives the maximum allowable value for Δt.

$$\Delta t \leq \frac{1}{4}\left(\frac{\text{light sheet thickness}}{\text{forward speed}}\right) \tag{5.7}$$

Not a significant number of particles will be lost between frames with this setting. As previously mentioned in section 4.3, some difficulties were experienced in adequately seeding the towing tank due to its volume, and further complications came with stirring them up for even distribution. With these factors in mind and for conservatism, the results given here (see Table 5.3) were determined with a factor of 1/5 instead of 1/4 to obtain the governing Δt based on forward speed used in the experiments:

$$\Delta t \leq \frac{1}{5}\left(\frac{0.003\,\mathrm{m}}{U_o}\right) \tag{5.8}$$

A different approach was needed for enforcing a further constraint on Δt based on transverse motion of the test article's cross-section of interest. In this case, the sectional transverse velocity itself with an arbitrary "safety factor" was applied, along with trial and error, to determine this additional constraint. Further still, the value of Δt was adjusted for directional dependency on the test article's motion. In the case where the section moves to starboard, or in the $+y$-direction away from the cameras, i.e. the local section's wake is observed (see Figure 5.6), a slightly smaller value of Δt was used than for the opposite scenario. This was done to capture inevitable wake disturbances caused by the transverse motions. For explicit disambiguation of the data and to allow setting unique Δt for each scenario, the port/starboard data was collected in separate runs. See Table 5.3 for a summary of the values selected for each case. All calculated values of Δt were rounded down to the nearest 100 µs.

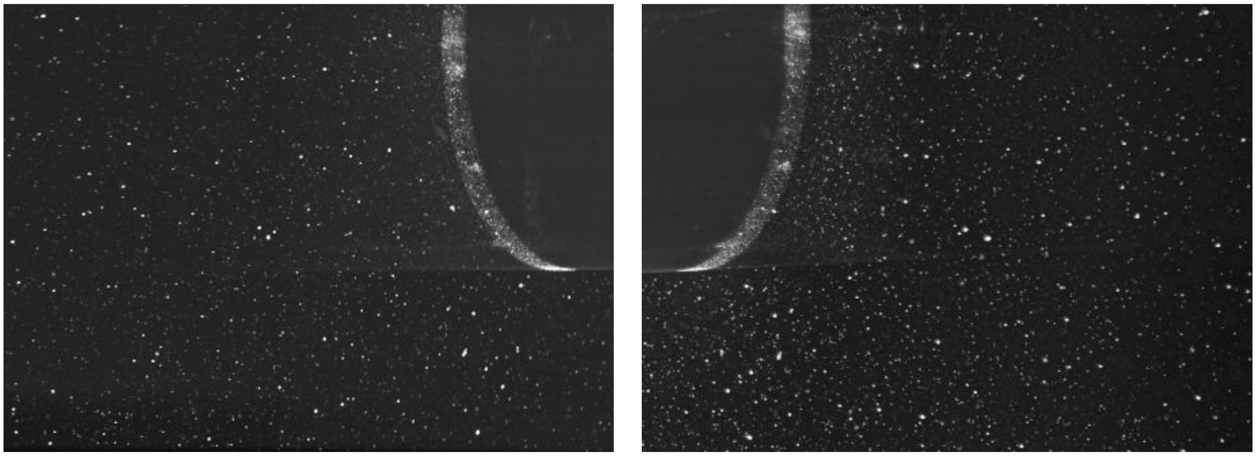

Figure 5.8: Cropped sample PIV images from cylinder experiments (left camera view on left, right camera view on right)

5.3 Image and Vector Processing Techniques

Sample SPIV images for the cylinder experiments are given in Figure 5.8 with the left camera's view shown in the left image and the right camera's view shown in the right image. Note that the images are actually mirrored horizontally due to the effect of the mirror modules indicated in Figures 3.2 and 5.7. The image samples were taken during an experiment for axisymmetric flow at $x = L/2$ and $U_o = 0.5\,\mathrm{m/s}$.

The cylinder's cross-section always appears in the raw images as an ellipse with constant major and minor axis dimensions (see Figure 5.8). This occurs naturally since the cylinder always passes through the PIV region of interest at the angle exactly parallel to the direction of forward travel. The oblique, fixed viewpoint of each camera causes the horizontal axis to be smaller than the cylinder's natural radius leading to elliptical perceived cross-sections in the images. Stereo mapping generates circular cross-sections in the resulting vector fields, however.

The initial, mono PIV processing algorithms require signal processing and correlation techniques, as discussed previously in chapter 3. Only fluid regions with adequate particulate distributions are processed properly in these routines, therefore solid objects appearing in the images must be removed to prevent spurious measurements near boundaries. Rather than manipulating the raw data, one preferably generates *masks* to indicate regions in an image that should be ignored in correlation. Each mask must be a binary image with dimensions identical to the raw data. Image pixels with corresponding mask values of $2^{16} - 1$ (the saturation value for 16-bit images) are evaluated, and pixels with mask values of 0 are ignored by the processing engine.

Mask generation was performed programmatically with the help of a few simple image processing tools. First, a template identifying a unique, distinguishable feature (the bottom of the elliptical cross-section) in the image was saved, and normalized cross-correlation was employed to identify the exact location of that feature in all subsequent images. The cross-section's minor and major axes were determined from a sample data set and used to mask out the cross-section itself along with the upper region of image above cylinder center and all the area between a vertical line passing through the cylinder center and the image edge, on the side opposite the viewing direction. The cylinder center is easily determined after reckoning the feature's location.

Processing the resulting three-dimensional vector data from the towing tank experiments was a bit more cumbersome than the two-dimensional data from mono PIV measurements in the hydraulic flume. Vector fields from separate runs had to be stitched together, side-by-side, according to corresponding port/starboard motions of the same scenario. Additionally, since measurements were made on the same side of the test article, the vector field containing information regarding the local wake had to be flipped horizontally about a vertical line passing through the cross-sectional center. Fortunately, the masking methodology used in preparing SPIV processing greatly facilitated identification of the x, y coordinates associated with the cross-sectional center. Then, since meshgrids are employed, flipping the data is as simple reversing the order of columns and changing the parody of v, the y-component of velocity. Stitching the data simply involves appending the flipped vector field to the right side of the matrix containing local leading edge information.

The only caveat to this method of stitching vector fields is maintaining a constant number of rows in the meshgrid corresponding to equal vertical distances below the bottom edge of the cylinder. In some cases, especially with the robotic eel where the body would wave up and down slightly throughout the motion period, the vertical distance beneath the bottom edge along which velocity information is captured may fluctuate between periods. Therefore, in computing the ensemble-average, it is especially important to ensure that quantities are appropriately averaged according to the number of samples at each known spatial location. This was handled by populating a matrix of counters to keep track of these sample counts. At the end of adding corresponding velocity values, the matrix containing sums may be divided by the counters matrix, completing the average calculation.

Performing experiments with the cylindrical test article prior to the robotic eel provided numerous benefits, mostly in regards to time-saving and procedural formalities. Of particular interest is that most of the image and vector processing techniques discussed here carry over directly to processing data from the robotic eel experiments.

5.4 Results

Ensemble-averaging was again employed for the purpose of analyzing primary, mean, repeated flow characteristics in the near-field. As before, each component is averaged according to Equation (4.1) to produce the ensemble-averaged velocity vector $\widehat{\mathbf{v}}$. For consistency and more generalized comparison of relative magnitudes, all presented velocity results are normalized on the amplitude of the cylinder's trailing edge velocity, which includes motion the forward and transverse directions, prior to inclusion in the ensemble. The normalization is calculated as $\mathbf{v}/|\mathbf{v}|$ where

$$|\mathbf{v}| = \sqrt{U_o^2 + V^2} \tag{5.9}$$

where U_o is the inflow speed and V is the amplitude of the transverse velocity defined in Equation (5.3). Note that the normalization simplifies to $|\mathbf{v}| = U_o$ for the non-oscillating cylinder.

Flooded contours of velocity magnitude with overlaid vectors for steady, axisymmetric flow over the cylindrical test article are provided in Figures 5.9–5.11, while Figures 5.12–5.17 indicate the results for the oscillating cylinder. Note that the velocity fields for the non-advancing, oscillating cylinder display increasingly disturbed external flow with lower oscillation periods. If only the first one or two ensemble samples were used to display these contours, likely the far-field would appear more quiescent. However the nature of this situation is such that the test article repeatedly passes through the stationary image plane thereby reentering regions of fluid already disturbed during previous cycles. Ensemble-averaging dampens these disturbances somewhat, but consistent results are difficult to achieve for this reason.

Generally, the oscillating cylinder, with mean inflow as well as without, displays laterally accelerated flow producing overall higher velocities near the body surface, whereas deceleration is noticed for the axisymmetric conditions. Regions of acceleration are largely produced by inertial components added by the test article and apparently not by viscous action of the boundary layer which would diffuse these higher velocities. Cases where transverse speed greatly exceeds inflow velocity exhibit flow separation and vortex shedding in the local wake, but higher inflow speeds appear to dampen these effects. An example where a shed, free vortex is illustrated clearly is given by the contours corresponding to $x = 3L/4$ for $U_o = 0.5\,\mathrm{m/s}$ in yaw with $T = 2.7\,\mathrm{s}$ (bottom of Figure 5.17). For clarity, the vorticity field was calculated and plotted as shown in Figure 5.18. The vortex appears as strongly positive circulation centered at approximately $x = 35\,\mathrm{mm}$ and $y = -25\,\mathrm{mm}$. A radial band of strongly negative vorticity also appears near approximately $\varphi = 100°$ which is due to high linear shear. The wake field is disturbed with vortical structures that apparently easily survived ensemble-averaging. Near-body flow directions along angular offsets near $\varphi = 0°$ and 180° are primarily radial while those near $\varphi = 90°$ are largely angular, following intuitive streamlines for transverse flow.

Correlation between vortex shedding and Keulegan–Carpenter numbers appears to exist where vortex shedding increases proportionately with $\mathrm{K_C}$. Keeping track of corresponding values between Table 5.2 and Figures 5.12–5.17 corroborates this correlation. Contrasting results for sway and yaw at $L/4$ and $U_o = 0\,\mathrm{m/s}$ indicates that the significantly larger Keulegan–Carpenter numbers correspond directly with greater disturbances in the local section's wake. According to Keulegan and Carpenter (1958), for the figures listed in Table 5.2, sway conditions pose tremendously larger potential for energy loss overall for the test article. The low values of $\mathrm{K_C}$ associated with yaw oscillations lead to almost negligible disturbances to the local flow field. Furthermore, since high transverse velocities, V, are seen closer to the trailing edge, increases in transverse drag and thus energy loss are naturally associated with larger x.

These initial conclusions provide crucial intuition regarding periodic energy loss for the swimming characteristics of the robotic eel. Particular attention will be given to vortex formation and lateral acceleration of the local flow field, as these are the primary culprits of energy sinks for transversely oscillating cylindrical bodies. Correlation between $\mathrm{K_C}$ and x is evident here for oscillatory yaw, so it will likewise be analyzed for the swimming robot. Of primary concern is the quantification of local skin friction coefficients for verification of numerical simulations.

5.5 Comparison with CFD Results and Discussion

As with the flat plate experiments, numerical simulations were performed as part of a parallel effort in this project for analogous flow conditions for a submerged, finite cylinder with dimensions similar to those of the experimental test article. Commercial CFD software, i.e. ANSYS Fluent, was employed to carry out the solution procedure. Details regarding setup of the domain and solver settings are largely omitted here, since the author's primary contributions were experimental investigations. Srivastava (2020) principally discusses the numerical simulations contributed to this project, and further details will soon be published.

A brief comment should be made, however, with regard to the approach taken for domain meshing. Since the immersed body moves (oscillates) temporally within the domain, some form of dynamic meshing needs to be implemented to reciprocate the motion for the computational grid. A method called *overset mesh* is used to accomplish this which eliminates the need for remeshing and allows greater control over local mesh characteristics for moving geometries (Ramakrishnan and Scheidegger, 2016; ANSYS, 2020). This property has recently proved exceptionally useful when meshing the undulating robot due to the strong dependency on both time and space of the shape function (2.41). The working principle of overset meshing is to arrange a background grid and an overlapping, or intersecting, component grid which can move with an immersed body it accompanies.

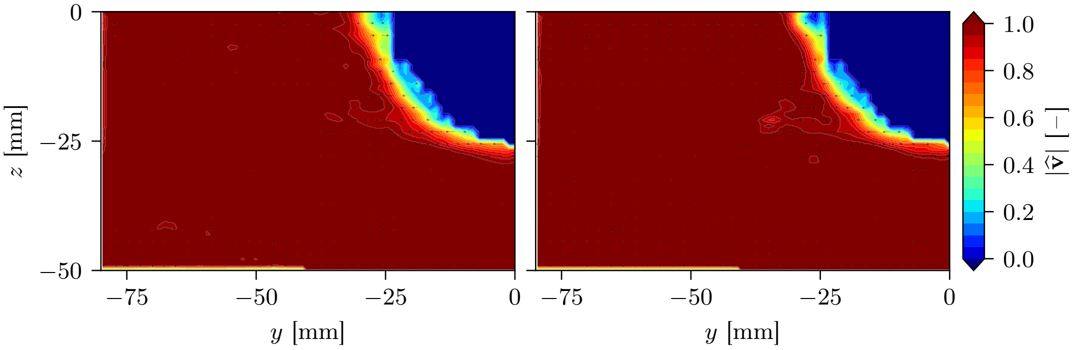

Figure 5.9: Contours of velocity magnitude for axisymmetric flow at $x = L/4$ for $U_o = 0.25\,\mathrm{m/s}$ (left) and $0.5\,\mathrm{m/s}$ (right)

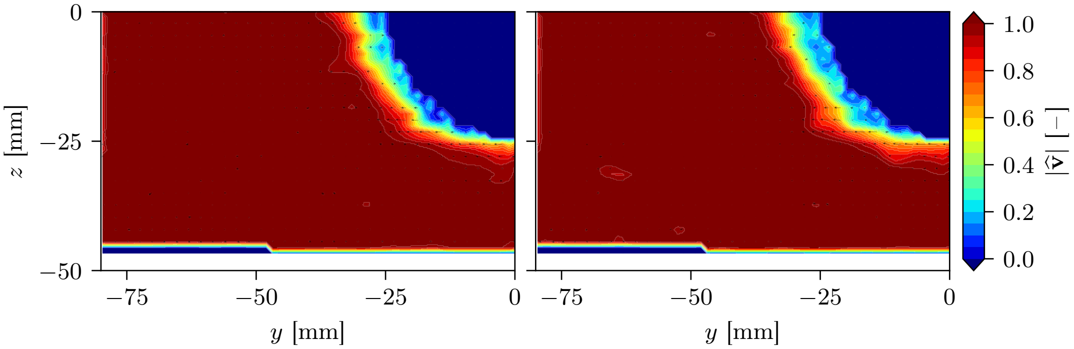

Figure 5.10: Contours of velocity magnitude for axisymmetric flow at $x = L/2$ for $U_o = 0.25\,\mathrm{m/s}$ (left) and $0.5\,\mathrm{m/s}$ (right)

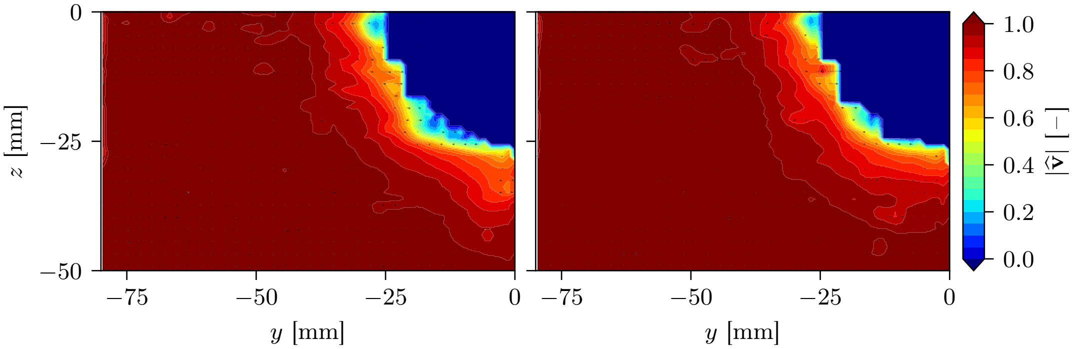

Figure 5.11: Contours of velocity magnitude for axisymmetric flow at $x = 3L/4$ for $U_o = 0.25\,\mathrm{m/s}$ (left) and $0.5\,\mathrm{m/s}$ (right)

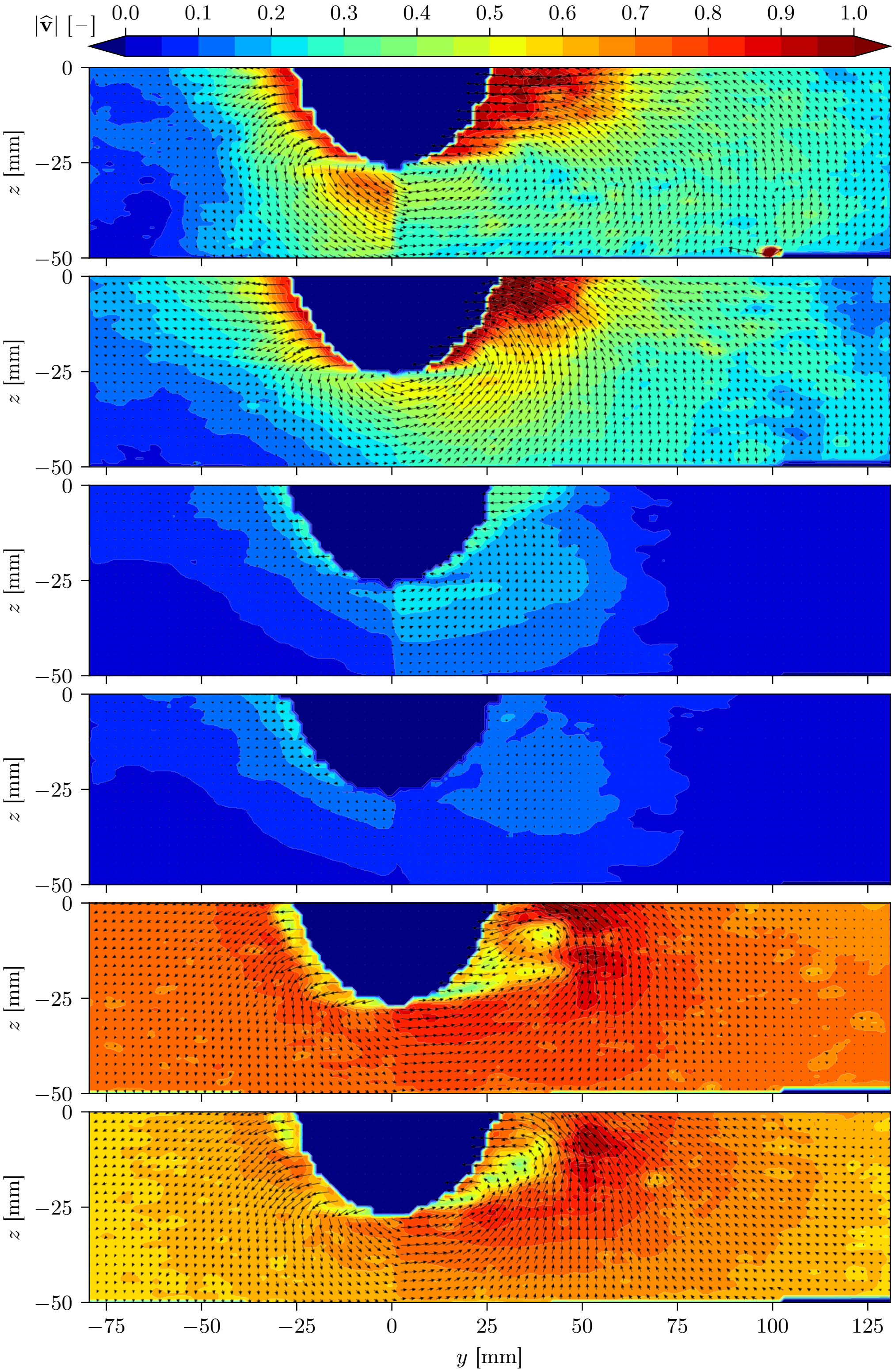

Figure 5.12: Contours of velocity magnitude at $x = L/4$ for (top to bottom): $U_o = 0\,\mathrm{m/s}$ in sway with $T = 4$, $2.7\,\mathrm{s}$ and in yaw with $T = 4$, $2.7\,\mathrm{s}$; $U_o = 0.25\,\mathrm{m/s}$ in sway with $T = 4$, $2.7\,\mathrm{s}$

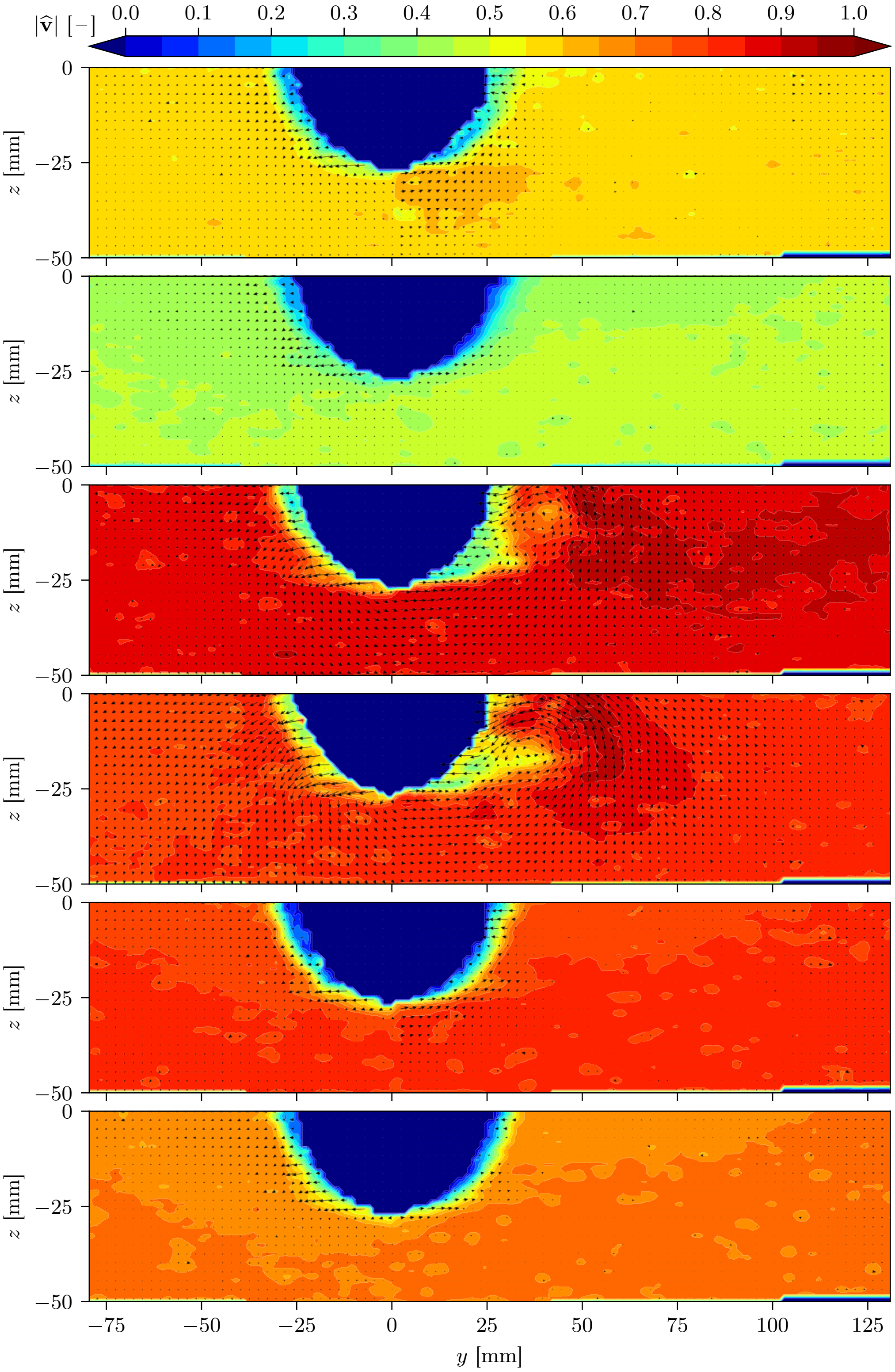

Figure 5.13: Contours of velocity magnitude at $x = L/4$ for (top to bottom): $U_o = 0.25\,\mathrm{m/s}$ in yaw with $T = 4$, $2.7\,\mathrm{s}$; $U_o = 0.5\,\mathrm{m/s}$ in sway with $T = 4$, $2.7\,\mathrm{s}$ and in yaw with $T = 4$, $2.7\,\mathrm{s}$

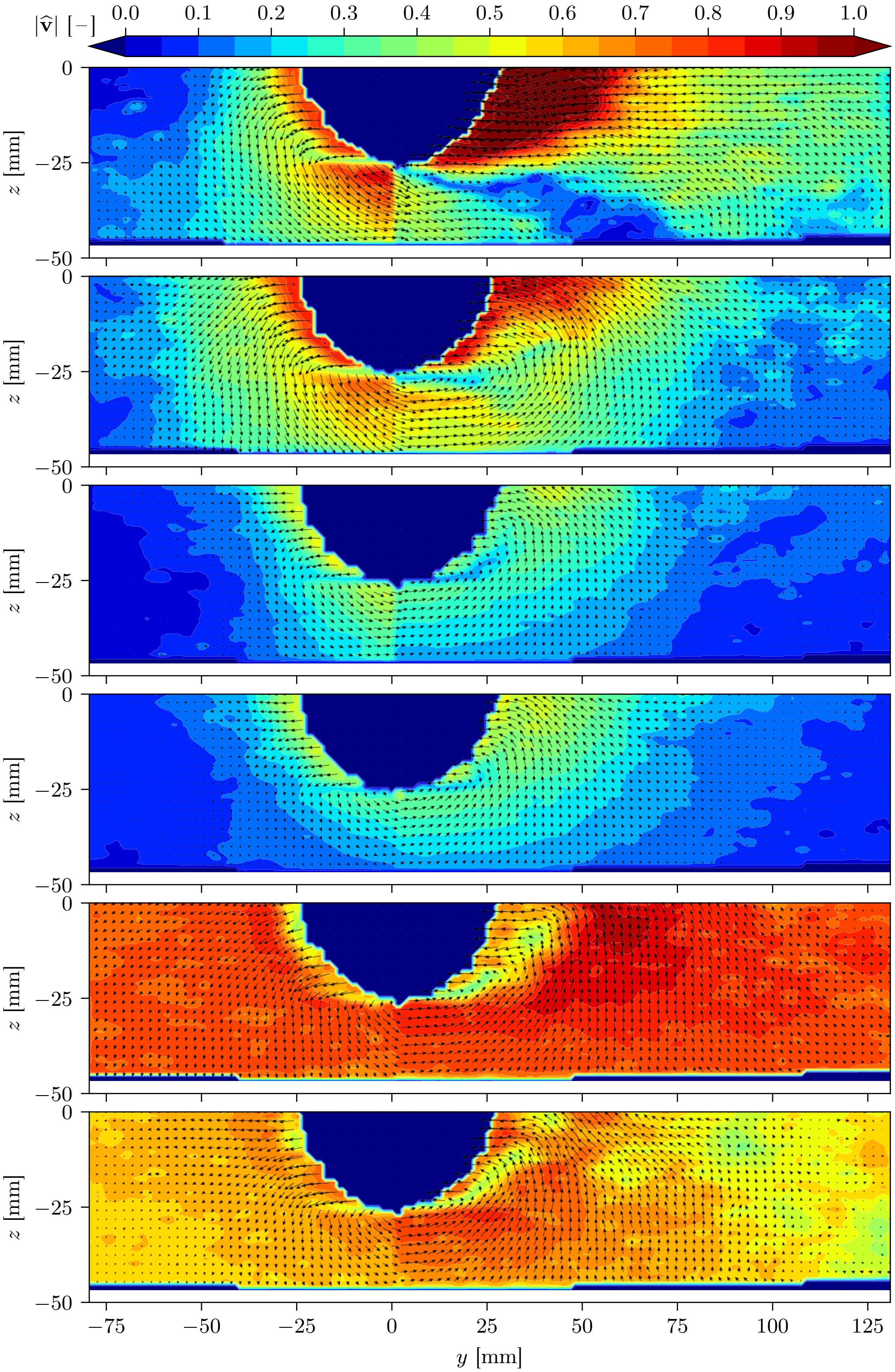

Figure 5.14: Contours of velocity magnitude at $x = L/2$ for (top to bottom): $U_o = 0\,\mathrm{m/s}$ in sway with $T = 4$, $2.7\,\mathrm{s}$ and in yaw with $T = 4$, $2.7\,\mathrm{s}$; $U_o = 0.25\,\mathrm{m/s}$ in sway with $T = 4$, $2.7\,\mathrm{s}$

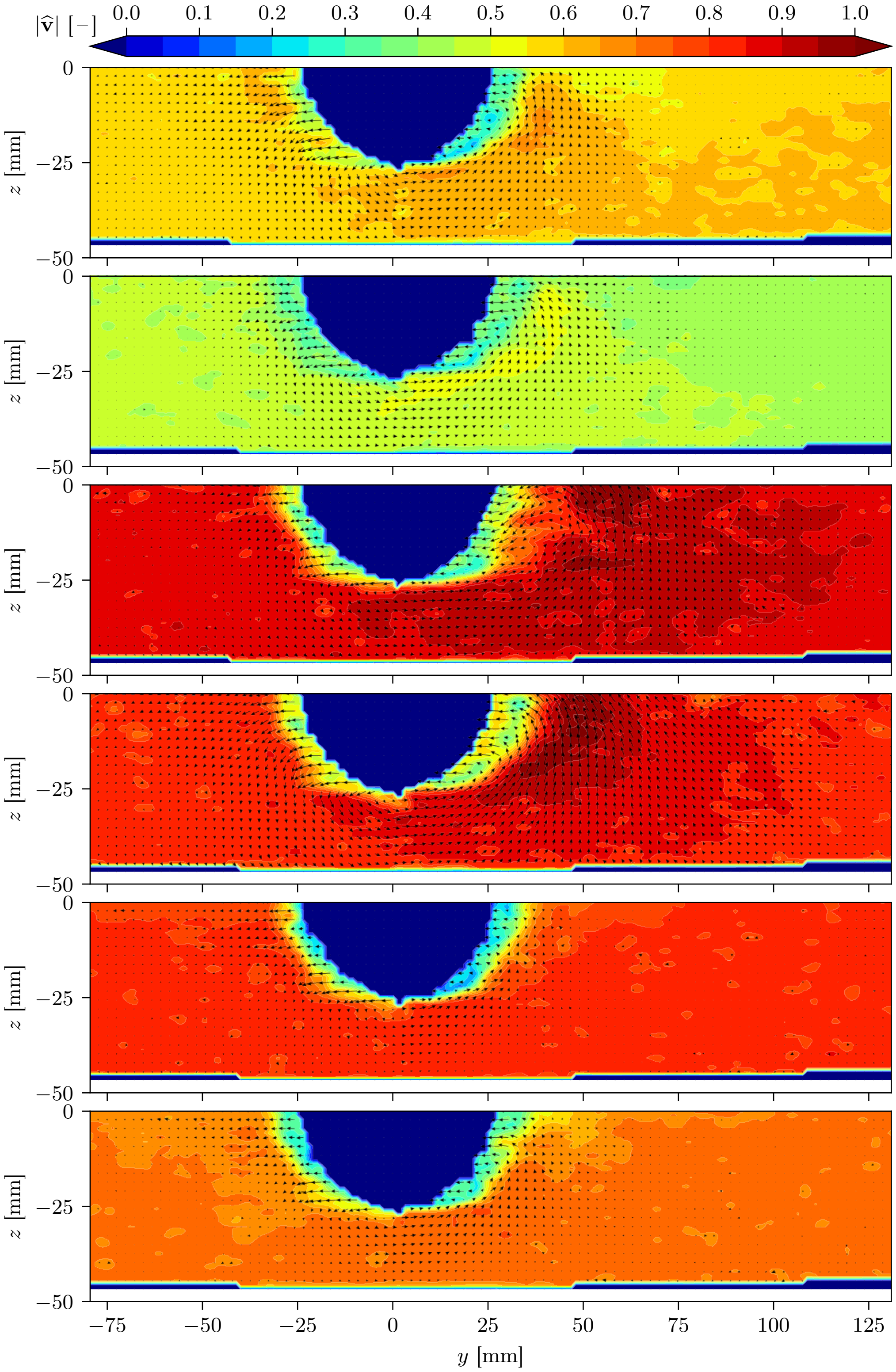

Figure 5.15: Contours of velocity magnitude at $x = L/2$ for (top to bottom): $U_o = 0.25\,\mathrm{m/s}$ in yaw with $T = 4,\ 2.7\,\mathrm{s}$; $U_o = 0.5\,\mathrm{m/s}$ in sway with $T = 4,\ 2.7\,\mathrm{s}$ and in yaw with $T = 4,\ 2.7\,\mathrm{s}$

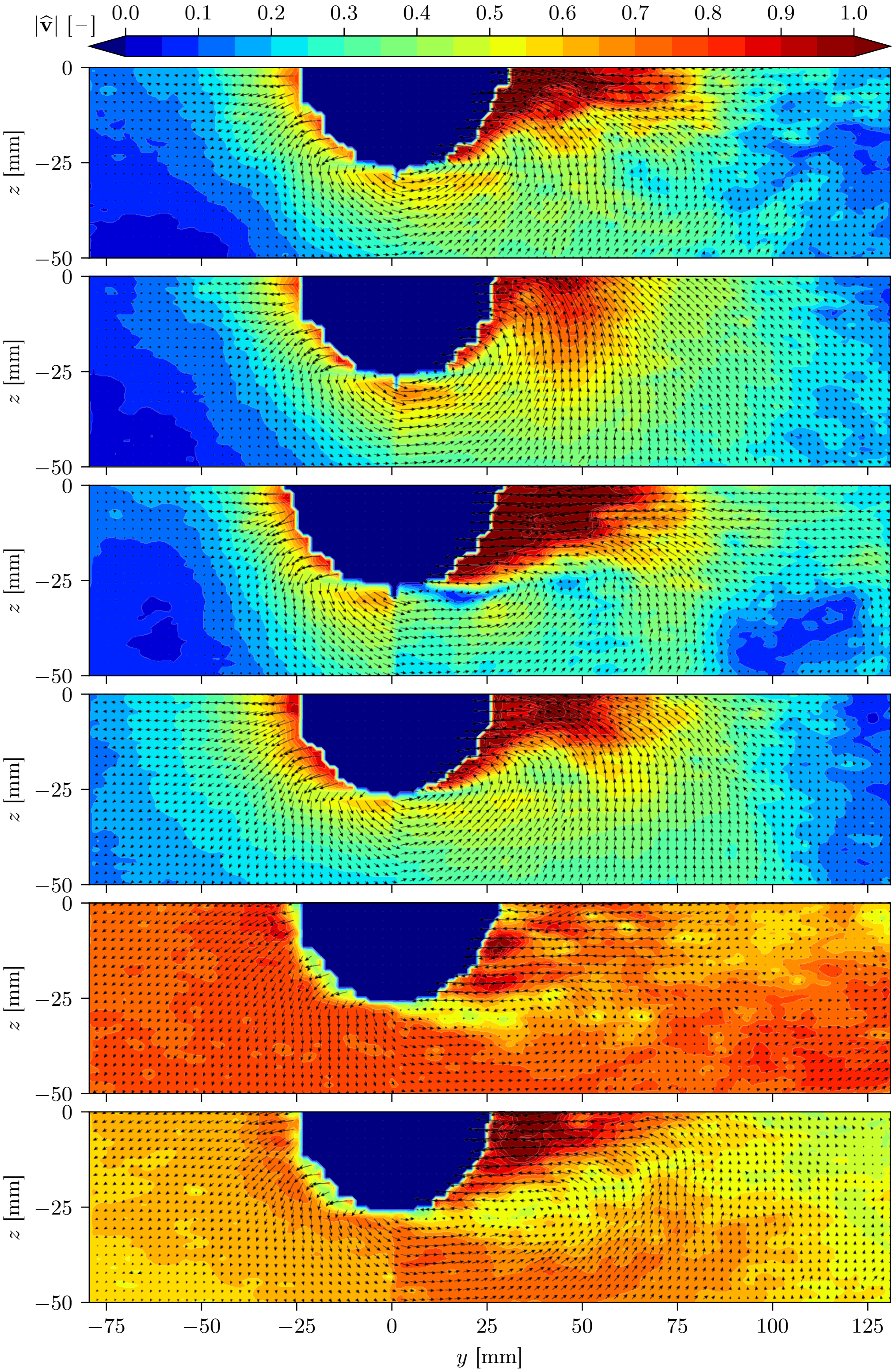

Figure 5.16: Contours of velocity magnitude at $x = 3L/4$ for (top to bottom): $U_o = 0\,\mathrm{m/s}$ in sway with $T = 4$, $2.7\,\mathrm{s}$ and in yaw with $T = 4$, $2.7\,\mathrm{s}$; $U_o = 0.25\,\mathrm{m/s}$ in sway with $T = 4$, $2.7\,\mathrm{s}$

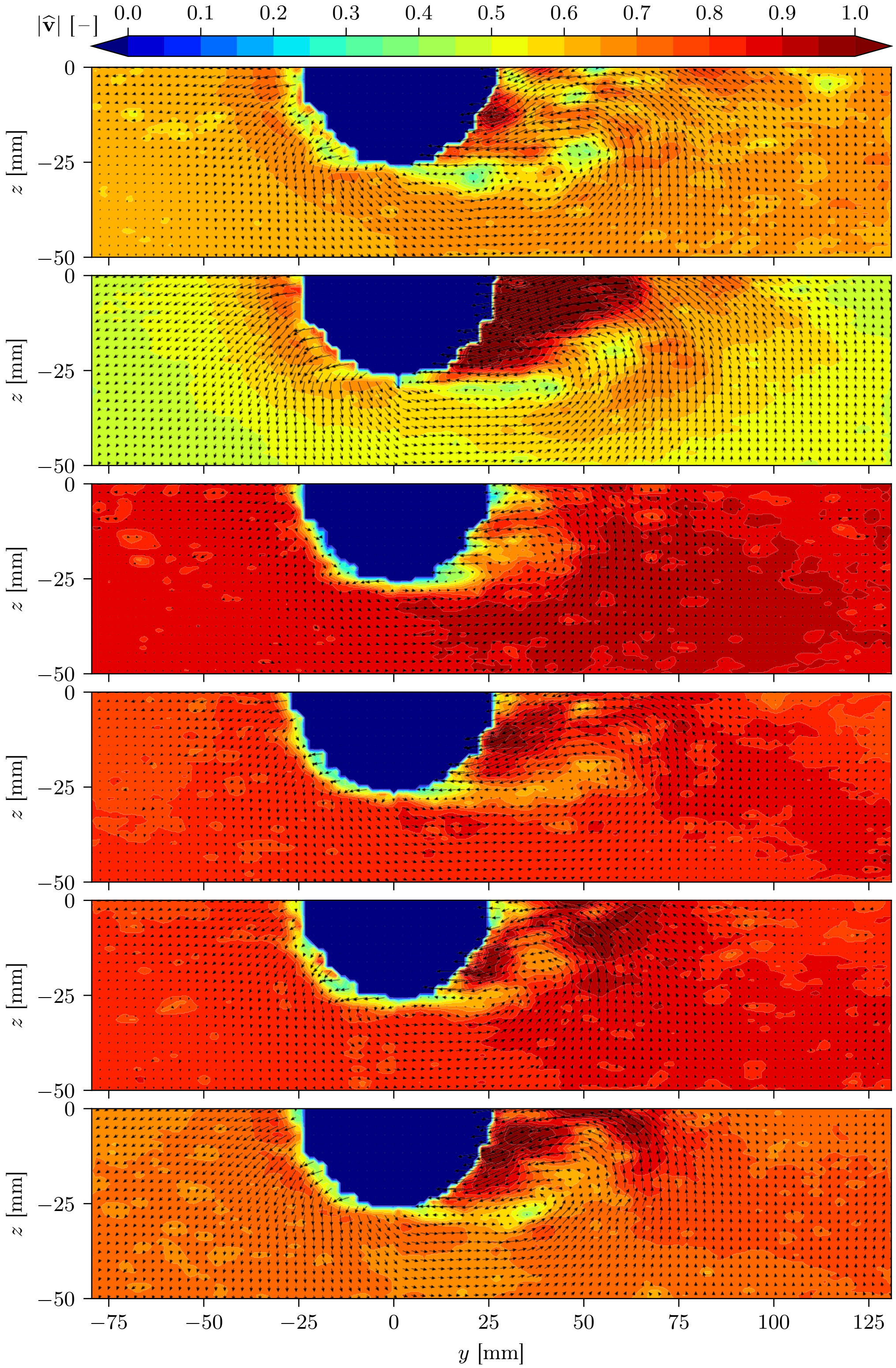

Figure 5.17: Contours of velocity magnitude at $x = 3L/4$ for (top to bottom): $U_o = 0.25\,\text{m/s}$ in yaw with $T = 4,\ 2.7\,\text{s}$; $U_o = 0.5\,\text{m/s}$ in sway with $T = 4,\ 2.7\,\text{s}$ and in yaw with $T = 4,\ 2.7\,\text{s}$

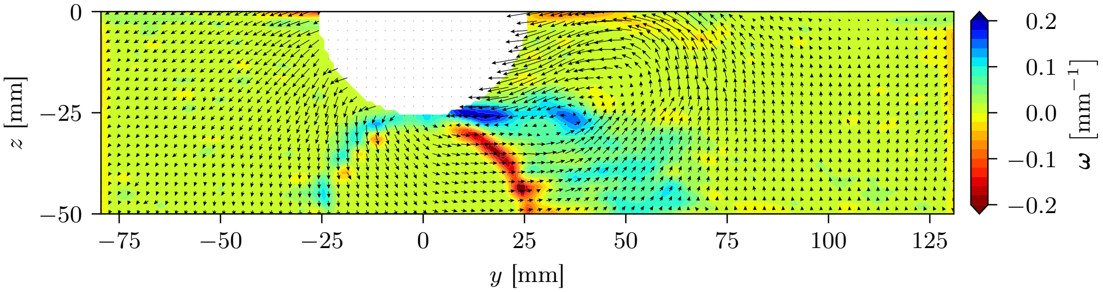

Figure 5.18: Contours of vorticity magnitude at $x = 3L/4$ for $U_o = 0.5\,\mathrm{m/s}$ in yaw with $T = 2.7\,\mathrm{s}$

Sophisticated interpolation schemes are utilized to communicate the solution between grids at the intersection.

For both axisymmetric and oscillatory flow conditions, a horizontal x–y plane of symmetry passing through the test article's longitudinal centerline was exploited in the numerical simulations for approximation and reduced computation time. Again, transverse sections are considered at $L/4$, $L/2$, and $3L/4$ from the leading edge. In-plane velocity fields are visualized in Figures 5.19–5.21. Note the angular discrepancies and disturbances appearing to eliminate the notion or presumption of axisymmetry. Similar disturbances are exhibited by the experimental velocity data in Figures 5.9–5.11.

Distances, r, measured in an outward normal direction beginning at the wall may be taken along radial lines extending from the body's cross-sectional center, $y = z = 0$. Analyzing axial velocity along these lines at a variety of angular values, φ, provides intuition into the relative axisymmetry, characteristic wall shear stresses, and vaguely (as usual) the boundary layer thickness. An arbitrary line extending radially from the body surface must be interpolated for velocity values, however, due to the rectangular nature of grid points in the experimental velocity fields. For consistency, this is done also for the numerical solution data so that analogous values of φ could be analyzed.

Figure 5.22 illustrates these radial lines and their termination points as they appear overlaid on contour lines of velocity for axisymmetric flow with $U_o = 0.5\,\mathrm{m/s}$ at $x = 3L/4$ according to numerical simulation. Angular spacing increments of 5° were used for the sample lines given in Figure 5.22. A cubic interpolation scheme for structured or unstructured two-dimensional data was employed to evaluate the velocity at any desired point within the experimental vector field, and linear interpolation was used for the numerical solution data. The results of this method are plotted in Figures 5.23–5.25 along with predictions from numerical simulations, given in each respective case as a red curve. Note that due to the lack of angular similarity, each curve representing a radial velocity profile according to the numerical predictions actually represents the average profile of a set evaluated at $\varphi \in [1°, 3°, \ldots, 89°]$ measured counter-clockwise from the $-y$-axis—technically, according to the coordinate system, the angles actually appear in the range [180°, 270°], but 180° is subtracted for reporting clarity. Also note that in Figure 5.22, radial lines are drawn starting from the circle center, though the offset of the cylinder radius, R_c, was subtracted from the radial coordinate, r, in analyzing profiles and for plotting.

5.5.1 Axisymmetric Conditions

Boundary layer action for the axisymmetric conditions appears to displace the outer inviscid flow considerably more at $x = 3L/4$ (Figure 5.11) than the other two locations (Figures 5.9 and 5.10). It does not appear that this is due to a transition to turbulence as the behavior seems overall to resemble the shape of Blasius profiles. The sharp transition from high shear to low shear, apparent

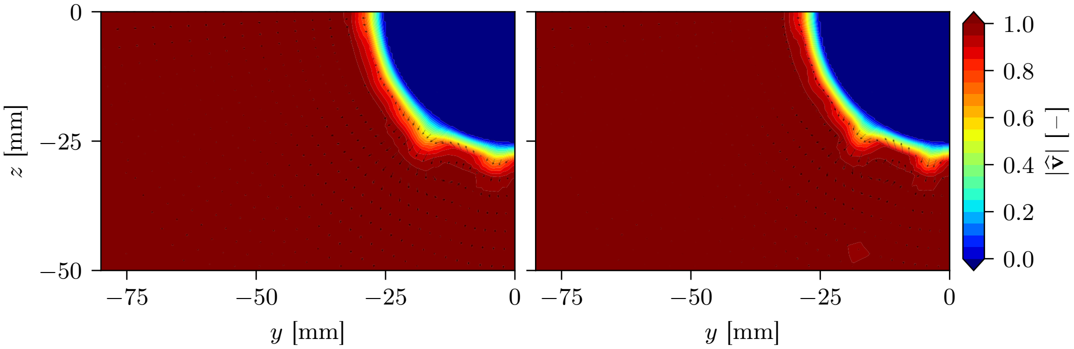

Figure 5.19: Contours of velocity magnitude for axisymmetric flow at $x = L/4$ for $U_o = 0.25\,\mathrm{m/s}$ (left) and $0.5\,\mathrm{m/s}$ (right) according to numerical simulations

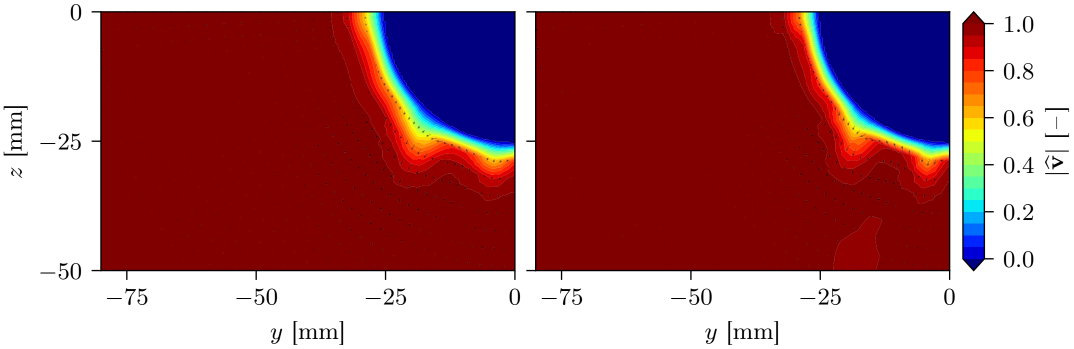

Figure 5.20: Contours of velocity magnitude for axisymmetric flow at $x = L/2$ for $U_o = 0.25\,\mathrm{m/s}$ (left) and $0.5\,\mathrm{m/s}$ (right) according to numerical simulations

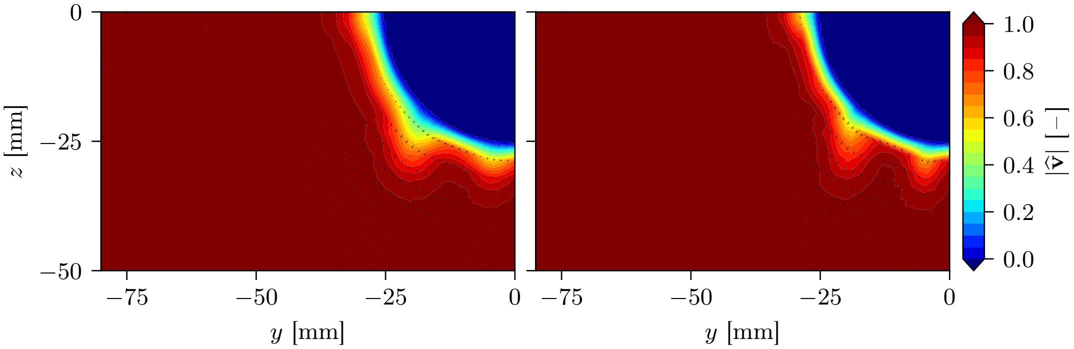

Figure 5.21: Contours of velocity magnitude for axisymmetric flow at $x = 3L/4$ for $U_o = 0.25\,\mathrm{m/s}$ (left) and $0.5\,\mathrm{m/s}$ (right) according to numerical simulations

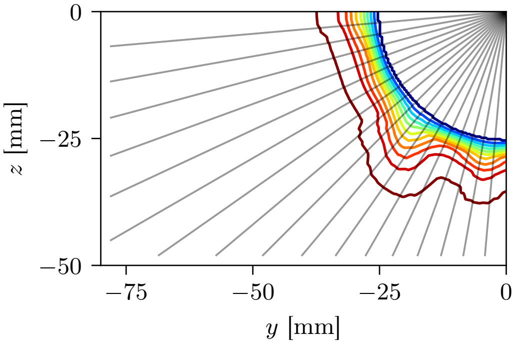

Figure 5.22: Radial profile lines overlaid on contour lines at $x = 3L/4$ for axisymmetric flow with $U_o = 0.25\,\mathrm{m/s}$ according to numerical simulation

Table 5.4: Tabulated comparison of experimental estimation of skin friction coefficients, C_f $[10^{-3}]$, and boundary layer thickness, δ [mm], with the Blasius and Seban–Bond–Kelly theoretical predictions

	0.25 m/s				0.5 m/s			
x	$C_{f,\mathrm{Blasius}}$	$C_{f,\mathrm{SBK}}$	$C_{f,\mathrm{exp}}$	$C_{f,\mathrm{num}}$	$C_{f,\mathrm{Blasius}}$	$C_{f,\mathrm{SBK}}$	$C_{f,\mathrm{exp}}$	$C_{f,\mathrm{num}}$
$L/4$	2.567	2.803	2.451	2.470	1.815	1.935	1.456	1.509
$L/2$	1.815	2.046	1.617	1.628	1.283	1.402	0.955	1.098
$3L/4$	1.482	1.709	1.448	1.404	1.048	1.165	0.904	0.877
x	$\delta_{\mathrm{Blasius}}$	δ_{SBK}	δ_{exp}	δ_{num}	$\delta_{\mathrm{Blasius}}$	δ_{SBK}	δ_{exp}	δ_{num}
$L/4$	5.891	2.027	6.111	6.735	4.166	1.432	5.234	6.486
$L/2$	8.331	2.869	8.507	9.479	5.891	2.027	8.047	7.359
$3L/4$	10.204	3.519	16.373	10.103	7.215	2.483	14.362	9.230

in Figure 5.23 and Figure 5.24, is not present in the profiles of Figure 5.25. The numerical simulation indicates a more gentle transition than closer to the leading edge, but still it has not dampened as quickly as the experimental flow. This could be due to strong influences from transverse curvature or perhaps adverse effects from the two vertical suspending struts causing the high shear within the boundary layer to diffuse.

Comparisons with the analytical solutions from (White, 1969) are omitted since they deal with fully developed turbulent flow for arbitrarily large distances from the leading edge. Instead, the predictions of (Seban and Bond, 1951; Kelly, 1954) are examined more closely in relation to the experimental results of the steadily advancing cylinder undergoing no oscillations. Plots of the skin friction coefficient as predicted by these authors as well as Young (1939) and Glauert and Lighthill (1955) are shown in Figure 5.26. The abscissae are dimensional coordinates measuring the downstream distance from the cylinder's leading edge, and two separate plots are provided illustrating the difference in magnitude and behavior of each function for two different values of the flow parameter, $\nu x/(U_o R_c^2)$, evaluated at $x = L = 1.2192\,\mathrm{m}$.

Each of the prediction curves, with the exception of Glauert–Lighthill, are essentially the Blasius flat plate shear stress formula with correction factors added for surface transverse curvature. The shear stress may be related to the non-dimensional flow parameter as follows:

$$\frac{R_c \tau_{\mathrm{w}}(x)}{\mu U_o} = \frac{1}{\alpha} = \mathcal{F}\left(\frac{\nu x}{U_o R_c^2}\right) \tag{5.10}$$

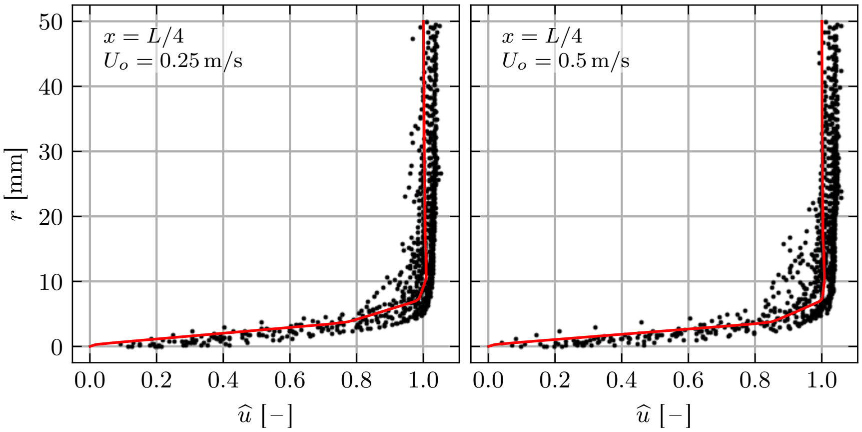

Figure 5.23: Radial profiles of stream-wise velocity, $\widehat{u}$, at $x = L/4$ for axisymmetric flow. Numerical results are given in red as averaged profile over $\varphi \in [1°, 3°, \ldots, 89°]$.

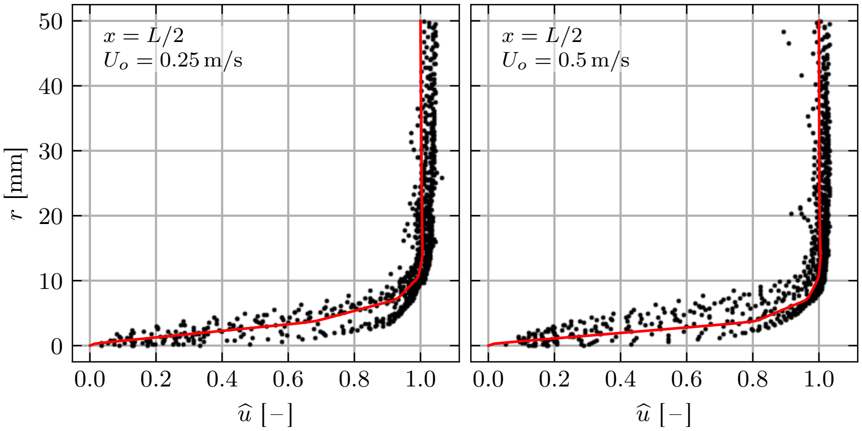

Figure 5.24: Radial profiles of stream-wise velocity, $\widehat{u}$, at $x = L/2$ for axisymmetric flow. Numerical results are given in red as averaged profile over $\varphi \in [1°, 3°, \ldots, 89°]$.

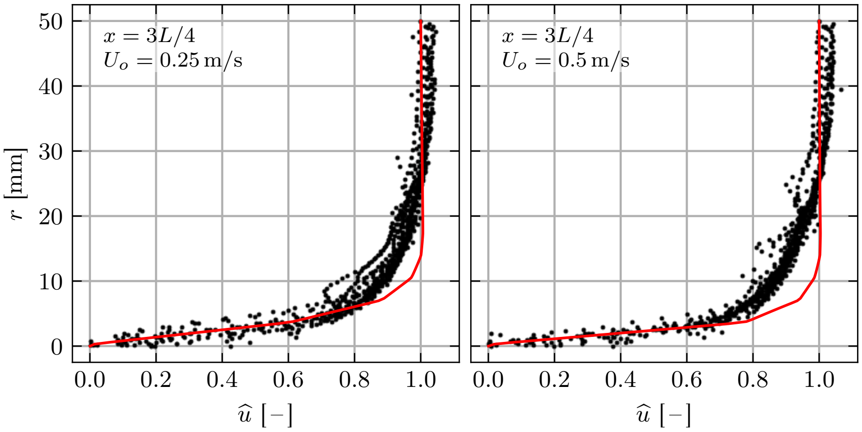

Figure 5.25: Radial profiles of stream-wise velocity, $\widehat{u}$, at $x = 3L/4$ for axisymmetric flow. Numerical results are given in red as averaged profile over $\varphi \in [1°, 3°, \ldots, 89°]$.

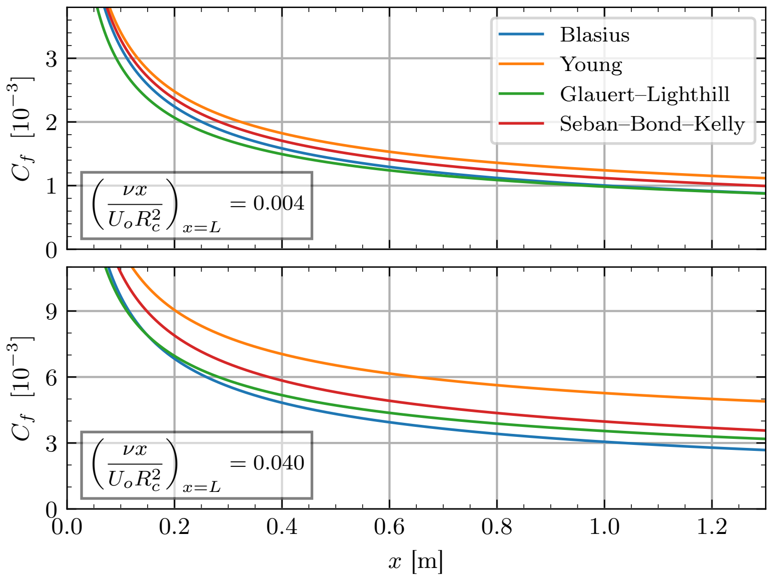

Figure 5.26: Coefficients of skin friction for axisymmetric flow near a cylinder as predicted by Young (1939), Seban and Bond (1951), Kelly (1954), and Glauert and Lighthill (1955). The curves in the upper plot were evaluated for $U_o = 0.5\,\mathrm{m/s}$ while the lower plot was evaluated for maximum $\nu x/(U_o r_o^2)$ ($0.054\,\mathrm{m/s}$) at $x = L$.

One may arrive at this relationship according to the following analytical approximation:

$$\tau_\mathrm{w} = \mu \left(\frac{\partial |\mathbf{v}|}{\partial r}\right)_{r=R_c} \approx \frac{\mu U_o}{R_c \alpha} \tag{5.11}$$

Then the friction coefficient is written as

$$C_f = \frac{\tau_\mathrm{w}}{\frac{1}{2}\rho U_o^2} = \frac{\mu U_o}{R_c \alpha \frac{1}{2}\rho U_o^2} = \frac{2\nu}{R_c \alpha} \tag{5.12}$$

Taking $p = \nu x/(U_o R_c^2)$ for clarity, the $1/\alpha$ relationship according to Blasius (1908) would be

$$\frac{1}{\alpha} = \frac{0.332}{\sqrt{p}} = \beta \tag{5.13}$$

Then, each (truncated) estimation of $1/\alpha$ according to Young (1939), Seban and Bond (1951), Kelly (1954), and Glauert and Lighthill (1955) is calculated as

$$\frac{1}{\alpha} = \begin{cases} \beta + 1.328 + \cdots & \text{Young} \\ \beta + 0.697 - 0.797\sqrt{p} + \cdots & \text{Seban–Bond–Kelly} \\ 0.870\beta + 0.667 - 0.750\sqrt{p} + \cdots & \text{Glauert–Lighthill} \end{cases} \tag{5.14}$$

The formula provided by Seban and Bond (1951) and Kelly (1954) for boundary layer thickness may be written in a similar fashion as

$$\delta = \frac{\mathit{\Delta}}{2\pi R_c} \tag{5.15}$$

where, using the flow parameter, p,

$$\mathit{\Delta} = \pi R_c^2 \left(3.44 p^{\frac{1}{2}} - 0.15p + 3.20 p^{\frac{3}{2}} + \cdots\right) \tag{5.16}$$

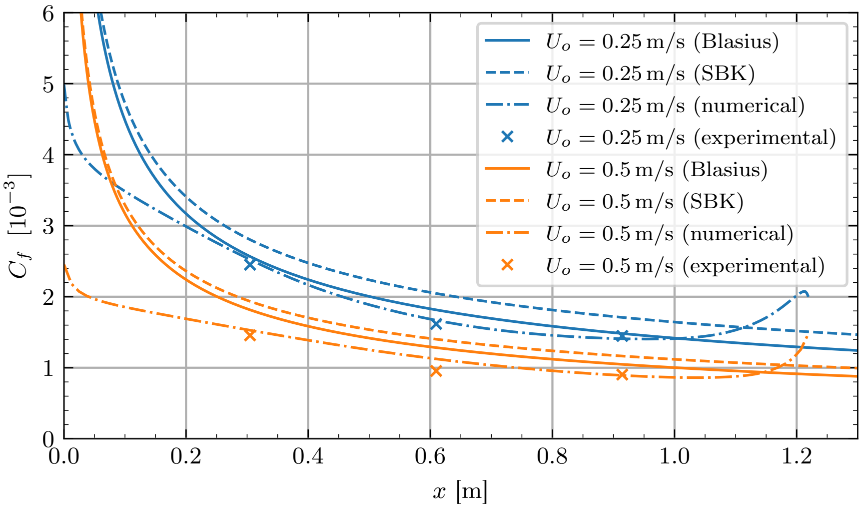

Figure 5.27: Comparison of experimental estimation of skin friction coefficients with numerical predictions and Blasius and Seban–Bond–Kelly analytical curves

Table 5.5: Percentage deviations of experimental results for C_f from theoretical predictions

	0.25 m/s			0.5 m/s		
x	Blasius	SBK	numerical	Blasius	SBK	numerical
$L/4$	4.7	14.4	0.8	24.7	32.9	3.6
$L/2$	12.2	26.5	0.7	34.3	46.8	15.0
$3L/4$	2.3	18.0	3.0	15.9	28.9	3.0

which provides a relationship to the cylinder's physical cross-sectional area. It can also be written in terms of an analytically estimated displacement thickness, δ_1, as

$$\mathit{\Delta} = \pi\Big((R_c + \delta_1)^2 - R_c^2\Big) = \pi\big(\delta_1^2 + 2R_c\delta_1\big) \tag{5.17}$$

which represents the radial displacement of the outer streamlines due to effects caused by the boundary layer. The estimated displacement thickness is calculated as

$$\delta_1 = 1.721\sqrt{\frac{\nu x}{U_o}}\big(1 - 0.245\xi + 0.160\xi^2 + \cdots\big) \tag{5.18}$$

The constant and radical term outside the parentheses in (5.18) are the Blasius solution for boundary layer thickness, thus the truncated sum within the parentheses represents a scaling correction made to the Blasius solution where

$$\xi = \frac{4}{R_c}\sqrt{\frac{\nu x}{U_o}} = 4\sqrt{p} \tag{5.19}$$

For brevity, Seban–Bond–Kelly will be written here at various places, e.g. the plot legend in Figure 5.27 and subscripts in Table 5.4, using the acronym SBK.

Skin friction coefficients were calculated for the experimental data by fitting a regression curve to radial velocity profiles in a manner much similar to the method used in subsection 4.3.1. A function of the linear form

$$\widehat{u}(r) = a\,r \tag{5.20}$$

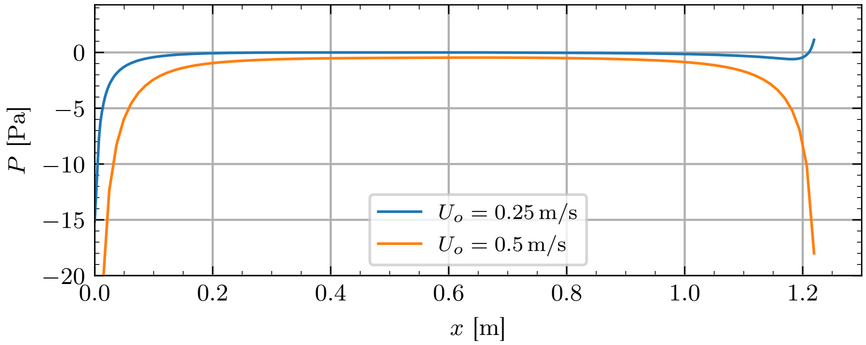

Figure 5.28: Hydrodynamic pressure distributions according to numerical predictions

was evaluated to fit the data points for optimal values of the constant a in the least-squares sense. Then, $\partial\widehat{u}/\partial r$ is simply the value of a after being re-scaled for dimensionalized velocity by multiplication with the corresponding normalization constant (5.9). For the axisymmetric experimental profiles shown in Figures 5.23–5.25, only the data points $\widehat{u} \leq 0.6$ were considered for the linear fit. Results from these estimations are given along with numerical and analytical predictions in Figure 5.27 and Table 5.4. Note that the ordinates in Figures 5.26 and 5.27 are scaled up by a factor of 1,000, according to common practice, for enhanced clarity and legibility.

Each estimation of C_f from the experimental data is slightly smaller than the theoretically predicted values, with deviations from the Blasius prediction appearing in the range 2.3–34.3%, from the Seban–Bond–Kelly prediction 14.4–46.8%, and from the numerical prediction 0.7–15.0%. A complete set of these deviations are provided in Table 5.5. The numerical and experimental estimations obviously agree much better, with significantly lower deviations. Each curve in Figure 5.27 agrees most closely at $x = L/2$ which supports the hypothesis that leading and trailing edge effects strongly influence boundary layer development. It would be very useful to extend these results to measurements taken at $L/16$, $L/8$, $7L/8$, and $15L/16$ for verification of the numerical results and to refine the spacing of data points in Figure 5.27.

A plot of the longitudinal, hydrodynamic pressure distributions according to the numerical simulations, taken at a single angular coordinate, φ, is given in Figure 5.28. Necessary assumptions to achieve the analytical formulas (5.14) include zero pressure gradients everywhere along the cylinder surface—this includes evaluation in both longitudinal and transverse directions. It has already been established that, as observed experimentally and numerically, the boundary layer is not perfectly axisymmetric, and numerical predictions allude to the intuitive hypothesis that longitudinal pressure gradients are nonzero. Hemispherical endcaps at the leading and trailing edges establish radial flow components affecting momentum exchange within the boundary layer as well as displacement of outer flow streamlines downstream and upstream of their respective locations. These influences likely lead to the stronger deviations at $x = L/4$, $3L/4$ evident in Table 5.5.

A rudimentary procedure for estimating boundary layer thickness, δ_{99}, similar to the method used in subsection 4.3.2, was employed for the steadily advancing cylinder. Basically, in each radial direction, criteria were set to evaluate the spatial point at which the axial velocity component achieves or exceeds 99% of the forward speed. The distance between the cylinder's edge, $r = R_c$, and the first measurement of velocity passing this criteria determines the value of δ. Table 5.4 indicates the theoretical predictions of boundary layer thickness according to Blasius' flat plate formula and the Seban–Bond–Kelly results for a long thin cylinder.

Note that Seban–Bond–Kelly calculate smaller thickness and higher wall shear stresses than Blasius' prediction. This is to be expected in cases where transverse surface curvature is present, stream-wise pressure gradients are exactly zero, and the flow is perfectly axisymmetric. Indeed, their scaling "corrections" were calculated to account for these effects. Also, both of these theoretical formulations assume zero boundary layer thickness at the leading edge, $x = 0$. These assumptions, with the exception of surface curvature for $x \geq 0$, are not physically accurate for the present scenario. A hemispherical endcap exists which displaces the flow radially outward beginning at $x = -R_c$. This initiates a boundary layer whose thickness is not insignificant at $x = 0$ and, importantly, that has radial velocity components within the boundary layer itself. Additionally, the two struts suspending the test article in the flow disrupt axisymmetry for downstream measurements. This evidently has at least a small influence in the velocity data plotted in Figure 5.25. These physical conditions obviously play substantial roles in the initiation of steeply positive pressure gradients near the leading edge, growth and behavior of the boundary layer, and the longitudinally and angularly varying wall shear stress, $\tau_\mathrm{w}(x, \varphi)$.

5.5.2 Oscillating Cylinder

Characterizing velocity along radially protruding lines was done for both experimental and numerical data from the oscillating cylinder analyses as well. Rather than axial velocity, the magnitude of all three components was considered. One oscillation frequency, $T = 4\,\mathrm{s}$, was considered at a single longitudinal cross-section, $x = 3L/4$, for both inflow speeds, $U_o = 0.25$ and $0.5\,\mathrm{m/s}$, and for both modes of oscillation, sway and yaw. Figures 5.29 and 5.30 display these profiles of $|\widehat{\mathbf{v}}|$ vs. r. Experimental data is denoted by black markers while numerical data is red. Note that for brevity and clarity in the comparisons, radial profiles at only five angular positions were considered, $\varphi \in [0°, 45°, \ldots, 180°]$. Note also that transverse wall shear manifests as both positive and negative, depending on the angular position and inflow velocity. This is evident by inspecting slope inflections at $y = 0$.

For the angular position $\varphi = 180°$ disturbances appear relatively far from the boundary. The profile at this angle obviously corresponds to velocity data in the local section's wake, hence the relatively dramatic disturbances. Agreement in the asymptotic approach to the mean outer flow is displayed universally, and generally, wall behavior is comparable, especially for the lower values of φ, i.e. where the flow has not yet separated. Using velocity magnitude, it is difficult to tell exactly where separation occurs, but inspection of the contours of Figures 5.12–5.17 indicates separated flow, especially for the higher oscillation frequency, $T = 2.7\,\mathrm{s}$.

Discontinuities appear where gradients remain relatively large at approximately $r = 50\,\mathrm{mm}$ in the numerical profiles due to differences in interpolation of the background and component grids of the overset mesh when extracting the data from Fluent's post-processor. The component grid was designed to extend 50 mm beyond the cylinder's edge, so this interface with the background grid causes trouble in the interpolation. No user control over this interface was available when exporting the data.

Notice that differences in wall shear between Figure 5.29 ($U_o = 0.25\,\mathrm{m/s}$) and Figure 5.30 ($U_o = 0.5\,\mathrm{m/s}$) depend quite loosely on Keulegan–Carpenter numbers and more heavily on inflow magnitude. This confirms that low oscillation frequency influences wall shear relatively insignificantly compared to local axial velocities and could bear significant consequences for the robotic eel. Longitudinal velocity components clearly influence the magnitude of skin friction coefficients more readily than transverse components, especially since it is the squared outer flow velocity that is found in the denominator of Equation (5.12) and will reduce its value for larger inflow and equal shear stress. Hence, it is the slope of the profile at the wall that should be carefully considered in evaluating the viscous effects on resistance. The skin friction coefficient merely provides a non-dimensional relationship between the wall shear stress and the characteristic dynamic pressure.

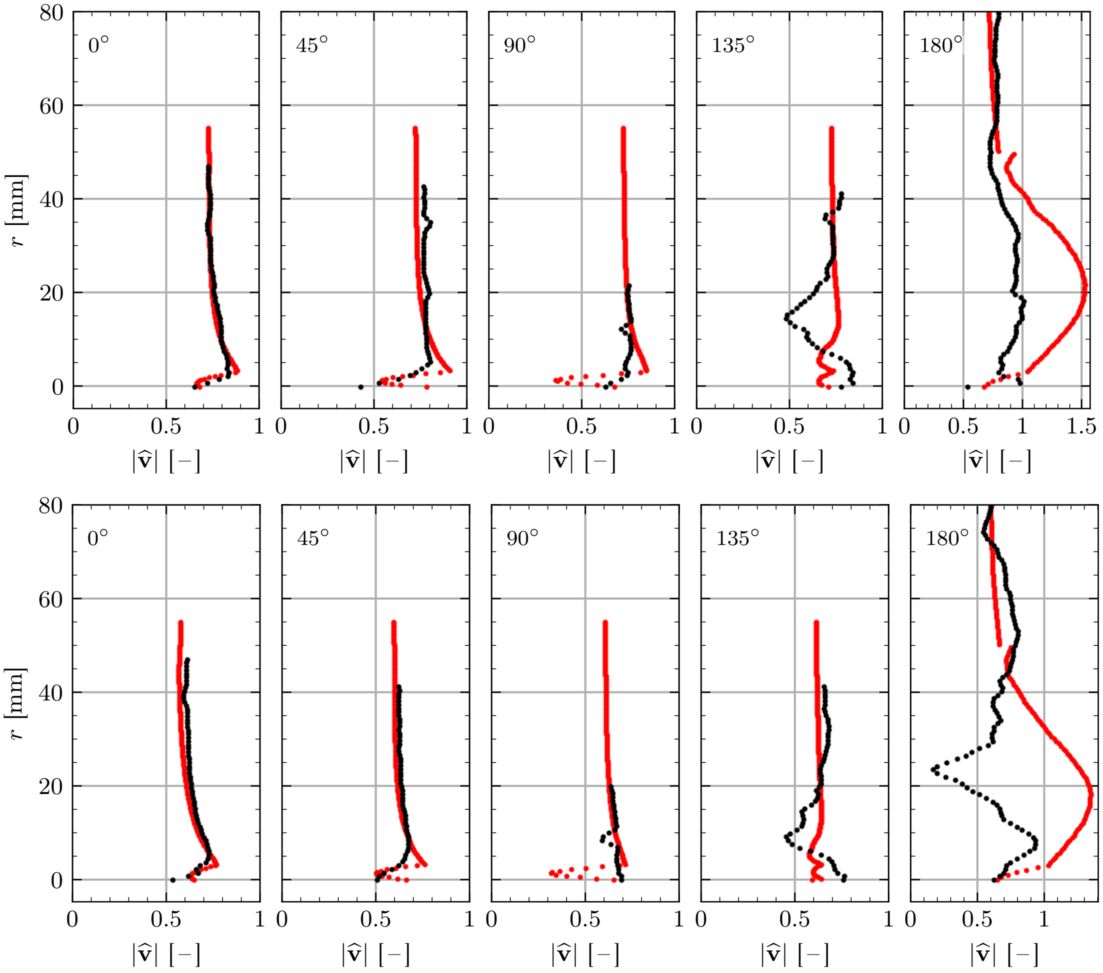

Figure 5.29: Radial profiles of velocity magnitude plotted with CFD results for $x = 3L/4$, $U_o = 0.25\,\mathrm{m/s}$, and $T = 4\,\mathrm{s}$ in sway (top) and in yaw (bottom). Numerical results are given in red.

Estimates for local skin friction coefficients for the oscillating cylinder are given in Table 5.6. Note that each value is calculated according to Equation (5.12) as usual but with the fixed value of $U_o = 0.25\,\mathrm{m/s}$ in the dynamic pressure calculation. This was done to eliminate division by zero errors for $U_o = 0\,\mathrm{m/s}$ and to provide better correspondence later with robotic eel results. Further note that more radial profiles were used in determining these estimates than were used for the non-oscillating cases: 2° increments of φ from 1° to 179°. The velocity profiles obviously fluctuate much more aggressively with φ for the oscillating cylinder than in cases with only longitudinal inflow, so more angular offsets were considered to better characterize this dependence.

A few specific observations from the friction coefficient predictions listed in Table 5.6 may be summarized as follows:

1. Forward carriage speed influences magnitude more strongly than oscillation mode, period, or longitudinal measurement location.
2. Slight increases are generally seen for increasing oscillation frequency.
3. Yaw oscillations generate slightly higher shear stress than sway.
4. Unlike results from axisymmetric conditions, friction coefficients increase with x rather than decrease.

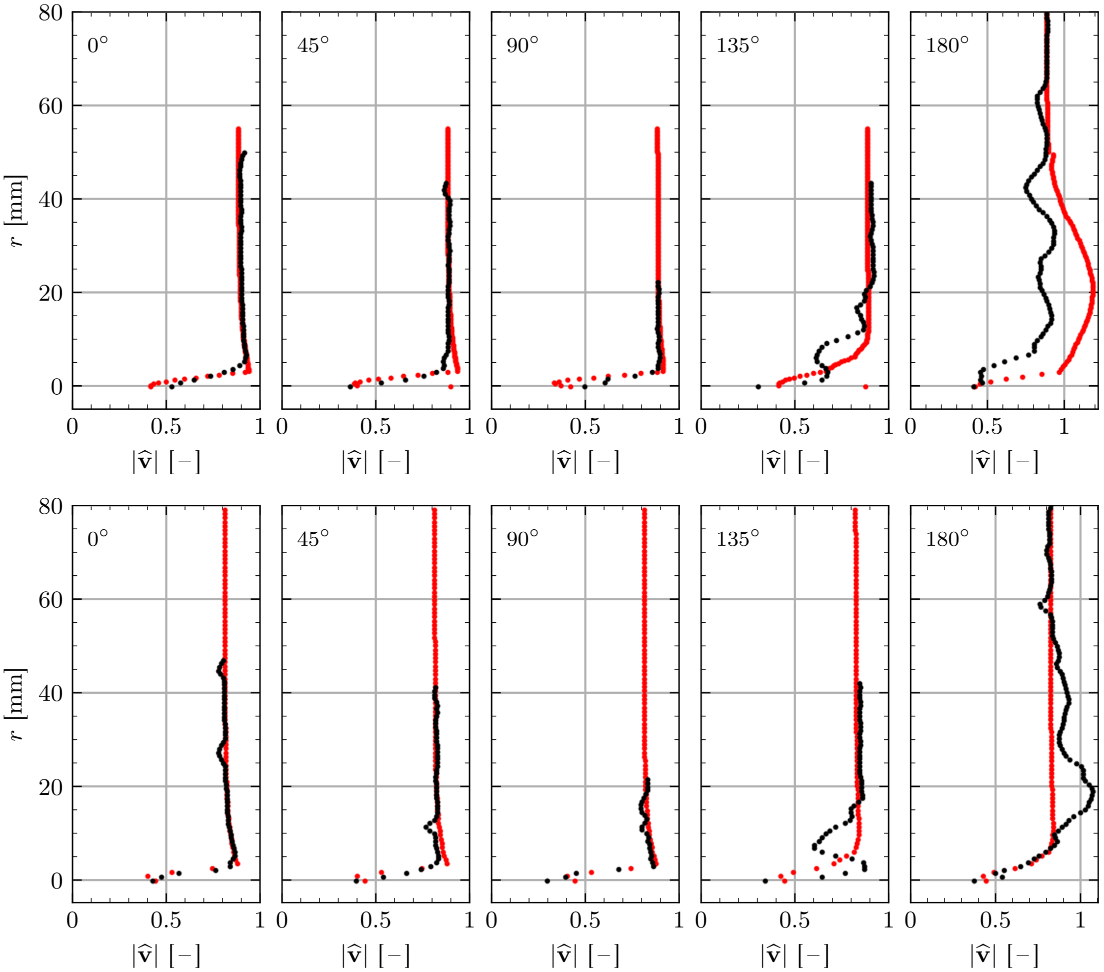

Figure 5.30: Radial profiles of velocity magnitude plotted with CFD results for $x = 3L/4$, $U_o = 0.5\,\mathrm{m/s}$, and $T = 4\,\mathrm{s}$ in sway (top) and in yaw (bottom). Numerical results are given in red.

Table 5.6: Skin friction estimates, C_f $[10^{-3}]$, for the oscillating cylinder at each measurement location and for each carriage speed, oscillation mode, and period

		0 m/s	0.25 m/s	0.5 m/s
$L/4$	4 s, sway	0.143	2.861	4.847
	4 s, yaw	0.090	2.841	5.186
	2.7 s, sway	-0.011	3.375	5.224
	2.7 s, yaw	0.474	2.799	5.686
$L/2$	4 s, sway	-0.249	2.737	4.736
	4 s, yaw	-0.004	2.604	4.959
	2.7 s, sway	0.362	2.985	5.180
	2.7 s, yaw	0.175	2.591	5.537
$3L/4$	4 s, sway	0.303	3.633	6.235
	4 s, yaw	0.912	5.719	7.854
	2.7 s, sway	0.428	3.853	6.448
	2.7 s, yaw	0.516	4.605	7.626

Increases in C_f along x are probably due to boundary layer thinning caused by the oscillations. Additionally, some artificial scaling is present for the column of highest outer flow rate, $U_o = 0.5\,\mathrm{m/s}$, because the denominator of Equation (5.12) is smaller than it would be with the actual carriage speed substituted for U_o. Overall, comparing with the coefficients given in Table 5.4 for the non-oscillating cylinder, appreciably larger values are found to be due to transverse oscillations. No estimates based on the results of numerical simulations are yet prepared for comparison, but they should be evaluated in a similar manner as used presently. Nevertheless, these figures provide some benchmark groundwork for comparisons with the robotic eel test results.

6 Robotic Eel Experiments

Returning to the discussion of drag-thrust balance for NEELBOT, this chapter presents experimental measurements of fluid velocity within three two-dimensional flow regions near the robot at particular discrete time steps. In order to confidently predict the robot's drag at a particular swimming mode, one should completely characterize boundary layer information over the entire length $x \in [0, L]$ throughout the undulation cycle $t \in [0, T]$. According to Lighthill (1971), "it would be the balance, existing between viscous diffusion of vorticity away from the fish's surface and convection of vorticity towards the surface by relative lateral motion between it and the water, that would determine the boundary-layer thickness, and hence also the skin-friction drag associated with the tangential u-motion." Theoretically, no vorticity should be found in the flow surrounding the robot when operating at design speed, but this balance will certainly be an important phenomenon to analyze if vorticity is to be identified in off-design scenarios to evaluate the robot's thrust production capabilities as they relate to reciprocal incident drag.

For robot reference lengths, a "nominal length" is computed as described by Potts (2015, eq. (2.64)) as

$$L = \frac{1}{N}\sum_{n=0}^{N} L_n \tag{6.1}$$

This length is formulated to describe the time-averaged, contracted body length throughout its oscillation cycle, and it is illustrated in Figure 6.1 for $t = 0$ and for the parameters of round 1 in Table 6.1. Thus, N represents the number of discrete time steps for the programmed motion, and L_n is the contracted body length at time step n. The non-dimensionalization formulas from (2.17) still apply, and now the nominal length L is accounted for. Again, V is the displacement wave speed [m/s], $T = L/V$ is the time period of the displacement wave [s], $U = 1 - \text{slip} = U_o/V$ is the dimensionless advance ratio, U_o is the advance speed [m/s], and r_o is the robot's constant body radius [m].

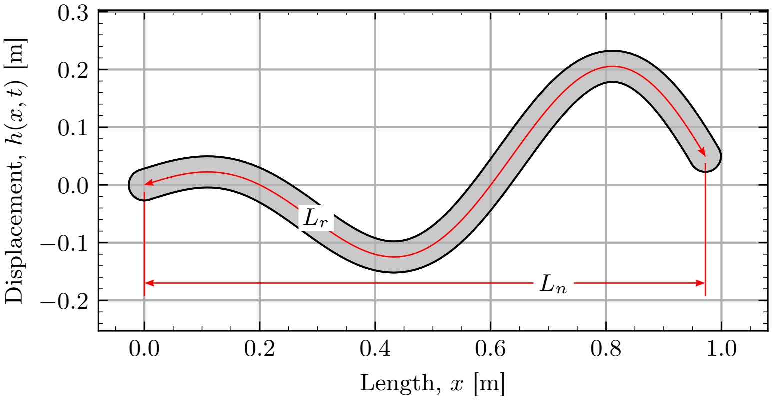

Figure 6.1: Annotations denoting the length parameters of the anguilliform shape (replotted from Potts (2015))

Table 6.1: Experimental parameters for the robotic eel experiments

		round 1	round 2	round 3
carriage speeds	U_o	0, 0.16, 0.25, 0.4 m/s (all for each round)		
advance speed (design)	$U_{o,d}$	0.25 m/s	0.25 m/s	0.25 m/s
advance ratio	U	0.7	0.7	0.78
displacement wave speed	V	0.357 m/s	0.357 m/s	0.321 m/s
displacement wave amplitude	Γ	0.11767	0.09414	0.14120
displacement wave period	T	2.721 s	2.917 s	3.204 s
robot nominal length	L	0.972 m	1.042 m	1.030 m
thrust coefficient	C_T	0.7985×10^{-3}	0.6388×10^{-3}	0.8070×10^{-3}

Figure 6.2: NEELBOT-1.1 on a tabletop without its waterproofing skin (from (Potts, 2015))

As described by Potts (2015), the robot's nominal length for a particular motion is determined by this time-averaged method (6.1). However, the theory assumes that the arc length of the anguilliform shape, denoted by L_r in this paper, is able to change in time and keep the nominal length constant—a result of the slender-body theory linearization. This, along with the non-dimensionalizations, is done to make the mathematical derivations of the hydrodynamic theory easier. With current, practical robots this is physically infeasible. So, instead the constant time-averaged length in the x-direction is used to approximate the length specified by Vorus (2005).

The constructed robot is shown in Figure 6.2 without its waterproofing skin. Its "straight" length (also the arc length or the centerline length when contracted), L_r, with all segment angles set to 0°, is 1.3 m, and its diameter, $D_r = 2r_o$, is 55.5 mm. This diameter includes the approximately uniform thickness of a latex waterproofing skin—the robot's diameter without the latex skin is 54 mm. Liquid latex mask-making rubber was used to create this waterproofing skin for the robot. In order to attenuate undesirable laser light reflection, a generous amount of black dye was mixed into the latex before making the skin. This was unnecessary for the previous two test articles, as they contain no water-sensitive electronic equipment and are made of smoothly-polished acrylic which allows the laser light to pass uninhibited through their surfaces.

Potts (2015) constructed NEELBOT-1.1 with 20 equal-length, 3D-printed segments and 19 servo-actuated joints. The segments are made up of two pieces, a top and bottom, that screw together and attach to adjacent segments via the servo output shafts. Each servo is a Dongbu

Herkulex DRS-0201 which has a closed-loop PID position controller with programmable PID gains. Angular position is measured by an onboard encoder which, in turn, is read by a microcontroller that handles closing the feedback loop of the actuator. The microcontroller is also responsible for communicating with the computer program written by Potts (2015) to instruct the robot to achieve the desired anguilliform motions. For further details of the robot's design, construction, and motion programming see (Potts, 2015).

Some minor modifications to NEELBOT were made for the accomplishment of the current investigation. With autonomy in mind, Potts (2015) incorporated a radio for wireless communication and installed 38 nickel-metal hydride 1,000 mAh AA batteries—32 cells for remote power delivery to the servo actuators and 6 for the head circuity. The experiments conducted herein required a duration of power delivery beyond that which was feasible given the existing storage, so electrical power was wired directly through the robot's head segment to partially supply the required power and to recharge the batteries between runs. For this reason, hard-wiring communication signals was also easily implemented, eliminating the possibility of transmission blips. Otherwise, only minor ballasting adjustments were made. Programmatic and servo settings were unchanged to maintain experimental consistency with Potts' 2015 wake field investigations.

Three "rounds" of similar analogous tests were performed in the present investigation with the robotic eel. Experimental parameters for the first round matched those used by Potts (2015) as the *design* parameters for $U_{o,d} = 0.25\,\mathrm{m/s}$. Two "off-design" conditions were also considered. In each case the displacement wave amplitude $\mathit{\Gamma}$ was changed—one a 20% decrease over the original value and the other a 20% increase. It was desired that all other parameters be held constant with only $\mathit{\Gamma}$ changing, but this proved impossible for the increase in amplitude. Required servo angles (to achieve the desired motion) exceeded the physical angular limitations of the robot's segments of 45°. For this reason, the wave speed, V, was reduced by 10% which extends the body wave period and reduces the maximum transverse displacements. Table 6.1 summarizes the parameters used in designing the robot's motion for each of the three rounds. For all the testing accomplished, the final set of PID gains used by Potts (2015) ("set D": $K_P = 150$, $K_I = 50$, $K_D = 100$) were used.

Clarification on the meaning of U_o is also needed. In this paper, it generally refers to the mean inflow speed, i.e. in this case, the carriage towing speed. In Table 6.1 a new subscript is introduced to designate the open water advance speed at which the robot is *designed* to swim for the purpose of programming the correct swimming motion. For experimental testing purposes, a zero advance speed case, $U_o = 0\,\mathrm{m/s}$, is considered as well as three positive speeds at which the robot is towed beneath the towing carriage in UNO's towing tank, $U_o \in [0.16, 0.25, 0.4\,\mathrm{m/s}]$. These off-design speeds were chosen for consistency with the work of Potts (2015). In particular, 0.16 m/s was tested because it corresponds to the towing speed at which minimal net axial force was measured acting on the tether when towing the robot. Potts (2015) collected net force data while towing the robot at a variety of speeds with the robot waving according to the design parameters of $\mathit{\Gamma} = 0.11767$, $U_{o,d} = 0.25\,\mathrm{m/s}$, and $U = 0.7$ and determined thrust–drag balance to exist when towing at 0.16 m/s. See (Potts, 2015, sec. 4.2) for more details.

Non-dimensional waveform displacements at ten equally spaced time steps over the undulation period for each round are shown in Figure 6.3. All of the necessary motion parameters required to reproduce these curves are tabulated in Table 6.1. The top plot illustrates the minor differences in shape predicted by each set of parameters for $\bar{t} = 0$. The effects of reducing $\mathit{\Gamma}$ for round 2 are easily distinguished since it is simply a transverse scaling factor. Note that the round 3 curve exhibits slight phases differences from the former two curves.

Although it is not explicitly stated, Potts (2015) probably chose these parameters (round 1, Table 6.1) for the design motion to reasonably achieve the largest possible relative segment angles without over-torquing the servos or exceeding physical restraints. Figure 6.4 indicates the distribu-

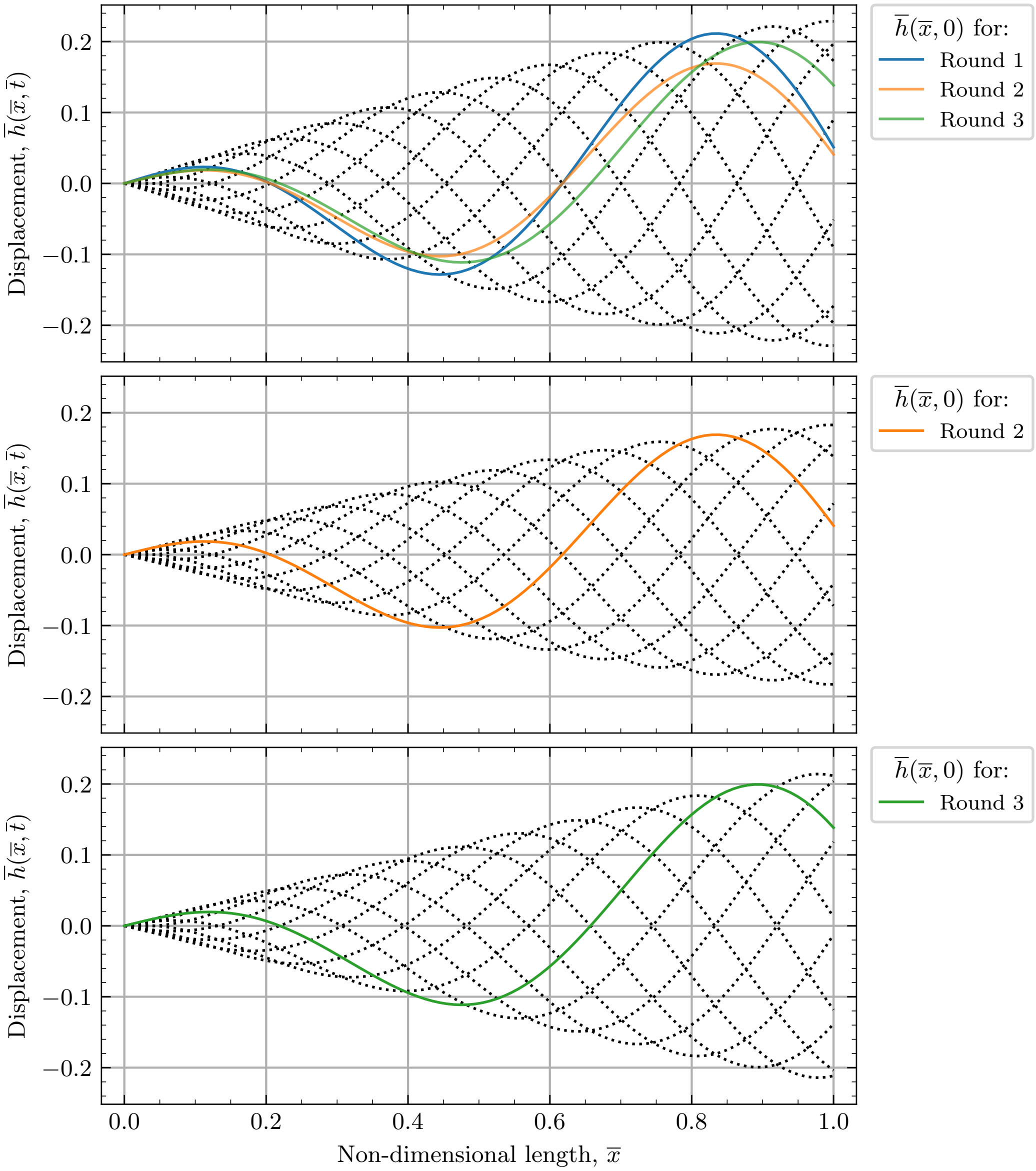

Figure 6.3: Non-dimensional waveforms for ten equally spaced time steps over the undulation period using the parameters from Table 6.1 (replotted with different parameters from (Potts, 2015))

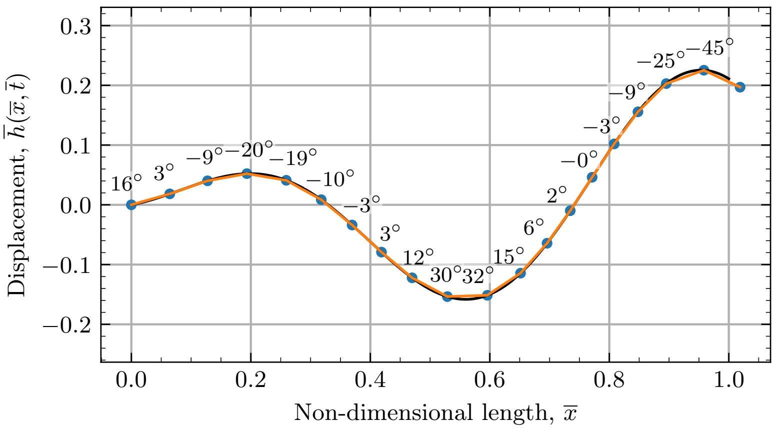

Figure 6.4: Relative angles for each servo at the time step corresponding to the greatest servo angle, 44.7° at $\overline{t} = 0.15$ (replotted with different parameters from (Potts, 2015))

tion of servo angles prescribed at the time step corresponding to the greatest angle appearing in the motion, approximately $\vartheta = 44.7°$ at $\overline{t} = 0.15$. Note that the abscissae still denote non-dimensional coordinates in $\overline{x}$. The robot's physical angular constraint was determined from real-time readouts of servo feedback while manually adjusting individual angles. Maximum angular displacement, the angle at which adjacent segments make contact and, if forcefully exceeded, would lead to damage, was observed to be 45°—just higher than the motion programmed by Potts (2015).

As with the cylinder experiments, PIV testing with the robotic eel required the prediction of useful time increments, Δt, between image pairs for effectively capturing flow velocities in a particular cross-section's wake. In order to do this, transverse velocities of the cross-sections of interest were needed to ensure sufficiently small values were chosen to capture all flow structures. For the robot's waving motion, these transverse velocities may be computed as the time derivative of the displacement function (2.41) which provides transverse offsets for the robot's motion.

$$\overline{h}_{\overline{t}}(\overline{x},\overline{t}) = \frac{\partial \overline{h}(\overline{x},\overline{t})}{\partial \overline{t}} = -2\pi\mathit{\Gamma}\left[\cos\left(2\pi\left(\frac{\overline{x}}{U}-\overline{t}\right)\right)-\cos\big(2\pi\left(\overline{x}-\overline{t}\right)\big)\right] \tag{6.2}$$

In the same way that the transverse displacement (2.41) was converted into a product of sinusoids (2.43) by means of the product-to-sum identity (2.42), the transverse velocity function can also be rewritten as

$$\overline{h}_{\overline{t}}(\overline{x},\overline{t}) = \frac{\partial \overline{h}(\overline{x},\overline{t})}{\partial \overline{t}} = 4\pi\mathit{\Gamma}\sin\left(\pi\left(\frac{\overline{x}}{U}-\overline{x}\right)\right)\sin\left(\pi\left(\frac{\overline{x}}{U}+\overline{x}-2\overline{t}\right)\right) \tag{6.3}$$

A plot of the predicted transverse displacement and its corresponding transverse velocity is given in Figure 6.5 for $\overline{t} = 0$. Notice that two ordinate axes are present which share an abscissa axis and give a sense of the 2π scaling present in the non-dimensional transverse velocity.

PIV experiments in the towing tank involved the measurement of fluid velocities at transverse cross-sections of the robot at three longitudinal positions. Similar to the cylinder, positions $L/4$, $L/2$, and $3L/4$ are investigated. However, here L refers to the "nominal length" as in (6.1). This implies that, for example, $L/4$ no longer refers to 25% of the straight cylinder length.

In order to determine the transverse velocity of an arbitrary cross-section as it passes through the vertical centerplane $y = 0$, the offset function $\overline{h}(\overline{x},\overline{t})$ shall be set equal to zero, evaluated at the relevant coordinates $\overline{x} = 0.25, 0.5, 0.75$, and solved for the desired unknown, $\overline{t}$, which can sub-

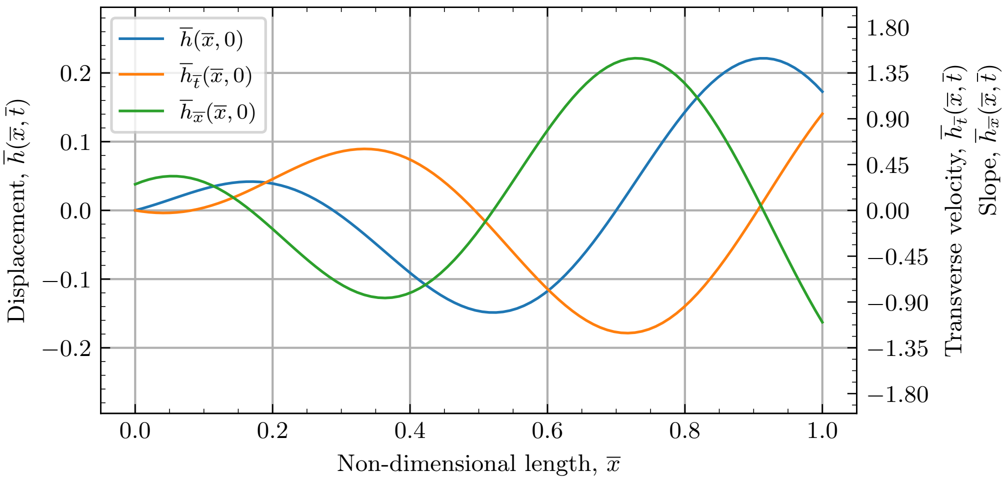

Figure 6.5: Comparison of transverse displacement, velocity, and slope for the ideal anguilliform swimming motion—note the use of two non-dimensional ordinate axes

sequently be substituted into Equation (6.3) for velocity. Rearranging (2.41) accordingly provides

$$\sin\left(2\pi\left(\frac{\overline{x}}{U}-\overline{t}\right)\right)-\sin\bigl(2\pi(\overline{x}-\overline{t})\bigr)=0 \tag{6.4}$$

This nonlinear equation has infinitely many solutions, but it is known that exactly two values of $\overline{t}$ should fall in the range $\overline{t}\in[0,\ 1]$ for a particular $\overline{x}$ (one for motion in the $+y$ and one in the $-y$-directions). So the solution space is limited to this range. A numerical scheme known as "Algorithm 748" (Alefeld, Potra, and Shi, 1995) from SciPy's `root_scalar` routine in the `optimize` module is used, which guarantees convergence to a root within an enclosing interval (for sufficiently well-behaved functions). In such a way, the desired non-dimensional time steps may easily be found. Table 6.2 tabulates the resulting calculated roots. The dimensional quantities are determined by rearranging the formulas for non-dimensionalization (2.17). The time step column is calculated similarly as *time step* $=\lfloor\overline{t}N\rfloor$. These numbers are floored because they refer to a discrete time step in which the event is expected to occur. Also, in practice, a few of the calculated time steps varied slightly from the predicted ones, probably due to the robot's imperfect achievement of the programmed motion and the inevitable length contraction.

These roots given in Table 6.2, along with their corresponding non-dimensional $\overline{x}$ locations, are then used to evaluate the velocity function (6.2) which is subsequently made dimensional according to

$$h_t(x,t)=\left(\frac{L}{T}\right)\overline{h}_{\overline{t}}(\overline{x},\overline{t}) \tag{6.5}$$

Plotting the displacement curves for the time steps indicated in Table 6.2 verifies that the correct roots were found. This is illustrated in Figure 6.6. A curve is given for both time steps corresponding to each of the three cross-section/vertical centerplane intersections.

Rationale for choosing the number of time steps N is discussed in (Potts, 2015, pp. 79, 88). Basically, too few time steps makes the robot's motion jerky, and too many causes the time interval between steps to become too short for sufficient computation time and signal transmission and reception between the computer and servos (both the computer and robot transmit and receive data). $N=40$ was eventually chosen, mostly through trial and error, as a reasonable compromise such that the motion appears smooth yet still allows enough time for computations and communication.

Table 6.2: Transverse velocities, sectional slopes, and time steps for each round of experiments with the robotic eel

	location, $\overline{x}$	(roots) time, $\overline{t}$	dimensional time, t [s]	corresponding time step	transverse velocity [m/s]	sectional slope [deg]
$\mathit{\Gamma} = 0.11767$	$\overline{x} = 0.25$	0.053571	0.1458	2	0.1744	−30.67
		0.553571	1.5063	22	−0.1744	30.67
	$\overline{x} = 0.5$	0.357143	0.9718	14	0.3293	−48.23
		0.857143	2.3323	34	−0.3293	48.23
	$\overline{x} = 0.75$	0.160714	0.4373	6	−0.4472	56.67
		0.660714	1.7978	26	0.4472	−56.67
$\mathit{\Gamma} = 0.09414$	$\overline{x} = 0.25$	0.053571	0.1563	2	0.1396	−25.38
		0.553571	1.6148	22	−0.1396	25.38
	$\overline{x} = 0.5$	0.357143	1.0418	14	0.2635	−41.85
		0.857143	2.5003	34	−0.2635	41.85
	$\overline{x} = 0.75$	0.160714	0.4688	6	−0.3578	50.57
		0.660714	1.9273	26	0.3578	−50.57
$\mathit{\Gamma} = 0.14120$	$\overline{x} = 0.25$	0.035256	0.1130	1	0.1253	−23.98
		0.535256	1.7150	21	−0.1253	23.98
	$\overline{x} = 0.5$	0.320513	1.0269	12	0.2445	−40.96
		0.820513	2.6289	32	−0.2445	40.96
	$\overline{x} = 0.75$	0.105769	0.3389	4	−0.3518	51.31
		0.605769	1.9409	24	0.3518	−51.31

Since empirical, quasi-static estimations for overall frictional drag were considered, Potts (2015) defined a Reynolds number using the centerline length, L_r, as a fixed reference length and the *design* swimming speed $U_{o,d}$ as the fixed reference velocity:

$$\mathrm{Re_L} = \frac{U_{o,d} L_r}{\nu} = 292{,}898 \tag{6.6}$$

This was used for evaluating empirical frictional drag formulae, e.g. the ITTC-1957 skin friction line, and was satisfactory given that the robot's aftward wake field was of interest for a single design speed. However, it proves insufficient for the present analysis. It is more desirable to characterize flow properties local to an axial cross-section. For this, a local Reynolds number with dimensional x length scale is used

$$\mathrm{Re_x} = \frac{U_o x}{\nu} \tag{6.7}$$

along with Keulegan–Carpenter numbers analogous to those defined in the previous chapter. All of these numbers are summarized in Table 6.3. Equations (6.3) and (6.5) were employed to determine sectional transverse velocities for evaluating the ratio of $\mathrm{K_C}$:

$$\mathrm{K_C} = \frac{h_t(x,t)T}{D_r} \tag{6.8}$$

Here, t is the corresponding value taken from the dimensional time column of Table 6.2, and T is from Table 6.1.

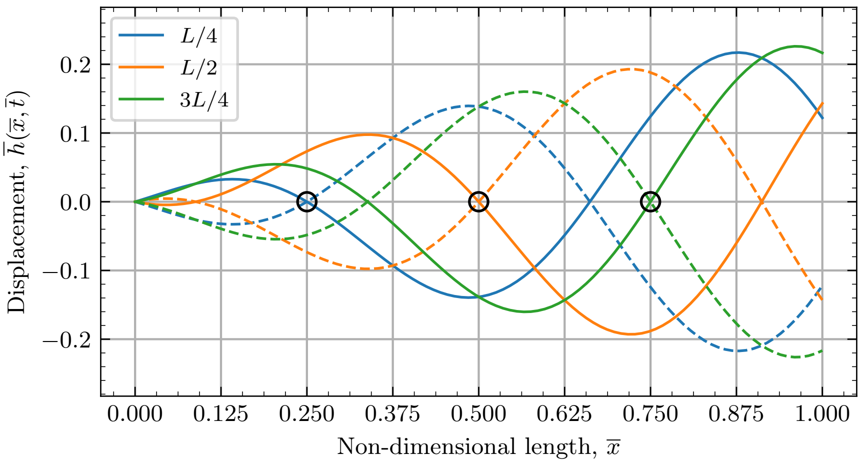

Figure 6.6: Transverse velocities for ideal motion at the instant when each of the three cross-sections ($L/4$, $L/2$, $3L/4$) pass through the vertical centerplane

Table 6.3: Reynolds and Keulegan–Carpenter numbers for robotic eel experiment runs

		$\mathrm{Re_x}$			$\mathrm{K_C}$
		0.16 m/s	0.25 m/s	0.4 m/s	—
$\Gamma = 0.11767$	$L/4$	34,147	53,355	85,368	8.550
	$L/2$	68,294	106,710	170,736	16.145
	$3L/4$	102,442	160,065	256,104	21.925
$\Gamma = 0.09414$	$L/4$	36,606	57,197	91,516	7.337
	$L/2$	73,213	114,395	183,032	13.849
	$3L/4$	109,819	171,592	274,548	18.805
$\Gamma = 0.14120$	$L/4$	36,185	56,539	90,462	7.234
	$L/2$	72,370	113,077	180,924	14.115
	$3L/4$	108,554	169,616	271,386	20.309

6.1 Experimental Configuration

A photograph of NEELBOT in its latex rubber waterproofing skin is shown in Figure 1.1. Note the appearance caused by the flat black dye added to the liquid latex for the suppression of undesirable light scattering on the skin's surface. It is speculated that a great deal of improvement was gained thanks to the dye, but still some reflection seemed inevitable due to the laser's required, yet seemingly overwhelming, intensity. Potts (2015) painted the 3D-printed hemispherical tail segment flat black to mitigate reflection from its already matte surface into the robot's wake. Notice, in Figure 6.9, the intersection of the light sheet with the robot's latex skin. Some adverse effects, whose consequences range from minor to possibly major, were found in the PIV results because of this reflection, which will be mentioned in discussing the results.

The testing configuration for NEELBOT-1.1 was arranged identically to the setup for experiments with the cylindrical test article. See Figure 3.3 for the stereo PIV module's placement location on the towing carriage, and see Figure 5.7 for a schematical representation of the relative positions between the test article and PIV module. A rendered 3D drawing of the experimental PIV arrangement for the robotic eel experiments is shown in Figure 6.7. The carriage rails are depicted with relevant suspension apparatuses for the robot and PIV torpedo. Photographs of NEELBOT

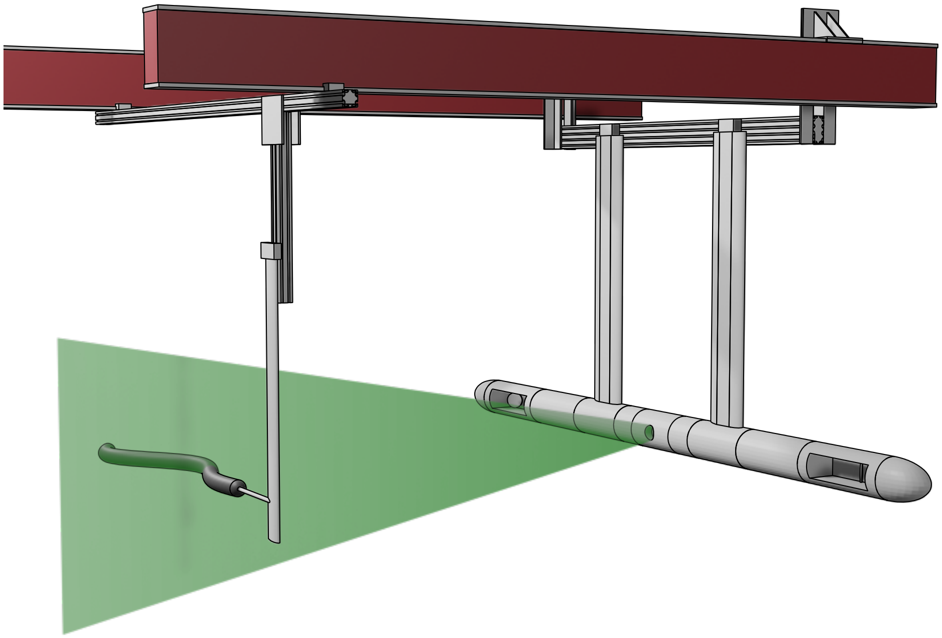

Figure 6.7: PIV configuration for robotic eel experiments

swimming in the UNO towing tank behind the vertical foil strut and tether are given in Figures 6.8–6.9. The latter figure depicts moments of laser light sheet emission collected half a period out of the robot's swimming phase. Both figures were taken for swimming motions according to round 2 parameters from Table 6.1.

Sample SPIV images for the robotic eel experiments are given in Figure 6.10 with the left camera's view shown in the left image and the right camera's view shown in the right image. Bear in mind that the images are actually mirrored horizontally due to the effect of the mirrors. The image samples were taken during a round 3 experiment at $x = 3L/4$, $U_o = 0.16\,\mathrm{m/s}$, and during the section's travel towards port (towards the PIV module). Thus the body's slope at $L/4$ was positive at this instant, and the right camera had an almost perpendicular view of the section while the left camera had a more oblique view. This is why the laser sheet's reflection on the body is wider in the right image plane. Notice that seed particles are easier to identify close to the body surface in the left image. This particular set of images was chosen as samples for the purpose of demonstrating the most egregious case of reflection in all the collected data—most of the images are better conditioned, more like those shown in Figure 5.8.

6.2 PIV Settings and Data Processing

Appropriate values for the time increment Δt used in SPIV experiments with the robotic eel were estimated in much the same way as for the oscillating cylinder. Criteria for maximum values were established based on both the forward (carriage) speed and on the local section transverse velocity at the moment of passing through the centerplane. Since the diameters of the robot and cylinder are similar, only minor changes needed to be made to the criterion based sectional transverse velocity.

The results of formula (6.2)—with reductions applied, similar to those made for the results of Equation (5.3) for the cylinder—were used to determine the governing values of Δt based on the robot's sectional transverse velocities. Again, the value of Δt as governed by sectional transverse velocity was adjusted for directional dependency on the section's motion with reductions for wake

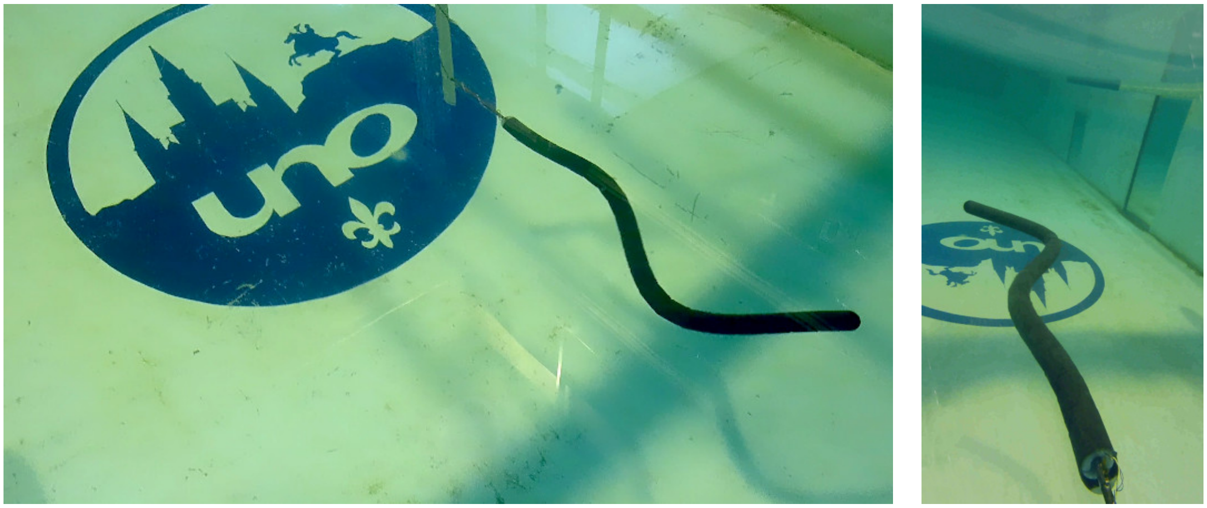

Figure 6.8: NEELBOT swimming in the UNO towing tank

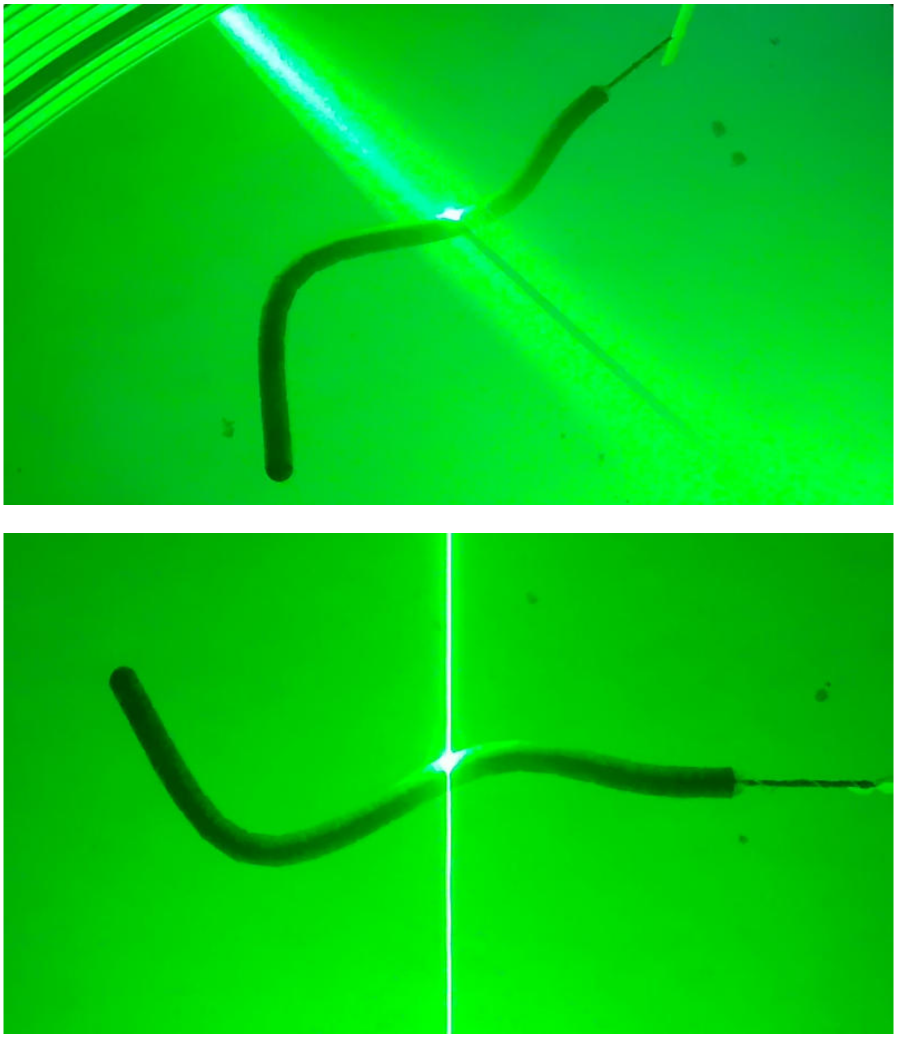

Figure 6.9: NEELBOT swimming through the laser light sheet as seen from a perspective above, behind, and on starboard side (top) and directly above (bottom)

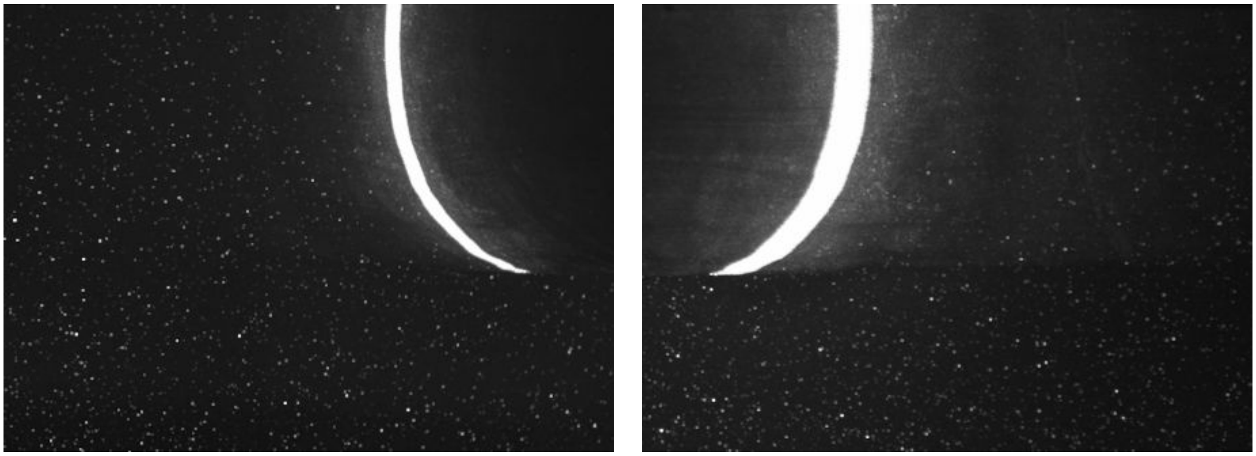

Figure 6.10: Cropped sample PIV images from robotic eel experiments (left camera view on left, right camera view on right)

Table 6.4: Δt [µs] for robotic eel experiment runs. Values given for port/stbd runs.

		0 m/s	0.16 m/s	0.25 m/s	0.4 m/s
$\Gamma = 0.11767$	$L/4$	4200/3800	3700/3700	2400/2400	1500/1500
	$L/2$	2200/1800	2200/1800	2200/1800	1500/1500
	$3L/4$	1600/1300	1600/1300	1600/1300	1500/1300
$\Gamma = 0.09414$	$L/4$	4800/4400	3700/3700	2400/2400	1500/1500
	$L/2$	2500/2100	2500/2100	2400/2100	1500/1500
	$3L/4$	2000/1600	2000/1600	2000/1600	1500/1500
$\Gamma = 0.14120$	$L/4$	5200/4800	3700/3700	2400/2400	1500/1500
	$L/2$	2700/2300	2700/2300	2400/2300	1500/1500
	$3L/4$	2000/1600	2000/1600	2000/1600	1500/1500

observation. Obviously, no changes were necessary for the criterion based on forward speed, thus those governing values are calculated as before by (5.8). See Table 6.4 for a summary of the values selected. Once again, each figure was rounded down to the nearest 100 µs for consistency and conservatism.

At the end of section 5.3 it was mentioned that the techniques developed for preparing, processing, and analyzing SPIV image and vector data from the cylinder experiments carry over almost directly to the evaluation of robotic eel data; indeed, only a few comments are needed to distinguish the procedures used here. Most significantly, three features differentiate the data:

1. The robot's body cross-section passing through the image plane is always sloped rather than parallel with the forward direction.
2. Reflection artifacts appear in some of the PIV images and may propagate malignantly into the resulting vector fields.
3. The robot's body moves minimally but perceptibly in z in the image planes, resulting in minimal data losses beneath the cross-section and requiring more careful stitching of the resulting vector fields.

Although ordered by descending prominence and consequence, each of these items had to be addressed. It was noted in section 5.3 that all raw PIV images taken of the cylindrical test article display the cross-section as an elliptical artifact with constant major and minor axis dimensions and that this was due to the cylinder's always being parallel with x at the moment of image capture. Though the data collection location did not change when swapping test articles, the cross-section no longer appears with constant elliptical shape properties requiring customized image masking and more general methodologies for analyzing vector fields.

Clearly, the cylinder body cross-section appears in resulting PIV vector fields as a circle; this is what one would expect as in Figure 5.6. However, the robot's cross-section is elliptical even in the resulting vector fields due to its orientation at the moment of image capture. The exact predicted body slope may be calculated by differentiating the equation for transverse offsets (2.41) with respect to $\overline{x}$:

$$\overline{h}_{\overline{x}}(\overline{x},\overline{t}) = \frac{\partial \overline{h}(\overline{x},\overline{t})}{\partial \overline{x}} = 2\pi \mathit{\Gamma} \left[\frac{1}{U} \cos\left(2\pi \left(\frac{\overline{x}}{U} - \overline{t} \right) \right) - \cos\big(2\pi (\overline{x} - \overline{t}) \big) \right] \tag{6.9}$$

This is plotted along with transverse displacement and velocity in Figure 6.5. Then, the slope may be calculated as an angle in radians according to

$$\vartheta(\overline{x},\overline{t}) = \arctan\big(\overline{h}_{\overline{x}}(\overline{x},\overline{t}) \big) \tag{6.10}$$

Note that ϑ represents the angle between the robot's body at any location $x = \overline{x}L$ and the $\overline{x}$-axis—this is not the same as the relative angles used for programming the servos. Relevant values pertaining to these experiments are provided in Table 6.2. These angles are useful in making corrections to the equally spaced radial trajectories along which the velocity field is evaluated to analyze velocity profiles. The expected inclination is used to quantify the *oblateness* or *ellipticity* of the apparent cross-section. Since no vertical inclination occurs, the semi-minor axis, b, of the ellipse will remain equal with the robot body radius, r_o, but lateral angles generate scaling in y according to $1/\cos(\vartheta) = \sec(\vartheta)$ such that $a = r_o \sec(\vartheta)$. The semi-minor and semi-major axis dimensions permit the calculation of the inclined cross-section's radius at any angular value φ as

$$r_{o,\,\mathrm{inc}}(\varphi) = \frac{ab}{\sqrt{b^2 \cos^2(\varphi) + a^2 \sin^2(\varphi)}} \tag{6.11}$$

These radial offsets are subtracted from the profiles evaluated in analyzing velocity gradients at the robot's surface for estimating skin friction. An illustration depicting these radial lines extending 15 mm from an elliptical surface at 10° increments is shown in Figure 6.11. For this example, the ellipse's shape is representative of the cross-section of a cylinder inclined horizontally through the page at $\vartheta = 40°$.

Item number 2 in the above list was not approachable in data post-processing. Attenuating harmful reflective saturation was only possible as preemptive efforts in blackening the latex skin and reducing laser intensity as low as possible without losing sight of seed particles. However, item 3 was handled more readily in vector processing by identifying the cross-section's center and aligning these in adjacent vector fields when stitching. Thanks to the tether, the robot is restricted from unwanted motion in both y and z at the attachment point, i.e. the robot's head, $x = 0$. However, vertical motion error amplifies with x and becomes mildly problematic near the tail. In fact, many experimental runs were repeated to ensure sufficient data was acquired to satisfy the self-imposed requirement of having at least ten images for participation in ensemble-averaging.

6.3 Results

Only preliminary results of CFD simulations have been achieved at the time of this writing, so experimental–computational comparisons will have to made in future works—Srivastava (2020), for

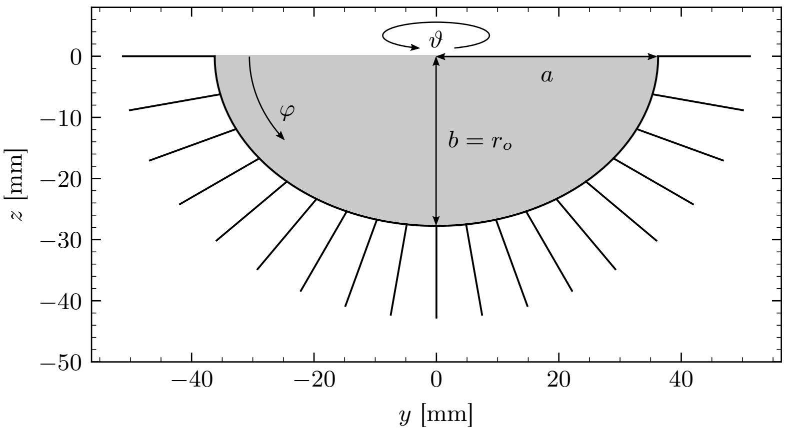

Figure 6.11: Illustration of radial lines spaced by 10° and extending 15 mm from the robot's cross-sectional surface for an example sectional inclination of $\vartheta = 40°$

example, expounds on the numerical efforts. Nonetheless, this investigation endeavors to quantify boundary layer information at particular, realizable locations for key moments in the undulation cycle to establish estimates for local wall shear stress and ultimately local frictional drag characteristics according to experimental measurements.

Similar to the cylinder, all velocities are normalized prior to ensemble-averaging according to $\mathbf{v}/|\mathbf{v}|$ using the motion amplitude as measured at the trailing edge, i.e. the robot's tail, $x = L$ (non-dimensionally, $\overline{x} = 1$), where

$$|\mathbf{v}| = \sqrt{U_o^2 + h_t(L, t)^2} \tag{6.12}$$

Here, t is the dimensional time calculated in the same manner as the times reported in Table 6.2. Note that the right hand side of (6.12) incorporates dimensional transverse velocity which is calculated according to (6.5).

Since no comparison with numerical results are yet prepared, results of these experiments may be summarized by visualizing the local near-body flow fields. Similar to the cylindrical test article, flooded velocity magnitude contours, with vectors overlaid to give a sense of planar direction and magnitude, are delivered. Figures 6.12–6.17 display these contours for each case of interest. The figures are sorted according to the rounds listed in Table 6.1 and according to increasing x and U_o, for increasing figure number and from top to bottom.

Two sample plots of longitudinal velocity profiles for the robotic eel swimming with $\mathit{\Gamma} = 0.11767$, $U_{o,d} = 0.25\,\mathrm{m/s}$, $U = 0.7$, and $U_o = 0.4\,\mathrm{m/s}$ are provided in Figure 6.18 for $L/2$ and $3L/4$. The velocities are ensemble-averaged and shown only for the first 15 mm away from the boundary in each corresponding radial direction. They are plotted for the angular positions of $\varphi \in [10°, 30°, \ldots, 170°]$. Note the general similarity of profiles with corresponding angular offset between the plots. Also note that the 70°, 90°, and 110° profiles approach external flow after only approximately 8 mm, while other profiles, notably those closer to the horizontals, do not nearly approach undisturbed outer flow with low shear within the plot bounds. Careful examination reveals that the curves at 150° and 170° are associated with the lowest shear values which agrees with intuition that detriment of the longitudinal velocity component is found to be least severe in the local section's wake.

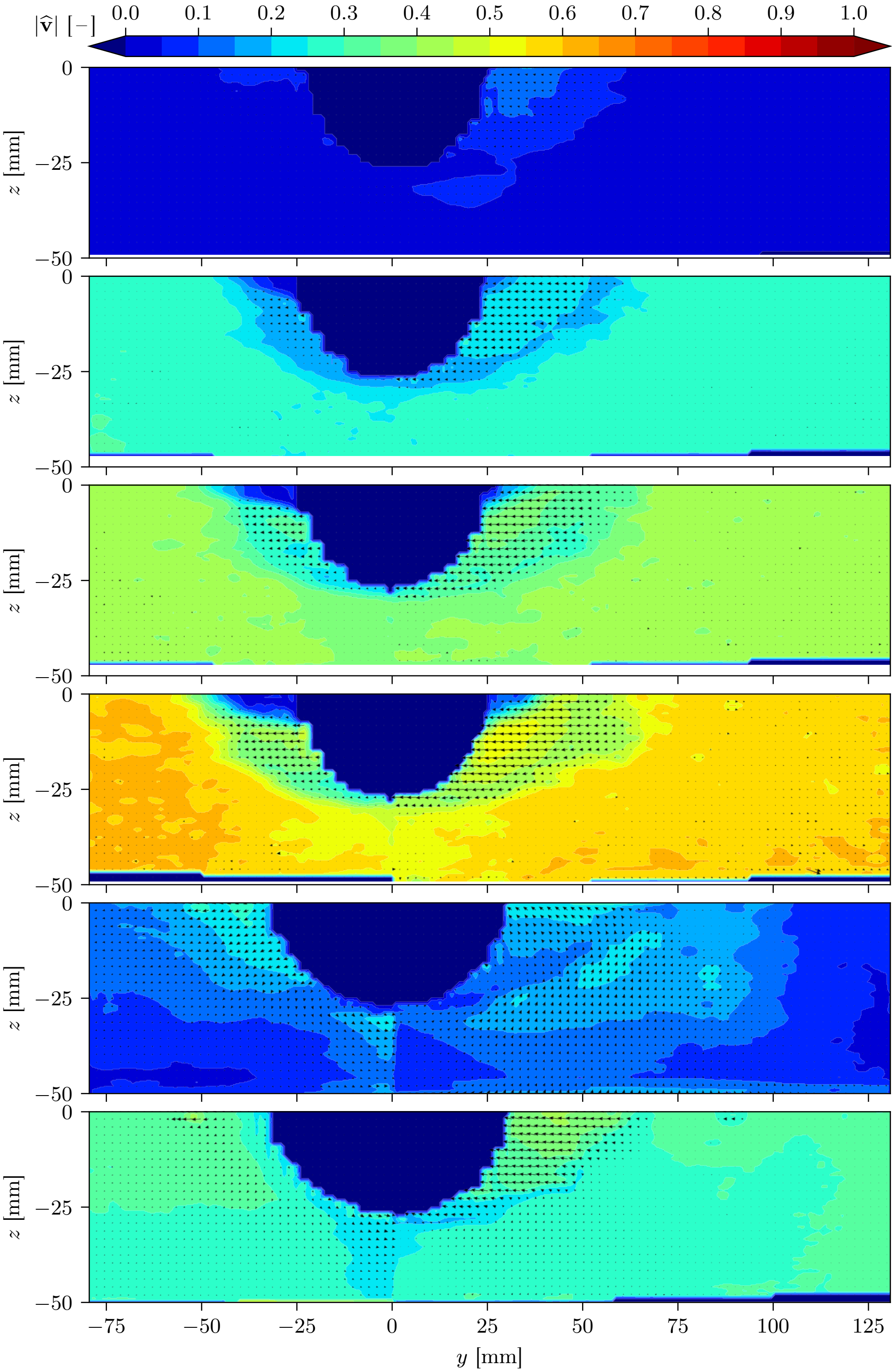

Figure 6.12: Contours of velocity magnitude with $\Gamma = 0.11767$ for (top to bottom): $x = L/4$ with $U_o = 0$, 0.16, 0.25, and 0.4 m/s; $x = L/2$ with $U_o = 0$ and 0.16 m/s

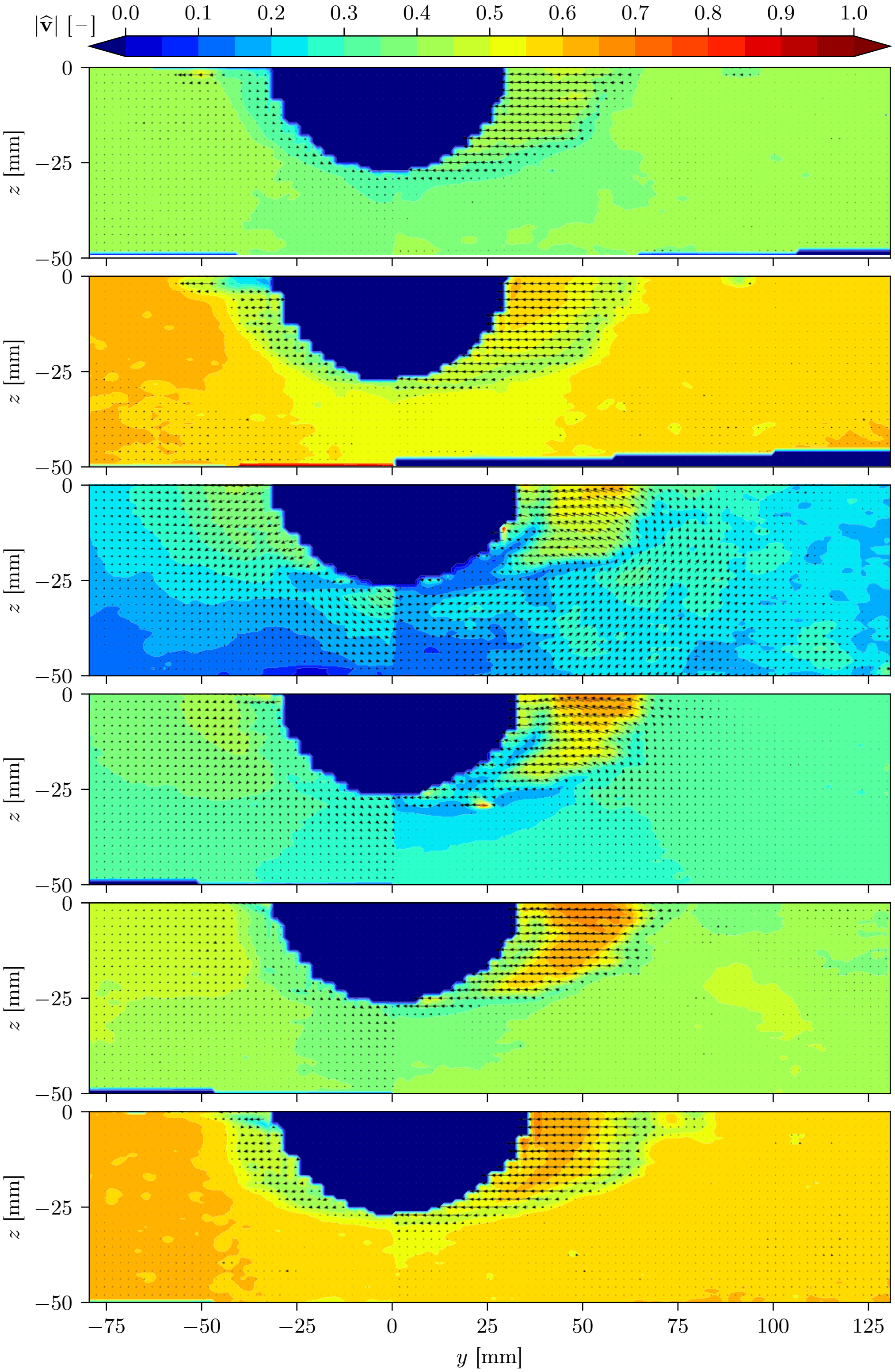

Figure 6.13: Contours of velocity magnitude with $\mathit{\Gamma} = 0.11767$ for (top to bottom): $x = L/2$ with $U_o = 0.25$ and 0.4 m/s; $x = 3L/4$ with $U_o = 0$, 0.16, 0.25, and 0.4 m/s

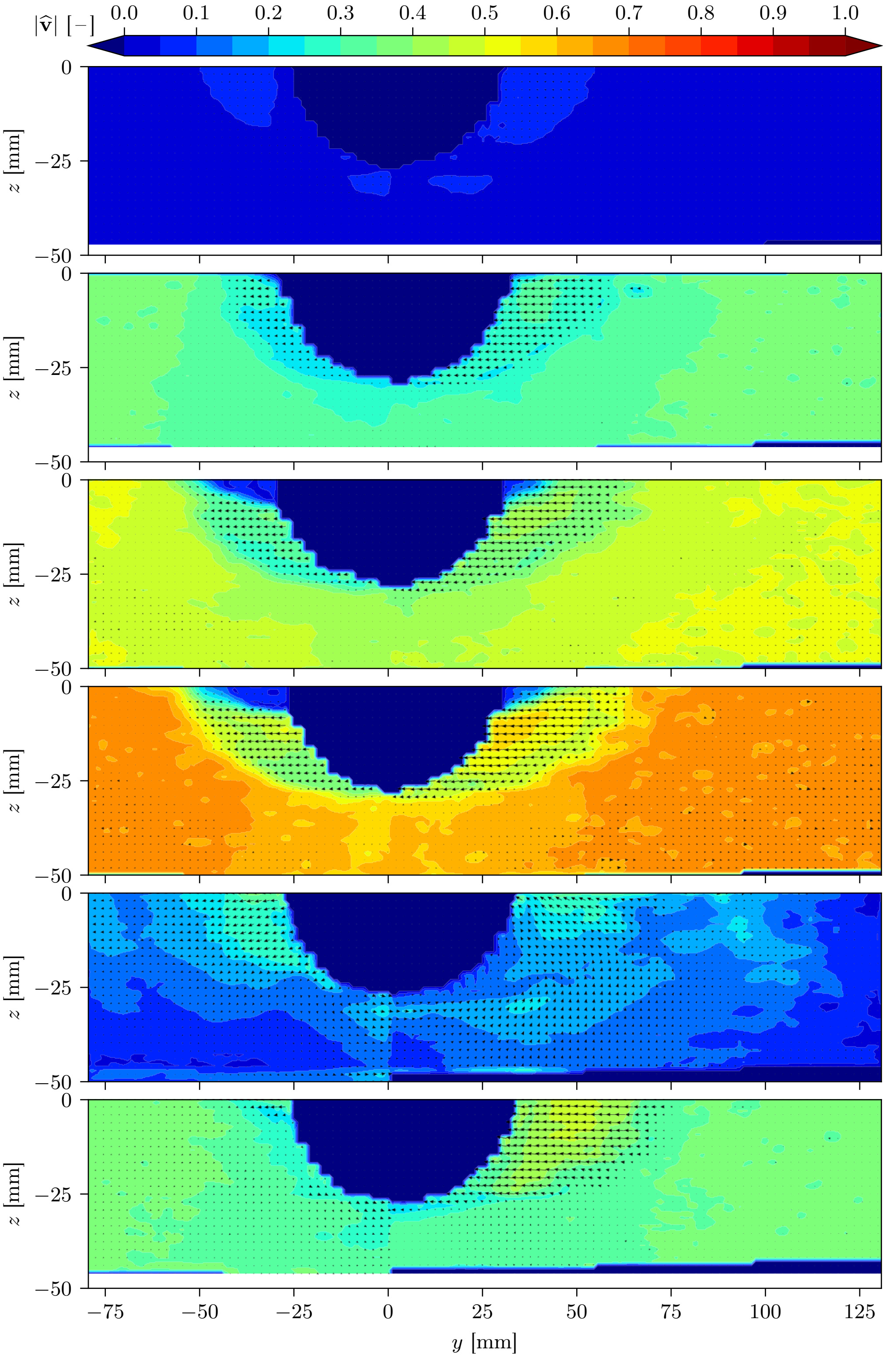

Figure 6.14: Contours of velocity magnitude with $\Gamma = 0.09414$ for (top to bottom): $x = L/4$ with $U_o = 0$, 0.16, 0.25, and 0.4 m/s; $x = L/2$ with $U_o = 0$ and 0.16 m/s

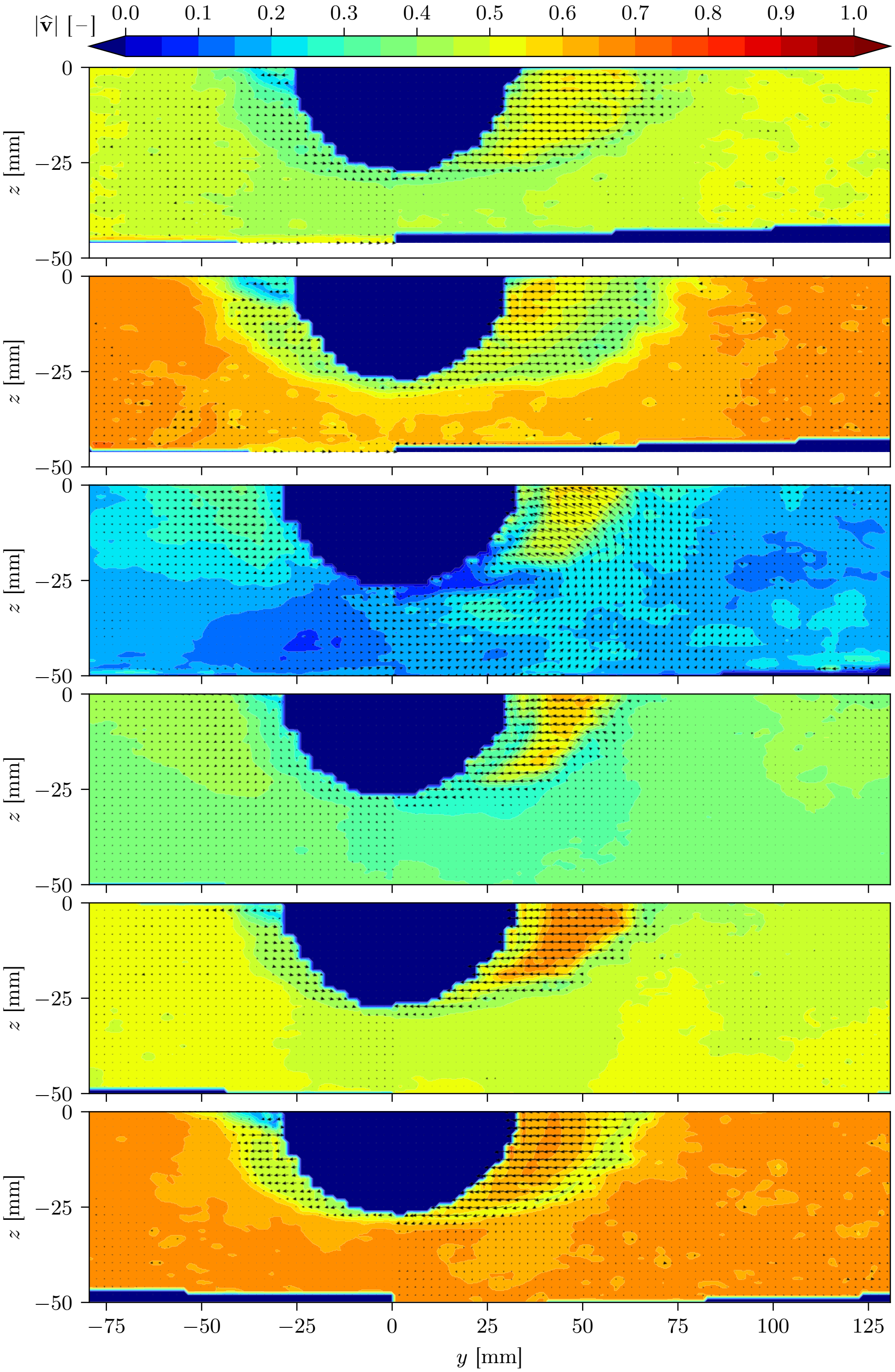

Figure 6.15: Contours of velocity magnitude with $\mathit{\Gamma} = 0.09414$ for (top to bottom): $x = L/2$ with $U_o = 0.25$ and 0.4 m/s; $x = 3L/4$ with $U_o = 0$, 0.16, 0.25, and 0.4 m/s

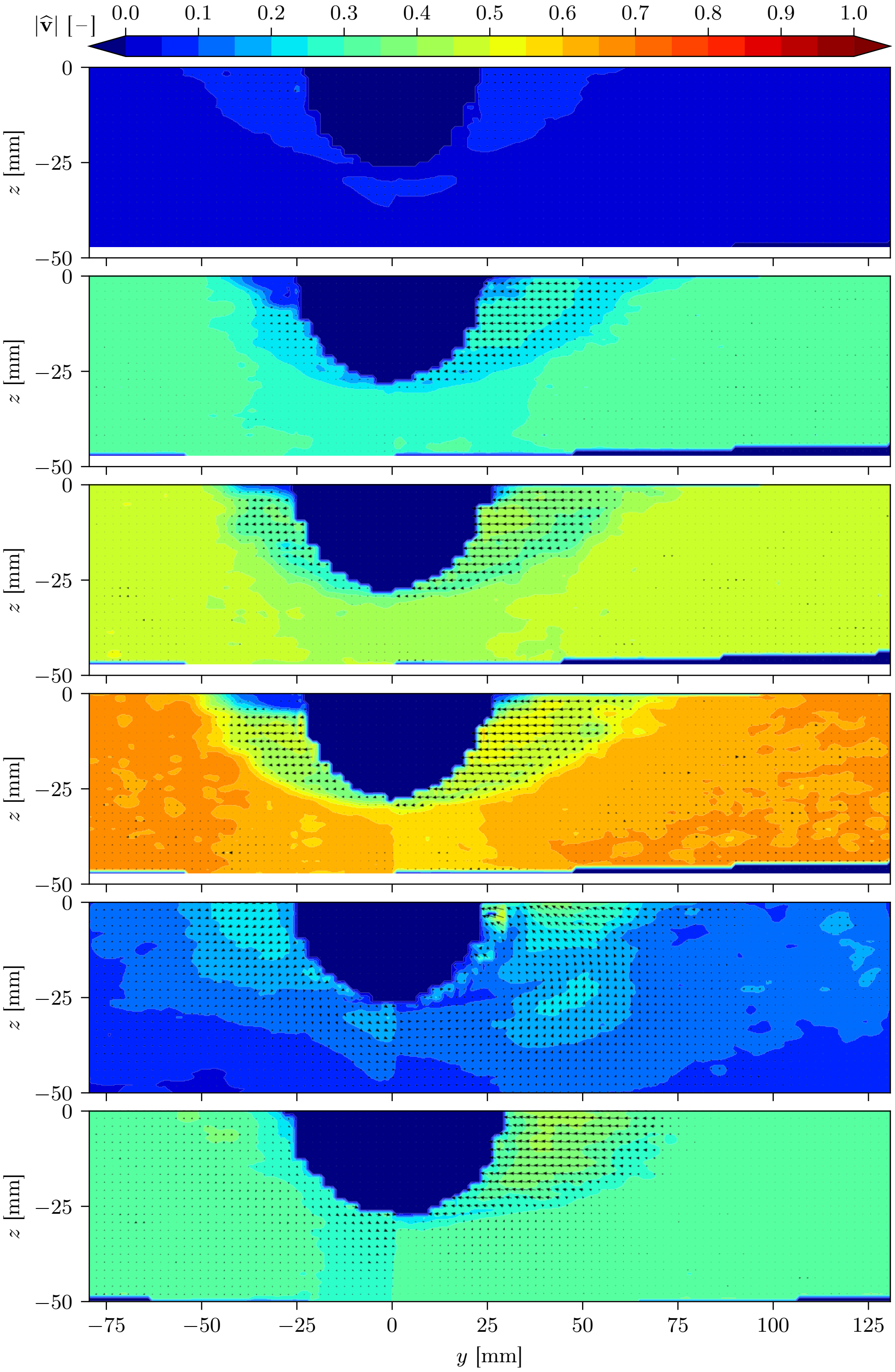

Figure 6.16: Contours of velocity magnitude with $\Gamma = 0.14120$ for (top to bottom): $x = L/4$ with $U_o = 0$, 0.16, 0.25, and 0.4 m/s; $x = L/2$ with $U_o = 0$ and 0.16 m/s

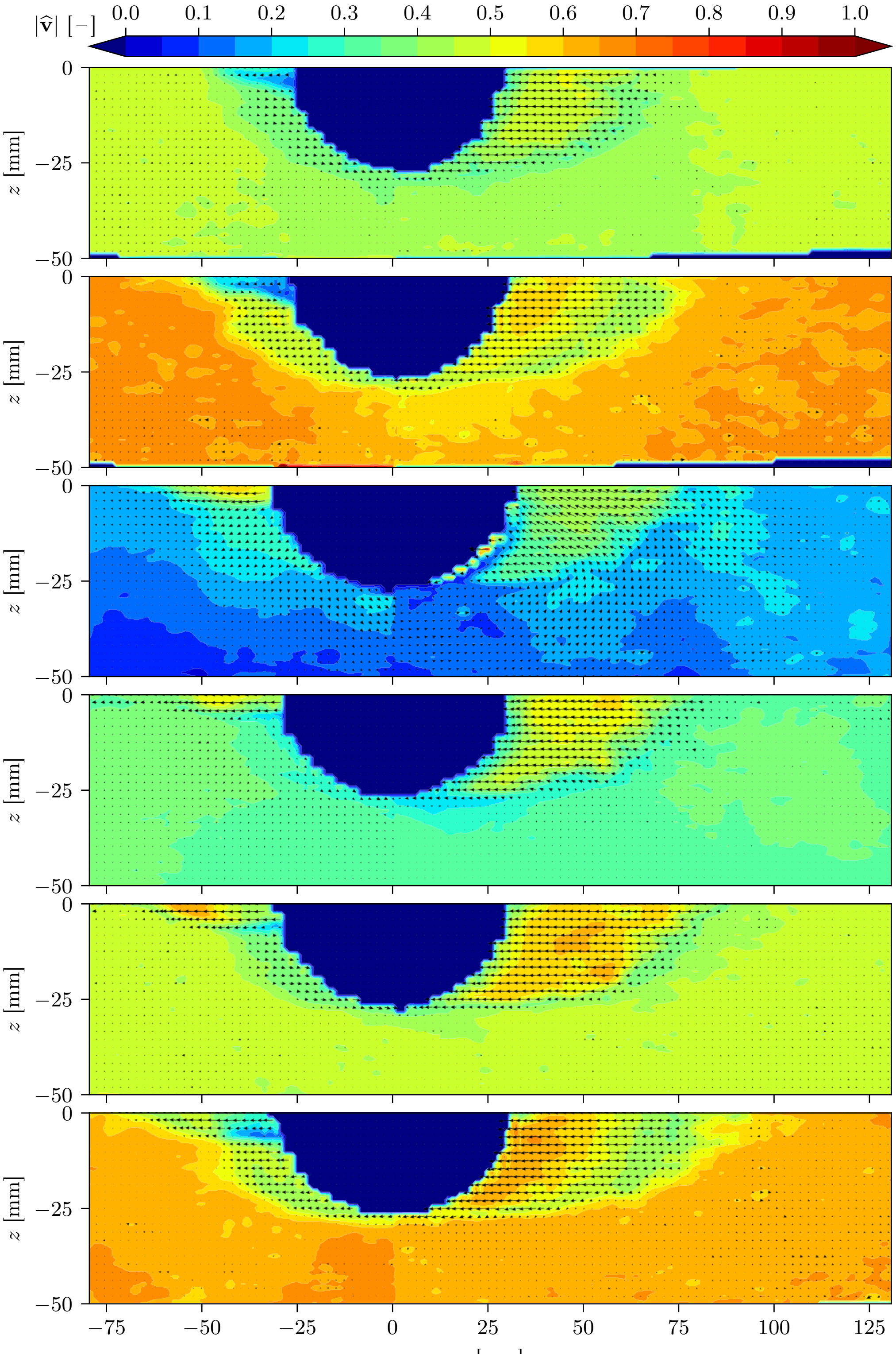

Figure 6.17: Contours of velocity magnitude with $\Gamma = 0.14120$ for (top to bottom): $x = L/2$ with $U_o = 0.25$ and 0.4 m/s; $x = 3L/4$ with $U_o = 0$, 0.16, 0.25, and 0.4 m/s

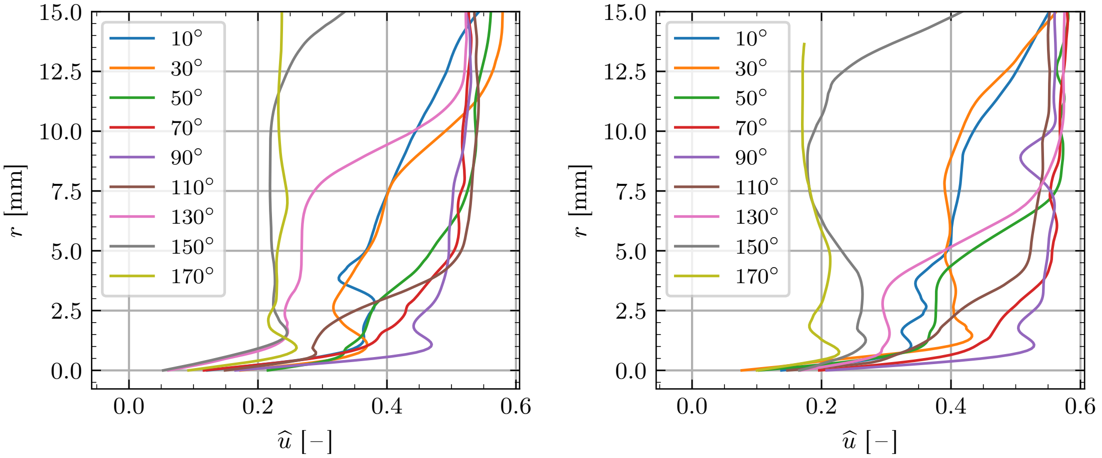

Figure 6.18: Radial profiles of axial velocity for the robotic eel swimming with $\mathit{\Gamma} = 0.11767$, $U_{o,d} = 0.25\,\mathrm{m/s}$, $U = 0.7$, and $U_o = 0.4\,\mathrm{m/s}$ at $L/2$ and $3L/4$

6.4 Discussion

Evaluation of skin friction at the measurement locations of interest remains to be addressed. Determination of local wall shear stress is crucial in calculating local skin friction coefficients, and the method used here is similar to the one used in chapter 5 with some key differences:

- Normal wall velocity gradients were no longer estimated using purely tangential flow components which would need to be calculated as a function of the slope, ϑ, Equation (6.10), of the body cross-section intersecting the plane of the light sheet at $y = 0$. Instead, the gradients were calculated using only the longitudinal flow component, $\widehat{u}$ (only $\widehat{u}$ was used for the cylinder as well, but in that case, it *was* the tangential component), to maintain that forces against the direction of motion are being analyzed without contributions from lateral accelerations.
- Radial offsets were calculated according to Equation (6.11) to compensate for ellipticity in interpolating along radial lines to determine fluid shear stress at the boundary.
- Least-squares linear fitting was no longer used to determine the slope of the velocity profile at the boundary. Instead, a univariate spline with a very small smoothing factor (1×10^{-6}, almost no smoothing—only to dampen potentially erroneous, outlier points) was employed for approximately the first 2 mm normal to the boundary.

It is also important to indicate that interpolation along lines *normal* to the boundary is not actually possible due to the body inclination angles φ. Technically, the radial lines should also be inclined, but the laser light sheet does not move to maintain normal intersection to allow this. Potential underestimations could culminate from this error, but any such consideration would only be necessary where inclination angles are large, i.e. near the tail. Still, scaling shear estimates by $\sec(\vartheta)$ makes insufficient differences to naïvely implement this correction.

Table 6.5 provides a summary of the estimated skin friction coefficients for the robotic eel which were calculated according to

$$C_f = \frac{\tau_\mathrm{w}}{\frac{1}{2}\rho U_{o,d}^2} \tag{6.13}$$

where $U_{o,d}$ is the fixed design velocity despite the fact that calculations are made for a variety of carriage speeds. This was done to alleviate the blowup arising for $U_o = 0\,\mathrm{m/s}$ and to scale the

Table 6.5: Skin friction estimates, C_f $[10^{-3}]$, for the robotic eel at each measurement location and for each swimming condition

		0 m/s	0.16 m/s	0.25 m/s	0.4 m/s
$\Gamma = 0.11767$	$L/4$	-0.064	2.326	3.517	5.839
	$L/2$	-0.465	3.049	4.934	7.642
	$3L/4$	0.025	2.845	4.806	7.834
$\Gamma = 0.09414$	$L/4$	-0.046	2.863	4.029	6.536
	$L/2$	0.122	3.122	4.384	6.771
	$3L/4$	0.417	3.609	5.386	8.363
$\Gamma = 0.14120$	$L/4$	0.041	2.603	4.415	6.569
	$L/2$	0.118	3.316	4.275	7.037
	$3L/4$	0.585	2.966	4.551	7.857

coefficients for comparison with towing at the design speed. Recall that this was done analogously for the oscillating cylinder in chapter 5. Careful comparison between operating and flow conditions for the cylindrical and robotic test articles appears to indicate that approximately 10–15% increases in C_f are observed for the robot over similar conditions for the cylinder. A number of physical factors could influence this augmentation, including surface inconsistencies for the robot and differences in oscillatory behavior within the boundary layer caused by undulatory boundary motion.

More specific observations are also warranted. Relatively small local coefficients are estimated for zero speed results which is consistent with the intuition that no drag should be experienced for no advancement. Rather, ideally, purely thrust should be generated leading to negative skin friction coefficients—this appears in four cases, yet still they manifest in low magnitude. Some observations for the design case of $\Gamma = 0.11767$:

- Negative friction coefficients appear at $L/4$ and $L/2$ for stalled speed, indicating that purely thrust is generated locally.
- Positive drag at $3L/4$ indicates that water is being accelerated partially aftward from action forward of the plane—thrust, at design speed, should be generated purely from lateral fluid accelerations.

For off-design cases ($\Gamma \neq 0.11767$):

- At design speed, C_f is higher at $3L/4$ than at $L/4$ and $L/2$. This is contrary to typical laminar boundary layer behavior—this was seen similarly for the oscillating cylinder and could lend toward support for either of the following conclusions:
    - The boundary layer may be exhibiting transitional behavior aft of $L/2$ causing wall shear stresses to increase.
    - While remaining completely laminar, boundary layer thinning may occur due to rapid lateral fluid displacement, which would appear to affirm the Bone–Lighthill drag augmentation hypothesis.

Not enough data has been collected to conclusively confirm either of the latter statements regarding increases in skin friction coefficients along x. The boundary layer certainly exhibits characteristics of unsteady flow processes and diffused disturbances. Rather than emitting vortical structures into the local sectional wake, apparently linear transverse accelerations are observed indicating almost "gliding" action which is contradictory to Lighthill's 1971 hypothesis. Still, the thinning concept makes no requirement on turbulence transition or vortex shedding. Laminar boundary layers are

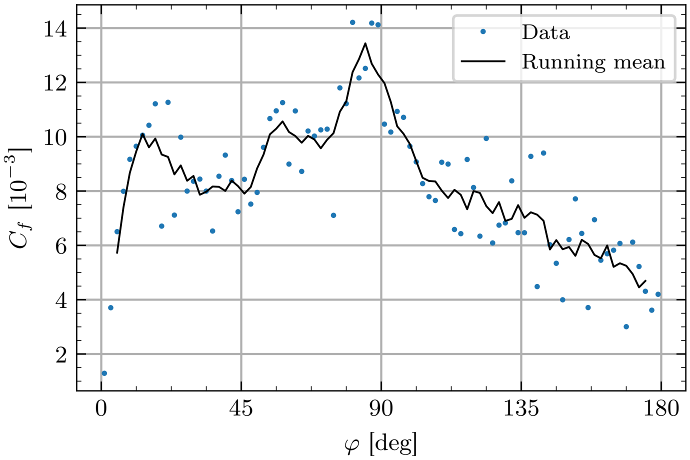

Figure 6.19: Sample plot of C_f versus φ for the robot at $x = 3L/4$ for $\mathit{\Gamma} = 0.11767$ and $U_o = 0.25\,\mathrm{m/s}$. The data is smoothed with a running mean using a moving window of 8° width (5 data points spaced at 2°).

typically associated with lower wall shear stress than their turbulent counterpart, and the absence of obvious circulation agrees with the ideal swimming theory (Vorus and Taravella, 2011).

Examination of the transverse plane flow fields in Figures 6.12–6.17 indicates that no boundary layer separation occurs, probably due in part to the oscillatory nature of the undulation wave and flow components manifesting intermittently normal to the boundary. Anderson, McGillis, and Grosenbaugh (2001) likewise observed no flow separation for the anguilliform swimmers. Furthermore, no obvious turbulence transition appears to arise near the robot which supports the thin boundary layer requirement of the wakeless swimming theory.

Comparing the data of Table 6.5 with the results given for the oscillating cylindrical test article in Table 5.6 and keeping in mind comparable transverse translation speeds and especially Keulegan–Carpenter numbers using Tables 5.2 and 6.3, one observes remarkable similarity between the estimates of skin friction. Differences in oscillation mode and frequency appear to have less of an effect than anticipated. In fact, for the critical towing speed of $U_o = 0.16\,\mathrm{m/s}$, almost negligible differences are found between rounds of changing motion amplitude, $\mathit{\Gamma}$. In some regard, this could be desirable, considering the hopeful increases in thrust capabilities for increasing amplitude.

Flow disturbances on the robot's underside near $\varphi = 90°$ are consistently very small. This was analogously seen in measurements taken on the transversely oscillating cylinder; note the relatively minor gradients apparent in the 90° profiles shown in Figures 5.29, 5.30, and 6.18. Transverse flow components beneath the robot are generally much smaller than those beside it. The dramatic spike in C_f at $\varphi = 90°$, corresponding to the vertical profile directly beneath the robot's body, shown in Figure 6.19 corroborates this observation. The plot qualitatively illustrates the general distribution of C_f over the cross-sectional surface with $\varphi = 0°$ representing the upstream side. Greater skin friction on the upstream side confirms periodic boundary layer thinning due to transverse translation.

Adverse effects of the aforementioned reflection artifacts are not obviously identifiable in Figures 6.12–6.17, assuming that the high fluid velocities downstream are attributed to acceleration of the robot's local added mass as predicted by Vorus and Taravella (2011). The PIV algorithms used to compute these results did not complain of any difficulties in resolving particle displacements near the boundary. Consistently high "good vector" percentages (generally, at least 95% good vectors and less than 5% interpolated vectors) were achieved. The only way to confidently verify that the robot's skin reflection is not saturating the near-body velocity vectors would be to manually identify and track particles in the stereo image pairs for confirmation of the PIV algorithms.

Difficulties were experienced by Anderson, McGillis, and Grosenbaugh (2001) in resolving displacements of near-boundary particles using automated PIV which is why they resorted to the more direct, yet immensely more tedious, method of PTV, whereby locations of individual particles are manually identified in pairs of images, in order to resolve those displacements. Undoubtedly, some improvement would be managed by individually analyzing the thousands of image pairs collected for this research and tracking the scores or even hundreds of particles appearing near the body surface in each pair. Time constraints and personnel limitations prevent the investment of required man-hours to do this analysis. However, leaving alone the better-conditioned results in favor of addressing the more ill-conditioned images may be sorted out in reasonably little time. Special effort may also be considered for verifying a single case to compare most closely with the predictions of numerical simulations. These ideas were conceived with too little time to be included in the present work, but they may serve as a starting point for additional analysis of the current data.

7 Concluding Remarks

Boundary layer information local to three longitudinal positions, i.e. $L/4$, $L/2$, and $3L/4$, has been characterized for NEELBOT-1.1 via analysis of stereo PIV data for key moments in the undulation cycle and for numerous combinations of swimming conditions and motion parameters, ideal and non-ideal. Skin friction coefficients were subsequently estimated for magnitude relative to the dynamic pressure associated with operation at the design swimming speed of $U_o = 0.25\,\mathrm{m/s}$. Estimates were correlated with measurements made for an oscillating and non-oscillating cylindrical test article that were benchmarked by initial mono PIV analysis of steady laminar flow over a flat plate at zero incidence which was tested while stationary and oscillating in its own plane. Approximately 10–15% increases in C_f are observed for the undulating robot over similar conditions for the oscillating cylinder. However, time-mean frictional drag for the robot—the principal target of this research project—is not yet measured. The results of this thesis will be used in validation of the numerical analysis performed in parallel with this research which will endeavor to decompose the robot's overall drag into its frictional and form components and to determine whether the robot can produce enough thrust to overcome its drag without simultaneously increasing it beyond realizable thrust generation capabilities. No other data is yet provided in the literature for comparison with the possible exception of (Anderson, McGillis, and Grosenbaugh, 2001) who studied live animals and were primarily interested in determining whether skin friction while swimming is higher than rigid body drag and whether the fish have any level of "hydrodynamic sensing" by which they can adapt their movements to minimize frictional and wake drag.

7.1 Lessons Learned

Analysis of the experimental flat plate data led to the development of image and vector processing techniques for use in boundary layer investigations and estimation methods for local skin friction. These tools came in handy for use in more general coordinate systems and for more complex unsteady scenarios. Comparisons with Blasius solution data in the flat plate analysis and Seban–Bond–Kelly predictions in the cylinder analysis guided the development of data processing. Plotting horizontal velocity profiles from the oscillating plate data before and after implementing ensemble-averaging greatly established the value of properly analyzing time-sensitive flow structures.

A major question of interest motivating this project was whether vortex shedding or flow separation may be readily observed for the robot operating at design and off-design conditions. Careful examination of the robot's flow fields depicted in Figures 6.12–6.17 and comparing them with similar results from the cylindrical test article shown in Figures 5.12–5.17 informs the conjecture that the undulating propulsor's near-body fluid does not receive strong circulation from non-ideal action of the robot's undulatory motion, barring the exception of vorticity due to linear shear within the boundary layer. Far less disturbance is noticeable in the swimmer's velocity fields. Contours of velocity magnitude at $x = 3L/4$ and radial profiles plotted at and adjacent to $\varphi = 90°$ in Figure 6.18 indicate relatively sharp gradients near the boundary layer's edge on the underside of the robot, and this could be indicative of incipient vortex shedding, though no substantial evidence is obvious. While preliminary and inconclusive, this hypothesis of vortex shedding avoidance and disturbance abatement suggests the significant benefit of minimal kinetic energy losses to near-body circulation production. Potts (2015) observed wake circulation for off-design scenarios, but this may be produced by strong trailing edge effects and disturbances which intensify with aftward propagation. Further analysis should be done near the robot's tail to substantiate this claim.

Skin friction coefficients pertaining to the robot being towed at the highest tested forward speed are smaller than those experienced by the steadily advancing cylinder. This was expected, considering that C_f was estimated for the non-oscillating cylinder using its true advance speed rather than a fixed velocity. This naturally scales friction coefficients corresponding to different carriage speeds accordingly. Nevertheless, potential loss of information in the very near-body regions of fluid could also influence these reductions. Since some laser light reflection was unfortunately unavoidable, some particles may have been lost in the PIV image processing algorithms of Insight 4G, and therefore some of the highest velocity gradients adjacent to the eel's skin may be underestimated.

Overall, considering different body radii and flow conditions, good agreement is found between C_f estimates for the oscillating cylinder (Table 5.6) and robot (Table 6.5). In light of the inability to analyze velocity profiles along lines exactly perpendicular to the body surface, C_f values predicted especially at $3L/4$ may be underestimated and should be considered in comparing the data. Furthermore, other physical attributes of the robot might contribute to these discrepancies. Its segmented structure coupled with the water's hydrostatic pressure causes depressions or indentations in the skin, especially at large relative angular displacements between segments. These periodic boundary fluctuations could disrupt the boundary layer in unpredictable ways. Additionally, the robot is towed by means of a tether attached between its head, or leading edge, and a foil-shaped vertical strut protruding down from the carriage, whereas the cylinder is supported by two cylindrical struts affixed well aft of the leading edge. Differences in surface material between the two test articles, i,e. finely polished acrylic for the cylinder and tacky latex rubber for the robot, could lend toward different interactions with the water and produce modified shear stresses for identical flow conditions. It has been proposed to reproduce certain tests with the same cylinder covered by latex to examine possible discrepancies. Finally, analysis of end effects has been neglected in the present study. Flow disturbances due exclusively to the test articles' hemispherical endcaps may possibly be mitigated with hydrodynamic shape optimization. Perhaps future numerical (and even experimental) investigations will incorporate some parametric analysis including endcap adjustments.

One of the assumptions upon which the ideal theory relies (Vorus and Taravella, 2011) is that the anguilliform swimmer's boundary layer remain thin and laminar throughout the undulation cycle. Although no measurements were taken aft of $3L/4$, no transition obviously occurs for the cases studied herein. Additionally, Potts (2015) makes no mention of observing turbulent structures in the robot's wake field which supports the speculation that no transition ensues even beyond $3L/4$. This important clarification could have crucial implications for modeling the situation numerically.

Ratios of thrust power production to rates of energy consumption appear to be unfortunately low. The working principle of accelerating added mass laterally, i.e. inputting kinetic energy into the fluid in a direction not opposite that of the desired motion, is due to the reliance upon second order lift generation for thrust and results in high efficiency in an ideal world. Experimental observations suggest that even with vortical wake cancellation, viscous effects, which are not treated by the theory, have too great an impact to permit achieving desired swimming speeds. The prodigious energy expenditures seemingly overwhelm the achievable thrust. However, these dismal conclusions will only be further supported or contradicted by comparisons with numerical simulations.

7.2 Call to Future Work

Improvements to the cylinder and robotic eel experiments would certainly be made with the incorporation of volumetric PIV (V3V). The primary benefit of the volumetric PIV upgrade over the current stereoscopic PIV arrangement is that the expanded system is able to measure three components of velocity in a volume. With the current SPIV arrangement, analysis is limited to measuring three-dimensional velocity components in a two-dimensional plane. Therefore, tests and recordings have to be taken at multiple planes and the velocity profiles have to be "stitched" together in order to approximate the flow characteristics within a volume. This becomes immensely tedious for unsteady flows and introduces numerous opportunities for errors in mapping the velocity components. With the proposed V3V system these errors can be eliminated by measuring the velocity components within the volume of interest with a single test, and no assumptions of compatibility and correlation have to be made. Additionally, interpolation along truly normal radial lines for inclined cylindrical test articles would be possible with the introduction of the third spatial dimension into the measured velocity fields.

Stitching planes of fluid displacement information in a time-dependent scenario requires sensitive timing and assumptions of repeatability. Using SPIV to study the cylindrical test article and the robotic eel, object planes oriented transversely to the direction of motion are collected as shown in Figures 5.2 and 6.7. Each test article must be physically moved longitudinally relative to the cameras and light sheet between runs to obtain a distribution of velocity data (hence the 80/20 slotted aluminum channel spanning the carriage rails used to suspend the robot). Since the motion is periodic, it is crucial to synchronize the grabbed frames to correspond with equivalent time steps of the period. This is possible, however a volumetric PIV system would eliminate this cumbersome work.

Assumptions of repeatability likely introduce significant levels of experimental uncertainty when stitching vector fields collected during different runs. Even if timing can be accurately achieved within microseconds of identical correspondence, the robot's motions physically cannot be exactly replicated for every experiment, due in part to battery drainage and the strongly time-dependent nature of the unsteady flow problem. The number of stitched vector fields for satisfactory distribution yields the minimum number of required runs to obtain the desired distributed data. This number of repetitions and the time required would be reduced greatly with V3V, and a much greater resolution of longitudinal distribution would also be possible.

Increasing camera resolution, to perhaps 25 MP which would be a tremendous improvement upon the 4 MP cameras used presently, would enable one to better characterize delicate boundary layer information and to do so with a larger field of view. Significantly more pixels would be available for capturing individual seed particles allowing greater seeding densities and increased magnification. Enhanced resolution could generate better opportunity for domain decomposition of the boundary layer into individual layers for spatial or even temporal characterization. This advanced level of analysis may possibly be approached by employing Fourier or wavelet transforms.

In the event that V3V will not soon become available, additional experiments with both the cylindrical test article and the robotic eel should be performed even with the current SPIV system at different longitudinal locations, especially closer to the leading and trailing edges. Good agreement was found between experimental and numerical estimations of skin friction near the cylinder's midsection, but better boundary layer characterization is required to determine more specific influences of end effects. This information would provide more data for comparison with the robot, which should be tested at analogous locations. Experimental measurements may also be taken for the same motions described earlier but at different steps of the undulation cycle. For the present work, only moments corresponding to zero transverse offsets were investigated, but better characterization of the cycle would substantiate numerical validation.

Numerical simulations of the various swimming conditions tested herein are ongoing and will deliver the information necessary for developing a formulation to predict the overall viscous drag experienced by the robot. Results from the numerical and experimental studies will be thoroughly analyzed and cross-examined for verification. Comparisons will be made for all of the data presented in this paper, and additional conditions will subsequently be simulated to adequately delineate thrust generation capabilities of the robot and to determine whether the robot is able to sufficiently overcome its overall resistance. The numerical data will need to be analyzed over the entire undulation period to fully characterize the unsteady skin friction and ultimately the viscous resistance.

Perhaps future work will also be performed to test lower Reynolds numbers associated with flow over a flat plate at zero incidence for which greater boundary layer thicknesses will be observed. This would hopefully include improvements in spatial resolution and measurements taken at locations further downstream (physically) where leading edge effects are more negligible. Other improvements may include the use of a larger flow channel (increases in length and depth would be of particular interest), better flow straightening, and direct pressure measurements for stream-wise pressure gradient characterization.

Further analysis may also be performed with regard to the oscillating cylinder to determine estimates of local friction coefficients for forward speed and transverse amplitude and period equal to those programmed for the robot at corresponding locations, $\overline{x}$. Characterizing angular dependency of the wall shear stress could lead to confirming the boundary layer thinning hypothesis, assuming the local upstream surface of the cross-section of interest would manifest substantial increases in shear with decreases appearing at local downstream angles. Likely, subsequent testing would need to be executed to collect this analogous data, but it would provide desirable validation for the development of a drag prediction method for the robot at various swimming conditions.

As discussed previously in section 6.4, additional effort should be invested to better resolve particle displacements within the robot's boundary layer because of complications arising in the automated PIV routines due to near-body velocity gradients and skin reflection artifacts. Anderson, McGillis, and Grosenbaugh (2001) resorted to manual PTV for more accurate estimations of wall shear stress which is certainly a sensible alternative, especially if seeding density is low. Expectant future work will include comparisons between experimental findings and the predictions of numerical simulations, and individual particle tracking may be considered for a particular case for verification. This becomes increasingly difficult for stereo imaging, because one must ensure that the *same* particle is identified in *both* cameras' image planes. Additional calculations will be required for stereo reconstruction for each particle. The drawbacks of this level of analysis are obvious, but they may be justified by the anticipated improvements.

References

Akhavan, R., Kamm, R. D., and Shapiro, A. H. (Apr. 1991a). “An investigation of transition to turbulence in bounded oscillatory Stokes flows. Part 1. Experiments”. In: *Journal of Fluid Mechanics* 225, pp. 395–422.

Akhavan, R., Kamm, R. D., and Shapiro, A. H. (Apr. 1991b). “An investigation of transition to turbulence in bounded oscillatory Stokes flows. Part 2. Numerical simulations”. In: *Journal of Fluid Mechanics* 225, pp. 423–444.

Alefeld, G. E., Potra, F. A., and Shi, Y. (Sept. 1995). “Algorithm 748: Enclosing zeros of continuous functions”. In: *ACM Transactions on Mathematical Software* 21.3, pp. 327–344.

Allen, J. J. and Smits, A. J. (Apr. 2001). “Energy harvesting eel”. In: *Journal of Fluids and Structures* 15.3–4, pp. 629–640.

Anderson, E. J., McGillis, W. R., and Grosenbaugh, M. A. (Jan. 2001). “The boundary layer of swimming fish”. In: *Journal of Experimental Biology* 204.1, pp. 81–102.

ANSYS (2020). *Overset Mesh.* URL: `www.ansys.com/products/fluids/ansys-fluent/overset-mesh` (visited on 05/11/2020).

Bailly, C. and Comte-Bellot, G. (2015). *Turbulence.* Experimental Fluid Mechanics. Cham, Switzerland: Springer International Publishing.

Benjamin, T. B. and Ellis, A. T. (July 1966). “The collapse of cavitation bubbles and the pressures thereby produced against solid boundaries”. In: *Philosophical Transactions of the Royal Society of London.* Series A. Mathematical, Physical and Engineering Sciences 260.1110, pp. 221–240.

Bernard, P. S. (Mar. 2019). *Turbulent Fluid Flow.* John Wiley & Sons Ltd.

Blasius, P. R. H. (1908). “Grenzschichten in Flüssigkeiten mit kleiner Reibung”. In: *Zeitschrift für Mathematik und Physik* 56.1, pp. 1–37. English translation in NACA Technical Memorandum 1256.

Burgers, J. M. (1924). “The motion of a fluid in the boundary layer along a plane smooth surface”. In: *Proceedings of the First International Congress for Applied Mechanics* (Apr. 22–26, 1924). Delft, pp. 113–128.

Carling, J., Williams, T. L., and Bowtell, G. (Dec. 1998). “Self-propelled anguilliform swimming: Simultaneous solution of the two-dimensional Navier-Stokes equations and Newton’s laws of motion”. In: *Journal of Experimental Biology* 201.23, pp. 3143–3166.

Cebeci, T. and Smith, A. M. O. (1974). *Analysis of Turbulent Boundary Layers.* New York: Academic Press.

Charonko, J. J. and Vlachos, P. P. (June 2013). “Estimation of uncertainty bounds for individual particle image velocimetry measurements from cross-correlation peak ratio”. In: *Measurement Science and Technology* 24.6. Article id. 065301 (16 pp.)

Chiu, W. S. and Lienhard, J. H. (Dec. 1967). “On real fluid flow over yawed circular cylinders”. In: *Journal of Basic Engineering* 89.4, pp. 851–857.

Dryden, H. L. (1934). “Boundary layer flow near flat plates”. In: *Proceedings of the Fourth International Congress for Applied Mechanics* (July 3–9, 1934). Cambridge, p. 175.

Dryden, H. L. (1937). *Air flow in the boundary layer near a plate.* NACA TR 562. Washington: National Advisory Committee for Aeronautics.

Dryden, H. L. (Jan. 1939). "Turbulence and the boundary layer". In: *Journal of the Aeronautical Sciences* 6.3, pp. 85–100.

Ehrenstein, U., Marquillie, M., and Eloy, C. (July 2014). "Skin friction on a flapping plate in uniform flow". In: *Philosophical Transactions of the Royal Society of London.* Series A. Mathematical, Physical and Engineering Sciences 372.2020, pp. 1–14.

Emmons, H. W. (July 1951). "The laminar-turbulent transition in a boundary layer—Part I". In: *Journal of the Aeronautical Sciences* 18.7, pp. 490–498.

Emmons, H. W. and Bryson, A. E. (1952). "The laminar-turbulent transition in a boundary layer—Part II". In: *Proceedings of the First U.S. National Congress of Theoretical and Applied Mechanics* (June 11–16, 1951). Chicago, pp. 859–868.

Erdogan, M. E. (Jan. 2000). "A note on an unsteady flow of a viscous fluid due to an oscillating plane wall". In: *International Journal of Non-Linear Mechanics* 35.1, pp. 1–6.

Falkner, V. M. and Skan, S. W. (Nov. 1931). "LXXXV. Solutions of the boundary-layer equations". In: *The London, Edinburgh, and Dublin Philosophical Magazine and Journal of Science* 12.80, pp. 865–896.

Fauci, L. J. and Peskin, C. S. (July 1988). "A computational model of aquatic animal locomotion". In: *Journal of Computational Physics* 77.1, pp. 85–108.

Freymuth, P. (Aug. 1966). "On transition in a separated laminar boundary layer". In: *Journal of Fluid Mechanics* 25.4, pp. 683–704.

Gao, Y.-y. et al. (Aug. 2017). "Experimental Study on Flow past A Rotationally Oscillating Cylinder". In: *China Ocean Engineering* 31.4, pp. 495–503.

Glauert, M. B. (May 1956). "The laminar boundary layer on oscillating plates and cylinders". In: *Journal of Fluid Mechanics* 1.1, pp. 97–110.

Glauert, M. B. and Lighthill, M. J. (June 1955). "The axisymmetric boundary layer on a long thin cylinder". In: *Proceedings of the Royal Society of London.* Series A. Mathematical, Physical and Engineering Sciences 230.1181, pp. 188–203.

Gray, J. (Jan. 1933a). "Studies in Animal Locomotion. I. The movement of fish with special reference to the eel". In: *Journal of Experimental Biology* 10.1, pp. 88–104.

Gray, J. (Oct. 1933b). "Studies in Animal Locomotion. II. The relationship between waves of muscular contraction and the propulsive mechanism of the eel". In: *Journal of Experimental Biology* 10.4, pp. 386–390.

Gray, J. (Apr. 1936a). "Studies in Animal Locomotion. VI. The propulsive powers of the dolphin". In: *Journal of Experimental Biology* 13.2, pp. 192–199.

Gray, J. (Apr. 1936b). "Studies in Animal Locomotion. IV. The neuromuscular mechanism of swimming in the eel". In: *Journal of Experimental Biology* 13.2, pp. 170–180.

Gray, J. (Apr. 1936c). "Studies in Animal Locomotion. V. Resistance reflexes in the eel". In: *Journal of Experimental Biology* 13.2, pp. 181–191.

Hansen, M. (1928). "Die Geschwindigkeitsverteilung in der Grenzschicht an einer eingetauchten Platte". In: *Zeitschrift für Angewandte Mathematik und Mechanik* 8.3, pp. 185–199. English translation in NACA Technical Memorandum 585.

Hultmark, M., Leftwich, M. C., and Smits, A. J. (Nov. 2007). "Flowfield measurements in the wake of a robotic lamprey". In: *Experiments in Fluids* 43.5, pp. 683–690.

Kelly, H. R. (1954). “A note on the laminar boundary layer on a circular cylinder in axial incompressible flow”. In: *Journal of the Aeronautical Sciences* 21.9, p. 634.

Kern, S. and Koumoutsakos, P. (Dec. 2006). “Simulations of optimized anguilliform swimming”. In: *Journal of Experimental Biology* 209.24, pp. 4841–4857.

Kestin, J., Maeder, P. F., and Wang, H. E. (Jan. 1961). “On boundary layers associated with oscillating streams”. In: *Applied Scientific Research* 10.1, pp. 1–22.

Keulegan, G. H. and Carpenter, L. H. (May 1958). “Forces on cylinders and plates in an oscillating fluid”. In: *Journal of Research of the National Bureau of Standards* 60.5, pp. 423–440.

King, R. (Sept. 1977). “Vortex excited oscillations of yawed circular cylinders”. In: *Journal of Fluids Engineering* 99.3, pp. 495–501.

Klebanoff, P. S., Tidstrom, K. D., and Sargent, L. M. (Jan. 1962). “The three-dimensional nature of boundary-layer instability”. In: *Journal of Fluid Mechanics* 12.1, pp. 1–34.

Kreplin, H.-P. and Eckelmann, H. (July 1979). “Behavior of the three fluctuating velocity components in the wall region of a turbulent channel flow”. In: *Physics of Fluids* 22.7, pp. 1233–1239.

Kumar, S. et al. (Nov. 2013). “Flow past a rotationally oscillating cylinder”. In: *Journal of Fluid Mechanics* 735, pp. 307–346.

Lauder, G. V. and Tytell, E. D. (2006). “Hydrodynamics of Undulatory Propulsion”. In: *Fish Biomechanics*. Vol. 23. Fish Physiology. Elsevier Inc, pp. 425–468.

Lee, S.-J. and Lee, J.-Y. (Sept. 2008). “PIV measurements of the wake behind a rotationally oscillating circular cylinder”. In: *Journal of Fluids and Structures* 24.1, pp. 2–17.

Leftwich, M. C. and Smits, A. J. (May 2011). “Thrust production by a mechanical swimming lamprey”. In: *Experiments in Fluids* 50.5, pp. 1349–1355.

Libby, P. A. (1996). *Introduction to Turbulence*. Combustion: An International Series. New York: Taylor & Francis.

Lighthill, M. J. (June 1954). “The response of laminar skin friction and heat transfer to fluctuations in the stream velocity”. In: *Proceedings of the Royal Society of London*. Series A. Mathematical, Physical and Engineering Sciences 224.1156, pp. 1–23.

Lighthill, M. J. (Oct. 1960). “Note on the swimming of slender fish”. In: *Journal of Fluid Mechanics* 9.2, pp. 305–317.

Lighthill, M. J. (Nov. 1970). “Aquatic animal propulsion of high hydromechanical efficiency”. In: *Journal of Fluid Mechanics* 44.2, pp. 265–301.

Lighthill, M. J. (Nov. 1971). “Large-amplitude elongated-body theory of fish locomotion”. In: *Proceedings of the Royal Society of London*. Series B. Biological Sciences 179.1055, pp. 125–138.

Lim, J. L. and Lauder, G. V. (July 2016). “Mechanisms of anguilliform locomotion in fishes studied using simple three-dimensional physical models”. In: *Bioinspiration & Biomimetics* 11.4, pp. 1–14.

Lueptow, R. M. (Sept. 1988). *Turbulent boundary layer on a cylinder in axial flow*. Tech. rep. 8389. New London, CT: Navy Underwater Systems Center.

Lueptow, R. M. and Haritonidis, J. H. (Oct. 1987). “The structure of the turbulent boundary layer on a cylinder in axial flow”. In: *Physics of Fluids* 30.10, pp. 2993–3005.

Miloh, T. and Galper, A. (Aug. 1993). “Self-propulsion of general deformable shapes in a perfect fluid”. In: *Proceedings of the Royal Society of London*. Series A. Mathematical, Physical and Engineering Sciences 442.1915, pp. 273–299.

Mittal, S. and Kumar, B. (Feb. 2003). “Flow past a rotating cylinder”. In: *Journal of Fluid Mechanics* 476, pp. 303–334.

Moré, J. J. (1978). “The Levenberg-Marquardt algorithm: Implementation and theory”. In: *Numerical Analysis: Proceedings of the Biennial Conference Held at Dundee, June 28–July 1, 1977.* Ed. by Watson, G. A. Vol. 630. Lecture Notes in Mathematics, pp. 105–116.

Müller, U. K., Smit, J., Stamhuis, E. J., and Videler, J. J. (Aug. 2001). “How the body contributes to the wake in undulatory fish swimming: flow fields of a swimming eel (*Anguilla anguilla*”. In: *Journal of Experimental Biology* 204.16, pp. 2751–2762.

Pedley, T. J. and Hill, S. J. (Dec. 1999). “Large-amplitude undulatory fish swimming: fluid mechanics coupled to internal mechanics”. In: *Journal of Experimental Biology* 202.23, pp. 3431–3438.

Potts III, J. B. (Dec. 2015). “Developing and testing an anguilliform robot swimming with theoretically high hydrodynamic efficiency”. PhD thesis. University of New Orleans. Paper 2103.

Prandtl, L. (1904). “Über Flüssigkeitsbewegungen bei sehr kleiner Reibung”. In: *Verhandlungen des Dritten Internationalen Mathematiker-Kongresses.* Heidelberg, pp. 484–491. English translation in NACA Technical Memorandum 452.

Raffel, M. et al. (2018). *Particle Image Velocimetry. A Practical Guide.* 3rd ed. Cham, Switzerland: Springer International Publishing AG.

Ramakrishnan, S. and Scheidegger, T. (Oct. 2016). “Overset Meshing in ANSYS Fluent”. In: *13th Symposium on Overset Composite Grids and Solution Technology* (Future of Flight Aviation Center, Oct. 17–20, 2016). Mukilteo, Washington.

Rozin, L. A. (1958). “The growth of a laminar boundary layer on a flat plate set impulsively into motion”. In: *Journal of Applied Mathematics and Mechanics* 22.3, pp. 568–575.

Rozin, L. A. (May 1960). *An approximation method for the integration of the equations of a nonstationary laminar boundary layer in an incompressible fluid.* NASA TT F-22. Washington: National Aeronautics and Space Administration.

Saffman, P. G. (May 1967). “The self-propulsion of a deformable body in a perfect fluid”. In: *Journal of Fluid Mechanics* 28.2, pp. 285–289.

Sarma, G. N. and El-Hadi, C. M. (1986). “Interaction of chord and spanwise oscillations in a flow past a yawed cylinder and asymptotic solutions”. In: *International Jounral of Engineering Schience* 24.5, pp. 675–684.

Sarpkaya, T. (July 1977). *Transverse oscillations of a circular cylinder in uniform flow, Part I.* NPS report 69SL77071. Monterey: Naval Post Graduate School.

Sarpkaya, T. (Aug. 1978). “Fluid forces on oscillating cylinders”. In: *Journal of The Waterway, Port, Coastal, and Ocean Division* 104.3, pp. 275–290.

Sarpkaya, T. (Nov. 1995). “Hydrodynamic damping, flow-induced oscillations, and biharmonic response”. In: *Journal of Offshore Mechanics and Arctic Engineering* 117.4, pp. 232–238.

Sarpkaya, T. (Apr. 2002). “Experiments on the stability of sinusoidal flow over a circular cylinder”. In: *Journal of Fluid Mechanics* 457, pp. 157–180.

Sarpkaya, T. (Nov. 2006). “Structures of separation on a circular cylinder in periodic flow”. In: *Journal of Fluid Mechanics* 567, pp. 281–297.

Schlichting, H. and Gersten, K. (2017). *Boundary-Layer Theory.* Trans. by Mayes, K. 9th ed. Springer-Verlag Berlin Heidelberg.

Schubauer, G. B. and Klebanoff, P. S. (1950). *Investigation of separation of the turbulent boundary layer*. NACA TN 2133. National Advisory Committee for Aeronautics.

Schubauer, G. B. and Klebanoff, P. S. (1955). *Contribution on the mechanics of boundary-layer transition*. NACA TN 3489. National Advisory Committee for Aeronautics. cf. also: NACA TR 1289 (1956).

Schubauer, G. B. and Skramstad, H. K. (Feb. 1947). "Laminar boundary-layer oscillations and stability of laminar flow". In: *Journal of the Aeronautical Sciences* 14.2, pp. 69–78.

Schubauer, G. B. and Skramstad, H. K. (1948). *Laminar boundary-layer oscillations and transition on a flat plate*. NACA TR 909. Washington: National Advisory Committee for Aeronautics.

Sears, W. R. (Jan. 1948). "The boundary layer of yawed cylinders". In: *Journal of the Aeronautical Sciences* 15.1, pp. 49–52.

Seban, R. A. and Bond, R. (Oct. 1951). "Skin-friction and heat-transfer characteristics of a laminar boundary layer on a cylinder in axial incompressible flow". In: *Journal of the Aeronautical Sciences* 18.10, pp. 671–675.

Shrestha, B., Ahsan, S. N., and Aureli, M. (Jan. 2018). "Experimental study of oscillating plates in viscous fluids: Qualitative and quantitative analysis of the flow physics and hydrodynamic forces". In: *Physics of Fluids* 30.1, pp. 1–16.

Spalart, P. R. and Baldwin, B. S. (May 1987). *Direct simulation of a turbulent oscillating boundary layer*. NASA TM 89460. National Aeronautics and Space Administration.

Srivastava, S. (2020). "Numerical Investigation into the Boundary Layer of a Robotic Anguilliform Propulsor". Unpublished manuscript.

Srivastava, S., Eastridge, J. R., Taravella, B. M., and Akyuzlu, K. M. (May 2019). "A Numerical Study of Laminar and Intermittently Turbulent Flow over a Flat Plate Using a Pseudo-Compressibility Model". In: *Proceedings of the ASME Verification and Validation Symposium* (Westgate Resorts, May 15–17, 2019). Les Vegas, Nevada.

Stokes, G. G. (1856). "On the effect of the internal friction of fluids on the motion of pendulums". In: *Transactions of the Cambridge Philosophical Society*. Vol. 9.2, pp. 8–106.

Taggart, R. (1969). *Marine Propulsion: Principles & Evolution*. Houston: Gulf Publishing Company.

Taravella, B. M. and Rogers, C. T. (Nov. 2017). "A computational fluid dynamics analysis of an ideal anguilliform swimming motion". In: *Marine Technology Society Journal* 51.6, pp. 21–32.

Taylor, G. (Aug. 1952). "Analysis of the swimming of long and narrow animals". In: *Proceedings of the Royal Society of London*. Series A. Mathematical, Physical and Engineering Sciences 214.1117, pp. 158–183.

Taylor, G. W. et al. (Oct. 2001). "The Energy Harvesting Eel a small subsurface oceanriver power generator". In: *IEEE Journal of Oceanic Engineering* 26.4, pp. 539–547.

Techet, A. H., Allen, J. J., and Smits, A. J. (May 2002). "Piezoelectric eels for energy harvesting in the ocean". In: *Proceedings of The Twelfth International Offshore and Polar Engineering Conference*. Kitakyushu, Japan: International Society of Offshore and Polar Engineers.

Triantafyllou, M. S., Triantafyllou, G. S., and Yue, D. K. P. (Jan. 2000). "Hydrodynamics of fishlike swimming". In: *Annual Review of Fluid Mechanics* 32.1, pp. 33–53.

Tropea, C., Yarin, A. L., and Foss, J. F., eds. (2007). *Springer Handbook of Experimental Fluid Mechanics*. Springer-Verlag Berlin Heidelberg.

Tytell, E. D. (Sept. 2004). "The hydrodynamics of eel swimming. II. Effect of swimming speed". In: *Journal of Experimental Biology* 207.19, pp. 3265–3279.

Tytell, E. D. and Lauder, G. V. (May 2004). "The hydrodynamics of eel swimming. I. Wake structure". In: *Journal of Experimental Biology* 207.11, pp. 1825–1841.

Van der Hegge Zijnen, B. G. (Oct. 1924). “Measurements of the velocity distribution in the boundary layer along a plane surface”. Thesis. Delft University of Technology.

Van Gorder, R. A. and Vajravelu, K. (June 2009). “Third-order partial differential equations arising in the impulsive motion of a flat plate”. In: *Communications in Nonlinear Science and Numerical Simulation* 14.6, pp. 2629–2636.

Vorus, W. S. (Jan. 2005). “Swimming of the semi-infinite strip revisited”. In: *Journal of Engineering Mathematics* 51.1, pp. 35–55.

Vorus, W. S. and Taravella, B. M. (June 2011). “Anguilliform fish propulsion of highest hydrodynamic efficiency”. In: *Journal of Marine Science and Application* 10.2, pp. 163–174.

Wang, R., Cheng, S., and Ting, D. S.-K. (Jan. 2019). “Effect of yaw angle on flow structure and cross-flow force around a circular cylinder”. In: *Physics of Fluids* 31.1, pp. 014107-1–15.

White, F. M. (1969). *Axisymmetric turbulent boundary layer on an extremely long cylinder.* Tech. rep. 1058. New London, CT: Navy Underwater Sound Laboratory.

White, F. M. (2006). *Viscous Fluid Flow.* 3rd ed. New York: McGraw-Hill, Inc.

Wolfgang, M. J. et al. (Sept. 1999). “Near-body flow dynamics in swimming fish”. In: *Journal of Experimental Biology* 202.17, pp. 2303–2327.

Wu, T. Y.-T. (May 1961). “Swimming of a waving plate”. In: *Journal of Fluid Mechanics* 10.3, pp. 321–344.

Wu, T. Y.-T. (Mar. 1971a). “Hydromechanics of swimming propulsion. Part 1. Swimming of a two-dimensional flexible plate at variable forward speeds in an inviscid fluid”. In: *Journal of Fluid Mechanics* 46.2, pp. 337–355.

Wu, T. Y.-T. (Apr. 1971b). “Hydromechanics of swimming propulsion. Part 2. Some optimum shape problems”. In: *Journal of Fluid Mechanics* 46.3, pp. 521–544.

Young, A. D. (Apr. 1939). *The calculation of the total and skin friction drags of bodies of revolution at zero incidence.* Reports and Memoranda 1874. Aeronautical Research Committee.

Vita

Jonathan Eastridge was born in Charlotte, North Carolina in 1992, was raised in Clover, South Carolina, and is the younger of two sons to Tom and Laura Eastridge. In 2013 he moved to New Orleans, Louisiana to study Naval Architecture and Marine Engineering at the University of New Orleans. He enjoys reading nautical fiction and non-fiction, being active in his local church, motorcycling, exercising, hiking, and mostly any other outdoor activity. Overall, he has enjoyed his time spent pursuing a PhD but is glad to have reached its completion. Currently residing in Metairie, Louisiana, Jonathan and his wife, Kristy, excitedly anticipate a new chapter in life.

levo oculos meos in montes (ps. 121)